The University Of Sheffield.

The Role of Dystroglycan in Nuclear Mechanics

Ben Stevenson

A thesis submitted in partial fulfilment of the requirements for the degree of Doctor of Philosophy

The University of Sheffield
Faculty of Science
Department/School of Biomedical Science

July 2021

Abstract

It has recently been suggested that β-dystroglycan localises to the nucleus in a range of cell types. At the nucleus it is thought that β-dystroglycan plays a role in maintaining nuclear morphology and regulating structural nuclear proteins lamin B1 and emerin in mouse C2C12 myoblasts. It is hypothesised that β-dystroglycan is involved in regulating the mechanical properties of nuclei through interactions with lamin B1 and emerin or by adding additional support to the Linker of Nucleoskeleton and Cytoskeleton complex. This hypothesis was investigated using CRISPR/Cas9 disruption of the dystroglycan gene (*DAG1*) in human myoblast cells. In this *DAG1* disrupted cell line, the previous reports of abnormal nuclear shape were not observed, however, it was found that both nuclear and cell size was greater in *DAG1* disrupted cells. This increase in size was also rescued by the addition of exogenous dystroglycan. The increase in size was not due to a senescence phenotype as previously suggested, however, the reason for an increase in size has yet to be fully understood.

As with nuclear shape, the previously reported abnormal levels and localisation of lamin B1 and emerin in *DAG1* disrupted C2C12 cells were not observed in the human myoblasts. Further, following analysis of nuclear mechanical properties of *DAG1* disrupted and control cells using atomic force microscopy it was found that there was no difference in nuclear mechanics at a whole cell level. However, when nuclei were isolated from the whole cell environment, the *DAG1* disrupted nuclei were less stiff than control nuclei.

The results described here suggest that disruption of the *DAG1* gene has little effect on nuclear shape, regulation of nuclear proteins or nuclear mechanics. This suggests previously published results from C2C12 mouse myoblasts are not universal across cell lines and species and may require broader investigation.

Acknowledgements

There are many people who have helped me get through this PhD and I am immensely thankful to everyone who has been a part of it. Firstly, I would like to thank my supervisors Steve Winder and Jamie Hobbs for giving me the opportunity to complete my PhD with them and for giving me the confidence to believe in my own results even if they go against what has been done previously. I would like to thank my advisor Kai Erdmann for providing useful discussions about the project. I would also like to thank Nic and Xinyue for training me on the AFM and always being there to fix problems that came up. Thank you to Chris Hill for carrying out all EM work. All members of the KA/SW/ER lab for helpful scientific discussions, but more importantly for the non-scientific chats. I would like to thank Adam for putting up with making almost all the communal solutions when I hadn't done it, Mona for constantly reminding me to clean TC despite my best efforts to evade it and Stella for turning any calm and peaceful situation into one of complete panic.

To those outside of the lab who have helped keep me sane over the last 4 years, particularly George, Tom, Josh and Cieran. The constant entertainment of pub visits, pub quizzes, catan evenings and even FIFA spankings that helped remind me that there is life outside the lab. Also, a huge thank you to all my friends both in Sheffield and outside for again providing an interesting social life away from the lab.

Finally, to those who mean the world to me. My family, Mum and Dad for supporting me throughout life whether that is taking me to tennis as a youngster, driving a 6-hour round trip to pick me up from Uni or just being proud of everything I do. My amazing wife Sarah, whom I couldn't function without. Nan and Nanna who have always been the proudest grandparents and the best people to be around. Last but not least, Daniel, Emily and the newest, fluffiest member of the Stevenson family, Blue. Thank you to all of you!

Contents

Abstract **2**

Acknowledgements **4**

List of Figures **9**

List of tables **12**

Abbreviations **13**

1 Introduction ***16***

1.1 Dystroglycan **16**
1.1.1 *DAG1* Gene and Biosynthesis 16
1.1.2 α-dystroglycan 18
1.1.3 β-dystroglycan 26
1.1.4 The Role of Dystroglycan at the Plasma Membrane 37
1.1.5 Dystroglycan and Disease 45

1.2 Nuclear Dystroglycan **50**
1.2.1 Dystrophin Associated Protein Complex in the Nucleus 50
1.2.2 Nuclear Import and Export of β-dystroglycan 53
1.2.3 Role of β-dystroglycan in the Nucleus 56

1.3 Project Hypothesis **63**

2 Materials and Methods ***65***

2.1 Bacteria and Molecular Biology **65**
2.1.1 Bacterial Growth 65
2.1.2 Transformation of Competent Bacteria 65
2.1.3 Bacterial Glycerol Stocks 66
2.1.4 Plasmid Purification 66
2.1.5 DNA Sequencing 66

2.2 Cell Culture **67**
2.2.1 Growth of Cells 67
2.2.2 Cell Counting 67
2.2.3 Cell Seeding Based on Confluency 68
2.2.4 Cell Synchronisation with Thymidine Block 68
2.2.5 Cell Synchronisation with Serum Starvation 68
2.2.6 Lipofectamine 2000 Cell Transfection 69

2.3 Atomic Force Microscopy **70**
2.3.1 Whole Cell Sample Preparation 70
2.3.2 Trichostatin A Treatment 70
2.3.3 Cytochalasin D Treatment 70
2.3.4 Poly-L-Lysine Coating of Dishes 70
2.3.5 Nuclear Sample Preparation 71
2.3.6 AFM Cantilever Preparation 72
2.3.7 Whole Cell Data Acquisition 72
2.3.8 Nucleus Data Acquisition 73
2.3.9 Data Analysis 73

2.4 Microscopy **74**
2.4.1 Immunofluorescence Microscopy 74
2.4.2 Leica Fluorescence Microscope 75
2.4.3 Nikon A1 Confocal 75
2.4.4 Live Cell Imaging for Cell Migration 76

2.4.5 Propidium Iodide Staining for FACS 77
2.4.6 Fluorescence-Activated Cell Sorting (FACS) 77
2.4.7 Scanning Electron Microscopy 77

2.5 Image Analysis 78
2.5.1 Nuclear Morphology 78
2.5.2 Nuclear/Cell Area Ratio 78
2.5.3 Nuclear Fluorescence Intensity Quantification 78
2.5.4 Cell Migration 79

2.6 Biochemistry 80
2.6.1 Whole Cell Lysate Sample Preparation 80
2.6.2 Nuclear Fractionation Sample Preparation 80
2.6.3 Determining Protein Concentration 80
2.6.4 SDS-Polyacrylamide Gel Electrophoresis (SDS-PAGE) 80
2.6.5 Electrotransfer 81
2.6.6 Western Blotting 81
2.6.7 Membrane Stripping 82
2.6.8 Quantification of Western Blots 82

2.7 Cellular Stress Assays 84
2.7.1 Oxidative Stress 84
2.7.2 Osmotic Stress 84
2.7.3 Mechanical Stress 84

3 Investigating the effect of disrupting DG on nuclear morphology of human myoblast cells 86

3.1 Introduction 86
3.1.1 Nuclear Shape 86
3.1.2 Nuclear Membrane Integrity 87
3.1.3 Nuclear Size 89
3.1.4 Hypothesis and Aims 91

3.2 Results 92
3.2.1 β-DG localises to the nucleus in KM155 human myoblast cell lines 92
3.2.2 *DAG1* disruption results in loss of β-DG protein 95
3.2.3 The effect of *DAG1* disruption on nuclear shape in KM155 cells 98
3.2.4 Comparing the nuclear and cell size of control and *DAG1* KO cells 103
3.2.5 Is increased nuclear size and cell size in *DAG1* KO cell lines due to an increase in cellular senescence? 112
3.2.6 Is increased nuclear and cell size in *DAG1* KO cell lines due to changes in nuclear proteins lamin A/C, lamin B1 or emerin? 117

3.3 Discussion 130
3.3.1 Limitations of β-DG antibodies 130
3.3.2 Differences in observed nuclear shape phenotype 132
3.3.3 Differences in observed nuclear size phenotype 134
3.3.4 Differences in observed nuclear envelope protein levels and localisation 136

4 Investigating the effect of perturbing DAG1 on the inherent mechanical properties of myoblast nuclei using atomic force microscopy (AFM) 139

4.1 Introduction 139
4.1.1 Mechanical properties of cells and nuclei are determined by the cytoskeleton, nucleoskeleton and chromatin 139
4.1.2 Hypothesis and Aims 142

4.2 Results 142
4.2.1 Optimising the functionalisation of tipless cantilevers with 5μm polystyrene beads 142

4.2.2 Force mapping of a single control cell in order to determine height and stiffness of different cellular regions 145
4.2.3 Investigating the mechanical properties of asynchronous populations of control and *DAG1* KO cells 147
4.2.4 Investigating the mechanical properties of synchronised control and *DAG1* KO cells 151
4.2.5 Investigating the mechanical properties of synchronised control and *DAG1* KO cells following trichostatin A treatment 159
4.2.6 Investigating the mechanical properties of synchronised control and *DAG1* KO cells following Cytochalasin D treatment 162
4.2.7 Investigating the relationship between nuclear area and nuclear stiffness in control and *DAG1* KO cells 167
4.2.8 Optimisation of nuclear isolation in order to measure mechanical properties of isolated nuclei 169
4.2.9 Investigating the mechanical properties of nuclei isolated from control and *DAG1* KO myoblast cells 173

4.3 Discussion 176
4.3.1 Comparison of Young's moduli 176
4.3.2 Reasons for variations in measurements 177
4.3.3 Differences in Young's modulus of isolated nuclei 178

5 Investigating the role of DG in maintaining nuclear morphology and DNA integrity following mechanical stress 181

5.1 Introduction 181
5.1.1 Extreme cell/ nuclear compression results in an accumulation of DNA damage 181
5.1.2 Cyclic cell stretching results in cyto- and nucleoskeleton reorganisation in order to minimise DNA damage 185
5.1.3 Sheer stress results in changes in nuclear architecture 186
5.1.4 Hypothesis and aims 187

5.2 Results 188
5.2.1 Determining baseline levels of DNA damage and nuclear morphology prior to mechanical and chemical stress 188
5.2.2 Investigating the response of control and *DAG1* KO cells to oxidative stress following treatment with H_2O_2 190
5.2.3 Investigating the response of control and *DAG1* KO cells to osmotic stress following treatment with NaCl and PEG 194
5.2.4 Investigating the response of control and *DAG1* KO cells to nuclear compression following migration through narrow pores 202
5.2.5 Investigating the response of control and *DAG1* KO cells to nuclear compression *in situ* 209

5.3 Discussion 212
5.3.1 Discrepancies from PEG4000 treatment 212
5.3.2 Observations from Transwell migration experiments 214
5.3.3 Limitations of passive cell compression assay 217
5.3.4 Other forms of mechanical stress that were investigated 218

6 Discussion 220

6.1 Role of DG in the nucleus 220
6.1.1 Nuclear localisation of β-DG 220
6.1.2 Regulation of the levels and localisation of lamin B1 and emerin 223
6.1.3 Contribution to mechanical properties of myoblast nuclei 224

6.2 Conclusions and future work 226

7 References 228

List of Figures

Figure 1.1 Schematic of DAG1 gene and DG protein. 18
Figure 1.2 Structure of Core M1, M2 and M3 O-glycans associated with α-DG. 21
Figure 1.3 Schematic of the interacting partners of a-DG containing laminin globular domains. 25
Figure 1.4 Schematic of β-DG. 27
Figure 1.5 Schematic of the components and organisation of the DAPC. 38
Figure 1.6 Schematic depicting the domain organisation of different dystrophin isoforms and utrophin. 40
Figure 1.7 Schematic illustrating the retrograde trafficking of β-DG from the PM to the NE via the ER. 55
Figure 3.1 Immunofluorescence staining with the β-DG antibodies MANDAG2, LG5, JAF1, C20 and 1709 demonstrate nuclear localisation. 93
Figure 3.2 Cell fractionation demonstrates the nuclear localisation of β-DG. 94
Figure 3.3 Disruption of the DAG1 gene in human myoblasts results in a reduction in β-DG immunofluorescence staining. 97
Figure 3.4 Disruption of the DAG1 gene in human myoblasts results in a loss of β-DG in a western blot analysis. 98
Figure 3.5 Representative nuclei from control and DAG1 KO clones. 99
Figure 3.6 Average nuclear circularity of control and DAG1 KO clones A-E using DAPI to identify the nuclear region. 100
Figure 3.7 Average nuclear circularity of control and DAG1 KO clones A and B using DAPI or lamin B1 to identify the nuclear region and imaged using two different microscopes. 101
Figure 3.8 Average nuclear sphericity of control and DAG1 KO clone B using DAPI to identify the nuclear region. 102
Figure 3.9 Percentage of control or DAG1 KO clone A-E cells that had micronuclei. 103
Figure 3.10 Average nuclear area of control and DAG1 KO clones A-E using DAPI to identify the nuclear region. 105
Figure 3.11 Average nuclear area of control and DAG1 KO clones A and B using DAPI or lamin B1 to identify the nuclear region and imaged using two different microscopes. 106
Figure 3.12 Average nuclear volume of control and DAG1 KO clone B using DAPI to identify the nuclear region. 107
Figure 3.13 DAG1 KO cells are larger than control cells and cell size scales with nuclear size. 108
Figure 3.14 Representative images of control and DAG1 KO clones B-C transiently transfected with GFP or HA and Myc tagged DG. 110
Figure 3.15 Average nuclear area of control and DAG1 KO clones B-C following transient transfection of GFP or HA & Myc tagged DG. 111
Figure 3.16 Proliferation of control and DAG1 KO clones A-E over 8 days. 113
Figure 3.17 Relative H3K9me3 intensity for control and DAG1 KO clones A-E. 115
Figure 3.18 Relative γH2AX intensity for control and DAG1 KO clones A-E. 116
Figure 3.19 Relative Lamin A/C intensity for control and DAG1 KO clones A-B at a low cell density determined by immunofluorescence. 118
Figure 3.20 Relative Lamin A/C intensity for control and DAG1 KO clones A-B at a high cell density determined by immunofluorescence. 120
Figure 3.21 Relative Lamin A/C levels of control and DAG1 KO clones A-B at a high cell density determined by western blot. 121
Figure 3.22 Relative Lamin B1 intensity for control and DAG1 KO clones A-B at a low cell density determined by immunofluorescence. 122
Figure 3.23 Relative Lamin B1 intensity for control and DAG1 KO clones A-B at a high cell density determined by immunofluorescence. 124
Figure 3.24 Relative Lamin B1 levels of control and DAG1 KO clones A-B at a high cell density determined by western blot. 125
Figure 3.25 Relative nuclear Emerin intensity for control and DAG1 KO clones A-B at a low cell density determined by immunofluorescence. 126
Figure 3.26 Relative whole cell Emerin intensity for control and DAG1 KO clones A-B at a low cell density determined by immunofluorescence. 127

Figure 3.27 Relative emerin intensity for control and DAG1 KO clones A-B at a high cell density determined by immunofluorescence. 128
Figure 3.28 Relative Emerin levels of control and DAG1 KO clones A-B at a high cell density determined by western blot. 129
Figure 3.29 Cross-reactivity between β-DG antibody C-20 and emerin antibody in KM155 human myoblast cells. 132
Figure 4.1 SEM of MLCT-O10 cantilevers. 144
Figure 4.2 Topographical height map of gRNA control cell. 145
Figure 4.3 Modulus maps of a gRNA control cell. 146
Figure 4.4 Measurements of whole cells using AFM. 148
Figure 4.5 No difference in average nuclear Young's modulus between control and DAG1 KO cell lines in asynchronous populations. 149
Figure 4.6 No difference in average cytoplasmic Young's modulus between control and DAG1 KO cell lines in asynchronous populations. 150
Figure 4.7 Comparison between nuclear and cytoplasmic Young's modulus of asynchronous control and DAG1 KO cell lines. 151
Figure 4.8 Cell cycle synchronisation of control cells using double thymidine block and serum starvation. 152
Figure 4.9 Average nuclear Young's modulus of control and DAG1 KO cell lines in G1 synchronised populations using functionalised cantilevers. 153
Figure 4.10 Average nuclear Young's modulus of control and DAG1 KO cell lines in G1 synchronised populations using commercial cantilevers. 155
Figure 4.11 Average cytoplasmic Young's modulus of control and DAG1 KO cell lines in G1 synchronised populations using functionalised cantilevers. 156
Figure 4.12 Average cytoplasmic Young's modulus of control and DAG1 KO cell lines in G1 synchronised populations using commercial cantilevers. 157
Figure 4.13 Comparison between nuclear and cytoplasmic Young's modulus of G1 synchronised control and DAG1 KO cell lines measured with functionalised cantilevers. 158
Figure 4.14 Comparison between nuclear and cytoplasmic Young's modulus of G1 synchronised control and DAG1 KO cell lines measured with commercial cantilevers. 158
Figure 4.15 Treatment with Trichostatin A results in an increase in nuclear area. 159
Figure 4.16 Average nuclear Young's modulus of control and DAG1 KO cell lines following 300nM Trichostatin A treatment using functionalised cantilevers. 160
Figure 4.17 Treatment of 300nM Trichostatin A for 24 hours results in a decrease in nuclear Young's modulus in control and DAG1 KO cell lines. 161
Figure 4.18 Comparison between nuclear and cytoplasmic Young's modulus of control and DAG1 KO cell lines following 300nM Trichostatin A treatment using functionalised cantilevers. 161
Figure 4.19 Treatment with varying concentrations of cytochalasin D result in perturbation of actin filaments. 163
Figure 4.20 Average nuclear Young's modulus of control and DAG1 KO cell lines following 500nM cytochalasin D treatment using functionalised cantilevers. 164
Figure 4.21 Average cytoplasmic Young's modulus of control and DAG1 KO cell lines following 500nM cytochalasin D treatment using functionalised cantilevers. 165
Figure 4.22 Treatment with 500nM Cytochalasin D for 24 hours results in a decrease in nuclear and cytoplasmic Young's modulus in control and DAG1 KO cell lines. 166
Figure 4.23 Comparison between nuclear and cytoplasmic Young's modulus control and DAG1 KO cell lines following 500nM CytoD treatment using functionalised cantilevers. 167
Figure 4.24 There is no correlation between nuclear size and nuclear Young's modulus in control cells. 168
Figure 4.25 There is no correlation between nuclear size and nuclear Young's modulus in control and DAG1 KO cells. 169
Figure 4.26 Nuclear isolation methods. 171
Figure 4.27 Refined method of nuclear isolation involved mechanical lysis followed by high-molar sucrose gradient evaluated by microscopy. 172
Figure 4.28 Refined method of nuclear isolation involved mechanical lysis followed by high-molar sucrose gradient evaluated by western blotting. 173

Figure 4.29 Isolated nuclei from DAG1 KO cells are less stiff than isolated nuclei from control cells. 175
Figure 5.1 Baseline averages for nuclear morphology and levels of γH2AX in control and DAG1 KO clones A and B without additional cell stress. 189
Figure 5.2 Optimisation of H_2O_2 concentration. 191
Figure 5.3 Average nuclear levels of γH2AX in control and DAG1 KO clones A and B with and without H_2O_2 treatment. 192
Figure 5.4 Nuclear morphology of control and DAG1 KO clones A and B with and without H_2O_2 treatment. 193
Figure 5.5 Optimisation of NaCl concentration based on nuclear area of control cells. 195
Figure 5.6 Average nuclear levels of γH2AX in control and DAG1 KO clones A and B following 0mM, 200mM or 500mM NaCl treatment. 196
Figure 5.7 Nuclear morphology of control and DAG1 KO clones A and B following 0mM, 200mM or 500mM NaCl treatment. 198
Figure 5.8 Optimisation of PEG4000 concentration based on nuclear area of control cells. 199
Figure 5.9 Average nuclear levels of γH2AX in control and DAG1 KO clones A and B following 0%, 20% or 40% PEG4000 treatment. 201
Figure 5.10 Nuclear morphology of control and DAG1 KO clones A and B following 0%, 20% and 40% PEG4000 treatment. 202
Figure 5.11 Migration velocity and distance in control and DAG1 KO clones A and B. 204
Figure 5.12 Average nuclear levels of γH2AX in control and DAG1 KO clones A and B before and after migration through 8μm pores. 205
Figure 5.13 Nuclear morphology of control and DAG1 KO clones A and B before and after migration through 8μm pores. 206
Figure 5.14 Average nuclear levels of γH2AX in control and DAG1 KO clones A and B before and after migration through 3μm pores. 207
Figure 5.15 Nuclear morphology of control and DAG1 KO clones A and B before and after migration through 3μm pores. 208
Figure 5.16 Nuclear morphology of control and DAG1 KO clones A and B subjected to passive compressional stress. 210
Figure 5.17 Mechanical response to cell compression. 211

List of tables

Table 1.1 List of species DG has been identified in and the protein and DNA similarity to human DG. 16
Table 1.2 List of possible glycosylation sites of α-DG. 21
Table 1.3. Table of the binding affinities for α-DG and different types of laminin. 23
Table 2.1 List of cells used. 67
Table 2.2 List of primary antibodies used for immunofluorescence detection. 74
Table 2.3 List of secondary antibodies used for immunofluorescence detection. 75
Table 2.4 List of primary antibodies used for western blotting. 82
Table 2.5 List of secondary antibodies used for western blotting. 82

Abbreviations

A.U – Airy units

ABD – Actin binding domain

AChR – Acetylcholine receptor

AFM – Atomic force microscopy

AQP – Aquaporin

CH – Calponin homology

CMD – Congenital muscular dystrophy

Co-IP – Co-immunoprecipitation

Control – gRNA control

CytoD – Cytochalasin D

DABCO - 1,4-Diazabicyclo[2.2.2] octane

DAPC – Dystrophin associated protein complex

DG – Dystroglycan

DGC – Dystrophin glycoprotein complex

E – Young's modulus

ECM – Extracellular matrix

EDMD – Emery-Dreifuss muscular dystrophy

ER – Endoplasmic Reticulum

ERK – Extracellular signal regulated kinase

FCMD – Fukuyama-type congenital muscular dystrophy

GalNAc – N-acetylgalactosamine

GlcNAc – N-acetylglucosamine

ICD – Intracellular domain

INM – Inner nuclear membrane

KASH – Klarsicht, ANC-1, Syne homology

KD – Knockdown

KO – Knockout

LCMV – Lymphocytic chorionic meningitis virus

LEM – Lap2-Emerin-Man1

LFV – Lassa fever virus

LG – Laminin globular

LGMD – Limb girdle muscular dystrophy

LINC – Linker of nucleoskeleton and cytoskeleton

LMB – Leptomycin B

MD – Muscular dystrophy

MDDG – Muscular dystrophy dystroglycanopathy

MEF – Mouse embryonic fibroblast

MEK2 – Mitogen-activated protein kinase kinase 2

MMP – Matrix metalloproteinase

N/C – Nuclear/cytoplasmic

NE – Nuclear envelope

NES – Nuclear export signal

NLS – Nuclear localisation signal

NMJ – Neuromuscular junction

NPC – Nuclear pore complex

OE – Overexpression

OMIM – Online mendelian inheritance in man

ONM – Outer nuclear membrane

PBS – Phosphate buffered saline

PEG4000 – Polyethylene glycol 4000

PFA – Paraformaldehyde

PM – Plasma Membrane

PVDF – Polyvinylidene fluoride membrane

r – Correlation coefficient

Rapsyn – Receptor associated protein at synapse

RIPA – Radio immunoprecipitation assay buffer

SDS-PAGE – SDS-polyacrylamide gel electrophoresis

SEA – Sea urchin, enterokinase, agrin

SH2 – Src-homology 2

SH3 – Src-homology 3

SUN – Sad and UNC-84

TM – Transmembrane

TSA – Trichostatin A

UAPC – Utrophin associated protein complex

UBF – Upstream binding factor

WCL – Whole cell lysate

WT – Wild-type

WWS – Walker-Warburg syndrome

1 Introduction

1.1 Dystroglycan

1.1.1 *DAG1* Gene and Biosynthesis

The human *DAG1* gene is 2685 base-pairs (excluding introns) and is located on chromosome 3 at band p21. The gene consists of three exons and two introns, the smaller intron is located 5' of the ATG region while the larger intron is 3' of the ATG region (Figure *1.1*) (Gee et al., 1993; Ibraghimov-Beskrovnaya et al., 1993; Smalheiser and Schwartz, 1987). The gene organisation is highly conserved across the metazoan phyla with the large intron 3' of the ATG region conserved across the whole phyla. The small intron 5' of the ATG region is conserved except in cnidaria, placozoa or porifera (Brancaccio and Adams, 2017).

The *DAG1* gene is transcribed into a single mRNA which encodes the dystroglycan (DG) precursor protein. *DAG1* is ubiquitously expressed in human adult and foetal tissue (Ibraghimov-Beskrovnaya et al., 1993). In addition to the ubiquitous expression in human tissue, *DAG1* is highly conserved in vertebrates and somewhat conserved in invertebrates (Table *1.1*). Despite a lack of sequence similarity the general domain structure of the protein is conserved across the metazoan phyla (Adams and Brancaccio, 2015). As the majority of studies involving DG use either human or mouse cell lines or mouse models, further reference to DG will discuss mammalian DG unless otherwise stated and the human numbering system will be used.

Table 1.1 **List of species DG has been identified in and the protein and DNA similarity to human DG**.

Species	NCBI Gene ID	Gene Name	% Protein Identity	% DNA Identity
Vertebrates				
H. sapiens	1605	DAG1	100	100
P. troglodytes	460372	DAG1	99.4	99.6

M. mulatta	706179	DAG1	97.7	98.0
C. lupus	476623	DAG1	95.2	88.8
M. musculus	13138	Dag1	93.5	87.0
B. taurus	281439	DAG1	93.2	87.8
R. norvegicus	114489	Dag1	92.9	86.0
G. gallus	100049058	DAG1	77.2	73.0
X. tropicalis	549272	dag1	69.9	66.9
X. laevis	Xenbase Gene ID: XB-GENE-1015774	dag1	67.3	
D. rerio	286829	dag1	64.8	63.3
Invertebrates				
D. melanogaster	UniPort: Q8STB9	Dg	32.8	
C. elegans	UniPort: Q22629	dgn-1	23.72	

The translation of the *DAG1* mRNA produces a 97kDa precursor protein which consists of a signal peptide (aa 1-29), α-DG subunit (aa 30-653) and a β-subunit (aa 654-895) (Figure *1.1b*). The cleavage of the precursor protein into the α- and β-subunits occurs between Gly653 and Ser654 and occurs upon translocation to the endoplasmic reticulum (ER) (Akhavan et al., 2008; Deyst et al., 1995; Esapa et al., 2003; Holt et al., 2000). The cleavage event is the result of an autoproteolytic SEA (sea urchin, enterokinase, agrin) domain identified in DG. SEA domains have been mostly characterised in mucin proteins such as MUC1 (Macao et al., 2006). Although the exact mechanism of cleavage has not been described for DG, it has been determined that the cleavage occurs between Gly653 and Ser654 located in the loop connecting sheets β2 and β3 of the SEA domain (Akhavan et al., 2008). The cleavage site of MUC1 is also located between a Gly and Ser on the connecting loop of β2 and β3 and the cleavage is facilitated by conformational strain within the loop region (Macao et al., 2006). It is highly likely that DG autoproteolysis occurs via the same mechanism. Interestingly, one study suggests that the inhibition of the proteasome via lactacystin prevents cleavage of the DG precursor, however, this has not been tested in other members of the SEA domain family (Esapa et al., 2003).

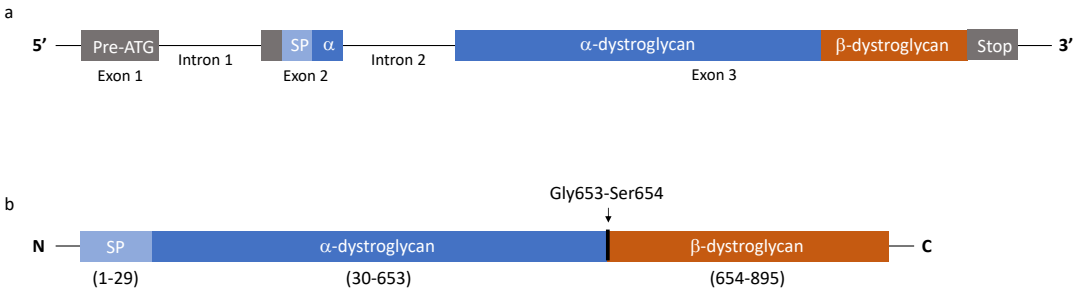

Figure 1.1 **Schematic of *DAG1* gene and DG protein.** (a) schematic of the DAG1 gene. (b) Schematic of the DG protein.

Following the cleavage of precursor DG into the α- and β-subunits within the ER, the two subunits are translocated to the plasma membrane (PM) via the secretory pathway. During this translocation both subunits are subject to post-translational modifications, specifically glycosylation (Barresi and Campbell, 2006). Glycosylation is not required for cleavage of the DG precursor (Holt et al., 2000) and DG targeting to the PM was not dependent on precursor cleavage (Esapa et al., 2003). Post-translational modifications will be discussed in detail in the following sections however, there is contradicting evidence as to whether glycosylation is essential for localisation of DG to the PM. Holt (2000) and colleagues found that upon treatment with tunicamycin, an inhibitor of N-linked glycosylation, there was aberrant β-DG localisation. Without treatment β-DG localised to the PM and following tunicamycin treatment β-DG showed perinuclear localisation. However, this study did not address the contribution of O-linked glycosylation. On the other hand, Esapa (2003) and colleagues showed that inhibiting both N- and O-linked glycosylation did not prevent the targeting of α-DG to the PM. This would appear to disagree with data from Holt's (2000) study, however, both studies are looking at the localisation of the two different subunits. Taken together these two studies suggest abnormal glycosylation may have different effects on the localisation of α- and β-subunits.

1.1.2 α-dystroglycan

1.1.2.1 Structure

The structure of α-DG was first investigated in 1995 with the use of electron microscopy (EM). Brancaccio and colleagues used isolated α-DG from chicken cardiac muscle and were able to determine that α-DG had a dumbbell shape. The N- and C-terminus of α-DG formed globular domains separated by an elongated disordered region termed the mucin-like region (Brancaccio et al., 1995). Based on sequence analysis the mucin region contained more than 40 Ser/Thr residues and a high number of Pro residues (Brancaccio et al., 1995). Due to the highly disordered mucin-like region it has so-far not been possible to generate any high-resolution structural information of full-length α-DG. The globular N-terminus of human and murine α-DG has been determined to a high resolution using X-ray crystallography (Bozic et al., 2004; Bozzi et al., 2015; Covaceuszach et al., 2017a, 2017b). However, no structure has been determined for the central mucin domain or the globular C-terminal domain.

1.1.2.2 Glycosylation of α-Dystroglycan

As discussed above α-DG is post-translationally cleaved from the DAG1 precursor protein, α-DG then goes through extensive glycosylation before reaching the PM. Glycans that are associated with glycoproteins such as α-DG can be divided into two groups depending on the amino acids they link to. Glycans that are linked to asparagine residues are termed *N*-glycans while glycans linked to either a serine or threonine residue are termed *O*-glycans. For *N*-linked glycans a *N*-acetylglucosamine (GlcNAc) moiety is linked to the Asn residue via an aspartylglycosylamine linkage. Classically for *O*-linked glycans, a *N*-acetylgalactosamine (GalNAc) moiety is linked to the Ser or Thr residue via the hydroxyl group. In addition to the Ser/Thr-GalNAc there are alternative types of *O*-glycosylation such as *O*-mannosylation which is found extensively in α-DG (Nilsson et al., 2010; Stalnaker et al., 2010).

The extent of α-DG glycosylation was originally determined by SDS-PAGE. The predicted M_w of α-DG is ~74kDa however the observed M_w is significantly higher than that with a mass of between 100-156kDa in kidney, 120kDa in brain, peripheral nerve

and smooth muscle, 140kDa in cardiac muscle, 150kDa in lung tissue, 156kDa in epithelia and skeletal muscle and 190kDa in Torpedo electric organ (Barresi and Campbell, 2006; Martin, 2003). In addition to differences between tissues there are also differences within tissues at different developmental stages (Leschziner et al., 2000). This disparity between apparent M_w and predicted M_w is due to the extensive glycosylation of α-DG which appears to be tissue specific. It was initially confirmed that α-DG contains *N*-linked glycans. However, when α-DG was treated with *N*-glycosidase F which specifically removes *N*-glycans, the apparent M_w only decreased by 4kDa, suggesting the majority of glycosylation is the *O*-linked form (Ervasti and Campbell, 1991). Further investigation of α-DG revealed that a high proportion of *O*-glycans were *O*-mannosyl glycans (Chiba et al., 1997; Sasaki et al., 1998).

α-DG consists of three main types of *O*-glycans which have been designated Core M1, M2 and M3 (Figure *1.2*). These three core structures all consist of Ser/Thr linked mannose and have similarities in their biosynthesis. The structure of Core M1 consists of a GlcNAc linked to the mannose, Core M2 is branched with two GlcNAc moieties linked to the mannose and Core M3 consists of GlcNAc and a phosphorylated mannose (Yoshida-Moriguchi et al., 2013). For all of these core *O*-glycan scaffolds, additional sugar moieties can be added (Meng et al., 2018).

In addition to *O*-mannosyl links there is also extensive *O*-GalNAc glycosylation of α-DG, however, the exact mechanisms of this have not been as extensively studied as *O*-mannosylation. A large number of the potential glycosylation sites of α-DG have been identified (Table *1.2*) while three studies have looked at the types of α-DG *O*-linked glycosylation in skeletal muscle of rabbit (Stalnaker et al., 2010), mouse (Harrison et al., 2012) and human (Nilsson et al., 2010). These studies agree that the type of glycosylation (*O*-mannosyl and *O*-GalNAcsyl) is not residue specific, both types have been detected using mass spectrometry (MS) at all identified *O*-glycosylation sites apart from Thr^{367} and Thr^{369} which have only identified *O*-Man-linked glycans (Nilsson et al., 2010). This suggests that the type of glycosylation does not depend on the primary sequence of α-DG.

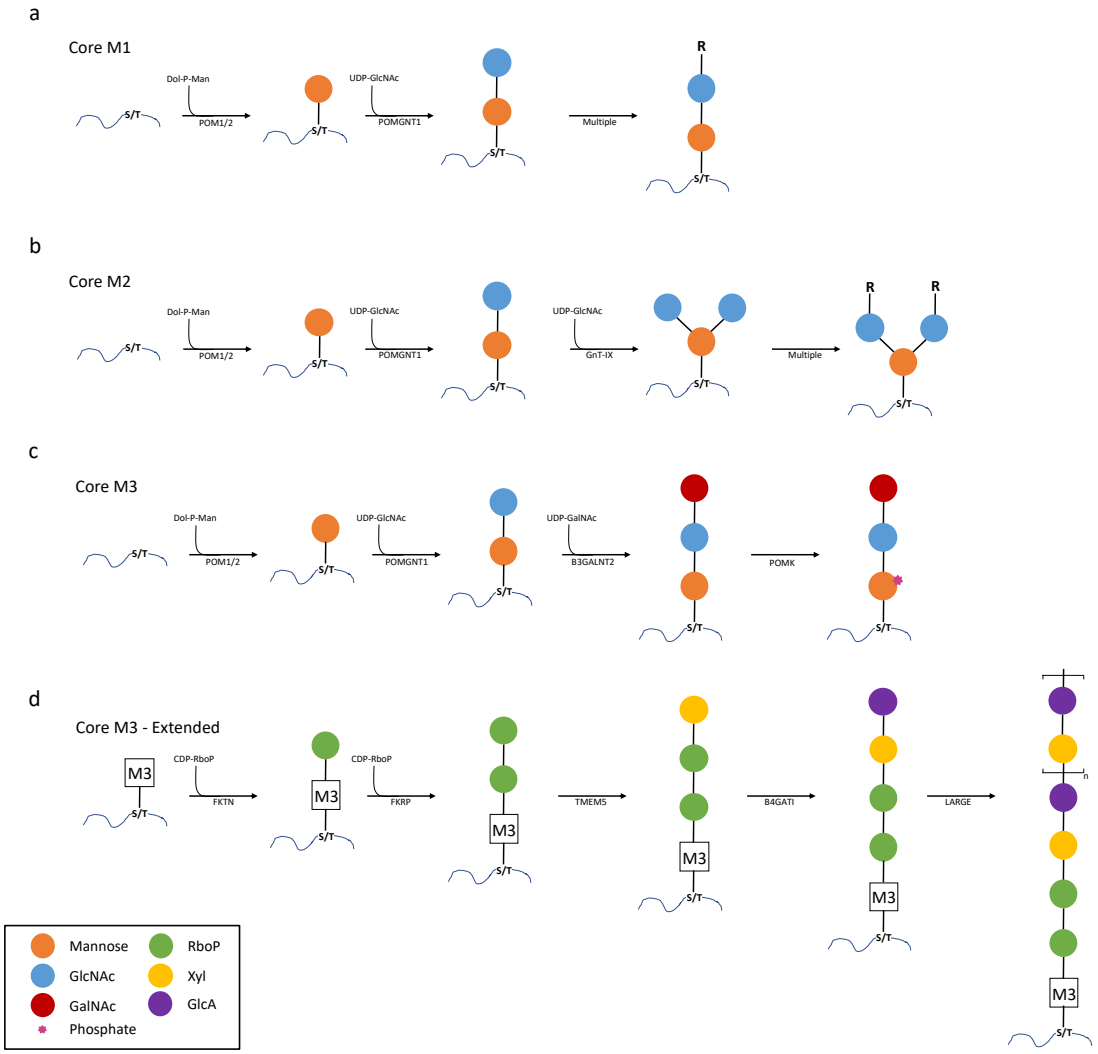

Figure 1.2 **Structure of Core M1, M2 and M3 O-glycans associated with α-DG**. (a) Structure of core M1, (b) core M2, (c) core M3, (c) extended core M3.

Table 1.2 **List of possible glycosylation sites of α-DG.** Confirmed glycosylation sites are indicated by "Yes" with the reference for the study that identified it. (1) Hara et al., 2011; Yagi et al., 2013, (2) Nilsson et al., 2010, (3) Yoshida-moriguchi et al., 2010, (4) Stanlnaker et al 2010.

Possible Site of Glycosylation	Identified (Reference)	Possible Site of Glycosylation	Identified (Reference)
T317	**Yes** (1)	T423	No
T319	**Yes** (1)	T424	No
T322	No	S430	**Yes** (4)
T328	No	T431	No
T329	No	T436	No
S336	No	S438	No
T341	No	T439	No
T343	No	S441	No

S344	No	T442	No
T351	No	T443	No
T353	No	T444	No
T367	**Yes** (2)	T445	No
T369	**Yes** (2)	T446	**Yes** (4)
T372	**Yes** (2)	T450	**Yes** (4)
T379	No	T455	**Yes** (2)
T381	**Yes** (3)	T463	**Yes** (4)
T388	**Yes** (3)	T464	**Yes** (4)
S391	**Yes** (4)	S467	No
T395	**Yes** (4)	T469	**Yes** (4)
T396	No	T473	**Yes** (4)
T404	No	S475	**Yes** (4)
T406	No	T478	**Yes** (4)
T414	No	T482	No
T418	No	T483	**Yes** (4)
T421	No	T484	**Yes** (4)
T422	No	S485	No

1.1.2.3 Interactions of α- Dystroglycan

The known primary-binding partners of α-DG consist almost entirely of proteins with laminin globular (LG) domains. The LG domain was originally identified in laminins and the term comes from the five tandem domains, with repeat cystine residues, found at the C-terminus of all laminin α chains and each domain is generally separated by short linker sequences (Beck et al., 1990; Timpl et al., 2000). In addition to laminins a number of other proteins within the extracellular matrix (ECM) also contain LG domains (Figure 1.3) (Talts et al., 1998).

1.1.2.3.1 Laminins

Laminins consist of three peptide chains termed α, β and γ with the LG domains being found on in the α-chain (Figure 1.3). In humans there are 5 types of laminin; laminin-1, laminin-2, laminin-3, laminin-4 and laminin-5 and α-DG is capable of binding all except laminin-3 but with varying affinities (Table *1.3*) (McDearmon et al., 2006; Pall et al., 1996; Smirnov et al., 2002; Talts et al., 2000).

Table 1.3. **Table of the binding affinities for α-DG and different types of laminin**. References: (1) Pall et al., 1996, (2) Smirnov et al., 2002, (3) Talts et al., 2000, (4) McDearmon et al., 2006.

α-DG Tissue	**Laminin-1**	**Laminin-2**	**Laminin-4**	**Laminin-5**
Skeletal Muscle	8nM (1)	8-18nM (1,2)	400nM (3)	
Central Nervous System	20nM (4)		60-80nM (4)	80-1000nM (4)

In the late 1990's and early 2000's there was conflicting research as to how α-DG binds to and interacts with laminin. Initially, Ervasti and Campbell (1993) demonstrated that following treatment with N-glycanase α-DG retained laminin binding, suggesting *N*-glycosylation is not required for laminin binding. A number of studies have also shown that neither the N- or C- terminal of α-DG are capable of laminin binding (Brancaccio et al., 1997; Sciandra et al., 2001; Di Stasio et al., 1999). Taken together, these studies would suggest that the interaction between α-DG and laminin occurs in the highly glycosylated mucin region. Reports confirm this and suggest that the interaction is dependent upon glycosylation (Michele et al., 2002). However, in 2004 Bozic and colleagues provided data from solid-phase binding assays that suggested the N-terminal fragment (aa28-313) and just the N-terminal IG-like domain (aa28-168) was capable of binding murine laminin-1 (Bozic et al., 2004). This would suggest that the glycosylation was not required for binding, however, no data was provided to indicate binding affinities, so it is not known whether this binding is physiologically relevant. Overall, this early data would suggest that α-DG interacts with laminin via the mucin-like region and is dependent upon glycosylation.

In addition to glycosylation, it has also been shown that the interaction between α-DG and laminins requires Ca^{2+} ion binding and the essential amino acids required for laminin binding are positioned close to the Ca^{2+} ion (Timpl et al., 2000). It has been demonstrated that Ca^{2+} binding to LG4 of the α-chain of laminin-2 but not LG5 was required for efficient binding between laminin and α-DG (Wizemann et al., 2003). A 1.4Å structure has more recently been determined for the LG4 domain from the α-chain of laminin-2 in complex with the polysaccharide that is both generated by LARGE and present upon α-DG. This structure shows that a Xyl-GlcA disaccharide,

also termed matriglycan, straddles the Ca^{2+} ion (Briggs et al., 2016). This study confirms both the requirement for Ca^{2+} binding and the presence of the glycans, in particular LARGE generated matriglycan.

It is clear that the interaction between α-DG and laminins is dependent upon the glycosylation state of α-DG and the coordination of a stabilising Ca^{2+} ion, but there is a final feature of the LG domains that contribute to the relative binding affinities of different laminins. This additional feature is the presence of tandem LG domain repeats. However, the presence of these tandem repeats does not guarantee α-DG binding. For laminin-1 there are two sets of repeats; LG1-3 and LG3-4. LG1-3 does not bind α-DG whereas LG4-5 binds with high affinity. It is also worth noting that LG4 is capable of binding with high affinity without LG5 but LG5 cannot bind in the absence of LG4 (Durbeej et al., 2001). Laminin-2-5 all have the LG1-3 repeats but only in laminin-2 and laminin-4 is there evidence of binding at these regions. Additionally, all laminins (1-5) have the LG4-5 tandem repeats and all except laminin-3 (no α-DG binding) have some degree of α-DG binding. Taken together this suggest that the tandem LG repeats are important for α-DG binding but not essential.

1.1.2.3.2 Other LG Domain Containing Proteins

As discussed above the matriglycan component of α-DG is required for the binding of the LG domains of laminin and this interaction is stabilised by Ca^{2+} ions. Additionally, there are a number of other ECM proteins that contain LG domains and are capable of binding glycosylated α-DG (Figure 1.3). These ECM proteins include; agrin (Bowe et al., 1994; Campanelll et al., 1994; Gee et al., 1994) where LG1 and LG2 are required for binding while LG3 shows very weak binding (Gesemann et al., 1996; Stetefeld et al., 2004); Perlecan (Friedrich et al., 1999; Talts et al., 1999) which binds glycosylated α-DG with the three LG domains and all three are required for tightest binding (Friedrich et al., 1999); Pikachurin consists of three LG domains but only LG2 and LG3 are required for high affinity binding to glycosylated α-DG (Kanagawa et al., 2010); Neurexin is also capable of binding glycosylated α-DG (Sugita et al., 2001),

neurexin contains six LG domains but both LG2 and LG6 are capable of binding α-DG in an isolated manner and does not depend on a tandem array of LG domains (Sheckler et al., 2006); Finally, Slit2 is capable of binding glycosylated α-DG but only consists of a single LG domain (Wright et al., 2012).

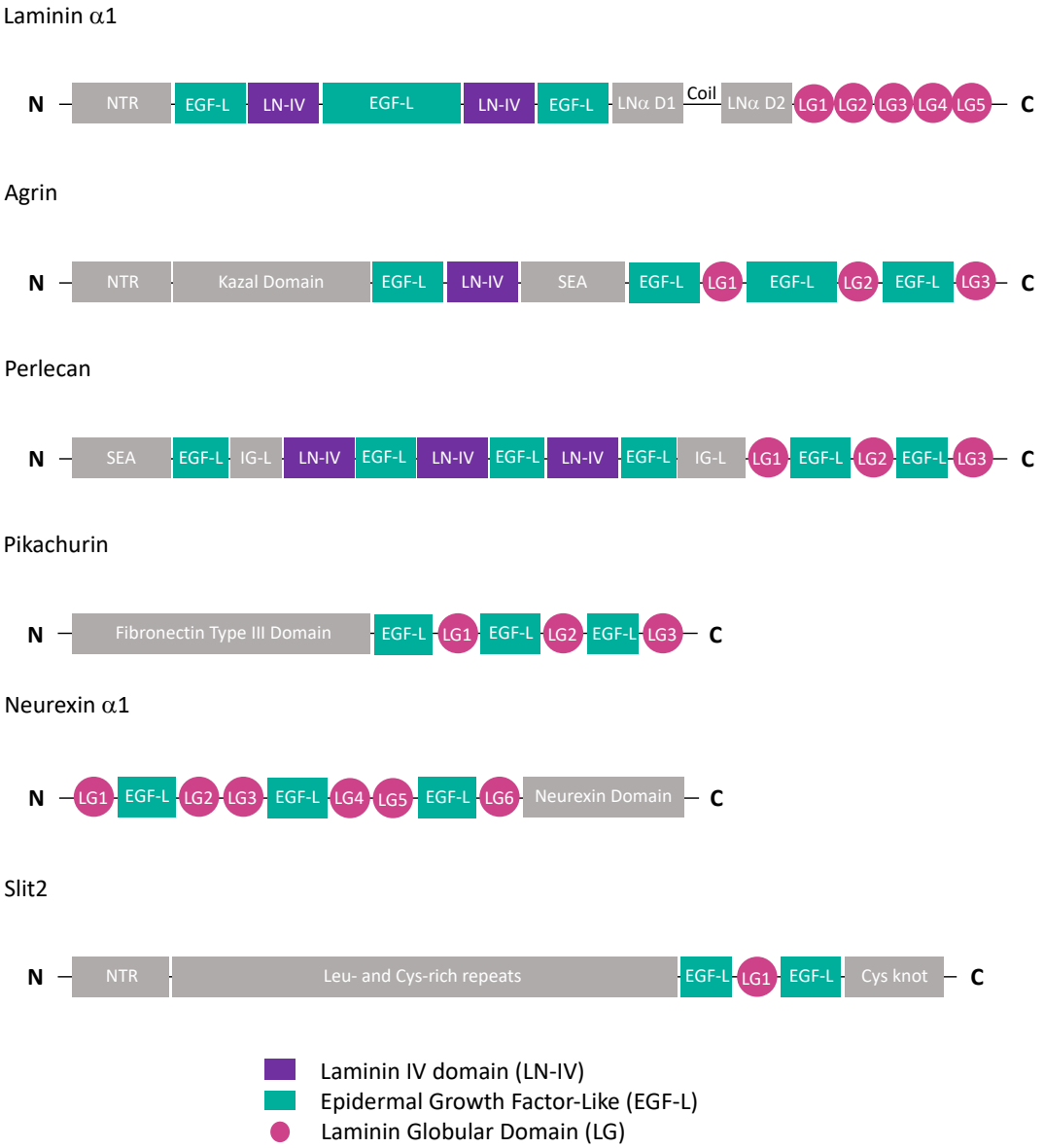

Figure 1.3 **Schematic of the interacting partners of a-DG containing laminin globular domains**.

1.1.2.3.3 Non-LG Domain Interactions

In addition to the LG domain containing proteins there are also a small number of α-DG interactors that do not rely on the classical LG domain interaction. Biglycan is a

small sulphate proteoglycan that interacts with α-DG despite containing no LG domain, the interaction also does not depend on α-DG glycosylation. The interaction between α-DG and biglycan occurs via α-DGs C-terminal domain (Bowe et al., 2000). Possibly the most important interaction α-DG makes is with the transmembrane (TM) domain protein β-DG which anchors it to the membrane. The interaction between α- and β-DG occurs via the C-terminal region of α-DG and the extracellular N-terminal region of β-DG, this interaction is non-covalent and has a K_d between 1-10μM (Ervasti and Campbell, 1991; Sciandra et al., 2001; Di Stasio et al., 1999).

In addition to the beneficial interactions that α-DG makes with laminin, agrin, perlecan, pikachurin, neurexin, Slit2, biglycan and β-DG, it is also the receptor for viral and bacterial pathogens. α-DG acts as a receptor for the causative agent of leprosy, *Mycobacterium laprae*, this interaction requires laminin α2 as a cofactor (Rambukkana et al., 1998). Additionally, α-DG is the receptor for old world arena viruses such as lymphocytic chorionic meningitis virus (LCMV) and Lassa fever virus (LFV), these viruses bind directly to α-DG via the Gp1 viral protein. Neither LCMV nor LFV are able to bind recombinant α-DG which suggests that glycosylation is required for effective binding (Imperiali et al., 2005; Kunz et al., 2001, 2005).

1.1.3 β-dystroglycan

1.1.3.1 Structure

The β component of *DAG1* consists of 242 amino acids (654-895 of the precursor protein, human numbering) and has a predicted M_w of 26.6kDa. On SDS-PAGE it migrates with an apparent M_w of ~43kDa, this disparity is possibly due to glycosylation, relatively high basic amino acid content (particularly lysine), poly proline regions, the fact it is a TM protein or a combination of all of these factors. β-DG consists of an extracellular N-terminal region, a TM region and a cytoplasmic C-terminal region (Figure 1.4).

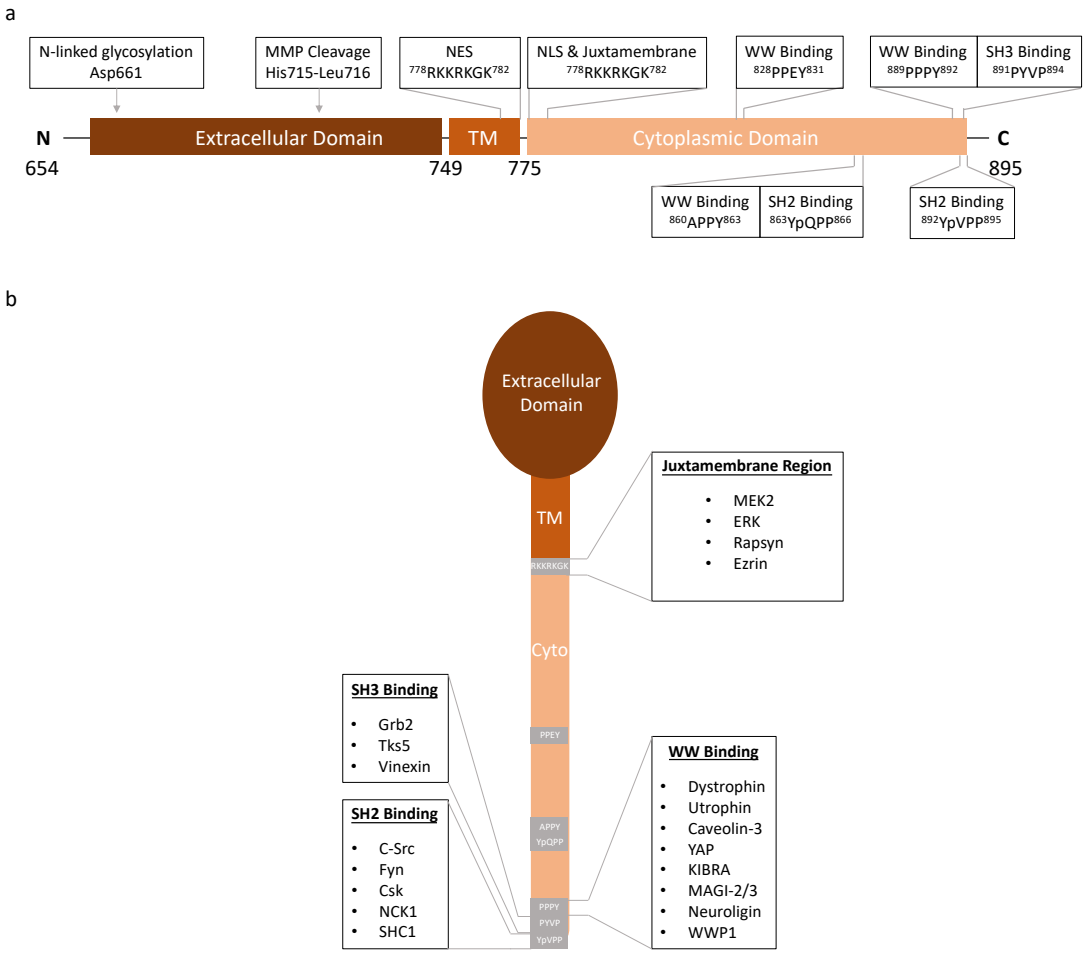

Figure 1.4 **Schematic of β-DG**. (a) Domain organisation and important residues and regions within those domains. (b) Schematic indicating the location of key binding sites and the proteins that interact at each binding site.

The structure of the extracellular N-terminal region of β-DG has been the most studied region. Di Stasio (1999) and colleagues produced an N-terminal recombinant fragment of murine β-DG consisting of amino acids 654-750 (equivalent to 652-748 in humans) (Di Stasio et al., 1999). Using circular dichroism, they determined that the fragment consisted of relatively few secondary structural elements and that at least the extreme N-terminal region of the fragment was flexible. This was later expanded upon, again using the 654-750 murine β-DG fragment and was investigated using circular dichroism, Fourier-transform inferred spectroscopy and the secondary structure prediction method GOR. They identified an α-helix between positions 674-684 and a β-sheet between positions 702-726. They also identified a smaller β-sheet and a few β-turns but the majority of the fragment could not be assigned secondary structure suggesting that the N-terminal fragment (654-750) is flexible and

disordered (Boffi et al., 2001). The high probability that the N-terminal β-DG fragment is disordered makes it difficult to crystallise which is one possible reason that a crystal structure has not been determined.

In addition to a disordered N-terminal region, β-DG also consists of a TM and an intracellular C-terminal domain. β-DG is a type 1 TM protein owing to the single pass TM domain with an extracellular N-terminus and an intracellular C-terminus (Ott and Lingappa, 2002). There have been no structural studies of the C-terminus of β-DG and this is likely due to the high level of flexibility within this region. The C-terminus is highly enriched for proline residues and consists of 120 residues. Within the C-terminus in the juxtamembrane region is a nuclear localisation signal (NLS) at position 776-782 (Lara-Chacón et al., 2010) and a number of protein binding motifs that will be discussed in detail below.

1.1.3.2 Post-Translational Modifications

β-DG is not subject to the high levels of glycosylation characteristic of α-DG however, there are some post-translational modifications that play an important functional role. The modifications of β-DG include glycosylation, phosphorylation, ubiquitination and protein cleavage.

1.1.3.2.1 Glycosylation

The glycosylation of β-DG was first determined in 1991, it was found that when β-DG was treated with N-glycosidase F there was a reduction in mass of 2kDa, suggesting the presence of *N*-linked glycans (Ervasti and Campbell, 1991). It was later suggested, based on the primary structure of mouse β-DG, that an *N*-glycosylation consensus motif in the N-terminus at Asn^{661} was present as were three *O*-glycosylation sites at Ser^{725}, Ser^{728} and Ser^{729} however, neither Ser^{725} or Ser^{729} are conserved in other mammalian β-DG sequences (Di Stasio et al., 1999).

1.1.3.2.2 Phosphorylation

At least two types of phosphorylation have been identified experimentally in β-DG, phosphorylation of threonine at position 790 (Bian et al., 2014; Zhou et al., 2013) and tyrosine phosphorylation at position 892 which is located within the important PPxY binding motif (James et al., 2000; Sotgia et al., 2001). The functional relevance of the Thr^{790} is not known but Y^{892} has been studied extensively. The phosphorylation of Y^{892} is regulated by the binding of extracellular ligands to α-DG, namely, laminin and agrin (James et al., 2000; Sotgia et al., 2003). The binding of laminin or agrin results in the phosphorylation of Y^{892} by the Src kinase and Src-family kinases (Sotgia et al., 2003). The tyrosine phosphorylation has two important effects i) it results in the internalisation of β-DG for degradation or for localisation to intracellular compartments (Lara-Chacón et al., 2010; Sotgia et al., 2003) and ii) it acts as a molecular switch in order to regulate the binding partners of β-GD (Bozzi et al., 2009; Ilsley et al., 2001).

1.1.3.2.3 Protein Cleavage

As described in section 1.1.3.1, β-DG is identified as a ~43kDa protein by SDS-PAGE, however, two other species of β-DG have been identified according to their migration on SDS-PAGE at M_w ~30kDa and 26kDa (Figure 1.4). All three of these fragments are identified by the monoclonal antibody MANDAG2 which is specific for the extreme C-terminus region of β-DG (Leocadio et al., 2016; Yamada et al., 2001).

The 30kDa fragment has been identified in peripheral nerve, kidney, lung and smooth muscle but was apparently absent in skeletal muscle, cardiac muscle and brain (Yamada et al., 2001). In this same study they determined that the 30kDa fragment was the result of matrix metalloproteinase (MMP) activity which proteolytically cleaved the extracellular N-terminal of β-DG (Yamada et al., 2001). Using inhibitor and knockout assays it was determined that the MMPs responsible for the cleavage of β-DG are the gelatinases, also known as MMP-2 and MMP-9 (Agrawal et al., 2006;

Zhong et al., 2006). One of the MMP-9 cleavage sites is between His^{715} and Leu^{716} which results in the release of a peptide consisting of 61 amino acids (Bozzi et al., 2009). Cleavage sites for MMP-2 and additional sites of MMP-9 have yet to be identified.

Further cleavage of the 30kDa fragment has been described based on the identification of a 26kDa fragment. The generation of this fragment was dependent upon cell density in LNCaP prostate cancer cells and it was suggested that high cell density increased cleavage of the 30kDa fragment into the 26kDa fragment (Leocadio et al., 2016). The functional protease involved in this cleavage is γ-secretase which cleaves β-DG at the juxtamembrane region releasing the cytoplasmic C-terminal domain (Leocadio et al., 2016). It has also been shown that γ-secretase plays a similar role in a number of other type 1 membrane proteins (Hemming et al., 2008). Recombinant β-DG cytoplasmic domain also migrates at 26kDa on SDS-Page despite only consisting of 120 amino acids (Chen et al., 2003; Mathew et al., 2013).

1.1.3.3 Interactions

β-DG has a plethora of binding partners, with the exception of α-DG binding the N-terminal region (Sciandra et al., 2001; Di Stasio et al., 1999), all known interactions occur in the cytoplasmic C-terminal region. The C-terminal region is packed with potential binding sites (Figure 1.4), including binding sites for WW domain containing proteins, Src-homology 3 (SH3) domain containing proteins and Src-homology 2 (SH2) domain containing proteins. All of these binding sites are in close proximity and often overlap which requires intricate regulation to ensure effective signal transduction and cytoskeletal organisation. The juxtamembrane region of C-terminal β-DG is involved in a number of protein interactions.

1.1.3.3.1 Proteins Containing WW Domains

The WW domain, so named after two tryptophan residues separated by 20-21 amino acids (Bork and Sudol, 1994) is a key binding domain that interacts with β-DG, via the PPxY binding motif. Recently the PPxY-WW interaction has been shown to also include PY motifs in addition to the classical PPxY motif (Lin et al., 2019). The most well studied PPxY (or PY) binding motif is found at the extreme C-terminus of β-DG (Figure 1.4*a*) and consists of the PPPY (889-892) sequence in human β-DG but there is also PPEY at position 828-831 and APPY at 860-863. There are multiple proteins that interact with β-DG via a WW-PPxY interaction; dystrophin (Jung et al., 1995), utrophin (James et al., 2000), caveolin-3 (Sotgia et al., 2000), YAP (Morikawa et al., 2017), KIBRA (Lin et al., 2019), MAGI-2 (Sumita et al., 2007), MAGI-3 (Lin et al., 2019), neuroligin-2 (Sumita et al., 2007) and WWP1 (Cho et al., 2018) (Figure 1.4*b*).

Dystrophin is the most well characterised of the WW domain proteins known to interact with β-DG. Dystrophin is found almost exclusively in muscle and plays an essential role in connecting the extracellular matrix with the intracellular cytoskeleton via the dystrophin-associated protein complex (DAPC) which will be discussed in detail below. The WW domain of dystrophin is located in the C-terminus within a cystine-rich domain (Bork and Sudol, 1994) and the crystal structure of C-terminal dystrophin in complex with the β-DG binding site has been solved to 1.9Å (Huang et al., 2000). Based on the structural analysis it was found that the WW domain of dystrophin embeds within an adjacent EF-hand-like domain and β-DG binds to the surface produced from the WW domain and EF-hand domain (Huang et al., 2000). In addition to the presence of the EF-hand domain the interaction between the WW domain of dystrophin and the PPPY domain of β-DG is stabilised by Ca^{2+} ions (Ervasti and Campbell, 1991). The regulation of the interaction between dystrophin and β-DG occurs via phosphorylation of Y^{892} (discussed above), this phosphorylation event prevents the binding of dystrophin (Ilsley et al., 2001).

Utrophin is both a structural and functional paralogue of dystrophin and is found in muscle and non-muscle cells. As with dystrophin, utrophin consists of a WW domain in the C-terminus and requires the presence of an EF-hand domain to stabilise the

interaction. Additionally, the phosphorylation of Y^{892} negatively regulates the utrophin-β-DG interaction as phosphorylation resulted in loss of utrophin binding in co-immunoprecipitation (Co-IP) assays (James et al., 2000).

In the early 2000's the protein caveolin-3 was identified as WW domain containing protein that interacts with β-DG (Sotgia et al., 2000). Caveolin-3 is a muscle specific protein that associates with small invaginations of the PM known as caveolae. A number of other caveolin proteins also contain WW domains including caveolin-2 but based on Co-IP assays there is no interaction between β-DG C-terminal fragment or caveolin-2 (Sotgia et al., 2000). This study also suggests that caveolin-3 and dystrophin compete for the β-DG PPPY binding site. However, interestingly the interaction between caveolin-3 and β-DG is not regulated by tyrosine phosphorylation. This was tested with phosphorylation at both Y^{892} and Y^{886} and binding was unaffected by either (Sotgia et al., 2000).

The Hippo pathway, identified in *Drosophila*, is involved in regulating organ size and responding to mechanical stimuli. This pathway relies on WW domain and PPxY motif containing proteins. Recently, β-DG has been identified as a binding partner for the WW domain containing proteins KIBRA and YAP. These play opposing roles in the Hippo pathway with KIBRA inhibiting the pathway while YAP, a transcriptional cofactor, is a downstream effector of the pathway. YAP was initially identified as a β-DG binding protein in 2017 where it was shown to be involved in murine cardiomyocyte proliferation (Morikawa et al., 2017). More recently, a mass spec analysis of DG in *Drosophila* identified Yki (YAP homologue) and Kbr (KIBRA homologue) as interaction partners of β-DG (Yatsenko et al., 2020). Perhaps the most compelling evidence is the detailed structural analysis of the interaction between KIBRA and the C-terminal binding region of β-DG (Lin et al., 2019). In this paper they determined that highest affinity binding between WW domain and PY motifs occur when both tandem WW domain and tandem PY motifs are only separated by a short linker sequence. KIBRA and β-DG fit this category and bind with an K_d of ~96nM. The authors did not asses binding between YAP and β-DG but did find that the two WW

domains found in YAP were separated by a much longer linker sequence suggesting a lower affinity between β-DG and YAP compared with β-DG and KIBRA (Lin et al., 2019).

In the case of MAGI-2 and neuroligin-2, MAGI2 is a synaptic scaffold molecule while neuroligin-2 is a post-synaptic protein involved in the maturation of GABAergic synapses. Both proteins were identified in rat hippocampal neurones where they were demonstrated to interact with β-DG (Sumita et al., 2007). Interestingly, their binding was not restricted to the PPPY motif at position 889-892, they were also able to bind to the PPEY and APPY sequences located N-terminally of the C-terminal motif (Sumita et al., 2007). As with MAGI-2, MAGI-3 is a scaffold protein and contains tandem WW domains. These tandem WW domains allow binding with β-DG with a K_d of 2.7μM (Lin et al., 2019).

The WW domain proteins discussed thus far are either structural proteins, in the case of dystrophin, utrophin, caveolin-3, MAGI-2/3 and neuroligin-2, or involved in signal transduction, in the case of KIBRA and YAP. WWP1 on the other hand is a protein that itself regulates levels of β-DG (Cho et al., 2018). It is a member of the NEDD4 E3 ubiquitin ligase family which ubiquitinates proteins targeting them for subsequent degradation. Cho and colleagues found that WWP1 interacts with β-DG via the WW domains. Both dystrophin and utrophin compete for the binding site and decrease binding of WWP1. The mutation of Y^{831} or Y^{892} in β-DG resulted in decreased interaction, suggesting WWP1 is able to bind to either of the PY motifs. In this study they also investigated other members of the NEDD4 family which are also WW domain containing proteins, they found that WWP2, Itch, Smurf1/2, NEDD4 and NEDD4L all resulted in decreased levels of β-DG but a direct interaction was not investigated (Cho et al., 2018). Conversely, it was found that NEDD4L doesn't interact with β-DG in SPOT assays, direct biochemical interactions, immunoprecipitation or immunofluorescence assays (Piggott, 2014).

1.1.3.3.2 Proteins Containing SH3 Domains

Many proteins identified as β-DG binding proteins contain a SH3 domain, SH3 domain containing proteins are generally involved in cell signalling resulting in the regulation of the cytoskeleton. SH3 domain proteins bind proline-rich regions. The SH3 domain proteins that interact with β-DG include Grb2 (Yang et al., 1995), Tks5 (Thompson et al., 2008) and vinexin (Thompson et al., 2010a) (Figure 1.4*b*).

Grb2 is an important protein involved in signalling, by linking receptor tyrosine kinases with small GTP binding proteins that are involved in cytoskeletal organisation induced by growth factors. The β-DG-Grb2 interaction was identified in 1995. It was identified in both brain tissue (Cavaldesi et al., 1999) and skeletal muscle and was confirmed *in vitro* with a GST-fusion protein interaction assay and *in vivo* with a Co-IP assay from rabbit skeletal muscle and brain tissue (Yang et al., 1995). The interaction between β-DG and Grb2 occurs between the extreme C-terminus of β-DG and the SH3 domains of Grb2 but the N-terminal SH3 domain binds β-DG with a higher affinity than the C-terminal SH3 domain. The K_d of the interaction between the 20 amino acids at the C-terminus of β-DG and Grb2 was in the nanomolar range (between 240-280nM) (Russo et al., 2000). The binding site on β-DG was identified as the PxxP motif that overlaps with the PPxY motif involved in WW domain binding. Additionally, the binding of Grb2 was found to be inhibited by binding of dystrophin to β-DG (Russo et al., 2000).

The SH3 domain protein Tks5 was identified as a β-DG interaction partner using a phage display library (Kärkkäinen et al., 2006). This interaction was then verified using a combination of Co-IP and GST pulldown assays and co-localisation was determined using immunofluorescence microscopy (Thompson et al., 2008). Tks5 plays a key role in actin bundling and regulation of podosomes, which are involved in cell motility and extracellular matrix degradation. The Tks5-β-DG interaction is dependent upon phosphorylation of β-DG as the interaction requires phosphorylation to facilitate the interaction (Thompson et al., 2008). Other than the

original research by Thompson and colleagues there has been no further research into this interaction, thus the exact sites of interaction have yet to be described.

Vinexin is a vinculin binding partner and is localised to focal adhesions, as with Tks5, vinexin was identified via a SH3 phage display library and was then validated using GST-SH3 domain affinity column, Co-IP and SPOT arrays (Thompson et al., 2010a). The specific vinexin-β-DG interaction occurs between the 3rd SH3 domain of vinexin and the proline-rich SH3 binding motif PYVP at position 891-894 which overlaps with the WW binding domain motif PPPY. The cytoskeletal protein vinculin was also associated with the β-DG-vinexin complex however, there was no direct interaction detected between β-DG and vinculin suggesting the β-DG-vinexin-vinculin complex is stabilised by vinexin binding both β-DG and vinculin (Thompson et al., 2010a).

1.1.3.3.3 Proteins Containing SH2 Domains

SH2 domain proteins, as with SH3 domain proteins are generally involved in signalling pathways. SH2 domains are capable of binding phosphorylated tyrosine residues which generally have a proline or leucine residue at the +3 position from the phosphotyrosine. There are a number of these sites present on the cytoplasmic domain of β-DG with the most prominent of these being the YVPP sequence (892-895) which overlaps with the PPPY binding motif. As discussed above, Src kinase is responsible for the phosphorylation of tyrosine residues on β-DG and this phosphorylation event is responsible for switching the PPPYVPP (889-895) from a WW domain binding motif to a SH2 binding motif (Sotgia et al., 2001, 2003). In order to investigate SH2 domain proteins that bind β-DG Sotgia and colleagues (2001) carried out GST-tagged pulldown experiments and probed for a number of both catalytic and adaptor SH2 containing proteins. From this screen they identified five proteins that bound in a phosphotyrosine-dependent manner, these included; c-Src, Fyn, Csk, NCK1 and SHC1 (Sotgia et al., 2001). C-Src, Fyn and Csk are all tyrosine protein kinases whereas NCK1 and SHC1 are both scaffold proteins but all SH2 domains identified are involved in signal transduction with many displaying overlap

between pathways that involve other β-DG binding proteins such as Grb2 and MAPK (Ahmed and Prigent, 2017; Chaki and Rivera, 2013). The binding of all five SH2 domain proteins were dependent upon phosphorylation of C-terminal β-DG and more specifically they required the PPxY motif at the extreme C-terminus (Sotgia et al., 2001).

1.1.3.3.4 Proteins Binding the Juxtamembrane Region of β-Dystroglycan

The juxtamembrane region of β-DG refers to the region immediately following the TM domain and consists of a cluster enriched for the basic amino acids Arg and Lys. This region is located at the opposite end of the cytoplasmic domain to the WW, SH2 and SH3 binding motifs. As with the binding motifs discussed above, the juxtamembrane region is capable of binding both signalling and structural proteins, in particular; MEK2, ERK (Spence et al., 2004a), rapsyn (Cartaud et al., 1998) and ezrin (Spence et al., 2004b) (Figure 1.4*b*).

Mitogen-activated protein kinase kinase 2 (MEK2) and extracellular signal regulated kinase (ERK) are both involved in the Ras-Raf-MEK-ERK kinase cascade pathway which is involved in regulating proliferation, differentiation, migration, senescence and apoptosis and is mis-regulated in a number of diseases including cancers (Sun et al., 2015). It was determined by yeast-two-hybrid and pulldown assays that the β-DG interacts with both MEK2 and phosphorylated (activated) ERK1 (Spence et al., 2004a). The exact site of β-DG-ERK1/MEK2 interaction has been predicted but not experimentally determined, ERK1 and MAK2 bind small clusters of basic residues (Tanoue et al., 2000) which are present in the juxtamembrane region of β-DG, additionally the juxtamembrane region has a predicted MAPK binding site (Gouw et al., 2018).

Receptor associated protein at synapse (rapsyn) is a scaffold protein localised to the neuromuscular junction (NMJ) where it plays an essential role in clustering and anchoring the acetylcholine receptor (AChR) (Gautam et al., 1995). The interaction

between β-DG and rapsyn was investigated in the in *Torpedo* electric organ where there is a high concentration of AChR. Using a combination of affinity chromatography and ligand blot assays it was determined that the fragment consisting of just the juxtamembrane region of β-DG was necessary for binding of rapsyn (Cartaud et al., 1998).

Ezrin is a protein involved in the linking of TM proteins with the actin cytoskeleton via an actin binding domain. The direct interaction between β-DG and ezrin was determined using a combination of GST pulldown and Co-IP assays (Spence et al., 2004b). The juxtamembrane binding site was identified by mutating the RKKRK basic sequence to AAAAA which resulted in loss of β-DG-ezrin interaction and also resulted in loss of actin-rich surface protrusions within cultured cells (Spence et al., 2004b). This interaction is likely to be important for maintaining the connection between the extracellular matrix and the cytoskeleton.

1.1.3.3.5 Interacting Partners with Unknown Binding Sites

As evidenced above, β-DG is capable of interacting with a large number of proteins at both the extreme C-terminus of the cytoplasmic domain and at the juxtamembrane region. However, there are some proteins that have been demonstrated to be β-DG interacting partners, but the specific site of interaction has yet to be determined. These include actin (Chen et al., 2003), plectin (Rezniczek et al., 2007), integrinβ1, tubulin, talin (Cerecedo et al., 2008), myosin IIA (Buisson et al., 2014) and plakoglobin (Eid Mutlak et al., 2020) (Figure 1.4*b*).

1.1.4 The Role of Dystroglycan at the Plasma Membrane

1.1.4.1 Components of the Dystrophin/Utrophin Associated Protein Complex

The DAPC, and the dystrophin glycoprotein complex (DGC) are interchangeable terms describing the PM complex that has dystrophin at its centre, additionally the

complex containing utrophin is termed the utrophin associated protein complex (UAPC). Based on personal preference the term DAPC (or UAPC) will be used henceforth. The DAPC contains multiple components, some of which form their own subcomplexes but broadly the core components can be separated into three groups (i) the extracellular component (ii) the membrane components, and (iii) the cytoplasmic components. There is only a single extracellular component of the DAPC and that is α-DG which interacts with extracellular proteins including laminin, perlecan and agrin and is non-covalently bonded to β-DG (see section 1.1.2.3). The membrane proteins associated with the DAPC are β-DG, sarcoglycans and sarcospan while the cytoplasmic proteins include dystrophin, dystrobrevins and syntrophins (Figure 1.5).

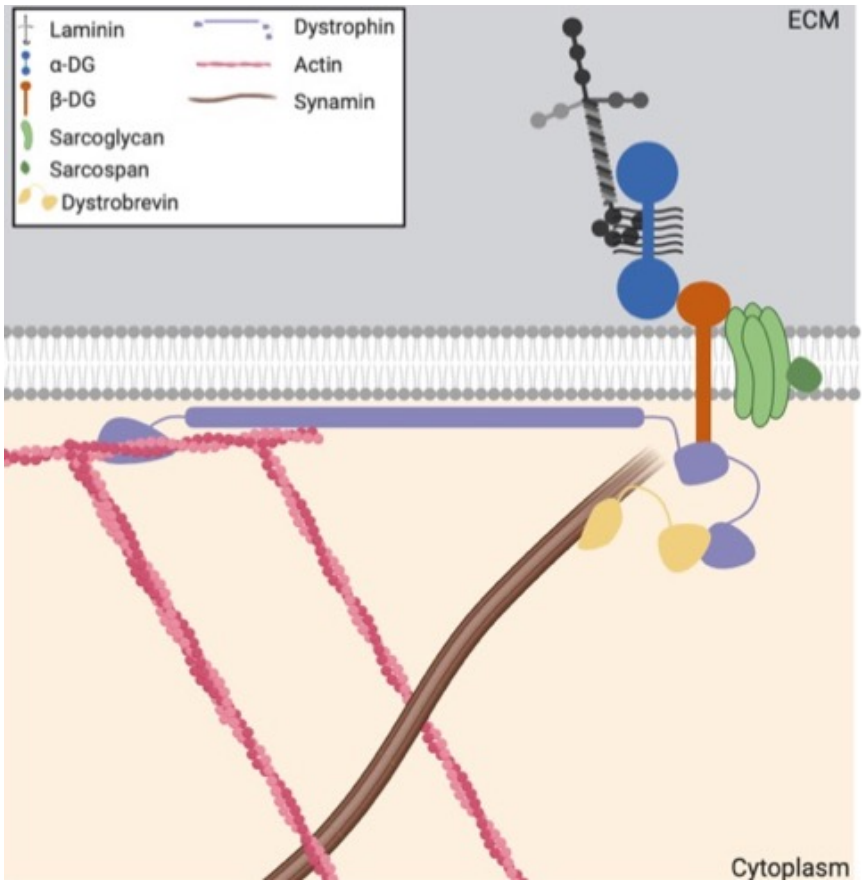

Figure 1.5 **Schematic of the components and organisation of the DAPC.** Dystroglycan forms the central component of the DAPC. α-DG interacts with the ECM proteins and is anchored to the membrane through interactions with β-DG. β-DG then directly interacts with dystrophin which is the key protein in interacting and organising the cytoskeleton. Figure was made using BioRender.

1.1.4.1.1 Membrane Components

The structure and interacting partners of β-DG have been discussed in detail in section 1.1.3. Additionally, β-DG is the predominant TM protein involved in anchoring the DAPC/UAPC at the PM as it provides the direct connection between the extracellular α-DG and the cytoplasmic dystrophin (Ervasti and Campbell, 1991; Ibraghimov-Beskrovnaya et al., 1992).

In addition to β-DG the sarcoglycans and sarcospan make up the membrane components of the DAPC/UAPC. The sarcoglycans, which are single pass TM proteins, form a heterotetrameric complex (Chan et al., 1998) where α-, β-, γ- and *δ*-sarcoglycan form the main complex in skeletal muscle but both ε- and ζ-sarcoglycan are found in the smooth muscle and replace the α- and γ-sarcoglycans respectively (Imamura et al., 2005; Wheeler et al., 2002). Sarcospan is an additional component of the sarcoglycan complex and consists of four TM regions (Crosbie et al., 1997) and is required for stabilising interactions within the DAPC (Crosbie et al., 1999; Yoshida et al., 2000).

1.1.4.1.2 Dystrophin and Utrophin

Dystrophin is the central cytoplasmic component and the namesake for the DAPC. It is anchored to the PM, and the rest of the DAPC, in part by the interaction with β-DG as discussed in section 1.1.3.3. Dystrophin is encoded by the *DMD* gene which is controlled by three upstream promoters; the brain (Boyce et al., 1991), the muscle (Chelly et al., 1990) and the Purkinji (Holder et al., 1996) promoters which allow tissue specific expression. These promoters result in the expression of full-length dystrophin which is termed Dp427. In addition to upstream promoters there are four internal promoters which result in the expression of shorter isoforms of dystrophin including; Dp260, Dp140, Dp116 and Dp71, the smallest isoform Dp40 is the result of alternative splicing of the Dp71 transcript (D'souza et al., 1995; Górecki et al., 1992). The different isoforms are expressed in different tissues with Dp260 expressed in the

retina (D'souza et al., 1995), Dp140 expressed in both the brain and the kidney (Lidov et al., 1995), Dp116 expressed in the Schwann cells of peripheral nerves (Byers et al., 1993) and Dp71 is the most abundant of all the isoforms and most uniformly expressed but found at highest levels in the neurones and glia within the brain (Blake et al., 1992).

The full-length Dp427 contains four main domains: a C-terminal region which consists of α-helical coiled-coils (Blake et al., 1995a) which is only found in dystrophin and related proteins (Tinsley et al., 1992); Adjacent to the C-terminal region is the cystine-rich domain containing the WW binding domain that interacts with β-DG (Bork and Sudol, 1994); The region next to the WW binding domain consists of a long flexible central rod domain made up of spectrin-like repeats and contains more than 2800 amino acids arranged in triple helical repeats (Koenig and Kunkel, 1990); The final region is the N-terminus which contains two calponin homology (CH) regions which are responsible for binding actin filaments, this N-terminal domain is also referred to as actin binding domain 1 (ABD1) (Way et al., 1992) (Figure 1.6). The smaller dystrophin isoforms are lacking the N-terminal region and parts, or all, of the central rod domain.

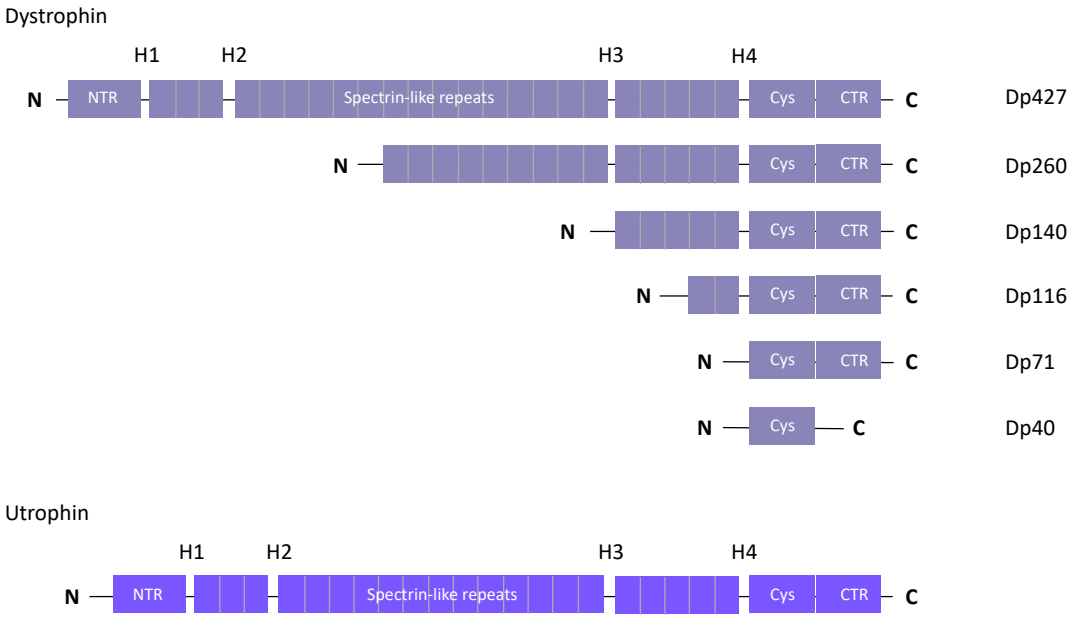

Figure 1.6 **Schematic depicting the domain organisation of different dystrophin isoforms and utrophin.**

Dystrophin plays the essential role of binding actin filaments as part of the DAPC. The DAPC is capable of binding 24 actin monomers per dystrophin molecule. This is due to both ABD1 found in the N-terminus but also a second ABD identified in the central rod domain (Rybakova et al., 1996). It was found that multiple spectrin repeats were rich in basic residues which facilitates the interaction with actin filaments (Amann et al., 1998; Rybakova et al., 2000). Investigation into the binding affinities of the isolated ABDs within dystrophin had a binding affinity in the μM range while full length dystrophin had a binding affinity in the nM range suggesting the whole protein is required for high affinity binding of actin (Rybakova and Ervasti, 1997). In addition to actin binding, the DAPC was also shown to decrease the rate of actin depolymerisation, thus stabilising the actin filament. The interaction between dystrophin and actin filaments was similar to that observed between the DAPC and actin suggesting that dystrophin is the key protein for the DAPC-actin interaction despite other members of the complex having proposed actin binding abilities (Rybakova et al., 1996).

In addition to actin binding, dystrophin also plays a role in binding other cytoskeletal elements and linking them to the DAPC. Dystrophin is capable of interacting with the cytolinker protein plectin which is involved in linking together actin filaments, microtubules and intermediate filaments. The interaction between dystrophin and plectin occurs via the cystine-rich domain adjacent to the C-terminal domain (Rezniczek et al., 2007). The intermediate filament synemin has also been suggested to interact with dystrophin *in vitro*, in particular the interaction requires the central rod region and the interaction site overlaps the actin binding site (Bhosle et al., 2006). A direct interaction between dystrophin and the intermediate filament cytokeratin 19 has been identified, this interaction involves the N-terminal ABD1 (Stone et al., 2005, 2007). There is also indirect evidence suggesting that dystrophin is involved in microtubule interactions as the WW domain of dystrophin co-sediments with microtubules and when dystrophin is absent in mice the microtubule lattice is less organised than control mice (Prins et al., 2009). Taken together, these studies suggest that dystrophin not only binds actin but is able to interact both directly and indirectly with other members of the cytoskeleton. However, these interactions

appear to occur in regions responsible for actin binding suggesting different cytoskeletal components compete for dystrophin interaction sites.

Dystrophin is capable of interacting with cytoskeletal proteins and other proteins within the DAPC, but it has also been reported that dystrophin is capable of binding membrane phospholipids. It was found that dystrophin lacking ABD1 was still capable of localising to the PM (Corrado et al., 1996), as was a construct lacking the WW domain required for β-DG interaction (Gardner et al., 2006). This suggests the β-DG-dystrophin interaction is not essential for localising dystrophin to the PM. Dystrophin's ability to localise to the PM is in part due to the direct interaction with membrane phospholipids that contain phosphatidylserine and phosphatidylcholine (DeWolf et al., 1997). Tryptophan residues were identified as important for the dystrophin-lipid interaction (Le Rumeur et al., 2003, 2007) while the coiled-coil region that includes repeat 1-3 strongly binds lipids and result in conformational changes in dystrophin which affects the binding of actin (Legardinier et al., 2008; Mias-Lucquin et al., 2020; Dos Santos Morais et al., 2018).

Utrophin is a homolog of dystrophin with highly conserved structural organisation. As with dystrophin, the transcript responsible for producing utrophin is controlled by a number of promoter sequences both upstream and within the gene (Burton et al., 1999; Dennis et al., 1996) and there is also evidence suggesting shorter isoforms of utrophin are produced (Blake et al., 1995b; Lumeng et al., 1999; Wilson et al., 1999). The full length utrophin protein consists of the same domains as dystrophin including the C-terminal α-helical coiled coils, an adjacent cystine-rich region involved in binding β-DG, a central rod domain consisting of spectrin-like repeats and an N-terminal ABD (Blake et al., 1992; Khurana et al., 1990; Love et al., 1991) (Figure 1.6).

As with dystrophin, utrophin is capable of binding other DAPC/UAPC proteins including β-DG which is discussed above (James et al., 2000), sarcoglycans (Matsumura et al., 1992), α-dsytrobrevin-1 (Peters et al., 1998) and syntrophins (Kramarcy et al., 1994; Peters et al., 1997a). The C-terminal ABD domain of utrophin

is very similar to the ABD of dystrophin (Keep et al., 1999a, 1999b; Moores et al., 2000) and binds with high affinity to actin filaments (Winder et al., 1995). However, utrophin does not appear to have the ABD2 present in the central rod domain of dystrophin, it lacks the basic repeat region present in dystrophin (Amann et al., 1999). Despite this, utrophin is still capable of binding actin with high affinity and with a ratio of 14 actin monomers for every 1 utrophin molecule (Rybakova et al., 2002). The interactions between dystrophin and cytolinker plectin and the intermediate filament synemin are also found in utrophin (Bhosle et al., 2006; Rezniczek et al., 2007). However, the indirect interaction between dystrophin and microtubules was not observed for utrophin (Belanto et al., 2014).

1.1.4.1.3 Additional Cytoplasmic Components

The two key cytoplasmic components of the DAPC/UAPC other than dystrophin/utrophin are dystrobrevin and syntrophin. There are two types of dystrobrevins; α- and β-dystrobrevins which are encoded by the *DTNA* and *DTNB* genes respectively (Blake et al., 1996; Peters et al., 1997b). Both α- and β-dystrobrevins have homology with the cystine-rich C-terminal region of dystrophin which contains the WW domain (Ambrose et al., 1997; Blake et al., 2002; Loh et al., 1998). Dystrobrevins are capable of binding DAPC/UAPC components dystrophin (Butler et al., 1992; Sadoulet-Puccio et al., 1997; Suzuki et al., 1992), utrophin (Nawrotzki et al., 1998), sarcoglycans (Yoshida et al., 2000) and syntrophins (Dwyer and Froehner, 1995), in addition to cytoskeletal components synemin (Mizuno et al., 2001), syncoilin (Newey et al., 2001; Poon et al., 2002), desmin (Sandoval et al., 1983), α-actinin (Bellin et al., 1999) and vinculin (Bellin et al., 2001).

The syntrophin family consists of α-, β- and γ-syntrophins and each of these are expressed in different tissues (Adams et al., 1993; Ahn et al., 1996; Peters et al., 1997a; Piluso et al., 2000). The syntrophins contain a PDZ binding domain as well as a domain unique to syntrophins termed SU domain. As with dystrobrevins, syntrophins are capable of binding DAPC/UAPC components including dystrophin,

utrophin (Ahn and Kunkel, 1995; Suzuki et al., 1995) and dystrobrevin (Dwyer and Froehner, 1995; Newey et al., 2000) while also able to interact directly with the actin cytoskeleton (Iwata et al., 2004).

1.1.4.2 Functions of the DAPC/UAPC

1.1.4.2.1 Mechanical Support of the Sarcolemma

As discussed above dystrophin and the DAPC are localised at the sarcolemma (Zubrzycka-Gaarn et al., 1988) where it makes up, along with integrins, the costamere which links the basal lamina to the sarcomere within the muscle fibre (Porter et al., 1992; Straub et al., 1992). This physical connection occurs via the basal lamina components interacting with α-DG, α-DG in turn binding β-DG and associating with the sarcoglycan-sarcospan subcomplex, the β-DG-sarcoglycan-sarcospan TM complex interacts with dystrophin, dystrobrevin and syntrophins which in turn interact with the cytoskeleton linking the whole complex with the sarcomere. (Figure 1.5) The loss of the central dystrophin molecule results in the general loss of the DAPC components and reduces this linkage. The *mdx* mouse model lacks the dystrophin gene and many muscle specific phenotypes have been described including reduced force generation (Consolino and Brooks, 2004; Dellorusso et al., 2001), increased permeability to membrane impermeable dyes following force generation (Petrof et al., 1993), increased release of creatine kinase (Bulfield et al., 1984), increased centrally nucleated fibres (Coulton et al., 1988) which is an indicator of muscle fibre regeneration and increased muscle fibre necrosis (Matsuda et al., 1995) compared with control mice. Together this data suggests that the loss of DAPC at the sarcolemma results in muscle damage which emphasises the role the DAPC plays in maintaining muscle membrane integrity.

1.1.4.2.2 Non-mechanical Roles of DAPC/UAPC

The DAPC/UAPC is known to play an essential role in synaptic formation and organisation, particularly in the NMJ. The NMJ is a specific synapse that is formed between the neurone and the muscle. The role of the DAPC/UAPC at the NMJ involves the binding of agrin to α-DG, this binding event results in the localisation of the DAPC/UAPC to the NMJ in addition to the rapsyn-dependent clustering of DAPC/UAPC with AChR (Gautam et al., 1995; Rybakova et al., 2002).

A great deal of research has gone into understanding the interactions and the functional role of DAPC/UAPC and membrane channels; including ion channels and aquaporins (AQP). It is apparent that the interaction between the DAPC/UAPC and these channels is predominantly mediated through the syntrophins, and particularly via their PDZ domains. The DAPC/UAPC has been shown to interact with voltage-gated channels such as $Na_v1.5$ (Gavillet et al., 2006); non-voltage-gated ion channels such as TRPC1 (Vandebrouck et al., 2006) and TRPC4 (Sabourin et al., 2009); inward-rectifier potassium channels such as $K_{ir}4.1$ (Connors et al., 2004); and aquaporins, specifically AQP4 (Amiry-Moghaddam et al., 2003; Neely et al., 2001).

1.1.5 Dystroglycan and Disease

1.1.5.1 Muscular Dystrophy

Muscular dystrophies (MD) are characterised generally by muscle weakness and wasting and can include ocular or mental abnormalities. The most common type of childhood MD is Duchenne MD and is caused by a lack of dystrophin resulting in loss of the DAPC (Ervasti et al., 1990). As well as dystrophin, mutations in other DAPC/UAPC components can also lead to various types of MDs (Duclos et al., 1998). However, here we focus on MDs caused by mutations in DG or mutations in proteins involved in the regulation and post-translational modifications of DG – together these diseases are termed dystroglycanopathies.

1.1.5.1.1 Dystroglycanopathies

Based on the Online Mendelian Inheritance in Man (OMIM) categorisation of diseases, muscular dystrophy dystroglycanopathies (MDDG) can be separated into three classes; (A) congenital MD (CMD) with brain/eye abnormalities, (B) CMD with mild brain abnormalities and (C) limb-girdle MD (LGMD) with A being the most and C being the least severe. The cause of MDDGs is predominantly hypoglycosylation of α-DG which reduces the ligand binding affinity and destabilises the ECM-cytoskeleton link. They can also be classified as 1°, 2° and 3° dystroglycanopathies, depending on whether mutations affect dystroglycan itself, genes involved in the glycosylation of dystroglycan or genes involved in the metabolic pathways supplying precursors for the glycosylation enzymes.

One of the most severe forms of MDDG is Walker-Warburg syndrome (WWS) which is a CMD and often results in death before the age of 1 year old. There has been one recorded example of WWS being caused by a mutation in *DAG1.* This mutation was a deletion of a cytosine at position 743 identified in 5 patients within a family, the deletion resulted in an absence of both α- and β-DG subunits (Riemersma et al., 2015). Other mutations have been identified in a number of enzymes involved in α-DG glycosylation (see section 1.1.2.2) including; POMT1 (Beltrán-Valero de Bernabé et al., 2002), POMT2 (Van Reeuwijk et al., 2005), fukutin (Beltrán-Valero de Bernabé et al., 2003), FKRP (Beltran-Valero de Bernabé et al., 2004), LARGE (van Reeuwijk et al., 2007), POMGNT2, POMK (Jae et al., 2013) and B3GALNT2 (Al Dhaibani et al., 2018). WWS is clearly a heterogenous disease based on the number of gene mutations associated, however, it has been shown that the relationship between disease severity and α-DG glycosylation is also heterogenous. Patients with mutations in POMT1, POMT2 or POMGNT1 have good correlation between α-DG glycosylation and disease severity whereas patients with mutations in fukutin or FKRP have no significant relationship between α-DG glycosylation and disease severity (Jimenez-Mallebrera et al., 2009). However, generally patients with WWS have reduced levels of α-DG glycosylation (Beltrán-Valero de Bernabé et al., 2002).

Muscle-eye-brain (MEB) disease, as with WWS, is a severe CMD but with additional ocular defects or symptoms of epilepsy and lissencephaly. Patients life expectancy varies between 10-30 years (Santavuori et al., 1989). As with WWS there has only been one documented account of a mutation in *DAG1* resulting in MEB disease (Geis et al., 2013). The mutation (c.2006G>T) is a missense mutation that results in a phenylalanine replacing a cystine at position 669 which is located within the β-DG subunit (Geis et al., 2013). This mutation has been investigated at the cellular level using the equivalent mutation in murine DG. Signorino and colleagues found that the mutation resulted in accumulation of the uncleaved precursor protein in the ER (Signorino et al., 2017). MEB disease is also a heterogenous disease as mutations have been identified in the α-DG processing enzymes; POMT2 (Mercuri et al., 2006), FKRP (Beltran-Valero de Bernabé et al., 2004) and POMGNT2 (Yoshida et al., 2001). These mutations result in the hypoglycosylation of α-DG (Kano et al., 2002).

Fukuyama-type congenital muscular dystrophy (FCMD) is found almost exclusively in Japanese patients and is classified as an autosomal recessive disorder that can result in muscle, neuronal and eye abnormalities (Toda et al., 2000). The gene involved in this type of CMD is almost exclusively *fukutin* with the majority of patients having a 3kb insertion into the 3' untranslated region resulting in reduced mRNA stability and reduced protein levels (Kobayashi et al., 1998). As with other CMDs described above, FCMD results in a decrease in glycosylation of α-DG (Hayashi et al., 2001).

LGMD is less severe than the other MDs discussed here but is still characterised by muscle weakness and sometimes associated with cardiomyopathy and mental insufficiency (eg LGMD2I). The disease onset ranges from adolescence to adulthood (Brockington et al., 2001). Two separate mutations in *DAG1* have been found in patients with LGMD. In 2011 Hara and colleagues identified a missense mutation resulting in the substitution of a threonine residue for a methionine at position 192 located in the α-DG subunit (Hara et al., 2011). The mutation was identified in a woman with LGMD who displayed some cognitive impairment. They further

characterised the mutation by investigating the equivalent mutation in a murine model and found the mutation prevents LARGE binding, thus inhibiting α-DG glycosylation (Hara et al., 2011). The second *DAG1* mutation was identified more recently in 2018 by Dai and colleagues. They identified a homozygous missense mutation in a 64 year old Chinese male who suffered from mild LGMD. The mutation (c.2326C>T) results in the substitution of arginine for cystine at position 776. This substitution is within the NLS signal region of β-DG, however based on immunoblotting evidence the mutation significantly reduced levels of α-DG (Dai et al., 2018). In addition to mutations in *DAG1*, mutations have also been identified in FKRP (Brockington et al., 2001) and POMK (Strang-Karlsson et al., 2018). In LGMD patients instead of a complete absence of DG there appears to be a reduction in molecular mass suggesting glycosylation is reduced (Brown et al., 2004).

In addition to those discussed above, two additional *DAG1* mutations have been identified in a 7 year old male patient. However, he shows very mild MD phenotype with no evidence of muscle weakness or wastage. There is immunohistological evidence including few regenerating fibres and mild fibrosis that are suggestive of a MD phenotype. Both mutations, V74I and D111N, are located within the N-terminus of α-DG and resulted in reduced α-DG glycosylation. The reduced glycosylation phenotype was tested in *DAG1* knockout cell lines and neither of the mutant forms rescued the phenotype but both resulted in regular expression and localisation of β-DG (Dong et al., 2015).

1.1.5.2 Cancer

The interactions between cells and the ECM are important when it comes to the progression of many cancer types, a loss or reduction in connectivity can result in tumour cell metastasis. With DG playing a key role in connecting cells with the ECM it is logical to assume that a reduction of DG or impaired function would lead to increased tumour metastasis. DG was first implicated in having a role in cancer as early as 1993 when it was determined that the *DAG1* gene was mapped to a genomic

region suggested to be involved in tumour suppression (Ibraghimov-Beskrovnaya et al., 1993). Since then, a number of reports have focused on the expression and localisation of DG in many cancer cell types. High-grade primary prostate and breast cancers showed reduced levels of DG (Henry et al., 2001). Sgambato and colleagues also looked at breast cancers and colon cancers and found that levels of DG were reduced compared to control tissue. Interestingly, they find that the mRNA levels are unaffected but protein levels are decreased suggesting an increase in protein degradation, they also suggest that levels of DG negatively correlate with tumour grade and stage (Sgambato et al., 2003).

The above studies have looked at DG as a whole, while some studies have decided to focus on either α- or β-DG. Sgambato and colleagues looked at the levels of α-DG in cervical, vulval and squamous tumours. They found in normal control cells more than 80% were α-DG positive while this decreased depending on grade and invasiveness with only 2.6% of invasive cervical tumours being α-DG positive (Sgambato et al., 2006). Shen et al (2012) investigated the expression of α-DG in gastric cancer and found that levels of DG decreased during tumour progression. They also found that α-DG expression correlated with patient survival, however, β-DG expression did not (Shen et al., 2012). In addition to α-DG protein levels, Shimojo et al (2011) investigated levels of α-DG glycosylation in prostate cancer. They argue that it is in fact a reduction in glycosylation which results in a decrease in laminin binding that correlates with increased tumour stage rather than a decrease in α-DG protein levels (Shimojo et al., 2011). Taken together, this data suggests that both α-DG protein levels and glycosylation states play a role in the progression of various types of cancer.

β-DG has also been investigated for its role in various cancer cell types – some studies have focused on the relative protein levels while others have focused on various post-translational modifications. When levels of β-DG in oesophageal tumours were compared with healthy tissue it was found that the protein levels were decreased in the tumour cells however, the levels of mRNA were unchanged suggesting increased

degradation (Parberry-Clark et al., 2011) This was also observed in oral cancers with MMPs being implicated as the mechanism for β-DG degradation (Jing et al., 2004). Additionally, in a large scale study it was found that β-DG expression in oesophageal and colorectal adenocarcinomas, uretic transitional cell carcinoma and breast cancer was reduced or absent (Cross et al., 2008) while it was found in prostate cancer that β-DG expression was decreased and then re-expressed following metastasis (Mathew et al., 2013).

As well as altered levels of β-DG in multiple cancer types there have been a number of reports of increased β-DG cleavage in cancer cells. The 30kDa fragment (discussed in section 1.1.3.2.3) was found to be expressed at higher levels in human breast cancer cell lines compared with controls. However, when they investigated a number of cancer cell lines some only had the 30kDa fragment, some had both the 43kDa and 30kDa fragment and some simply had the 43kDa fragment (Losasso et al., 2000). Building on this, Cross et al (2008) found one prostate cancer cell line (PC3) had just the 43kDa fragment while another prostate cancer cell line (DU145) had both the 30kDa and 43kDa fragments suggesting the differential cleavage of β-DG is not a universal sign of cancer. Additionally, Mitchell et al (2013) looked at the prostate cell line LNCaP and found that the cleavage events were cell density dependent. Work from the Winder lab suggest that the cleavage of β-DG in various cancer cells results in the localisation of the 30kDa fragment to the nucleus, however, the role the β-DG fragments may play in the nucleus of cancer cells has yet to be investigated (Mathew et al., 2013; Mitchell et al., 2013).

1.2 Nuclear Dystroglycan

1.2.1 Dystrophin Associated Protein Complex in the Nucleus

Components of the DAPC were identified as nuclear, following the discovery of isoforms of Dp71 that appeared to preferentially localise to the nucleus of C2C12 myoblasts and N1E-115 neuroblastoma cell lines (González et al., 2000). The two

isoforms were initially termed Dp71f and Dp71d; Dp71f was spliced at exon 78 while Dp71d was not (Aleman et al., 2001). Both isoforms were found in the nucleus but to varying degrees. The allocations of Dp71f and Dp71d were further divided into sub-groups (Aragón et al., 2016) but we will discuss them in terms of Dp71f and Dp71d below. The nuclear localisation of Dp71 was further investigated by Marquez and colleagues in a study of PC12 neuronal cells. They found that during differentiation of PC12 cells the Dp71f was localised throughout the cell while Dp71d was localised almost exclusively to the nucleus (Marquez et al., 2003). In addition to the predominantly cytoplasmic localisation of Dp71f and nuclear localisation of Dp71d identified in C2C12, N1E-115 (González et al., 2000) and PC12 (Marquez et al., 2003) cells, this localisation difference is also observed in HeLa (Fuentes-Mera et al., 2006), a variety of mammary epithelial (Oppizzi et al., 2008), hippocampal neurone (Rodríguez-Munoz et al., 2015) and HEK293 (Nishida et al., 2016) cell lines. The nuclear import of Dp71d is not dependent upon a classical NLS but is instead dependent upon a ZZ domain, specifically ZZ-4 and requires Zn^{2+} to facilitate the import. Importin α2 and β1 were identified as the key importins required for nuclear localisation while CRM1 was required for nuclear export (Suárez-Sánchez et al., 2014).

While it is evident that Dp71, particularly Dp71d, localises to the nucleus of multiple cell types there is still limited understanding as to the physiological function of this localisation. Multiple studies have investigated the localisation of other DAPC components in order to determine whether Dp71 functions as part of a nuclear DAPC or if it has an independent nuclear function. To this end it was found that β-DG, β-sarcoglycan, α/β-dystrobrevin, α/β-syntrophin and nNOS were identified in the nucleus of HeLa cells and found to form a nuclear DAPC complex (Fuentes-Mera et al., 2006); β-DG, α/β-dystrobrevin and α/β-syntrophin formed a DAPC in the nucleus of PC12 cells while α-, β- and δ-sarcoglycan were not identified in the nucleus (Villarreal-Silva et al., 2010); β-DG, α/β-dystrobrevin and α/β-syntrophin also associate to form a nuclear DAPC in hippocampal neurones (Rodríguez-Munoz et al., 2015). Additionally, the nuclear DAPC components were analysed in C2C12

myoblasts and C2C12 myotubes where it was found that a nuclear DAPC was present in both myoblasts and myotubes despite a lack of Dp71 expression in myotubes (Gonzalez-Ramirez et al., 2008). Taken together this evidence would suggest that nuclear Dp71 is associated with a nuclear DAPC in a range of cell lines and that the association of a nuclear DAPC does not explicitly require Dp71.

In addition to determining whether Dp71 is associated with a nuclear DAPC a number of other studies have focused on understanding the role of Dp71 in the nucleus by studying the localisation within the nucleus, protein interactions and the consequences of perturbing Dp71 expression. In determining the localisation of Dp71 within the nucleus Fuentes-Mera and colleagues used a high salt extraction method on HeLa cells to isolate the nuclear matrix which consists of the structural nuclear lamins, in addition to other proteins. Using this method they identified that Dp71, β-DG and β-dystrobrevin associated with the nuclear matrix and also identified interactions between Dp71 and lamin B1 (Fuentes-Mera et al., 2006). In addition to HeLa cells, this interaction between Dp71 and lamin B1 was also implied in PC12 cells where Dp71 and lamin B1 were found to colocalise (Rodríguez-Muñoz et al., 2008; Villarreal-Silva et al., 2011). In addition to the interaction between Dp71 and lamin B1, Suarez-Sanchez and colleagues identified an interaction between Dp71 and the nuclear envelope (NE) protein emerin using Co-IP assays. Taken together this evidence would suggest that Dp71 localises just inside the NE where it associates with the nuclear lamina protein lamin B1 and the NE protein emerin.

A number of studies have investigated the physiological effects of perturbing Dp71 expression, an important point here is that the methods used resulted in the depletion of all Dp71 isoforms not just the predominantly nuclear Dp71d isoform. It was found that upon depletion of Dp71 in PC12 cells there was a decrease in total levels of β-DG, α/β-dystrobrevin and ε-sarcoglycan while levels of α1-syntrophin were unaffected but the localisation shifted to mostly nuclear (Villarreal-Silva et al., 2010). When Dp71 depleted cells were compared with suitable controls they were found to have decreased cell proliferation but no difference in cell death. The depletion of Dp71 results in an increased number of cells in G0/G1 with delayed

G0/G1 to S phase transition. The Dp71 depleted cells also have a decrease in the levels of lamin B1 and no effect on levels of emerin or lamin A/C (Villarreal-Silva et al., 2011). Additionally, there is weak evidence suggesting that emerin may be mislocalised in Dp71 depleted cells (Suárez-Sánchez et al., 2014; Villarreal-Silva et al., 2011). As the depletion of Dp71 results in the depletion of other nuclear DAPC components including β-DG it is important to determine whether the decrease in Dp71 is responsible for these observable phenotypes, or if it is the subsequent depletion of another DAPC component.

1.2.2 Nuclear Import and Export of β-dystroglycan

As described above, β-DG is translocated to the nucleus either independently or as part of a nuclear DAPC. However, a number of studies have aimed to understand the precise nuclear translocation pathway of β-DG. The initial study into the nuclear translocation of β-DG identified a bipartite NLS in the juxtamembrane position that consists of the sequences ^{776}RKKRKGK^{782} and ^{793}KK^{794} (Oppizzi et al., 2008). The mutation of these sequences resulted in a predominant cytoplasmic localisation. It was also identified that the nuclear translocation of β-DG was independent of glycosylation and precursor protein cleavage (Oppizzi et al., 2008). The presence and function of the NLS was also confirmed by Lara-Chacon and colleagues but they suggest only the ^{776}RKKRKGK^{782} sequence was required and not the ^{793}KK^{794} (Lara-Chacón et al., 2010), this was also confirmed using mutational analysis. In this study they went a few steps further in identifying the import pathway by confirming the NLS sequence was able to translocate a tetra-GFP construct to the nucleus suggesting the sequence is solely responsible for nuclear translocation and is not dependent upon the rest of the β-DG protein. Through sequential mutational experiments they determined that the R^{779} and K^{780} were the key residues responsible for nuclear import. Additionally, it was determined that nuclear import was dependent upon nuclear pore complex (NPC) function and Ran activity and is mediated by an interaction between the NLS of β-DG and importin α/β with a K_D of <1nM (Lara-Chacón et al., 2010).

The importin α/β interaction with the NLS of β-DG was confirmed by another group who also found that the cytoskeletal organisation protein ezrin bound to the NLS of β-DG. However, when constitutively active ezrin was used there was an increase in nuclear localisation of β-DG while inactive ezrin resulted in cytoplasmic accumulation (Vásquez-Limeta et al., 2014). Mutation of the ezrin NLS did not inhibit nuclear accumulation of β-DG however, the deletion of the actin binding domain of ezrin did, suggesting that cytoskeletal organisation may play a role in the translocation of β-DG to the nucleus, this was validated by cytoskeletal disruption using cytochalasin B (Vásquez-Limeta et al., 2014).

In order to determine whether the nuclear pool of β-DG was being internalised at the PM or was simply transported to the nucleus following post-translational modifications, non-permeable biotinylation experiments were carried out (Gracida-Jiménez et al., 2017; Vásquez-Limeta et al., 2014). It was found that the nuclear β-DG was in part generated from the PM. In an elegant set of experiments, it was successfully shown that β-DG had to pass from the ER to the Golgi before it is transported to the nucleus. It is also shown that the PM pool of β-DG then goes through clathrin-mediated endocytosis where it then enters the ER. The protein Sec61β is then required, through direct interactions, to export β-DG from the ER into the cytoplasm where it can then interact with Impα/β and be transported through the NPC into the nucleus (Gracida-Jiménez et al., 2017). Ultimately, the model for the translocation of β-DG to the nucleus is a retrograde one where it has to be transported to the PM where it is then internalised, incorporated into the ER and then released to the cytoplasm where it can ultimately enter the nucleus through the NPC with the assistance of Impα/β (Figure *1.7*).

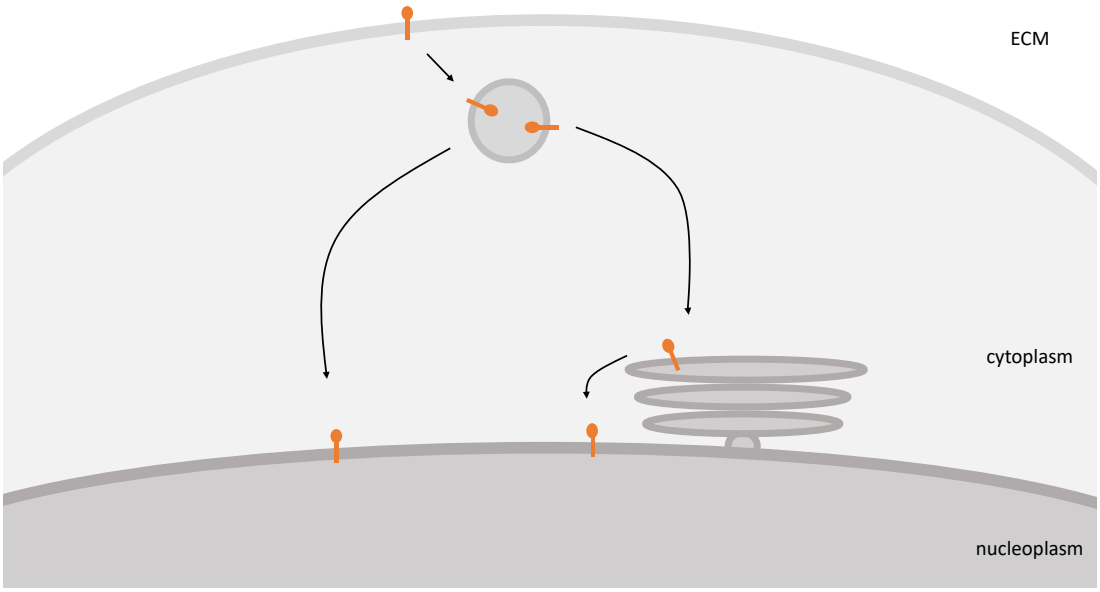

Figure 1.7 **Schematic illustrating the trafficking of β-DG from the PM to the NE via the ER**. Nuclear translocation of β-DG involves the retrograde trafficking from the PM to the NE. β-DG is post-translationally modified in the ER and then transported to the PM. At the PM β-DG is internalised and either transported to the NE or degraded. β-DG transport into the nucleus requires a NLS and interacts directly with importin α/β.

It has been established previously that phosphorylated β-DG, specifically phosphorylation at Y892, results in the increased internalisation of β-DG (Lipscomb et al., 2016; Sotgia et al., 2001). Thus, it stands to reason that phosphorylation may play a role in the nuclear translocation. However, there are conflicting results in the literature. In one study a phosphatase inhibitor is used to increase levels of phosphorylated β-DG and found an increased nuclear accumulation (Lara-Chacón et al., 2010). Furthermore, they used a mutant which replaced the Y892 with a phenylalanine which cannot be phosphorylated and somewhat surprisingly also found nuclear accumulation (Lara-Chacón et al., 2010). One experiment suggests unphosphorylated β-DG results in nuclear accumulation while the other suggests phosphorylation of β-DG results in nuclear accumulation. Additional evidence is found in the form of using a c-Src inhibitor, as c-Src is one of the kinases responsible for β-DG phosphorylation, inhibition of c-Src results in decreased phosphorylation of β-DG. This decrease in phosphorylation results in a decrease in nuclear β-DG suggesting phosphorylation may be required for nuclear translocation to the nucleus (Gracida-Jiménez et al., 2017). Taken together, these three experiments suggest a slightly different explanation than either author suggested. It would seem that while phosphorylation may be important for nuclear accumulation of β-DG it is not at the

Y892 site and may be one, or a combination of other phosphorylation sites responsible for this regulation.

There are some similarities between the nuclear import of Dp71 (see section 1.2.1) and β-DG, primarily the interaction between the protein and Impα/β which facilitates the translocation through the NPC. Additionally, there are some similarities between the nuclear export of Dp71 and β-DG, namely the interaction with the nuclear exporter CRM1 (Suárez-Sánchez et al., 2014; Vélez-Aguilera et al., 2018). Nuclear accumulation of β-DG occurs when cells are treated with leptomycin B (LMB) which specifically inhibits CRM1. A direct interaction between β-DG and CRM1 was also demonstrated using multiple pull-down assays. This interaction occurs between the nuclear export signal (NES) of β-DG and CRM1. The NES is located within the transmembrane region consisting of ^{763}ILLIAGIIAM^{772} where ^{763}ILL^{765} were determined to be the key hydrophobic residues - based on mutation experiments. Given the NES is located within the transmembrane region it was also shown that nucleoplasmic β-DG had a much higher turnover rate than the PM pool (Vélez-Aguilera et al., 2018).

1.2.3 Role of β-dystroglycan in the Nucleus

1.2.3.1 Nuclear Structure and Nuclear Protein Interactions

It is clear that β-DG is present in the nucleus and that it localises to the NE via the TM domain. Given that the NE is a double membrane it needs to be determined whether β-DG resides in both the outer nuclear membrane (ONM) and the inner nuclear membrane (INM) or if it is actually restricted to one of these. Using immuno-electron microscopy, it was determined that nuclear β-DG localises to just the INM and wasn't found at the ONM. Interestingly, when the soluble nuclear proteins were removed by an extraction buffer β-DG remained and appeared to be associated with the nucleoskeleton (Martínez-Vieyra et al., 2013). Additionally, nuclear β-DG has been

identified in the nucleoplasm and at the nucleoli (Azuara-Medina et al., 2019; Martínez-Vieyra et al., 2013).

The nucleoskeleton, as the name implies, makes up the structural component of the nucleus and is responsible for the overall shape and integrity of the nucleus in addition to being responsible for the mechanical properties. The key components of the nucleoskeleton are the lamins, lamins are type V intermediate filaments and are divided into A and B types. Both types form a meshwork of oligomers just below the NE where they are anchored to both the NE and the chromatin via protein interactions (Nmezi et al., 2019; Ranade et al., 2019; Shimi et al., 2015). As β-DG is an INM protein it is suggested that it may be involved in anchoring the lamins to the NE thereby ensuring the shape and integrity of the nucleus. It has been shown that when DG is perturbed, either by specific knockdown (KD) of β-DG or by knockout (KO) of the *DAG1* gene, there is a resultant disruption to the nuclear shape. In the KD experiment there was a significantly higher proportion of nuclei determined abnormal, this included nuclei that had irregular shape, nuclear blebbing or was either double or half the size of the control nuclei (Martínez-Vieyra et al., 2013). This result was confirmed in the KO experiments; a significantly higher proportion of abnormal nuclei in the KO condition compared with the control were observed – abnormal was defined as fissured, kidney shaped or blebbed (Gómez-Monsiváis et al., 2020). An additional study of DG KO cells confirmed these observations, they found that a significantly higher proportion of KO nuclei have nuclear blebs (8% and 10% for the KO samples and just 4% for the control), KO nuclei also have a significantly lower nuclear circularity compared with the controls and have a significantly larger nuclear area (Jimenez-Gutierrez et al., 2020). These experiments were all carried out in mouse C2C12 myoblasts. Taken together these perturbation experiments strongly suggest β-DG plays a role in the maintenance of nuclear shape and integrity in C2C12 myoblasts.

As it is clear that β-DG is localised to various regions within the nucleus it is important to understand its various interacting partners in order to understand its function.

Using a combination immunofluorescence microscopy and classical biochemical techniques a number of binding partners have been identified. A direct interaction has been determined between β-DG and p80-coilin which is a protein associated with Cajal bodies within the nucleus (Martínez-Vieyra et al., 2013). Additional interactions have been identified between β-DG and a number of nucleoli proteins including Nopp140 (Martínez-Vieyra et al., 2013), upstream binding factor (UBF) and B23 (Azuara-Medina et al., 2019). However, no direct interaction could be detected between β-DG and RNA polymerase I or SC35 a marker protein for splicing speckles. Additionally, no interaction could be confirmed between β-DG and the nuclear pore complex proteins Nup62 or Tpr. As β-DG was extracted as part of the insoluble nucleoskeleton it would be expected that it interacts with at least one component of the nuclear lamina. β-DG has been shown in multiple assays that it interacts directly with lamin A/C and lamin B1 (Martínez-Vieyra et al., 2013). In addition to the nuclear lamina, β-DG has been shown to interact directly with the INM protein emerin which also plays a role in connecting the nuclear lamina to the INM (Gómez-Monsiváis et al., 2020; Martínez-Vieyra et al., 2013).

1.2.3.2 Regulation and Localisation of Emerin and Lamin B1

1.2.3.2.1 Lamin B1

As discussed above lamin B1 was identified as an interacting partner of Dp71 as well as β-DG. More recent studies have also confirmed the interaction between β-DG and lamin B1 and have also investigated how perturbing β-DG (or DG) affects the regulation and localisation of lamin B1. When investigating the effects on lamin B1 following β-DG (or DG) perturbation either by KD, KO or use of a NES mutant resulting in excessive nuclear accumulation, it is reported that the overall protein levels of lamin B1 are reduced compared with controls (Gómez-Monsiváis et al., 2020; Martínez-Vieyra et al., 2013; Vélez-Aguilera et al., 2018). Despite the reduction in protein levels the mRNA transcript levels are unaffected suggesting that a lack of β-DG may reduce the stability of lamin B1 resulting in faster turnover. This was indeed

confirmed in the NES mutant study where accumulation of nuclear β-DG resulted in accelerated protein turnover via the nuclear proteosome (Vélez-Aguilera et al., 2018).

The DG perturbation studies described have also identified mislocalisation of lamin B1 and some phenotypes associated with lamin B1. When β-DG was specifically knocked down it was found that lamin B1 was mislocalised from the nucleus and formed distinct aggregates surrounding the nucleus (Martínez-Vieyra et al., 2013). This same abnormal staining was observed upon nuclear accumulation of β-DG via the NES mutant (Vélez-Aguilera et al., 2018). These two studies taken together suggest that it isn't just a decrease in β-DG levels responsible for maintaining correct lamin B1 localisation but also an increase which implies that the nuclear levels of β-DG are finely tuned and disruption of this results in inappropriate localisation of lamin B1.

It is important to note that despite lamin A/C being implicated as a binding partner of β-DG there is no evidence that reducing or eliminating β-DG results in a decrease in levels of lamin A/C or any abnormal localisation. However, it does appear that the nuclear accumulation of β-DG results in a decrease in total levels of lamin A/C but has no effect on mRNA levels or the protein localisation (Martínez-Vieyra et al., 2013; Vélez-Aguilera et al., 2018).

1.2.3.2.2 Emerin

As with lamin B1, emerin has been identified as a binding partner for β-DG in multiple studies and the mechanism of that interaction has been further elucidated. The interaction between the two NE proteins is facilitated primarily through their TM domains but additional regions – particularly the C-terminus of emerin – are required for tighter binding. The key residues within the TM domains, Met770 and Thr751 for β-DG and Ala238 and Phe236 for emerin were determined by computer modelling but are yet to be confirmed through mutagenesis assays. The dissociation constant

for the interaction between full-length β-DG and full-length emerin is 3.32nM as determined by surface plasmon resonance implying a very strong interaction (Gómez-Monsiváis et al., 2020).

Multiple studies have investigated the effects on emerin caused by perturbing β-DG (or DG) and the results are similar to those observed for lamin B1. The KD, KO or nuclear accumulation of β-DG (or DG) resulted in a decrease in overall emerin levels with no effect on the mRNA levels (Gómez-Monsiváis et al., 2020; Martínez-Vieyra et al., 2013; Vélez-Aguilera et al., 2018). The turnover of emerin was also shown to be increased in DG KO cells suggesting a decrease in protein stability as observed for lamin B1. Interestingly, in Emery-Dreifuss muscular dystrophy (EDMD) patient samples lacking emerin there was a decrease in levels of β-DG and NE staining suggesting the regulation and localisation may be reciprocal (Gómez-Monsiváis et al., 2020).

As with lamin B1, the localisation of emerin was disrupted in β-DG (or DG) perturbed cells. These cells displayed an emerin staining pattern similar to lamin B1 upon DG perturbation with aggregates forming both within and around the nucleus and a distinct loss of the NE ring staining (Martínez-Vieyra et al., 2013; Vélez-Aguilera et al., 2018).

Emerin is required for a number of processes within the nucleus and essential for correct cell functioning. These include the maintenance of the centrosome (Salpingidou et al., 2007) and regulating β-catenin activity which is an intracellular signal transducer involved in the Wnt signalling pathway (Markiewicz et al., 2006). These processes were investigated in β-DG (or DG) perturbed cells; when β-DG was knocked down there was an increase in the average distance between nucleus and centrosome to a similar extent as observed in emerin-null cells; a significantly higher proportion of KD cells with multiple centrosomes (17%) compared with the control (2%) was also observed (Martínez-Vieyra et al., 2013). A similar increase in nuclear-centrosome distance was observed in both DG KO cells and cells expressing the β-DG

NES mutant resulting in nuclear accumulation (Gómez-Monsiváis et al., 2020; Vélez-Aguilera et al., 2018). In addition to centrosomal organisation emerin plays a role in the regulation of β-catenin. Upon nuclear accumulation of β-DG there was a 2-fold increase in β-catenin activity compared with the controls (Vélez-Aguilera et al., 2018). However, this was not investigated in either the DG KO or the β-DG KD. Additionally, it hasn't been confirmed that the increased nucleus-centrosome phenotype is due to the mislocalisation of emerin or whether β-DG may play a more direct role.

1.2.3.3 Nucleoli Organisation and rRNA Transcription

As nucleoli organisation has been attributed, in part, to lamin B1 (Martin et al., 2009); the evidence suggesting localisation of β-DG to the nucleoli and a direct interaction determined between β-DG and Nopp140 it would appear that β-DG may be playing some functional role at the nucleoli. This functional role has been hinted at in β-DG KD cells and DG KO cells where there was a decrease in average size of nucleoli compared with the relevant control (Jimenez-Gutierrez et al., 2020; Martínez-Vieyra et al., 2013). Additionally, when β-DG accumulates in the nucleus due to mutation of the NES it was determined that the nucleoli of these cells where both smaller in size and decreased in number (Vélez-Aguilera et al., 2018).

More recently, a more detailed investigation into the role of β-DG at the nucleolus has been carried out which suggests β-DG may play a role in regulating transcription of rRNA (Azuara-Medina et al., 2019). In this study they identified a 30kDa fragment of β-DG which strongly localised to the nucleoli and increased in proportion relative to full-length β-DG following nucleoli stress. This fragment consists of the cytoplasmic domain of β-DG without the TM domain which they term the intracellular domain (ICD). Using multiple biochemical assays, they determined that both full-length β-DG and the ICD interact directly with nucleoli protein UBF and to a lesser extent B23. These interactions also demonstrated a preference for the ICD over full-length β-DG. They then investigated the effect of knocking down β-DG on

these proteins and found reduced levels of the nucleoli proteins UBF, B23 and fibrillarin despite no direct interaction between fibrillarin and β-DG. Additionally, overexpression of a GFP-β-DG ICD construct also resulted in mislocalisation of UBF but not B23 and results in a decrease in RNA polymerase I activity. Most interestingly, they suggest that KD of β-DG resulted in the nucleoli becoming larger and the total number decreasing compared with the control (Azuara-Medina et al., 2019). This is a direct contradiction of their previous results suggesting β-DG KD cells had smaller nucleoli (Martínez-Vieyra et al., 2013). These experiments were done in the same cell line (C2C12 mouse myoblasts) but with different RNAi molecules. The disparity between these two experiments calls into question the validity of these results. Despite this the authors further investigate the role of β-DG ICD at the nucleoli. They find KD of β-DG results in a decrease in levels of pre-rRNA 18S and an increase in 28S and further determine an interaction between β-DG and the promoter region of the rRNA. In this study they were unable to identify a nucleoli localisation or DNA binding sequence within the β-DG sequence suggesting that DNA binding is via interactions with other DNA binding proteins. Taken together, these experiments demonstrate a direct interaction between β-DG and nucleoli proteins with KD of β-DG resulting in decreased 18S and increased 28S rRNA expression while overexpression of GFP-β-DG-ICD resulted in increased 18S and decreased 28S rRNA expression suggesting β-DG plays a regulatory role in rRNA expression (Azuara-Medina et al., 2019).

1.2.3.4 Cellular Senescence

In two recent studies, it was noted that overexpression and the nuclear accumulation of β-DG in cells resulted in a decreased growth rate compared with controls (Azuara-Medina et al., 2019; Vélez-Aguilera et al., 2018). These results have recently been further expanded with evidence from DG KO cells which provides evidence for a decreased growth rate in cells lacking DG (Jimenez-Gutierrez et al., 2020). The decreased growth rate was investigated further to understand what caused this phenotype. It was found that a higher proportion of KO cells were in G0/G1 phase compared with the controls (Jimenez-Gutierrez et al., 2020), this was also observed

in the NES mutant (Vélez-Aguilera et al., 2018). Cell cycle progress at G0/G1 phase is indicative of senescent cells and it was found, following a β-galactosidase senescence assay that 20-25% of DG KO cells were senescent compared with just 5% for wild type (WT) cells. This senescence phenotype was also confirmed using other senescence markers including an increase in nuclear and cell size, a decrease in heterochromatin as determined by H3K9me3 intensity and decrease in average nucleoli area. Additionally, cells were treated with the senescence inducing molecule sodium butyrate. Treatment for 10 days induced senescence in almost 100% of WT cells but after 5 days of treatment 60-70% of KO cells were senescent compared with just 30% of WT. These data suggest the DG KO cells are already primed for a senescence phenotype and become senescent more readily. In order to determine what causes the senescence they investigated the mitotic process and levels of DNA damage. During mitosis there were significantly more mitotic abnormalities in DG KO cells compared with control – this included multipolar mitotic spindles and multidirectional alignment of chromosomes. This data would be in agreement with the increased number of centrosomes observed in KD and NES mutant cells described above. Following cell treatment with thymidine to release the cell cycle into S phase they found an increase in DNA damage, DNA damage response, the proportion of cells with nuclear blebs and telomere shortening in DG KO cells compared with WT cells. Taken together these data suggest that errors during mitosis as caused by multipolar spindles and multidirectional chromosome alignment lead to increased DNA damage which results in increased DNA damage induced senescence (Jimenez-Gutierrez et al., 2020).

1.3 Project Hypothesis

Dystroglycan plays a central role in maintaining a mechanical link between the extracellular matrix and the cytoskeleton with β-DG being the key anchor for the whole DAPC. In mouse C2C12 myoblast cells, β-DG localises to the nucleus where it is suggested to interact with a range of nuclear proteins including components of the nucleoskeleton. Disruption of DG in this cell line results in abnormal localisation and levels of structural nuclear proteins lamin B1 and emerin.

Based on the results described in mouse C2C12 myoblasts, one aim of this project was to investigate if the same observations are made in human myoblast cell lines. Additionally, a potential disruption of structural proteins lamin B1 and emerin would be expected to result in a change in the mechanical properties of the nucleus. Therefore, the overall aim of this project was to understand whether disrupting DG in a human myoblast cell line affects the mechanical properties of nuclei. This was investigated using a combination of biochemical and microscopy techniques including fluorescence microscopy and atomic force microscopy.

2 Materials and Methods

2.1 Bacteria and Molecular Biology

2.1.1 Bacterial Growth

Escherichia coli (DH5α) were grown in 5ml 2xYT liquid bacterial growth media (16g Tryptone, 10g Yeast extract and 5g NaCl made up to 1L with dH_2O) at 37°C in a shaking incubator overnight.

In order to generate competent bacteria 1ml of the overnight culture was transferred to 100ml of 2xYT and placed in the shaking incubator at 37°C. Cells were incubated until they reached an OD_{600} of between 0.4-0.6 AU, this was determined using a spectrophotometer (7315 spectrophotometer, Jenway). When the culture had reached the required density, the culture was centrifuged (Sigma 1-15K) at 700x g for 10 minutes at 4°C in order to pellet the cells. The supernatant was discarded, and the cell pellet was resuspended in 10ml of ice cold $CaCl_2$ at a final concentration of 100mM and incubated at 4°C for 2 hours. The cell suspension was then centrifuged at 700x g at 4°C for 10 minutes in order to pellet the cells. The supernatant was discarded, and the pellet was resuspended in 2ml of 100mM $CaCl_2$ and 15% glycerol. The cell suspension was then aliquoted into 100ml aliquots and flash frozen using liquid nitrogen. They were then stored at -80°C until they were used.

2.1.2 Transformation of Competent Bacteria

The competent DH5α cells described in section 2.1.1 were used for transformation. The cells were thawed on ice and then incubated on ice for a further 10 minutes. The plasmid DNA (100-200ng) was added to the competent cells and incubated on ice for 30 minutes. Following the 30 minute incubation the bacterial cells were heat shocked at 42°C for 30 seconds and then returned to the ice for 2 minutes. Following heat shock, 500ml of non-selective 2xYT was added and the cell suspension was incubated

at 37°C for 1 hour in the shaking incubator to allow recovery. The bacterial suspension was then centrifuged at 3000x g for 2 minutes to pellet the cells. The cell pellet was then resuspended in 100ml of 2xYT and plated on agar plates containing selection antibiotic. The plates were incubated at 37°C overnight.

2.1.3 Bacterial Glycerol Stocks

Transformed bacterial stocks were produced by selecting a colony from the agar plate and culturing it in 5ml 2xYT with the appropriate antibiotic. The culture was incubated overnight at 37°C in the shaking incubator. 750ml of the overnight culture was then added to 750ml of 50% glycerol and stored at -80°C.

2.1.4 Plasmid Purification

Plasmid purification was achieved using mini- or maxiprep kits (Qiagen) for either small- or large-scale purifications. The plasmids were purified from transformed *E. coli* cells. The purification was carried out as per the manufacturer's instructions. The cells were lysed using an alkaline lysis solution. The DNA was then bound to an anion exchange membrane (miniprep) or resin (maxiprep) and a salt wash was used to remove any impurities. The DNA was then eluted from the membrane or resin and subjected to isopropanol precipitation to concentrate and desalt the DNA. The concentrated DNA was then dissolved in sterile dH_2O and the concentration was determined using the NanoDrop Lite (Thermo Fisher Scentific, UK). The DNA solution was then stored at -20°C until use.

2.1.5 DNA Sequencing

DNA sequencing was carried out by MRC PPU DNA sequencing and services and results were interpreted using SnapGene Viewer.

2.2 Cell Culture

2.2.1 Growth of Cells

Human myoblast (Table *2.1*) (Mamchaoui et al., 2011; Santos-Zas et al., 2017) cell lines were maintained in Skeletal Muscle Cell Growth Media (PromoCell). Cells were grown to 70-80% confluency, determined on an inverted microscope (CETI) at 10x magnification. They were grown at 37°C and 5% CO_2 in a humidified environment. Cells were passaged using trypsin-EDTA (0.05% trypsin, 0.5mM EDTA, pH 7.4). Following dissociation of cells, media was added and centrifuged at 100x g (11030 rotor, Sigma) for 3 minutes. Cells were resuspended in media and plated at the required density in plastic culture flasks (Greiner Bio-one).

Table 2.1 **List of cells used.**

Cell Type	**Original clone number**	**Referred to in text**
Human Myoblast KM155		WT
gRNA Control	Clone 1.B8	Control
DAG1 Knockout	Clone 1.B6	*DAG1* KO A
DAG1 Knockout	Clone OG	*DAG1* KO B
DAG1 Knockout	Clone 2.D8	*DAG1* KO C
DAG1 Knockout	Clone 1.G4	*DAG1* KO D
DAG1 Knockout	Clone 1.G7	*DAG1* KO E

2.2.2 Cell Counting

20μl of cell suspension was added to 20μl 0.4% Trypan Blue (Lonza, US) and 20μl of this mixture added to the haemocytometer. The haemocytometer is etched with 4 x 1mm^2 squares, the number of cells in each square was counted, cells that had taken up Trypan Blue were not counted. This was done using a 10x magnification on an inverted microscope (CETI). Each mm^2 contains 100nl of liquid so to calculate the number of cells per ml the average number of cells must be multiplied by 10^4. The final viable cell count was calculated using this formula:

$$\frac{Total\ viable\ cells\ in\ all\ squares}{4} \times Dilution\ factor\ (\times 10^4)$$
$$= Total\ viable\ cells/ml$$

2.2.3 Cell Seeding Based on Confluency

Cell seeding based on confluency was used for cell density experiments. The initial cell density was determined using an inverted microscope (CETI) at 10x magnification. The area of the flask or dish that was being seeded was divided by the area of the initial flask to give a scaling value. The cells were centrifuged at 100x g (11030 rotor, Sigma) for 3 minutes and the pellet was resuspended in 10ml of media. The scaling value is the same as the volume of cell suspension in ml to get the same confluency as the initial flask, the correct confluency for each experiment was then calculated based on this.

2.2.4 Cell Synchronisation with Thymidine Block

As described by Jimenez-Gutierrez et al (2020). Cells were grown to 20-30% confluency as determined by an inverted microscope (CETI) at 10x magnification. Cells were treated with 2mM thymidine (Sigma-Aldrich) and cultured at 37°C, 5% CO_2 for 18 hours. Thymidine was then removed and replaced with fresh media and cultured for 9 hours. 2mM thymidine was then added and incubated for 18 hours. Cells were then either harvested for experiments and analysis or fresh media was added and harvested at indicated time points.

2.2.5 Cell Synchronisation with Serum Starvation

The system was similar to that outlined by Dreesen et al. (2013) and Villarreal-Silva et al. (2011). Cells were seeded at the required density and grown for 24 hours at 37°C, 5% CO_2 using Skeletal Muscle Cell Growth Media (PromoCell) with supplements added. Cells were then washed twice with 1 x phosphate buffered saline (PBS; 137mM NaCl, 10mM phosphate, 2.7mM KCl, pH 7.4) and Skeletal Muscle Cell Growth

Media (PromoCell) without supplements (serum free) was added and cells were incubated at 37°C, 5% CO_2 for 24 hours. Following serum starvation for 24 hours cells were washed twice with 1x PBS and fully supplemented media was added. Cells were then harvested either immediately or at the indicated time points.

2.2.6 Lipofectamine 2000 Cell Transfection

Transfecting DNA into myoblast cell lines used Lipofectamine 2000 and was carried out as per the manufacturer's instructions. Cells were seeded and grown to a high density (>80%) in antibiotic free cell growth media. Plasmid DNA (1-5μg) was added to 100μl low-serum media and 2μl (per well of a 12 well dish) lipofectamine 2000 was added to 100μl low-serum media and incubated at room temperature for 5 minutes. 100μl of lipofectamine and media mixture was added to 100μl of DNA and media mixture and incubated for 20 minutes at room temperature. Following incubation, the 200μl of lipofectamine, DNA and media mixture was added to each well containing cells. The cells were then incubated at 37°C and 5% CO_2 for 6 hours before changing media. Cells were then grown for a further 18 hours to allow protein expression and then fixed and stained as described in section 2.5.1.

2.3 Atomic Force Microscopy

2.3.1 Whole Cell Sample Preparation

Cells were seeded at 60% confluency in 40 x 11 mm petri dishes (TPP®) and incubated at 37°C, 5% CO_2 for 24 hours before measurements. For cell synchronisation experiments cells were seeded at 40% confluency and incubated at 37°C, 5% CO_2 for 24 hours. For synchronisation, serum free media was then added and incubated as above for 24 hours, regular media was added prior to measurements, the sample was measured within an hour of synchronisation release.

2.3.2 Trichostatin A Treatment

Cells were seeded at 40% confluency and incubated at 37°C, 5% CO_2 for 24 hours. Cells were then washed and 300nM of Trichostatin A (TSA; Cell Guidance Systems, UK) in serum free media was added to the sample. Cells were incubated at 37°C, 5% CO_2 for 24 hours. Prior to measurement the cells were washed with 1 x PBS and 300nM of TSA in normal media was added to the sample. The sample was then measured within an hour of synchronisation release (Hobson et al., 2020).

2.3.3 Cytochalasin D Treatment

Cells were seeded at 40% confluency and incubated at 37°C, 5% CO_2 for 24 hours. Cells were then washed and 500nM of Cytochalasin D (CytoD; Thermo Fisher Scientific, UK) in serum free media was added to the sample. Cells were incubated at 37°C, 5% CO_2 for 24 hours. Prior to measurement the cells were washed with 1 x PBS and 500nM of CytoD in normal media was added to the sample. The sample was then measured within an hour of synchronisation release.

2.3.4 Poly-L-Lysine Coating of Dishes

0.01% Poly-L-lysine solution with molecular weight 150,000-300,000 Da (Sigma-Aldrich) was added to the petri dish and incubated at room temperature for 30 minutes. Poly-L-lysine solution was then removed, the petri dish was then washed twice with sterile H_2O. The dish was then left at room temperature for at least 1 hour to dry to ensure complete coating of the surface.

2.3.5 Nuclear Sample Preparation

This protocol was adapted from the cell fractionation protocol described in Martínez-Vieyra et al. (2013). Cells grown to 80% confluency in T175 flask were washed twice in ice-cold 1x PBS and scraped into 2ml of ice-cold 1x PBS. Cells were then centrifuged at 3,500x g at 4°C for 15 minutes (Sigma 1-15K). The pellet was then resuspended in 0.5ml fractionation TM buffer (10mM Tris-HCl pH 8.0, 2mM $MgCl_2$ 0.5mM PMSF, 1x protease inhibitor cocktail (Roche)) and incubated on ice for 10 minutes. 0.5ml of 2% Triton X-100 (Sigma-Aldrich) in PBS was then added to the cell suspension and incubated on ice for 10 minutes. The cell suspension was then transferred to a Dounce homogeniser (Wheaton) and the cells were homogenised with between 18-26 strokes, the membrane integrity was monitored using an inverted microscope (CETI) at 10x magnification. The cell suspension was then centrifuged at 3,500x g at 4°C for 15 minutes. The supernatant containing the non-nuclear fraction was saved for further analysis. The pellet contained the nuclear fraction and was resuspended in 0.5ml of fractionation buffer I (0.32M sucrose, 3mM $CaCl_2$, 0.1mM EDTA, 10mM Tris-HCl pH 8.0, 1mM DTT, 0.5mM PMSF and 0.5% NP-40). 0.5ml of fractionation buffer II (2M sucrose, 0.1mM EDTA, 10mM Tris-HCl pH 8.0, 1mM DTT and 0.5mM PMSF) was then added to the nuclear suspension and pipetted to ensure thorough mixing. In an ultra-centrifuge tube (Beckman) 1ml of fractionation buffer II was added and the nuclear suspension was laid on top with 3ml of fractionation buffer I being laid on top of the nuclear suspension. This produces a sucrose gradient which was then centrifuged at 80,000 rpm using the MLA-80 rotor at 4°C for 1 hour. The supernatant was then removed, the pellet was resuspended in 4ml PBS, this was then added to the poly-L-lysine (Sigma) coated 40 x 11 mm petri dishes (TPP®) and left to attach for at least 30 minutes. After at least 30 minutes the PBS was removed and

fresh PBS was added, PBS was then removed and cell growth media was added ready for measurements.

2.3.6 AFM Cantilever Preparation

Tipless MLCT-O10 AFM probes (Bruker) were used, all triangular cantilevers (A,C,D,E and F) were removed using tweezers while the rectangular cantilever was retained (spring constant between 0.020-0.025N/m, length between 195-205mm, width between 15-25mm). The cantilever was then mounted on the AFM (Nanowizard III, JPK Instruments). Microscope slides were cleaned using Piranha solution (80% (v/v) H_2SO_4, 20% (v/v) H_2O_2) for at least 1 hour, washed with isopropanol and allowed to dry. The UV-curing adhesive (Norland Optical Adhesive 81, Norland) was added to the microscope slide and spread using a scalpel blade, the 5μm diameter polystyrene spheres (Sigma) were added to the slide above the adhesive and the slide was then placed on the microscope (Nikon A1). Using the manual height adjustment, the cantilever was lowered to contact the adhesive and retracted, followed by lowering to remove excess adhesive and then again to pick up the sphere. The cantilever was then removed from the mount and the adhesive was cured using UV for at least 5 minutes.

2.3.7 Whole Cell Data Acquisition

Data was acquired using the JPK Nanowizard III with either modified tipless MLCT-010 (described in section 2.4.6) with a nominal spring constant of 0.02N/m or MLCT-SPH-5UM (Bruker) with a nominal spring constant of 0.03N/m. The JPK Nanowizard was mounted on a Nikon A1 inverted microscope. Prior to measurements the cantilever was calibrated using the thermal vibration method to determine the spring constant. Prior to measuring the cells, the sensitivity of the cantilever in the cell growth media at 37°C was determined using the contact-based method. Using a 40x magnification on the optical microscope a single cell was identified and either the area over the nucleus or an area of the cytoplasm was measured with an approach

speed of 5μm/s and a setpoint of 3nN. Each area of the sample was measured at least 10 times to give an average of each sample point and allowed the removal of unsuitable curves while maintaining multiple useable curves for each sample point. For each experiment at least 15 cells were measured for each sample.

2.3.8 Nucleus Data Acquisition

As described in section 2.4.7 except only functionalised MLCT-O10 cantilevers were used with an extend speed of 3μm/s and a setpoint of 1nN. For each experiment at least 10 nuclei were measured for each sample.

2.3.9 Data Analysis

Data analysis was carried out using the JPK SPM data processing software. The curves for each sample point are processed as a batch where the baseline is subtracted to return everything to zero, the offset point is adjusted to determine the point of contact, the correct hight for cantilever bending is determined by subtracting the sensitivity measurement and converts the force-distance curve into a force-indentation curve. Any unsuitable curves are identified manually and are discarded during this process and are not included in the later analysis. Following this the elasticity for each curve is determined from the indentation using the Hertz/Sneddon model. The average Young's modulus for each sample point is then determined using Excel and exported into GraphPad Prism for statistical analysis.

2.4 Microscopy

2.4.1 Immunofluorescence Microscopy

Cells were seeded at required density in a 6 well or 12 well plate containing 13mm coverslips. 24-hours post-seeding the media was aspirated and cells were washed twice with 1x ice-cold PBS. 2ml of 3.7% (v/v) paraformaldehyde (PFA; Sigma-Aldrich) was added to each well and incubated at room temperature for 10 minutes to fix the cells. The PFA was then removed, and cells were washed twice with 1x ice-cold PBS. Cells were then permeabilised using 2ml of 0.2% Triton X-100 (Sigma-Aldrich) in PBS and incubated at room temperature for 3 minutes. The Triton X-100 solution was then removed and cells washed twice with 1x ice-cold PBS and kept at 4°C until staining. Coverslips were blocked using blocking buffer (3% BSA (w/v), 5% FBS (w/v) in PBS) for 1 hour in a humidified environment, following this 10μl of primary antibody (Table *2.2*) diluted in blocking buffer was added to each coverslip and incubated for at least 2 hours in a humidified environment at 4°C. Coverslips were then washed three times in 1x PBS and 10μl of fluorescent conjugated secondary antibody (Table *2.3*) diluted in blocking buffer was added to each coverslip and incubated at room temperature in a humidified environment for 1 hour. The coverslips were then washed twice in 1x PBS and once in dH_2O and allowed to dry. Following drying they were mounted onto 4μl hydromount (National Diagnostics) containing 2.5% 1,4-Diazabicyclo[2.2.2] octane (DABCO; Sigma-Aldrich) as an antifade preservative and the nuclear counterstain DAPI (Sigma-Aldrich) at 10ng/ml on glass slides (Fisher, 0.8-1.0mm). Coverslips were secured using nail varnish and stored in the dark at 4°C until imaging.

Table 2.2 **List of primary antibodies used for immunofluorescence detection**.

Antibody Target	**Species**	**Company**	**Concentration**
MANDAG2 (β-DG)	Mouse		Varied depending on batch
1709 (phospho-β-DG)	Rabbit		1:20
JAF1 (β-DG)	Rabbit		1:500

LG5 (β-DG)	Rabbit		1:500
C-20 (β-DG)	Goat	Santa Cruz	1:250
Lamin A/C	Mouse	Cell Signalling Technology (4C11)	
Lamin B1	Rabbit	ProteinTech	1:500
Lamin B2	Rabbit	Cell Signalling Technology (D8P3U)	1:500
Emerin	Rabbit	Santa-Cruz (FL-254)	1:250
γH2AX	Mouse	EMD Millipore	1:250
H3K9me3	Rabbit	BioVision	1:200
GFP	Mouse	Roche	1:250
HA-tag	Rat	Roche	1:250

Table 2.3 **List of secondary antibodies used for immunofluorescence detection**.

Antibody Target	**Species**	**Company**	**Concentration**
Anti-Mouse AlexoFlore 594	Goat	Life Technologies	1:500
Anti-Rabbit AlexoFlore 594	Goat	Life Technologies	1:500
Anti-Rabbit Alexoflore 488	Donkey	Life Technologies	1:500
Anti-Goat Alexoflore 488	Donkey	Life Technologies	1:500
Anti-Rat Alexoflore 488	Rabbit	Life Technologies	1:500

2.4.2 Leica Fluorescence Microscope

Fluorescent images were acquired using a Leica DMIRE2 inverted fluorescent microscope which was controlled by a Leica CTRMIC controller. Leica filters A4 (DAPI; excitation at 360nm and emission at 400nm), N2.1 (TexasRed, AlexaFluor 594; excitation515-560nm and emission at 580nm) and L5 (GFP, FITC, AlexaFluor 488; excitation at 480nm and emission at 505nm) were used. A Leica DC350F CCD camera was used and the images were acquired using Lieca Q-Fluoro software.

2.4.3 Nikon A1 Confocal

Confocal images were acquired using the inverted Nikon A1 Confocal system for both slides and glass bottom dishes. The CFI Plan Apochromat VC 60x oil (NA 1.4) objective was used. The excitation sources were 405nm, 457-514nm argon laser, 561nm sapphire laser, 642nm diode laser. Image acquisition used Nikon Elements Software.

Images were acquired with a pinhole of 1.0 Airy Units (A.U), a pixel size of 1024 x 1024, a pixel dwell of 1.1 and a Z-step of 0.4μm for intensity measurement experiments and 0.125μm for nuclear volume analysis. For all immunofluorescent experiments the laser power was set to 5.0 and the gain was set to 0. The exposure time was varied depending on sample and intensity to ensure a dynamic range for intensity quantification. Images were then processed and analysed in Fiji (is just ImageJ) software.

2.4.4 Live Cell Imaging for Cell Migration

Live cell images were acquired using the inverted Ti eclipse Nikon Widefield system for glass bottom dishes and cell migration chambers. The Plan Apo 20x (NA 0.75) objective was used. The excitation source was SpectraX LED excitation (395nm, 440nm, 470nm, 508nm, 561nm, 640nm) using the Quad filter for DAPI/GFP/RFP/Cy5 with matching emission filter wheel. The detection source used was Andor Zyla sCMOS (2560 x 2160; 6.5μm pixels). The environmental conditions of 37°C with 5% CO_2 were maintained using the Oko-lab environmental control chamber. Image acquisition used NIS Elements Software.

Control and KO cells were stained with CellTracker™ Red CMTPX (Invitrogen) and CellTracker™ Green CMFDA (Invitrogen) respectively. Control and KO cells were then co-cultured in a glass bottom petri dish (Ibidi). The environmental control chamber was equilibrated at 37°C with 5% CO_2 and the petri dish added. Each experiment was imaged over 15 hours with each XY position imaged every 10 minutes. For each time point a brightfield image was taken in addition to images in the red and green channels in order to identify the two cell types.

2.4.5 Propidium Iodide Staining for FACS

Cells were washed twice with 1x PBS and treated with 25%(v/v) trypsin-EDTA and incubated at 37°C for 5 minutes. Cells were then collected in 7ml of 1x PBS and centrifuged at 700x g for 5 minutes to pellet the cells – the supernatant was discarded. Cells were resuspended in 0.5ml ice-cold PBS with 2mM EDTA. The cell suspension was then added drop-by-drop into ice-cold 70% (v/v) ethanol and incubated at 4°C for at least 24 hours and stored at 4°C until staining. Fixed cells were pelleted by centrifugation at 800x g for 10 minutes. Cells were washed twice with 1x PBS and collected by centrifugation. The cell pellet was resuspended in 1x PBS containing 200μg/ml ribonuclease A (Sigma-Aldrich) to prevent RNA staining, this was incubated on ice for 5 minutes. The propidium iodide (Sigma-Aldrich) was added to a final concentration of 50μg/ml and incubated for at least 3 hours at 4°C in the dark until it was imaged.

2.4.6 Fluorescence-Activated Cell Sorting (FACS)

All FACS experiments and data processing was carried out by the flow cytometry core facility in the medical school.

2.4.7 Scanning Electron Microscopy

All electron microscopy was carried out by Chris Hill in the electron microscopy facility. AFM cantilevers were mounted onto an aluminium SEM examination stub with Liet-C carbon sticky tab and Leit-C carbon moulding putty. The cantilever was gold coated using an Edwards 150b Gold Coater. The cantilevers were then examined and imaged using a Tescan Vega 3 LMU Scanning Electron Microscope.

2.5 Image Analysis

2.5.1 Nuclear Morphology

In order to quantify the 2D nuclear morphology (area and shape) a specific macro was written for FIJI. Briefly, the macro split the green, blue and red channels and if applicable the Z-stack for each channel was converted into a maximum projection in order to retain all the signal from all the slices. Then the script was instructed to wait for user so the intensity could be thresholded to ensure the full nuclear area was selected. The analyse particles (set to size >100μm, circularity >0.3 and exclude on edges was selected) command was used on the thresholded image. The measurements collected were area and shape descriptors (circularity, aspect ratio, roundness and solidity). The data was copied from Fiji into Excel and GraphPad Prism for statistical analysis.

2.5.2 Nuclear/Cell Area Ratio

In order to determine the ratio between nuclear/cell area the area of the nucleus was determined as outlined in section 2.5.1 but without using the measurement shape descriptors. The area of the whole cell was determined using phalloidin staining where the cell was manually traced. This produced the area of nuclei and the area of the whole cell which was then copied into Excel. The nuclear area was divided by the cell area to give a ratio per cell and this was then exported to GraphPad Prism for statistical analysis.

2.5.3 Nuclear Fluorescence Intensity Quantification

In order to determine nuclear intensity a script for Fiji was written. This script, as with those discussed previously, split the channels and where necessary produced a maximum projection image. The DAPI channel was then used to determine nuclear area and the mask for each nucleus was added to the ROI manager. The mean grey

value within that mask on the channel of interest was then measured. These data were then exported to Excel for further analysis. The mean grey value was then normalised to the largest value across that repeat. The normalised data was then exported to GraphPad Prism for statistical analysis.

2.5.4 Cell Migration

Generated time laps images were processed using FIJI using the Manual Tracking plugin and the Chemotaxis and Migration Tool 2.0 (ibidi) plugin. Each XY position was separated into an individual time laps image sequence and then the three channels were split. Cells were manually tracked and this data was then entered into the Chemotaxis and Migration Tool which then calculated migration velocity and total migration distance. This data was then exported to Excel to collate and organise and then imported into GraphPad Prism for statistical analysis.

2.6 Biochemistry

2.6.1 Whole Cell Lysate Sample Preparation

Cells were grown to required density and then washed twice with 1 x ice cold PBS and then lysed with radio immunoprecipitation assay buffer (RIPA; 150mM NaCl, 1% NP-40, 0.5% sodium deoxycholate, 0.1% SDS, 25mM Tris pH 7.4) supplemented with appropriate protease and phosphatase inhibitors on ice for 15 minutes. Lysed cells were then harvested using a cell scraper. The lysed samples were then sonicated (Sanyo Soniprep 150) three times for 10 seconds with 10 seconds rest on ice between each. Samples were then centrifuged (Sigma 1-15K) for 15 minutes at 18,000x g at 4°C. The supernatant was retained and either used immediately or stored at -20°C until use.

2.6.2 Nuclear Fractionation Sample Preparation

See section 2.3.5.

2.6.3 Determining Protein Concentration

The protein concentration of samples was determined using the MicroBCA™ protein assay kit (Thermo Scientific) as per the manufacturer's instructions.

2.6.4 SDS-Polyacrylamide Gel Electrophoresis (SDS-PAGE)

SDS-PAGE mini-gels were cast using the Bio-Rad casting system, each gel was cast individually and consisted of 12% resolving gel (2ml H_2O, 4.15ml 40% Bis-Acrylamide, 5µl TEMED, 100µl 10% ammonium persulphate and 3.75ml gel stock pH 8.8 which consists of 1.5M tris and 0.4% SDS) and a 5% stacking gel (3.525ml H_2O, 800µl 40% Bis-Acrylamide, 15µl TEMED, 50µl 10% ammonium persulphate and 625µl gel stock pH 6.8 which consists of 1M tris and 0.75% SDS). Samples were boiled in Laemelli

sample buffer and loaded onto the cast mini-gels along with a molecular weight protein ladder. The mini-gels were run in Bio-Rad tanks that contained 1 x SDS running buffer (28.8g glycine, 6g Tris, 2g SDS, made up to 2L ddH_2O), the samples run at a fixed voltage of 120 – 150V through the whole gel.

2.6.5 Electrotransfer

Proteins that were separated via SDS-PAGE were electroblotted from the mini-gels to Polyvinylidene fluoride (PVDF; Immobilon-P, Merck) membranes using a mini Trans-Blot electrophoretic transfer cell (Bio-rad). The SDS-PAGE gel was then added to 1 x Towbin (2.5mM Tris, 19.2mM glycine, 20%(v/v) methanol, 0.025% SDS) transfer buffer in addition to methanol activated PVDF, filter paper and fibre pads. The components were then assembled into the transblot caseate, an ice pack was added to prevent excessive warming and Towbin transfer buffer was added as described by the manufacturer's instructions. The membranes were blotted at 100V for 75 minutes and then removed from the transfer apparatus.

2.6.6 Western Blotting

The electroblotted membranes were blocked using 5% (w/v) skimmed milk powder in tris-buffered saline with Tween 20 (TBST; 5mM Tris-Cl, 15mM NaCl, pH 7.6) for 1 hour at room temperature with slight rocking. Then primary antibody (3-10ml), diluted in blocking buffer to the required concentration (Table *2.4*), was added to the membrane and incubated at 4°C overnight with slight rocking. The membrane was then washed once with TBST for 10 minutes and then twice for 5 minutes. Following washing, secondary antibody conjugated to HRP (5-10ml) was diluted in blocking buffer to the required concentration (Table *2.5*) and added to the membrane where it was gently rocked at room temperature for 1 hour. The membrane was then washed once with TBST for 10 minutes and twice for 5 minutes. A chemiluminescent signal was produced using ECL western blot detection kit (GE Life Sciences) with equal volumes of ECL I and ECL II being added to the membrane. This was incubated at

room temperature for 5 minutes and then imaged using the Bio-Rad ChemiDoc XRS+ system. The chemiluminescence signal was recorded over a time course of between 5 seconds and 30 minutes.

Table 2.4 **List of primary antibodies used for western blotting.**

Antibody Target	Species	Company	Concentration
MANDAG2 (β-DG)	Mouse		Varied depending on batch
1709 (phospho-β-DG)	Rabbit		1:20
JAF1 (β-DG)	Rabbit		1:500
LG5 (β-DG)	Rabbit		1:500
Lamin A/C	Mouse	Cell Signalling Technology (4C11)	1:500
Lamin B1	Rabbit	ProteinTech	1:500
Emerin	Rabbit	Santa-Cruz (FL-254)	1:1000
Calnexin		Santa-Cruz (C-20)	
GAPDH	Mouse	Santa-Cruz (0411)	1:1000

Table 2.5 **List of secondary antibodies used for western blotting.**

Antibody Target	Company	Concentration
Anti-Mouse HRP	Sigma-Aldrich	1:10,000
Anti-Rabbit HRP	Sigma-Aldrich	1:10,000
GAPDAH HRP	Sigma-Aldrich	1:10,000

2.6.7 Membrane Stripping

Where the membrane was re-probed for a second protein then the antibodies were removed using mild stripping buffer (15g Glycine, 1g SDS, 10ml Tween 20 in 1L and pH adjusted with HCl to pH 2.2). The membrane was incubated twice with mild stripping buffer for 15 minutes at room temperature with gentle rocking. This was then followed by two 10 minute PBS washes and two 5 minute TBST washes. The membrane was then blocked and probed as described above.

2.6.8 Quantification of Western Blots

Intensity analysis of western blot bands was carried out using the Bio-Rad Image Lab Software. The band was manually outlined using the outline tool, 3 background areas were also selected, the background setting was set to global to automatically subtract the background. The adjusted intensity along with other data was exported to Excel where the intensity was normalised to the adjusted intensity of the loading control GAPDH.

2.7 Cellular Stress Assays

2.7.1 Oxidative Stress

Cells were seeded at 80% confluency as described in section 2.2.3 and allowed to settle and adhere to the coverslip for 24 hours. H_2O_2 (Sigma) was then diluted in media and added to cells at the described concentrations and incubated at 37°C, 5% CO_2 for the described time period. Following incubation, the cells on the coverslips were fixed and stained for immunofluorescence analysis. Nuclear shape and size were measured in addition to γH2AX intensity as outlined in sections 2.4.1 and 2.6.

2.7.2 Osmotic Stress

Hypertonic cell stress was induced using NaCl (Sigma) and Polyethylene Glycol 4000 (PEG4000; Sigma). Cells were seeded at 80% confluency as described in section 2.2.3 and allowed to settle and adhere to the coverslip for 24 hours. NaCl or PEG4000 was added at the described concentrations and incubated at 37°C, 5% CO_2 for the 1 hour or 30 minutes respectively. Following incubation, the cells on the coverslips were fixed and stained for immunofluorescence analysis. Nuclear shape and size were measured in addition to γH2AX intensity as outlined in section 2.4.1 and 2.6.

2.7.3 Mechanical Stress

2.7.3.1 Transwell Migration Assay

For these experiments 24-well Transwell migration inserts (Thermo Fisher) were used with either 8μm or 3μm pores. 1ml of media was added to the Transwell insert and incubated for 30 minutes prior to cell seeded. 2 x 10^6 cells/ml were seeded directly into the pre-warmed media and on top of the insert membrane, 1ml of media was also added to the bottom of the insert. Cells were then incubated at 37°C, 5% CO_2 for 48 hours to allow sufficient cell migration. Following migration, cells were

fixed and permeabilised as described in 2.4.1. The side of the membrane not being imaged was scrapped with a cotton bud to remove the cells that were not being imaged. Each individual membrane was then cut from the insert in order to stain cells using immunofluorescence. Once the inserts were removed, they were stained and mounted as described in section 2.4.1. Membranes were then imaged and nuclear shape and γH2AX intensity were measured as outlined in sections 2.4.1 and 2.6.

2.7.3.2 Passive Cell Compression

Cells were grown in glass bottom petri dishes (ibidi) and allowed to settle and attach for 24 hours. 1% agarose solution was made using 1g agarose in 100ml of cell culture media and this was poured into a 10cm petri dish and allowed to set. Once set it was incubated at 37°C, 5% CO_2 for 24 hours. After 24 hours cells were washed twice with PBS and fresh media containing Hoechst 33342 (Thermo Fisher) was added to the cells. 1.5cm discs of 1% agarose were cut out and placed over the top of the cells followed by a weighted insert (kindly provided by Ben Phillips, King lab). Cells were then incubated for 1 hour before imaging. Nuclear shape was then measured and analysed as described in section 2.6.

3 Investigating the effect of disrupting DG on nuclear morphology of human myoblast cells

3.1 Introduction

3.1.1 Nuclear Shape

Nuclear shape is determined by the underlying structural components of the nucleus such as the nuclear lamina and the NE proteins (Chen et al., 2018; Lammerding et al., 2006). Additionally, nuclear shape is organised and maintained by interactions with the cytoskeleton through the linker of nucleoskeleton and cytoskeleton (LINC) complex (Lüke et al., 2008). The maintenance of overall nuclear shape is determined by the balance between the nucleoskeleton and the cytoskeleton with the LINC complex bridging the two.

Experimentally, analysis of nuclear shape is generally reported in terms of nuclear circularity, nuclear sphericity or a nuclear contour ratio. The maintenance of nuclear shape is coordinated by the key structural components of the cells. Cytoskeletal actin, microtubules and intermediate filaments are required for maintaining nuclear shape as disruption of these structures results in abnormal shaped nuclei (Jacob et al., 2020; Patteson et al., 2019a; Sankaran et al., 2020). Additionally, the LINC complex which connects the cytoskeleton with the nucleoskeleton plays an essential role in maintaining nuclear shape as a reduction in levels of Klarsicht, ANC-1, Syne homology (KASH) domain protein nesprin 2G resulted in an increase in proportion of abnormally shaped nuclei (Lüke et al., 2008).

In addition to the role of the cytoskeleton in nuclear shape maintenance, the nucleoskeleton also plays an essential role. Multiple studies have investigated the effect of disrupting lamins or emerin on nuclear morphology. When emerin is perturbed there is a clear nuclear shape phenotype, in KD cardiomyocytes there was a decrease in nuclear invaginations (Shimojima et al., 2017) while in emerin null

mouse embryonic fibroblasts (MEFs) there was a greater proportion of irregularly shaped nuclei compared with controls and a lower nuclear contour ratio which is a similar measurement to circularity (Lammerding et al., 2005).

Lamin B1 is different, when lamin B1 is perturbed there is no increase in the number of abnormally shaped nuclei or contour ratio but there is a decrease in nuclear circularity. This was confirmed in two separate studies both using *lmnb1*$^{-/-}$ MEFs (Chen et al., 2018; Lammerding et al., 2006). The decrease in nuclear circularity was because *lmnb1*$^{-/-}$ MEFs had an increase in nuclear blebs (Chen et al., 2018). Additionally, it has been noted that overexpression of lamin B1 also results in a decrease in nuclear circularity but it is unclear if this is due to abnormal shape or nuclear blebs (Barascu et al., 2012).

The contribution of lamin A/C on the nuclear shape has been well studied in *lmna*$^{-/-}$ MEFs which result in no expression of lamin A or lamin C. Similarly to emerin null MEFs, *lmna*$^{-/-}$ MEFs have more irregularly shaped nuclei and a lower contour ratio compared with *lmna*$^{+/+}$ cells (Kim et al., 2017; Lammerding et al., 2005, 2006). Interestingly, when separating the functions of lamin A and lamin C it was found that cells lacking only lamin A had irregularly shaped nuclei and lower contour ratio while cells lacking only lamin C did not (Lammerding et al., 2006). Taken together this data suggests that lamin A and emerin are primarily responsible for the abnormal nuclear shape and not lamin C or B1.

3.1.2 Nuclear Membrane Integrity

Nuclear membrane integrity, or more specifically a loss of integrity, is often characterised by the presence of chromatin protrusions which are termed nuclear blebs, nuclear rupture events or membrane enclosed extranuclear DNA which are generally termed micronuclei. The presence of nuclear blebs, nuclear rupture events or micronuclei is indicative of a loss of membrane integrity or increase in DNA damage.

Nuclear blebs are weak points in the nuclear membrane which can go on to become sites of nuclear rupture (Chen et al., 2018). A cell population that had a higher proportion of nuclei with nuclear blebs would therefore be expected to have a higher proportion of nuclear rupture. This is confirmed in *lmnb1*$^{-/-}$ and *lmna*$^{-/-}$ cells, where *lmnb1*$^{-/-}$ cells have a greater number of nuclear rupture events compared with controls and *lmna*$^{-/-}$ cells. Additionally, a triple lamin KO – lamin A/C, B1 and B2 – resulted in increased nuclear ruptures. Interestingly, the treatment of triple KO cells with the actin perturbing agent Cytochalasin D rescues the nuclear rupture phenotype suggesting that the actin cytoskeleton plays a role in maintaining nuclear membrane integrity (Chen et al., 2018). Further evidence indicating the role of the cytoskeleton in membrane integrity is observed in vimentin null cells which also have greater numbers of nuclear rupture events (Patteson et al., 2019a).

As mentioned above lamin B1 appears to play a key role in preventing nuclear blebs. In *lmnb1*$^{-/-}$ MEFs there is a larger proportion of nuclei with blebs compared with controls and *lmna*$^{-/-}$ MEFs. When comparing *lmna*$^{-/-}$ with controls there is an increase but not as significant as *lmnb1*$^{-/-}$. This indicates lamin B1 plays more of a role in regulating nuclear membrane integrity than lamin A/C (Chen et al., 2018; Lammerding et al., 2006). When lamin localisation within the nuclear blebs was investigated it was found that lamin A/C staining within the bleb was continuous as observed throughout the nucleus whereas lamin B1 is not present in the bleb at all (Nmezi et al., 2019).

The presence of chromatin outside the nuclear membrane is generally due to severe DNA damage resulting in the release of fragmented DNA or due to an error in chromosome segregation (Fenech et al., 2011; Soto et al., 2018). There is almost no evidence to indicate that micronuclei occur following genetic perturbation of lamins or emerin, but these proteins are often present in the micronuclei (Maass et al., 2018). However, when the lamin B1 receptor was knocked down there was a greater number of cells with micronuclei compared with control cells (En et al., 2020). Lamin B1 receptor is a transmembrane protein that plays a role in binding and anchoring lamin B1 and tethering chromatin to the NE. It was also found that DIAPH3 KD cells

also had a greater proportion of cells with micronuclei and that these KD cells also had decreased levels of emerin and lamin A/C (Reis-Sobreiro et al., 2018).

3.1.3 Nuclear Size

Nuclear size is thought to scale with cell size (Edens et al., 2013). Nuclear size is an interesting parameter as many publications refer to it, particularly when investigating nuclear morphology. An increase or decrease in nuclear size is often used to imply a nuclear abnormality, however, the regulatory mechanisms that control nuclear size are not well characterised.

The perturbation of cytoskeletal and nuclear proteins often results in changes in nuclear size. Reducing the levels of mDia2 resulted in an increase in nuclear height (Sankaran et al., 2020) while *vim*$^{-/-}$ MEFs have larger nuclear area and volume compared with controls (Patteson et al., 2019a). Additionally, the depletion of nesprin-2G results in larger nuclei as does a nesprin-2G mutant lacking the actin binding domain (Lüke et al., 2008). Taken together these data suggest that the cytoskeleton plays a role in regulating nuclear size.

NE and nucleoskeleton proteins have also been implicated in the regulation of nuclear size, with increased nuclear area and volume being observed in emerin KD experiments and *emd*$^{-/-}$ MEFs (Lammerding et al., 2005; Shimojima et al., 2017). KO of another Lap2-Emerin-Man1 (LEM) domain protein, ANKLE2 which lacks a TM domain, also results in larger nuclear area compared with controls (Snyers et al., 2017). Lamin A/C null MEFs display increased nuclear area and volumes compared with controls (Kim et al., 2017; Lammerding et al., 2005) and KD or overexpression of lamin B1 also results in a significant change in nuclear size compared with controls (Barascu et al., 2012; Jevtić et al., 2015).

Understanding how nuclear size is regulated is an area that remains poorly understood, however, there have been recent studies using fission yeast in an attempt to understand the genetics and mechanics of nuclear size regulation. Fission

yeast make use of a homeostatic process to maintain their nuclear/cytoplasmic (N/C) ratio. Following size perturbation using a *Pom1* (a kinase involved in regulating cell division) deletion to induce asymmetric division the N/C ratio is rapidly restored (Cantwell and Nurse, 2019a). In a genetic screen looking for mutant yeast with higher or lower N/C ratios than WT yeast, 25 genes were identified (Cantwell and Nurse, 2019b). Among the identified genes were many involved in RNA and mRNA processing and gene expression. LINC complex proteins were also identified but resulted in opposing phenotypes – kms1 which is the fission yeast KASH protein results in a higher N/C ratio while sad1 the Sad and UNC-84 (SUN) domain protein results in a lower N/C ratio suggesting the link between the cytoskeleton and nucleoskeleton plays an important role in regulating nuclear size (Cantwell and Nurse, 2019b). The protein lem2 which is a NE protein containing a LEM domain has also been implicated in maintain the N/C ratio in fission yeast. It is suggested to do this by regulating the flow of membrane between ER and the NE (Kume et al., 2019).

Two recent studies by Jevtić and colleagues have looked at nuclear size regulation in mammalian cell lines and have suggested lamins and nuclear import/export play important roles in size regulation. The first of these studies originally identified the effect of lamins on nuclear size in *Xenopus* egg nuclei and found that nuclear size varied depending on lamin concentrations. Low concentrations of lamin A, B1 or B2 resulted in increased nuclear size while higher concentrations resulted in a decrease in nuclear size. This was also investigated in HeLa and MRC-5 cells where overexpression of lamin A/C, B1 or B2 resulted in increased nuclear size while KD of lamin A/C, B1 or B2 resulted in decreased nuclear size (Jevtić et al., 2015). The second study involved using an siRNA screen to identify proteins that resulted in a decreased nuclear area. They identified multiple proteins including SUN3 but focused on ELYS which is a nucleoporin that plays an important role in NPC formation. KD of ELYS resulted in smaller nuclei but also resulted in decreased levels of lamin B2 and mislocalisation of lamin B1. Conversely, overexpression (OE) of ELYS resulted in an increase in nuclear area. They also identified nuclear import and export as important mechanisms for maintaining nuclear size as when nuclear import was blocked nuclear size decreased and blocking nuclear export resulted in increased nuclear size

(Jevtić et al., 2019). Taken together these two studies imply a mechanistic role for nuclear lamins and nuclear import/export in the maintenance of nuclear size.

It is important to note that a larger nuclear size is likely to be correlated with a larger cell size (Edens et al., 2013). Some of the studies above have focused on abnormal nuclear size compared with cell size as reported by the N/C ratio, however, many have not discussed the possibility that increased or decreased cell size may be the reason for the observed nuclear phenotype. This is important as cell size and correspondingly nuclear size increase when cells become senescent (Sadaie et al., 2015). Lamin B1 is strongly implicated in the cell senescence phenotype with both increases and decreases in lamin B1 levels being associated with senescence phenotypes (Barascu et al., 2012; Dreesen et al., 2013; Freund et al., 2012).

3.1.4 Hypothesis and Aims

It has been suggested by the Cisneros lab that KD of β-DG or KO of the *DAG1* gene results in multiple nuclear phenotypes including a larger proportion of abnormally shaped nuclei, lower nuclear circularity, reduced nuclear integrity, increased nuclear and cell size, reduced levels of lamin A/C, lamin B1 and emerin and aberrant localisation of lamin B1 and emerin. They have also identified a number of nucleolar morphological defects in cells with reduced levels of DG. All of these nuclear and nucleolar phenotypes have been observed in C2C12 mouse myoblast cell lines (Azuara-Medina et al., 2019; Gómez-Monsiváis et al., 2020; Martínez-Vieyra et al., 2013; Vélez-Aguilera et al., 2018).

The aim of the experiments presented in this chapter is to validate these results in a human myoblast cell line that has a disrupted *DAG1* gene and therefore has no expression of β-DG. The original experiments in the C2C12 cell lines lack any rescue experiments, therefore the secondary aim here is to rescue any observed nuclear phenotypes to conclusively demonstrate the contribution of β-DG in maintaining and regulating nuclear morphology.

3.2 Results

3.2.1 β-DG localises to the nucleus in KM155 human myoblast cell lines

It has been frequently reported that β-DG is localised both within the nucleus and at the NE in multiple cell lines (Fuentes-Mera et al., 2006; Gonzalez-Ramirez et al., 2008; Martínez-Vieyra et al., 2013; Villarreal-Silva et al., 2010). The nuclear localisation of β-DG in the KM155 human myoblast cell line was examined using both immunofluorescence imaging (Figure *3.1*) and cell fractionation followed by western blotting analysis (Figure 3.2). To demonstrate the localisation visually, five different antibodies against β-DG were used, all of which detect the C-terminal cytoplasmic region of β-DG. Four of these antibodies; MANDAG2, JAF1, LG5 and C-20 are specific for β-DG irrespective of the phosphorylation state. 1709 on the other hand is specific for the phosphorylated version of β-DG at the Y892 residue. Despite all of these antibodies binding to very similar regions of β-DG there are some noticeable differences in the staining patterns. The clearest NE staining can be observed using MANDAG2 and 1709 which both display a clear nuclear ring (Figure *3.1*). Cells stained with LG5 or JAF1 have a more prominent perinuclear staining with the nucleus clearly outlined. However, there is still clear nuclear staining, but the NE ring staining is more difficult to observe using these antibodies. The commercially purchased C-20 antibody gives slightly different staining than the other antibodies, with very striking nucleoli staining and an almost complete absence of NE staining. All these antibodies clearly bind to β-DG as determined by peptide SPOT arrays (Jacobs, 2017), however, they have high levels of background signal when used for immunofluorescence assays. Despite this it can be concluded that β-DG appears to be localised to the nucleus as cells stained with all of the β-DG antibodies have nuclear staining with some evidence of NE and nucleoli staining.

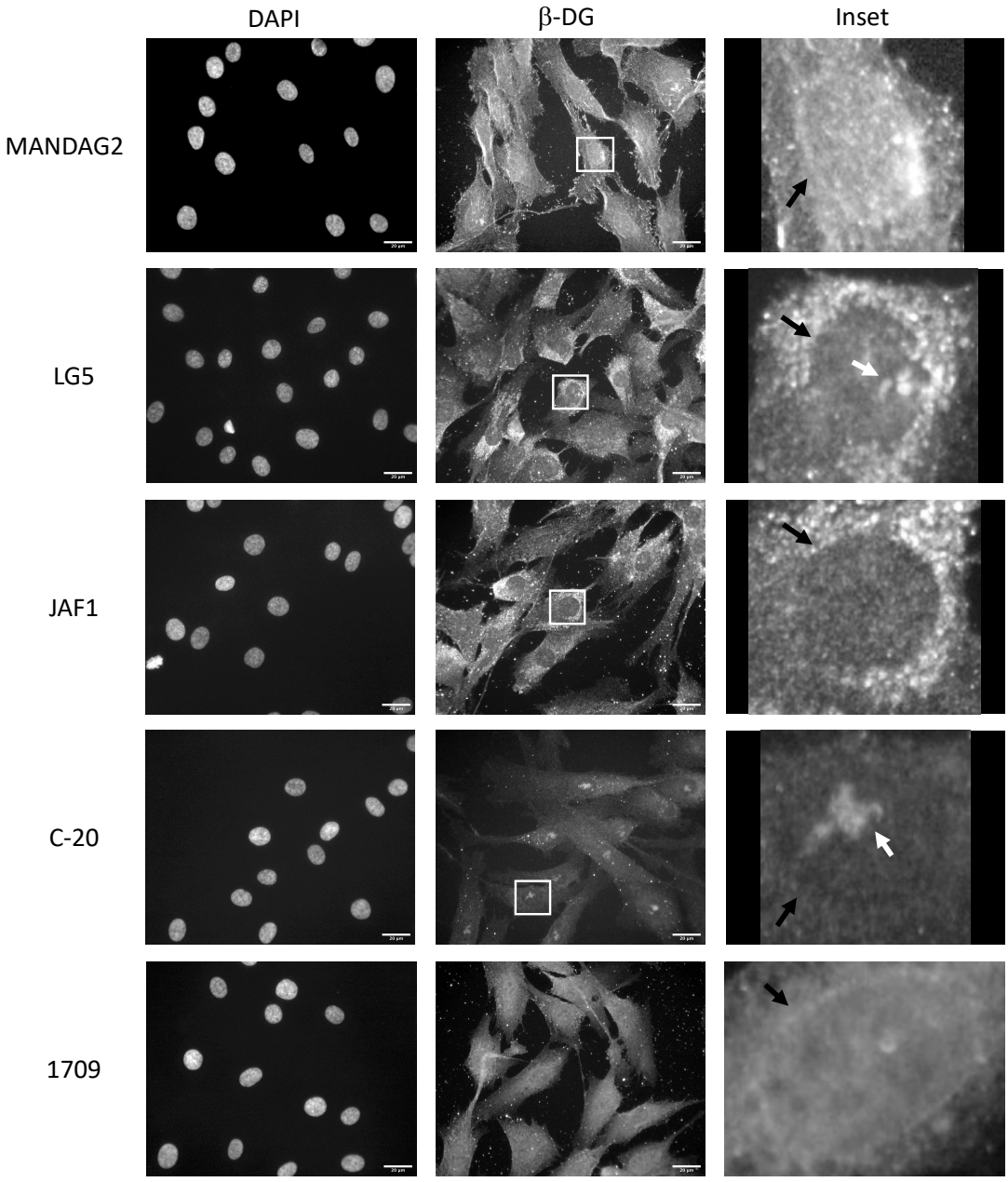

Figure 3.1 **Immunofluorescence staining with the β-DG antibodies MANDAG2, LG5, JAF1, C20 and 1709 demonstrate nuclear localisation.** Representative immunofluorescence images where β-DG staining is visible at the NE as indicated by black arrows. It is also present to some extent at the nucleoli as indicated by white arrows. MANDAG2 and 1709 have clear NE ring staining, JAF1 and LG5 have perinuclear staining and C-20 has nucleoli staining. All antibodies indicate nucleoplasmic staining. Scale bar = 20μm.

The localisation of β-DG to the nucleus of KM155 human myoblast cells was also confirmed using a fractionation experiment (Figure 3.2). Here, cells are separated into cytoplasmic and nuclear fractions using a combination of detergent and centrifugation. The non-fractionated sample (or whole cell lysate; WCL) was used as a positive control for both fractions. The purity of the fractionations was determined

by probing for the exclusively cytoplasmic protein GAPDH, the exclusively nuclear protein lamin A/C and the ER marker calnexin. The cytoplasmic marker was detected in both WCL sample and the cytoplasmic sample while the nuclear marker was detected in the WCL sample and the nuclear sample confirming the success of fractionation. Additionally, the ER marker calnexin was used as a finer quality control. As the ER is closely associated with the NE it is important to ensure that the nuclear proteins do not include ER proteins. The presence of calnexin in the WCL sample and the cytoplasmic sample but not the nuclear sample suggests that the nuclear sample is not contaminated by ER proteins. Based on these controls these data suggest that the strong β-DG band in the nuclear sample is due to the presence of β-DG in the nucleus and not due to contaminants from the cytoplasm or ER. Interestingly, only one β-DG band was identified in the WCL, nuclear and cytoplasmic fractions. This band was between the 36kDa and 55kDa marker suggesting it is the full-length 43kDa protein being detected. This suggests that β-DG is present in the nucleus of KM155 human myoblast cells as full-length protein rather than the smaller fragments. Alternatively, the smaller fragments may have been present at a much lower concentration that was not detected.

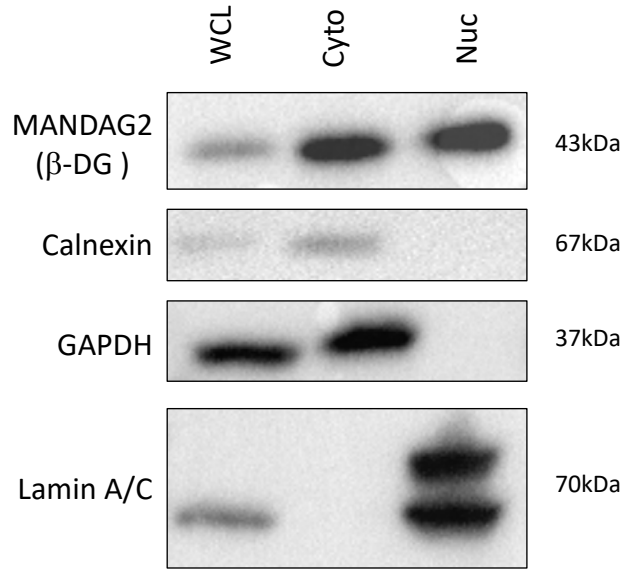

Figure 3.2 **Cell fractionation demonstrates the nuclear localisation of β-DG.** Whole cell lysate (WCL), cytoplasmic (Cyto) and nuclear (Nuc) samples were probed for the cytoplasmic marker GAPDH, the nuclear marker lamin A/C and the ER marker calnexin to demonstrate purity of fractions. The β-DG antibody MANDAG2 produced a band at 43kDa in all three samples indicating nuclear localisation in KM155 human myoblast cells.

Taken together the immunofluorescence and fractionation evidence suggests the localisation of full-length β-DG to the nucleus of KM155 human myoblasts. However, we cannot rule out the possibility that shorter fragments of β-DG are also present at much lower concentrations.

3.2.2 *DAG1* disruption results in loss of β-DG protein

The *DAG1* gene of KM155 human myoblasts was disrupted using CRISPR/Cas9 as described in Matthew Cook's thesis (Cook, 2021). The disrupted gene results in a loss of β-DG, therefore cells with disrupted *DAG1* will be termed *DAG1* KO for convenience. In addition to multiple *DAG1* KO cell lines termed KO A, B, C, D, E and F, a gRNA control cell line referred to henceforth as control (or simply C) was also generated. The resultant levels of β-DG were determined in all of these cell lines using immunofluorescence staining (Figure 3.3) and western blot analysis (Figure 3.4) to determine their suitability for further experiments and also verify the specificity of each of the β-DG antibodies.

For the immunofluorescence assay, control and KO cells were stained with each of the five antibodies specific for β-DG; MANDAG2, JAF1, LG5, C-20 and 1709. Each of these antibodies resulted in different levels of staining in the KO cells. MANDAG2 staining of control cells resulted in signal detected throughout the cell, in both the cytoplasm and nucleus in addition to PM, NE and ER staining. Conversely, when the KO cells were stained with MANDAG2 there was a slight decrease in intensity throughout the cell. Interestingly, the NE ring staining present in the control cells is not present in the KO cells, neither is the strong PM staining (Figure 3.3). These observations suggest that MANDAG2, as expected, is specific for β-DG. Staining with LG5 indicates more non-specific binding compared with MANDAG2, in the control sample the staining is throughout the cell but is most intense at the perinuclear region where the nucleus is clearly identifiable, there is also intense staining at the PM. In the KO cells the perinuclear staining is lost and the nuclei are no longer

discernible from the background staining, the PM staining is also reduced. There is reduced overall staining in all KO samples except KO B which appears to have a similar intensity to the control sample which again suggests issues with specificity. When control and KO cells were stained using JAF1 there is a very clear difference in staining intensity, the control cells had intense perinuclear and PM staining similar to LG5 with the nuclei clearly identifiable. In the KO cells stained with JAF1 there is a stark reduction in all cellular staining where the PM and nucleus are no longer visible from the background. In the case of C-20 staining in the controls there is general staining throughout the cell with the most intense signal at the nucleoli. In the KO cells stained with C-20 there is very little difference compared with the controls – there is a slight reduction in overall intensity but there is still prominent nucleoli staining suggesting the nucleoli signal is an artifact and not due to binding with β-DG. When control and DG KO cells were stained with 1709, which is specific for the phosphorylated version of β-DG, there is an overall reduction in signal intensity in the KO cells compared with the control. In the control cells there is intense staining throughout the cells with increased intensity at the PM and NE, this is not present in the KO cells (Figure 3.3). All these data together indicate that the CRISPR/Cas9 disruption of the *DAG1* gene results in reduced levels of β-DG, but it is not possible to conclude that there is a complete loss of protein due to the poor signal to noise ratios inherent in the use of these particular antibodies. Additionally, it gives some information on which antibodies are best for investigating β-DG via immunofluorescence. The data would suggest that MANDAG2, JAF1 and 1709 are the best antibodies, with the lowest background noise levels for immunofluorescence assays.

In addition to immunofluorescence analysis the control and KO cells were characterised using western blotting analysis (Figure 3.4). Here, whole cell lysate of control and KO samples were prepared and tested for levels of β-DG using the antibodies MANDAG2 and LG5 with GAPDH as a loading control. For the two β-DG antibodies there was a band present at 42kDa, with no other bands detected at any other molecular weight, in the control sample while there was no detectable band in

the KO sample (Figure 3.4). Based on this evidence it is clear that β-DG is perturbed, and the levels are reduced to the extent that it is not detectable in this assay. This does not confirm that there is no expression of DG it simply confirms that the levels are below the detectable limit of this assay.

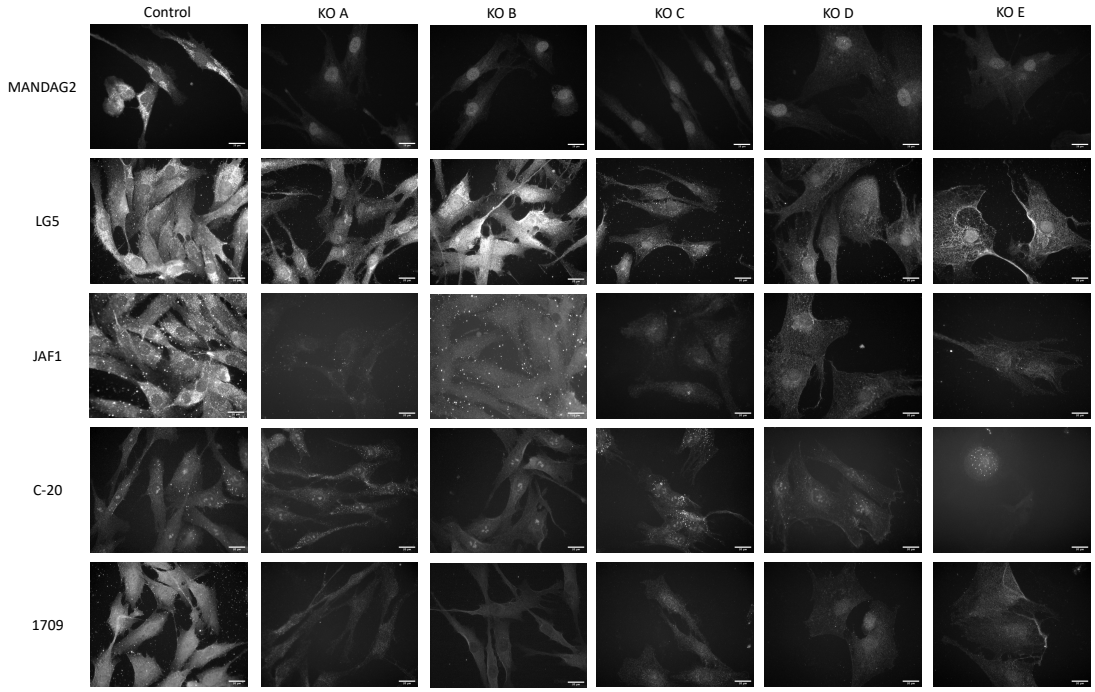

Figure 3.3 **Disruption of the DAG1 gene in human myoblasts results in a reduction in β-DG immunofluorescence staining.** Representative immunofluorescence images of control and DAG1 KO clones A-E stained with β-DG antibodies MANDAG2, LG5, JAF1, C-20 and 1709. Cells were grown for 24 hours prior to fixation and staining with DAPI and β-DG. Representative image of each cell line stained with each antibody. 3 independent repeats were carried out with at least 3 images per sample. Scale bar = 20μm.

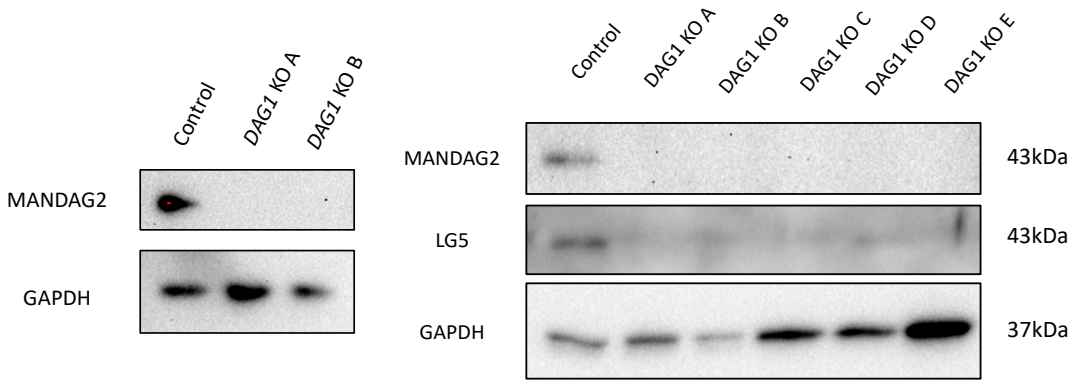

Figure 3.4 **Disruption of the DAG1 gene in human myoblasts results in a loss of β-DG in a western blot analysis.** Whole cell lysate of control and DAG1 KO clones A-E probed for β-DG using MANDAG2 or LG5. GAPDH was used as a loading control. The two separate blots are used to demonstrate the variation in quality of MANDAG2 between batches. MANDAG2 and LG5 only detected a band in the control samples and not in any of the DAG1 KO clones.

3.2.3 The effect of *DAG1* disruption on nuclear shape in KM155 cells

There are multiple parameters that can be used to indicate the shape of the nucleus in 2D, these are primarily nuclear circularity, nuclear aspect ratio and nuclear roundness. During analysis of nuclear shape all of these parameters are measured, however, for simplicity and consistency circularity will be discussed henceforth. The reason for this is that circularity generates a greater deviation from 1 for nuclei with protrusions and abnormal shapes compared with simply elongated nuclei.

Nuclear circularity was measured in a number of ways to ensure accurate results. The majority of the data was generated using DAPI staining and imaged using a Leica fluorescent microscope (Figure 3.5). The nuclear circularity of control and five *DAG1* KO clones (A-E) were measured (Figure 3.6). The average circularity of all *DAG1* KO clones was lower than that of the control but for clones A-C this difference was not significant. However, for clones D and E the difference was significant with a P value of 0.0012 and 0.0007 respectively. The difference between the control and KO clones D and E is unlikely to be due to a lack of DG and more likely to be a side effect of the KO process, this will be discussed below.

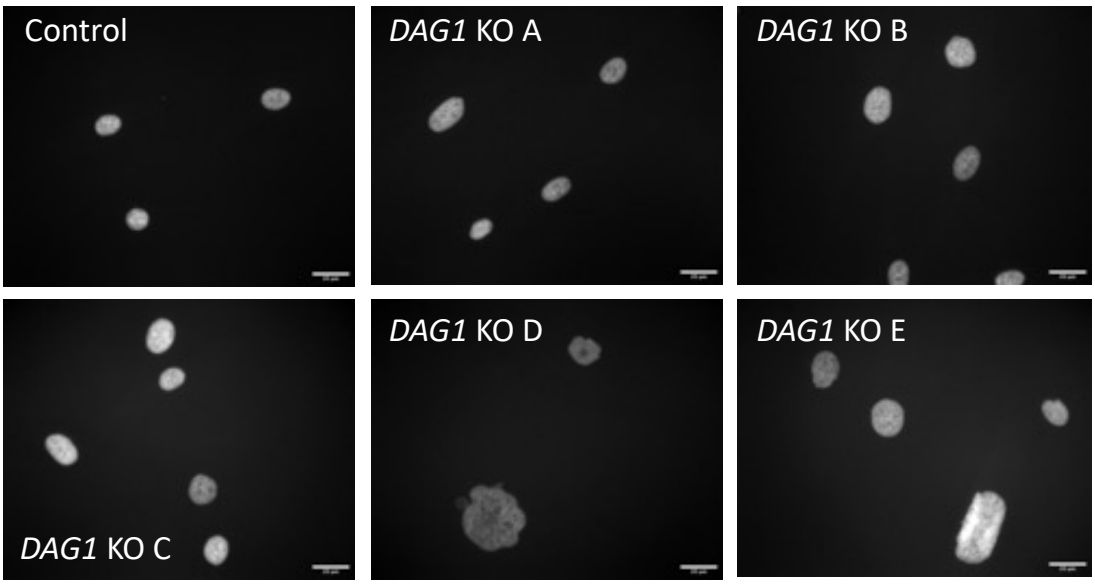

Figure 3.5 **Representative nuclei from control and DAG1 KO clones.** Cells were grown for 24 hours before fixing and staining with DAPI to identify nuclear region. Cells were imaged using the Leica fluorescence microscope. Scale bar = 20μm.

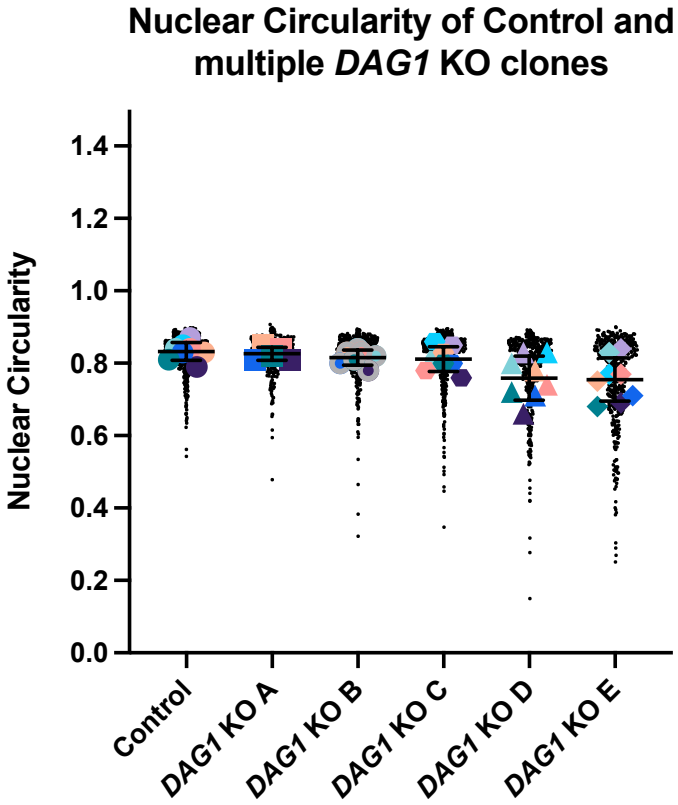

Cell Line	Average	SD	P value compared with control	Significance
Control	0.8325	0.0243	N/A	N/A
DAG1 KO A	0.8260	0.0182	0.7884	ns
DAG1 KO B	0.8157	0.0207	0.4467	ns
DAG1 KO C	0.8113	0.0340	0.3201	ns
DAG1 KO D	0.7588	0.0613	0.0012	**
DAG1 KO E	0.7550	0.0600	0.0007	***

Figure 3.6 **Average nuclear circularity of control and DAG1 KO clones A-E using DAPI to identify the nuclear region.** Cells were grown for 24 hours before fixing and staining with DAPI to identify nuclear region. Cells were imaged using the Leica fluorescence microscope and the nuclear shape determined for analysis. Small black points indicate values from individual cells while larger coloured points indicate the average for each independent experiment. 7 independent experiments were carried out with at least 25 individual nuclei measured per experiment. Graph shows mean and standard deviation. A significant difference was determined between the control and DAG1 KO D-E as determined by one-way ANOVA test p = 0.0014. p values for multiple comparisons using Dunnett's multiple comparisons test are in the table. Control n = 789, KO A n = 781, KO B n = 772, KO C n = 784, KO D n = 738, KO E n = 752.

This lack of difference between control and *DAG1* KO clones A-C was further confirmed with the use of confocal microscopy to confirm the type of microscopy did not affect the result. Additionally, nuclei stained with the nuclear marker lamin B1 was measured using the Leica fluorescent microscope and the confocal to again

validate the methodology. When control and *DAG1* KO clone A cells were stained with DAPI and imaged on the confocal microscope there was again no difference between the two samples (Figure *3.7*a). In agreement with this when control and *DAG1* KO clone A and B cells were stained for lamin B1 and imaged using either the Leica fluorescent microscope (Figure *3.7*b) or the confocal microscope (Figure *3.7*c) the nuclear circularity result was the same – there is no difference between the circularity of the *DAG1* KO clones and the circularity of control cells.

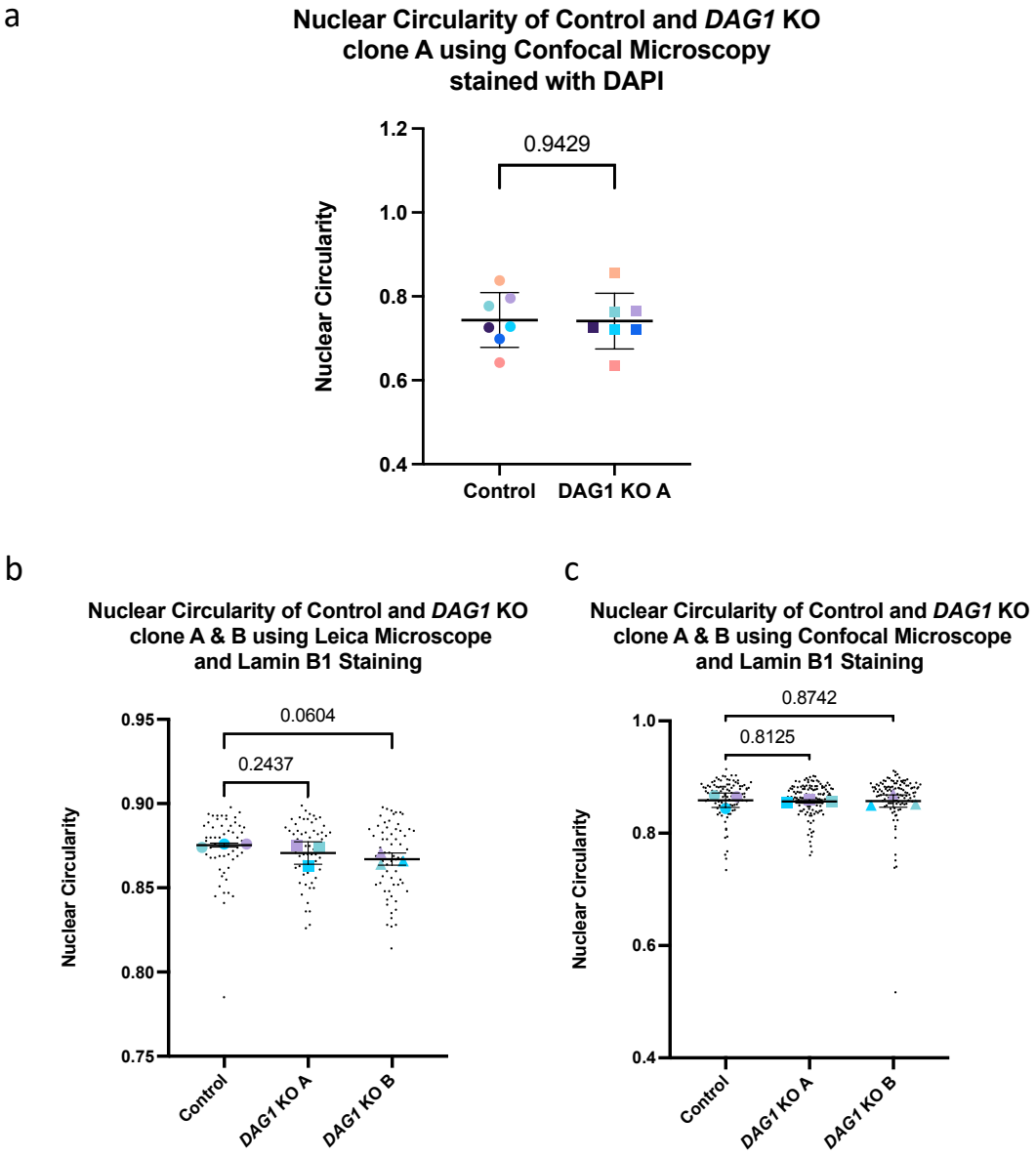

Figure 3.7 **Average nuclear circularity of control and DAG1 KO clones A and B using DAPI or lamin B1 to identify the nuclear region and imaged using two different microscopes.** (a) Cells were grown for 24 hours before fixing and staining with DAPI to identify nuclear region. Cells were imaged using the Nikon A1 confocal and the nuclear shape determined for analysis. Coloured points indicate the average value for each independent experiment. 7 independent experiments were carried out with 183 control and 177 KO A nuclei measured. Graph shows mean

and standard deviation. A significant difference was not determined between the control and DAG1 KO A as determined by t test p = 0.9429. (b) Cells were grown for 24 hours before fixing and staining with lamin B1 and DAPI to identify nuclear region. Cells were imaged using the Leica fluorescence microscope and the nuclear shape determined for analysis. Small black points indicate values from individual cells while larger coloured points indicate the average value for each independent experiment. 3 independent experiments were carried out with 83 control, 76 KO A and 96 KO B nuclei measured per experiment. Graph shows mean and standard deviation. A significant difference was not determined between the control and DAG1 KO A or B as determined by one-way ANOVA test p = 0.1476. p values for multiple comparisons using Dunnett's multiple comparisons test are in the table. (c) As above, except Nikon A1 confocal was used. A significant difference was not determined between the control and DAG1 KO A or B as determined by one-way ANOVA test p = 0.9688. p values for multiple comparisons using Dunnett's multiple comparisons test are on the graph. Control n = 102, KO A n = 100 and KO B n = 114.

Circularity gives an indication of how close the nuclei are to a perfect circle in 2D but it does not provide any 3D information. The 3D equivalent of circularity is sphericity which indicates how close the nuclei are to a perfect sphere. Using multiple Z-stacks from a confocal image the nuclei can be reconstructed and a value for sphericity can be determined. As this is a more time intensive experiment only control and *DAG1* KO B cells were compared (Figure 3.8). As with nuclear circularity there is no difference in sphericity values between the control or *DAG1* KO sample which confirms that the results observed in 2D also hold true in 3D.

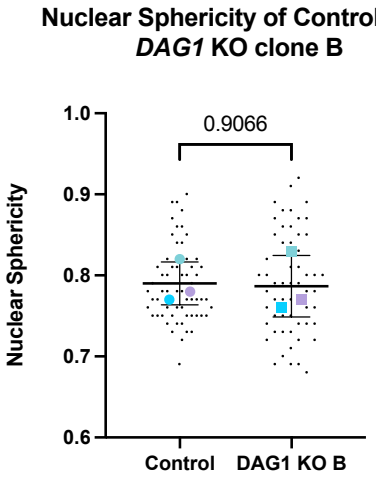

Figure 3.8 **Average nuclear sphericity of control and DAG1 KO clone B using DAPI to identify the nuclear region.** Cells were grown for 24 hours before fixing and staining with DAPI to identify nuclear region. Cells were imaged using the Nikon A1 confocal and the 3D nuclear shape determined for analysis. Small black points indicate values from individual cells while larger coloured points indicate the average value for each independent experiment. 3 independent experiments were carried out with 45 control and 49 KO B nuclei measured. Graph shows mean and standard deviation. A significant difference was not determined between the control and DAG1 KO B as determined by t test p = 0.9066.

In addition to measuring the circularity and sphericity of control and *DAG1* KO nuclei the proportion of cells with micronuclei was also assessed. Inspecting >800 cells per

cell line the results are similar to those observed for nuclear circularity. There is no difference between the percentage of control cells and the percentage of *DAG1* KO clone A-C cells with micronuclei. 0.61% of control cells had micronuclei while *DAG1* KO A, B and C cells had 0.94%, 1.12% and 1.39% respectively. In the case of *DAG1* KO D and E the percentage of micronuclei was larger with KO D having 4.27% and KO E having 7.66% (Figure 3.9).

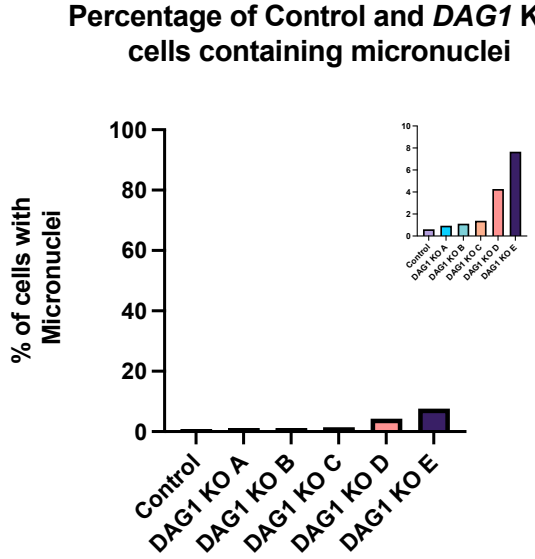

Figure 3.9 **Percentage of control or DAG1 KO clone A-E cells that had micronuclei.** Images were manually inspected and the number of cells containing micronuclei and the total number of cells was determined. Control n = 789, KO A n = 781, KO B n = 772, KO C n = 784, KO D n = 738, KO E n = 752, a very low percentage having micronuclei. (Inset) Zoomed in view of 0-10%.

Taken together this data suggests that the majority of *DAG1* KO cell lines have a normal nuclear shape as compared with control cells. However, two of the five *DAG1* KO cell lines have abnormal nuclear shape, and this will be discussed in further detail below.

3.2.4 Comparing the nuclear and cell size of control and *DAG1* KO cells

When discussing nuclear size, nuclear area is the main parameter. As with nuclear circularity the nuclear area of control and *DAG1* KO cells has been determined in multiple ways to confirm accuracy of the methodology. Determination of nuclear area was carried out predominantly by staining with DAPI and imaging with the Leica

fluorescence microscope. When nuclear area was measured for control and all *DAG1* KO clones (A-E) there was a clear difference in nuclear area (Figure *3.10*). The average nuclear area of control cells was 149±7μm while the average nuclear area for *DAG1* KO clones A-E were 163±6μm, 177±7μm, 173±19μm, 221±34μm and 220±32μm respectively. The difference between the average control area and each of the KO averages was statistically significant for all cell lines except clone A where the average nuclear size was consistently larger than the control, but the difference was not statistically significant.

Nuclear area was also measured using DAPI stained nuclei imaged on the confocal microscope (Figure *3.11*a) and lamin B1 stained nuclei on both the Leica fluorescence microscope (Figure *3.11*b) and the confocal microscope (Figure *3.11*c). Each of these results gives different absolute values for nuclear area but they all show the same overall result – there is no difference between control and *DAG1* KO clone A but a significant difference between control and *DAG1* KO clone B.

After confirming the *DAG1* KO cell lines had a larger nuclear area than the controls the nuclear volume was then investigated. This is important to understand if the KO nuclei were simply flatter and wider, giving them a larger cross-sectional area, or if they have an increased volume. Control and *DAG1* KO B cells were imaged following DAPI staining to define the nucleus. The resultant Z-stacks were then processed to generate a 3D reconstruction of each nuclei (Figure *3.12*a). The volume of each reconstructed nucleus was then measured for the two samples (Figure *3.12*b). The control nuclei had an average nuclear volume of 583±62μm^3 while the *DAG1* KO B nuclei had an average nuclear volume of 741±27μm^3. The difference between these two values is statistically significant as determined by a Student's t test with a p value of 0.0152. Based on this data it can be concluded that the nuclei of the KO cells have a larger volume as well as a larger area.

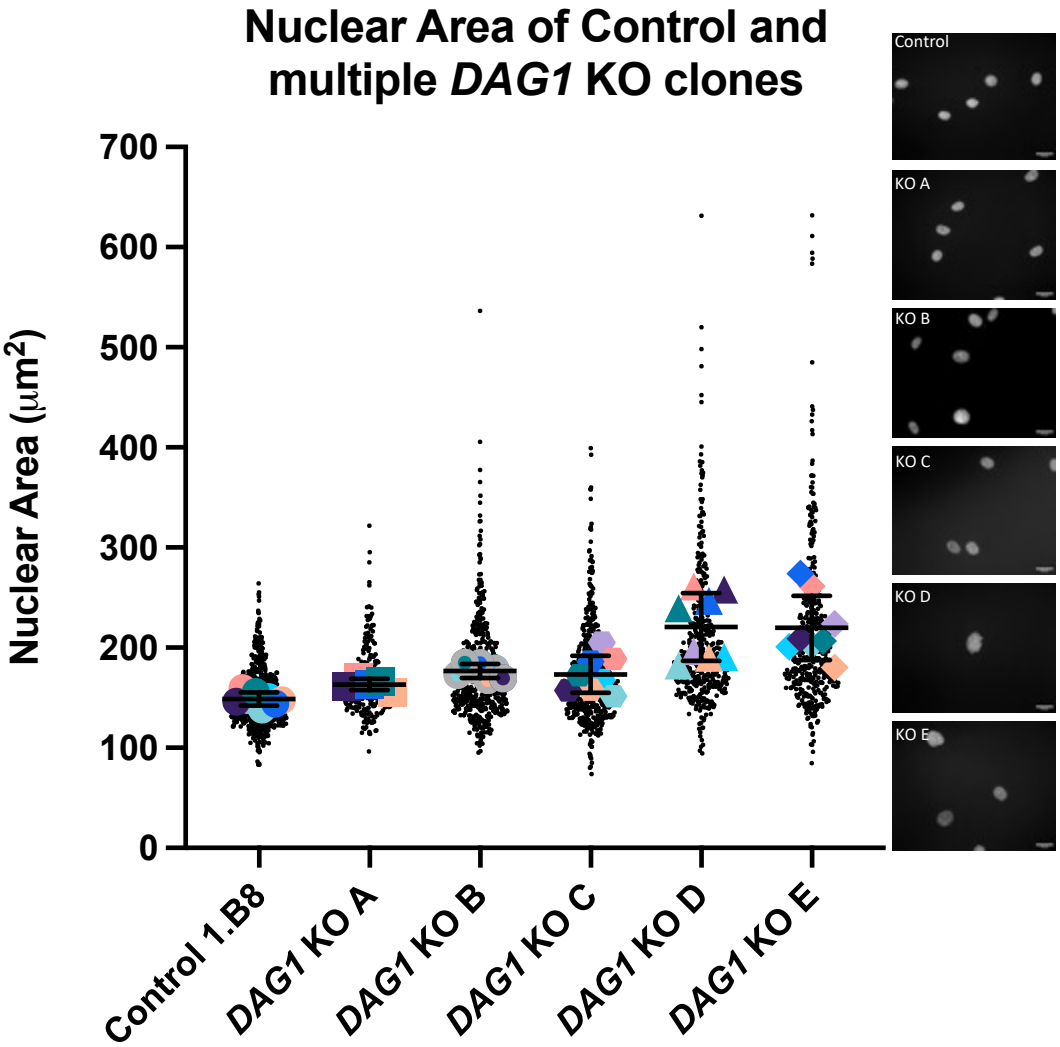

Cell Line	Average	SD	P value compared with control	Significance
Control	148.8	6.6	N/A	N/A
KO A	163.2	5.6	0.2569	ns
KO B	176.7	6.9	0.0185	*
KO C	173.4	18.6	0.0310	*
KO D	220.6	33.8	<0.0001	****
KO E	219.8	32.1	<0.0001	****

Figure 3.10 **Average nuclear area of control and DAG1 KO clones A-E using DAPI to identify the nuclear region.** Cells were grown for 24 hours before fixing and staining with DAPI to identify the nuclear region. Cells were imaged using the Leica fluorescence microscope and the nuclear area determined for analysis. Small black points indicate values from individual cells while larger coloured points indicate the average for each independent experiment. 7 independent experiments were carried out with control n = 789, KO A n = 781, KO B n = 772, KO C n = 784, KO D n = 738, KO E n = 752. Graph shows mean and standard deviation. A significant difference was determined between the control and DAG1 KO B-E as determined by one-way ANOVA test, p = <0.0001. p values for multiple comparisons using uncorrected Fisher's least significant difference test are in the table.

a

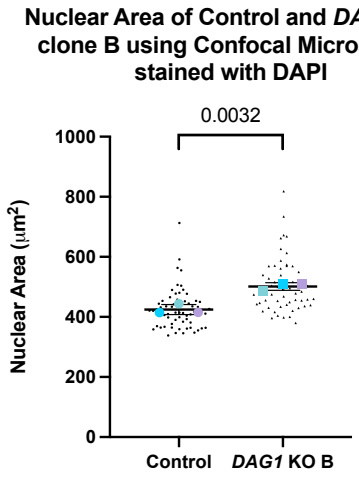

b

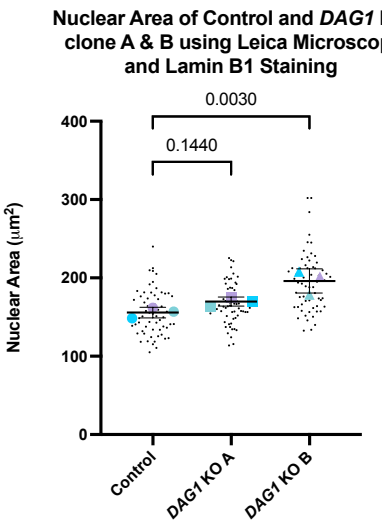

c

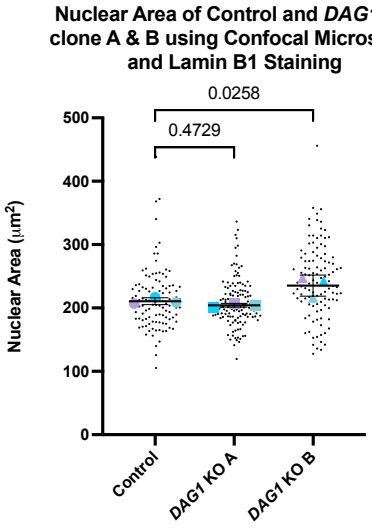

Figure 3.11 **Average nuclear area of control and DAG1 KO clones A and B using DAPI or lamin B1 to identify the nuclear region and imaged using two different microscopes.** (a) Cells were grown for 24 hours before fixing and staining with DAPI to identify nuclear region. Cells were imaged using the Nikon A1 confocal and the nuclear area determined for analysis. Coloured points indicate the average value for each independent experiment. 3 independent experiments were carried out with control n = 77 and KO B n = 77. Graph shows mean and standard deviation. A significant difference was determined between the control and DAG1 KO B as determined by t test, p = 0.0032. (b) Cells were grown for 24 hours before fixing and staining with lamin B1 and DAPI to identify nuclear regions. Cells were imaged using the Leica fluorescence microscope and the nuclear area determined for analysis. Small black points indicate values from individual cells while larger coloured points indicate the average value for each independent experiment. 3 independent experiments were carried out with 83 control, 76 KO A and 96 KO B nuclei measured. Graph shows mean and standard deviation. A significant difference was determined between the control and DAG1 KO A or B as determined by one-way ANOVA test, p = 0.0082. p values for multiple comparisons using Dunnett's multiple comparisons test are on the graph (c) As above, except Nikon A1 confocal was used. A significant difference was determined between the control and DAG1 KO A or B as determined by one-way ANOVA test, p = 0.0222. p values for multiple comparisons using Dunnett's multiple comparisons test are on the graph. Control n = 102, KO A n = 100 and KO B n = 114.

As the nuclei of *DAG1* KO cells are larger in both area and volume, the next important question is whether it is just the nuclei that are larger or is it in fact the cells are larger, and the nuclei are simply scaling with the cells. This question was addressed by staining cells with phalloidin to identify the whole cell. Control cells were compared with both *DAG1* KO clones A and B with similar results to those observed for nuclear area (Figure *3.13*a). The two KO clones had larger cell areas than the control cells. Control cells had an average area of 1494±341μm^2 while *DAG1* KO clones A and B had an average cell area of 2077±239μm^2 and 2199±453μm^2 respectively. As with nuclear area, both clones have a larger average cell area compared with the control but only for clone B is this difference statistically significant. Additionally, when the nuclear/cell area ratio is calculated for all cell lines there is no difference in the ratio for either KO clone compared with the control (Figure *3.13*b). This indicates that the increased nuclear size is also accompanied by an increase in cell size – thus the nucleus size scales with the cell size in all cell lines.

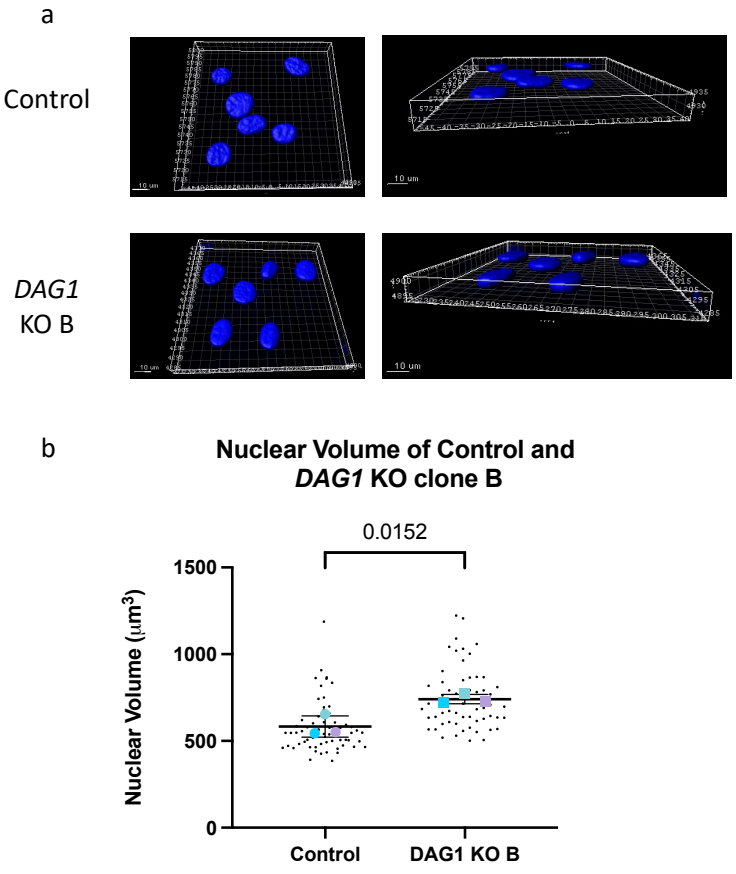

Figure 3.12 **Average nuclear volume of control and DAG1 KO clone B using DAPI to identify the nuclear region.** Cells were grown for 24 hours before fixing and staining with DAPI to identify nuclear region. Cells were imaged

using the Nikon A1 confocal and the 3D nuclear volume determined for analysis. (a) Representative reconstructions using Imaris software. (b) Graph showing nuclear volume of control and DAG1 KO clone B. Small black points indicate values from individual cells while larger coloured points indicate the average value for each independent experiment. 3 independent experiments were carried out with 45 control and 49 KO B nuclei measured. Graph shows mean and standard deviation. A significant difference was determined between the control and DAG1 KO B as determined by t test, p = 0.0152.

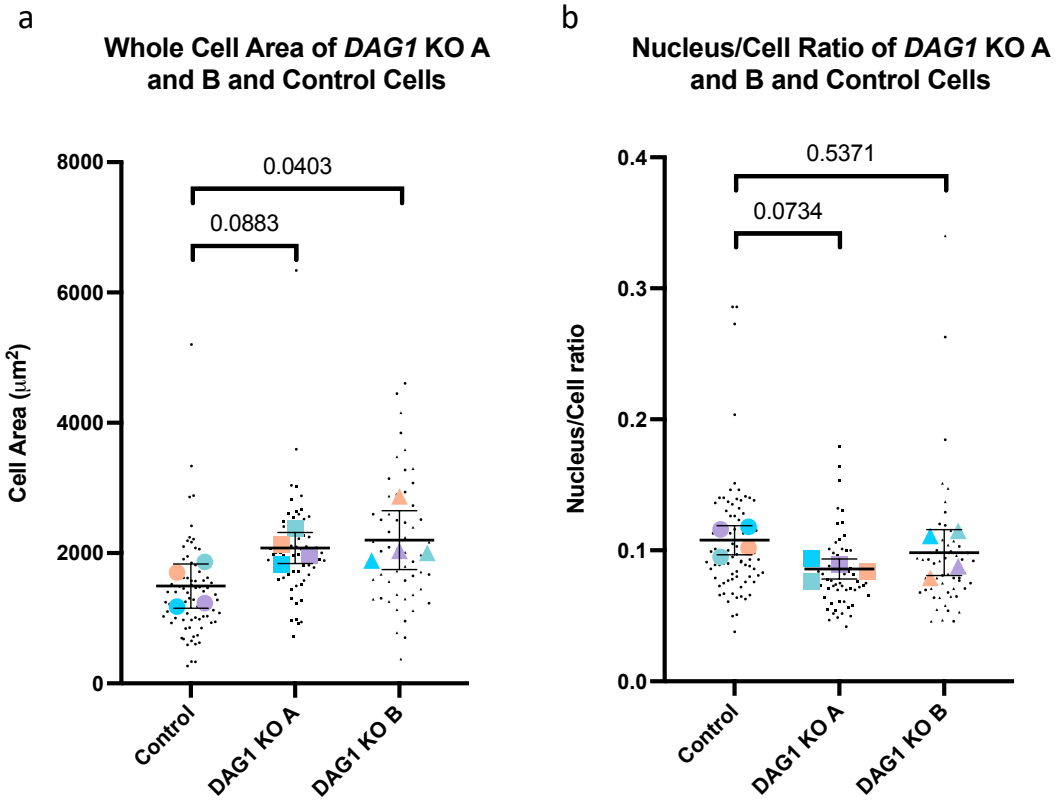

Figure 3.13 **DAG1 KO cells are larger than control cells and cell size scales with nuclear size.** Cells were grown for 24 hours before fixing and staining with DAPI and phalloidin to identify nuclear and cytoplasmic regions. Cells were imaged using the Leica fluorescence microscope and the nuclear and cellular area determined for analysis. (a) Whole cell area of control and DAG1 KO clones A-B. Small black points indicate values from individual cells while larger coloured points indicate the average for each independent experiment. 4 independent experiments were carried out with 66 control, 60 KO A and 72 KO B cells measured. Graph shows mean and standard deviation. A significant difference was determined by one-way ANOVA test, p = 0.0493. p values for multiple comparisons using Dunnett's multiple comparisons test are on the graph (b) Nuclear area/cell area ratio for control and DAG1 KO clones A-B. Small black points indicate values from individual cells while larger coloured points indicate the average for each independent experiment. 4 independent experiments were carried out with 66 control, 60 KO A and 72 KO B cells measured. Graph shows mean and standard deviation. A significant difference was not determined between the control and DAG1 KO clones A-B as determined by one-way ANOVA test, p = 0.1008. p values for multiple comparisons using Dunnett's multiple comparisons test are on the graph.

In order to determine whether the *DAG1* KO nuclei are larger because of a lack of DG or simply because of off-target effects from generating the knockouts, full-length DG with a HA and a Myc tag (Cook, 2021) were transiently transfected into *DAG1* KO B and C cells as they both display the larger nuclear phenotype. Control cells were

transiently transfected with a GFP construct while *DAG1* KO cells were transfected with either GFP or DG constructs (Figure *3.14*). Following transfection of GFP into control and *DAG1* KO cell lines the nuclear area was measured and as with previous results of untransfected cells, the KO cell nuclei had a significantly greater area compared with the control (Figure *3.15*a). This confirms that the transfection process does not affect the relative difference between nuclear area in control and *DAG1* KO cell lines. Following this, control cells were transfected with GFP while both *DAG1* KO clones were transfected with the HA/Myc tagged DG construct (Figure *3.15*b). Addition of the DG construct to the *DAG1* KO cells resulted in a reduction in nuclear area that did not differ significantly from that of the control cells. Additionally, there was a lower nuclear area for KO cell lines transfected with DG compared with when they were transfected with GFP (Figure *3.15*c). The difference is statistically significant for *DAG1* KO clone C and it is approaching significance for clone B with a p value of 0.0940. Taken together this data suggests that the addition of full-length DG rescues the large cell / large nuclei phenotype observed in untransfected and GFP transfected cells.

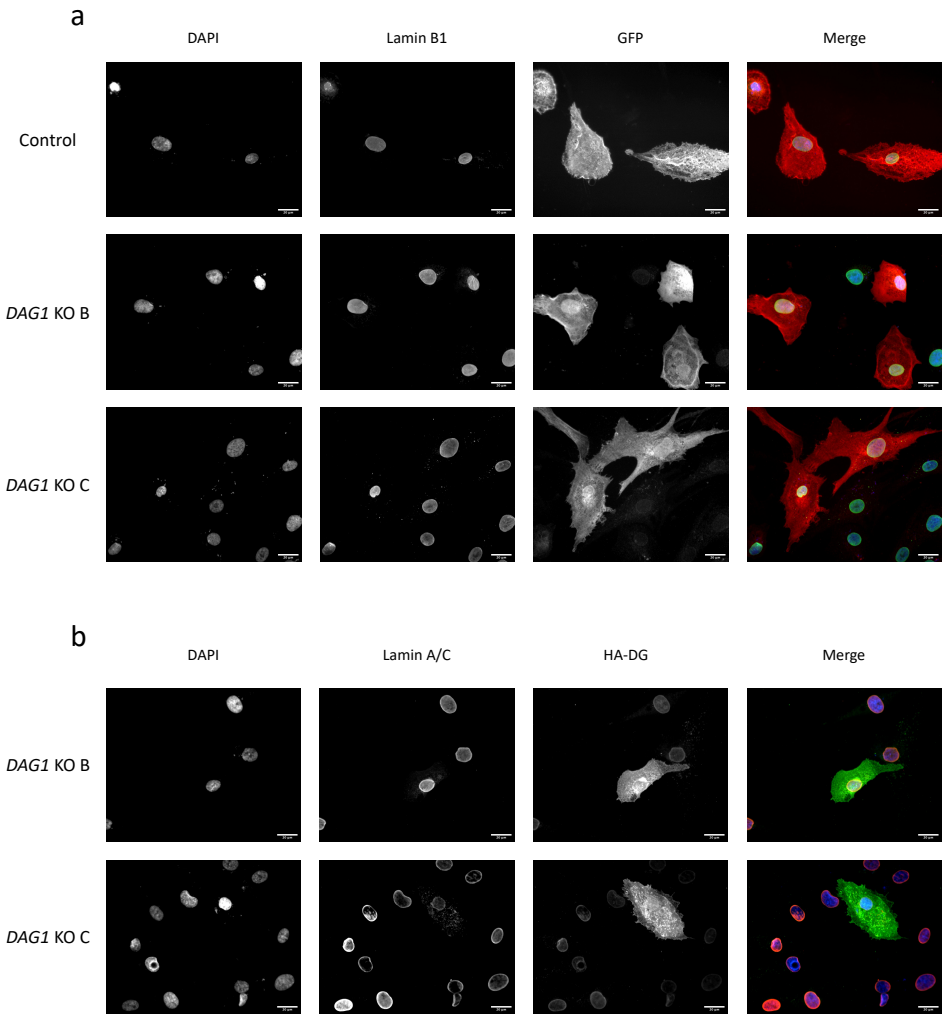

Figure 3.14 **Representative images of control and DAG1 KO clones B-C transiently transfected with GFP or HA and Myc tagged DG.** (a) Representative images of control, DAG1 KO A and B transiently transfected with GFP as determined by anti-GFP antibody, co-stained with DAPI and lamin B1 to identify the nuclear region. One representative image from each sample, at least 10 images were taken per sample per experiment with 4 independent experiments. (b) Representative images of DAG1 KO A and B transiently transfected with HA & Myc tagged DG as determined by anti-HA antibody, co-stained with DAPI and lamin A/C to identify the nuclear region. One representative image from each sample, at least 20 images were taken per sample per experiment with 4 independent experiments. Scale bar = 20μm.

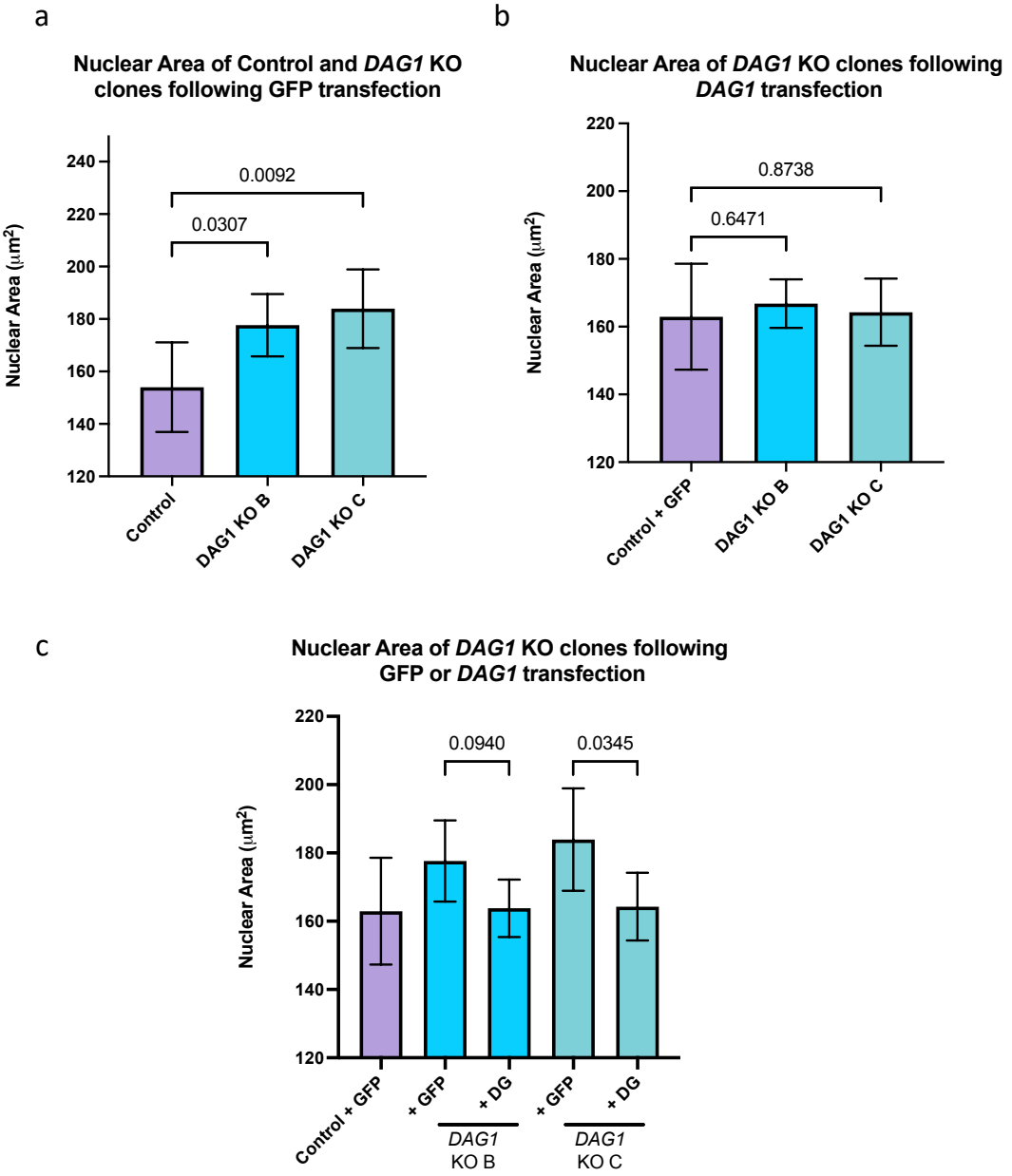

Figure 3.15 **Average nuclear area of control and DAG1 KO clones B-C following transient transfection of GFP or HA & Myc tagged DG.** Cells were grown for 24 hours before transfection and allowed to express proteins for at least 24 hours. Cells were then fixed and stained with DAPI, lamin A/C or B1 to identify the nuclear region and GFP or HA to identify transfected cells. Cells were imaged using the Leica fluorescence microscope and the nuclear area determined for analysis. (a) Nuclear area of control and DAG1 KO clones B-C following GFP transfection. The graph shows the mean with standard deviation, 4 independent experiments with 202 control, 200 KO A and 217 KO B cells measured. Graph shows mean and standard deviation. The difference between the samples was significant as determined by one-way ANOVA, p = 0.0172. p values for multiple comparisons using Dunnett's multiple comparisons test are on the graph (b) Nuclear area of control and DAG1 KO clones B-C following GFP transfection for control and DG transfection for DAG1 KO clones. The graph shows the mean with standard deviation, 4 independent experiments with 136 control, 147 KO A and 122 KO B cells measured . Graph shows mean and standard deviation. The difference between the samples was not significant as determined by one-way ANOVA, p = 0.8921. p values for multiple comparisons using Dunnett's multiple comparisons test are on the graph (c) Nuclear area of control and DAG1 KO clones B-C following GFP or DG transfection. The graph shows the mean with standard deviation, 4 independent experiments with 136 control, 147 KO A and 122 KO B cells measured. The differences between the samples was approaching significance as determined by one-way ANOVA, p = 0.0669. The difference between DAG1 KO clone C GFP and DG transfected was significantly different, p = 0.0345 while the difference between DAG1 KO clone B GFP and DG transfected was not quite significant p = 0.0940.

3.2.5 Is increased nuclear size and cell size in *DAG1* KO cell lines due to an increase in cellular senescence?

One indicator of cellular senescence is impaired proliferation as the cells do not progress through the cell cycle and divide. Therefore, the proliferative ability of control and *DAG1* KO cells was established. When the proliferation of the cells was assessed, it was clear that there is no reduction in the proliferation rate of the majority of *DAG1* KO cell lines compared with the control (Figure 3.16). For *DAG1* KO cell lines A and B there was no difference between the proliferation rates compared with the control at either day 4, 6 or 8. In the case of *DAG1* KO clone C the signal intensity was significantly lower than the control at day 4 but by days 6 and 8 there was no difference. For *DAG1* KO clones D and E there is a lower proliferation rate with a lower signal intensity for days 4, 6 and 8 when compared with the control. This data, taken together indicates that the majority of *DAG1* KO cell lines do not have impaired proliferation when compared with the control cells.

In addition to proliferation, an increase in the levels of euchromatin can be used as an indicator of cellular senescence. A change in the amount of decondensed chromatin can be detected by staining for the histone modification H3K9me3. An increase in intensity of H3K9me3 is indicative of increased heterochromatin while a decrease in intensity is indicative of an increase in euchromatin. The levels of H3K9me3 were assessed for *DAG1* KO cell lines and normalised to the control cells for each experiment. There was a large amount of variation in the levels with some experiments indicating an increased level while others indicated a decreased level. Overall, the average normalised intensity for all *DAG1* KO cell lines (A-E) was ~1 (Figure *3.17*) indicating no significant difference between the control and any of the KO cell lines. This data suggests that the levels of heterochromatin and euchromatin do not differ significantly in the *DAG1* KO cells when compared with the controls.

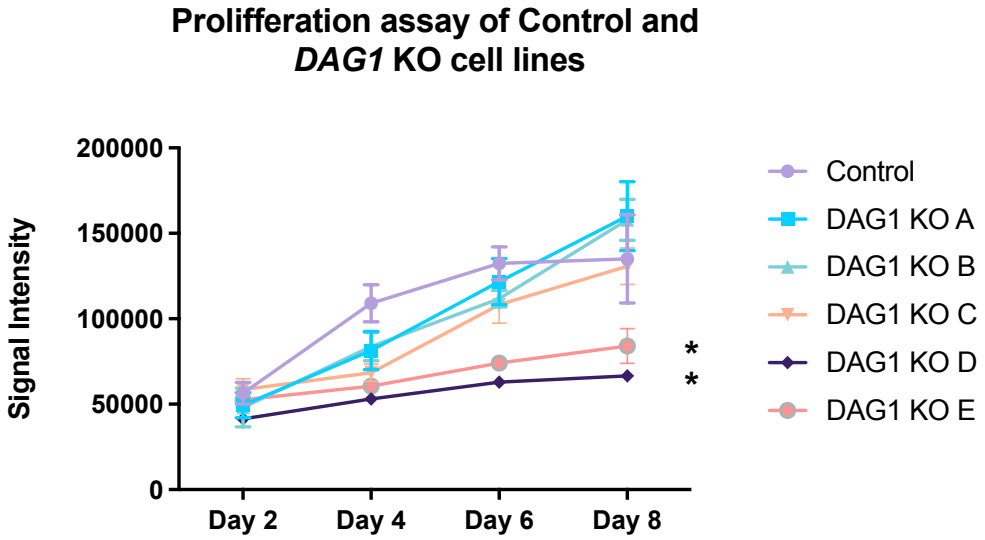

Time	KO A	KO B	KO C	KO D	KO E
Day 2	0.6574	0.7249	0.9858	0.1090	0.9169
Day 4	0.1091	0.1034	0.0315	0.0256	0.0379
Day 6	0.722	0.1311	0.1366	0.0158	0.0170
Day 8	0.6955	0.7061	0.9977	0.9999	0.3537

P values of KO compared with control

Figure 3.16 **Proliferation of control and DAG1 KO clones A-E over 8 days.** Cells were seeded and allowed to grow for 2, 4, 6 or 8 days where they were fixed. Cells were then stained with DRAQ5 to stain cell nuclei and the signal intensity of DRAQ5 was used as a measure of proliferation. 3 independent experiments were carried out. Points shows mean and standard deviation. Only DAG1 KO clones D-E grew significantly slower than the control cells while there was no statistically significant difference between control and DAG1 KO clones A-C. Statistical analysis used two-way ANOVA with Dunnett's multiple comparisons test, p values in the table.

Increased levels of DNA damage can be a further indicator of cellular senescence. Staining for the histone modification γH2AX is a common method of identifying DNA damage within cells. When the levels of γH2AX were compared between control cells and *DAG1* KO cell lines (A-E) there was no difference between control and KO cells A-C, whilst there was a significant increase in levels of γH2AX in *DAG1* KO clones D and E (Figure *3.18*). These data suggests that the majority of *DAG1* KO clones have levels of DNA damage similar to that of control cells when detected using γH2AX.

Taken together, these three pieces of evidence would suggest that the increased nuclear and cell size observed in *DAG1* KO cell lines A-C is not due to an increase in

cellular senescence. This is evidenced by similar proliferation rates to the control, no difference in heterochromatin levels and no difference in levels of DNA damage when compared with the control. On the other hand, *DAG1* KO clones D and E show strong signs of cellular senescence as evidenced by the greatly decreased proliferation rates and the increased levels of DNA damage compared with control cells.

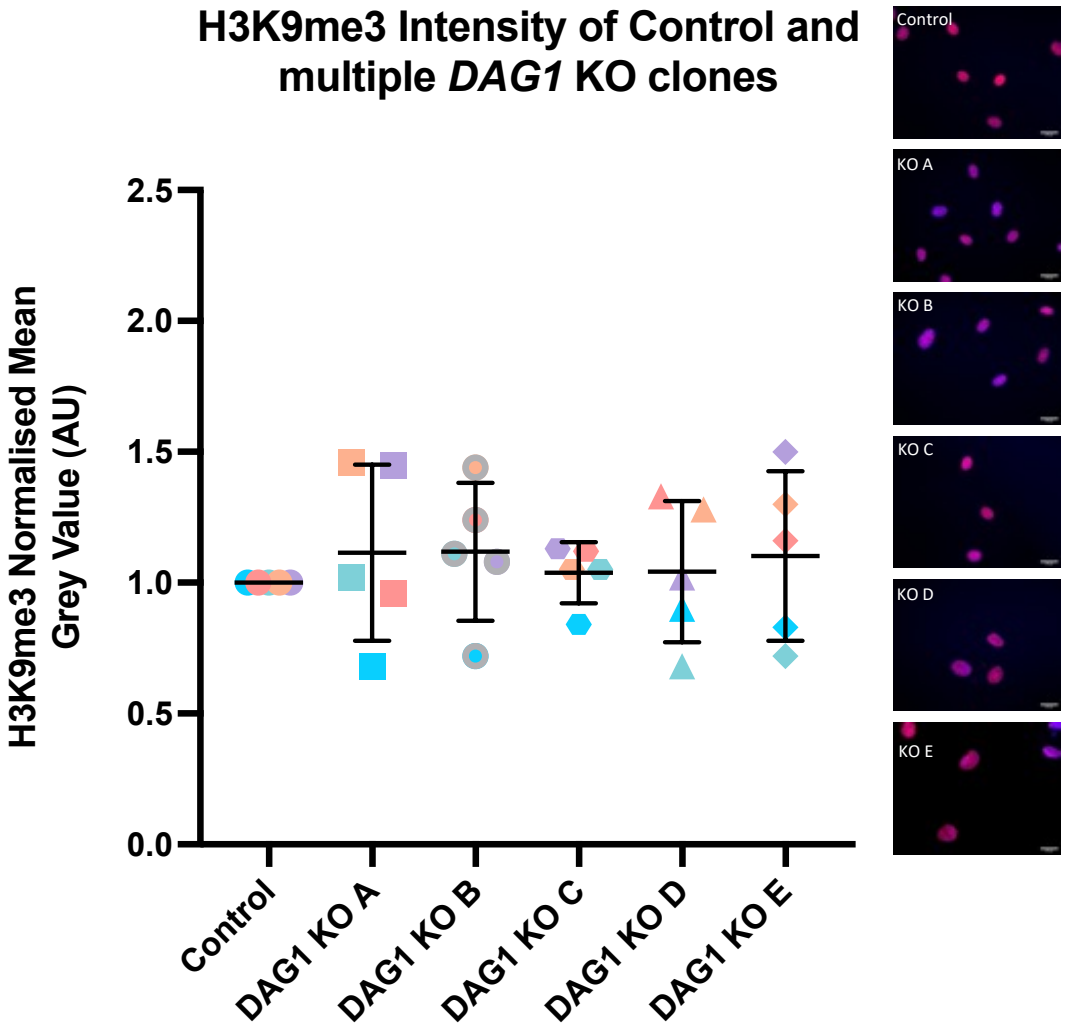

Cell Line	Average	SD	P value compared with control	Significance
Control	1.000	N/A	N/A	N/A
DAG1 KO A	1.114	0.3367	0.4777	ns
DAG1 KO B	1.118	0.2639	0.4626	ns
DAG1 KO C	1.038	0.1169	0.8120	ns
DAG1 KO D	1.042	0.2699	0.7927	ns
DAG1 KO E	1.102	0.3244	0.5248	ns

Figure 3.17 **Relative H3K9me3 intensity for control and DAG1 KO clones A-E.** Cells were grown for 24 hours before fixing and staining with DAPI and H3K9me3 to identify the levels of heterochromatin. Cells were imaged using the Leica fluorescence microscope and the nuclear H3K9me3 signal intensity was determined for analysis. Each coloured point indicates the average for each independent experiment which was normalised to the control value. 5 independent experiments were carried out with 173 control, 182 KO A, 169 KO B, 177 KO C, 156 KO D and 155 KO E nuclei measured. Graph shows mean and standard deviation. A significant difference was not determined by one-way ANOVA test, p = <0.9628. p values for multiple comparisons using Dunnett's multiple comparisons test are in the table. Scale bar = 20μm.

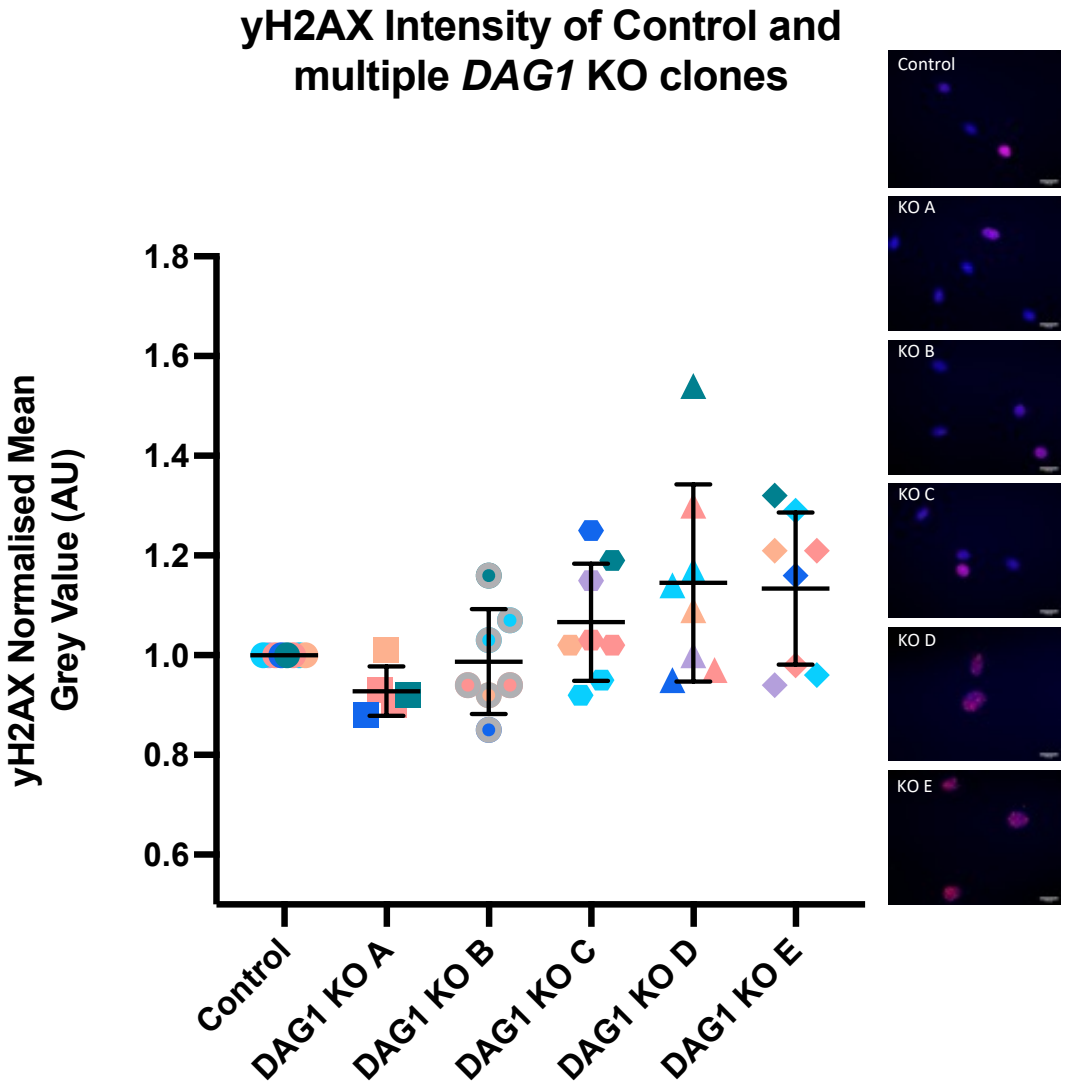

Cell Line	Average	SD	P value compared with control	Significance
Control	1.000	N/A	N/A	N/A
DAG1 KO A	0.9280	0.0497	0.3248	ns
DAG1 KO B	0.9871	0.1052	0.8455	ns
DAG1 KO C	1.054	0.1215	0.3019	ns
DAG1 KO D	1.166	0.2039	0.0276	*
DAG1 KO C	1.161	0.1414	0.0412	*

Figure 3.18 **Relative γH2AX intensity for control and DAG1 KO clones A-E.** Cells were grown for 24 hours before fixing and staining with DAPI and an antibody against γH2AX to identify the levels of DNA damage. Cells were imaged using the Leica fluorescence microscope and the nuclear γH2AX signal intensity was determined for analysis. Each coloured point indicates the average for each independent experiment which was normalised to the control value. 5 independent experiments were carried out with 179 control, 179 KO A, 183 KO B, 188 KO C, 162 KO D and 150 KO E nuclei measured. Graph shows mean and standard deviation. A significant difference was determined between the samples as determined by one-way ANOVA test, p = <0.0179. p values for multiple comparisons using Dunnett's multiple comparisons test are in the table. Scale bar = 20μm.

3.2.6 Is increased nuclear and cell size in *DAG1* KO cell lines due to changes in nuclear proteins lamin A/C, lamin B1 or emerin?

Levels of lamin proteins have been implicated in the regulation of nuclear and cell size and it has also been shown previously that knockout or knockdown of DG can result in mislocalisation and a reduction in levels of lamin B1 and emerin in mouse C2C12 myoblasts (Jimenez-Gutierrez et al., 2020; Martínez-Vieyra et al., 2013). In order to investigate the total levels of these proteins in control and *DAG1* KO cells, western blotting and immunofluorescence microscopy was used. Additionally, immunofluorescence microscopy was used to assess the protein localisation.

3.2.6.1 Levels of lamin A/C in control and *DAG1* KO human myoblasts

Localisation of lamin A/C was investigated and was very clearly localised to the nuclear periphery in both control and *DAG1* KO clones A and B (Figure *3.19*a). Manual inspection of all images from control and KO samples did not identify any occurrences of lamin A/C localised anywhere other than the nuclear periphery or nucleoplasm. Therefore, quantification of this parameter was not carried out. Following the initial manual inspection for localisation the images were analysed to determine the relative intensity of lamin A/C in *DAG1* KO nuclei compared with controls (Figure *3.19*b). The average relative intensity of lamin A/C for both *DAG1* KO clones A and B was 0.75 and 0.78 respectively compared with a relative value of 0.96 for the control. Despite the average relative value being lower for the KO clones these differences were not statistically significant with p values of ~0.5.

There was no clear difference in levels of lamin A/C in control and *DAG1* KO cells when cells were grown at low cell density and therefore had minimal cell-cell contacts. It has been suggested that levels of lamins are regulated by cell density and cell-cell contacts. Therefore, levels of lamin A/C were also investigated in control and *DAG1* KO cells grown at high cell density. Cells were grown to between 90% and 100% confluency and then stained for lamin A/C (Figure *3.20*a). As with the cells at low cell confluency, manual inspection did not indicate any mislocalisation. Relative intensity

of lamin A/C at high cell confluency gave similar results to the low cell confluency experiments with the average intensity being slightly lower for the *DAG1* KO clones but not significantly so (Figure *3.20*b). Control nuclei had a relative lamin A/C intensity of 0.94 while *DAG1* KO clones A and B had relative lamin A/C intensities of 0.84 and 0.59 respectively however, neither of these differences were significant.

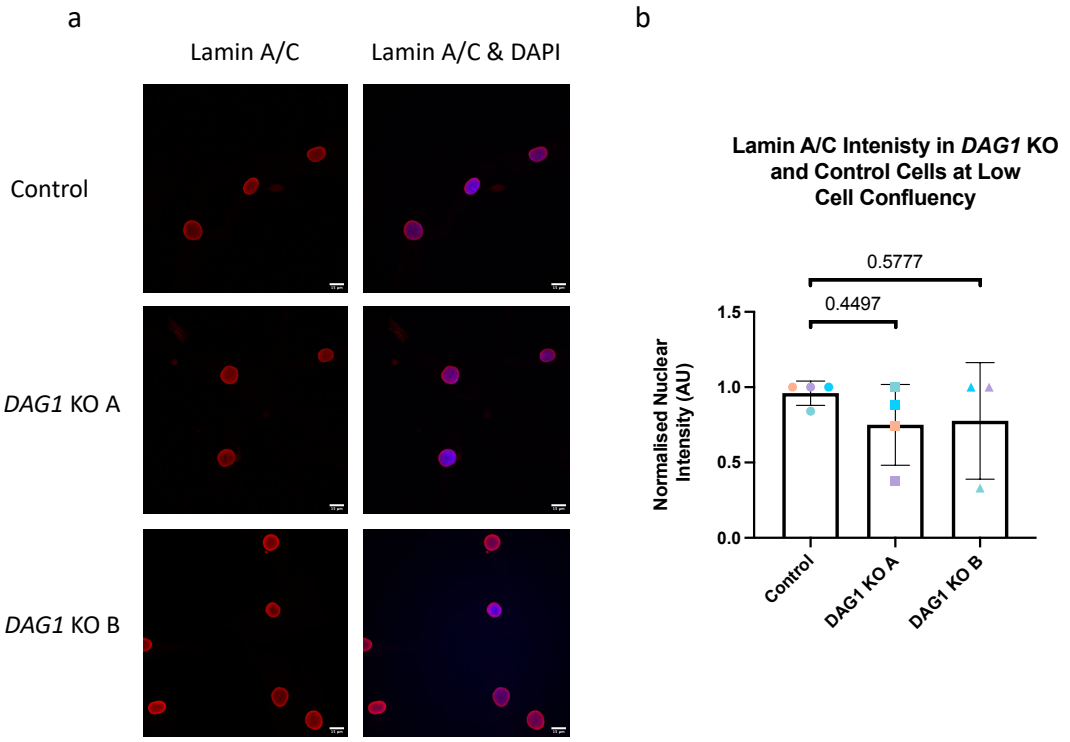

Figure 3.19 **Relative Lamin A/C intensity for control and DAG1 KO clones A-B at a low cell density determined by immunofluorescence.** Cells were grown for 24 hours before fixing and staining with DAPI and lamin A/C to identify the levels of nuclear lamin A/C. Cells were imaged using the Nikon A1 confocal and the nuclear lamin A/C signal intensity was determined for analysis. Scale bar = 15μm. (a) Representative maximum projection images of lamin A/C stained control and DAG1 KO clone A and B cells grown at a low cell density. (b) Normalised lamin A/C intensity in control and DAG1 KO clones A-B. The different coloured points indicate the 4 independent experiments. Control n = 145, KO A n = 139 and KO B n = 162. Graph shows mean and standard deviation. There is no significant difference between the samples as determined by one-way ANOVA, p = 0.4988. p values for multiple comparisons using Dunnett's multiple comparisons test are on the graph.

In addition to there being no clear difference in levels of lamin A/C as determined by immunofluorescence staining, the total cellular levels of lamin A/C were further determined by western blot analysis. Whole cell lysate for each sample at high cell density was probed with lamin A/C antibody and GAPDH was used as a loading control (Figure *3.21*). There was great variation between each biological repeat as observed with the immunofluorescence staining but overall, there was no

statistically significant difference between the control levels of lamin A/C and the *DAG1* KO levels. *DAG1* KO clone A had a slightly increased normalised level while clone B had a slightly decreased normalised level, however, neither of these differences are statistically significant. Taken together this data demonstrates that there is no difference in the levels of lamin A/C between control and *DAG1* KO human myoblasts, indicating β-DG does not influence levels or localisation of lamin A/C in this cell type.

a

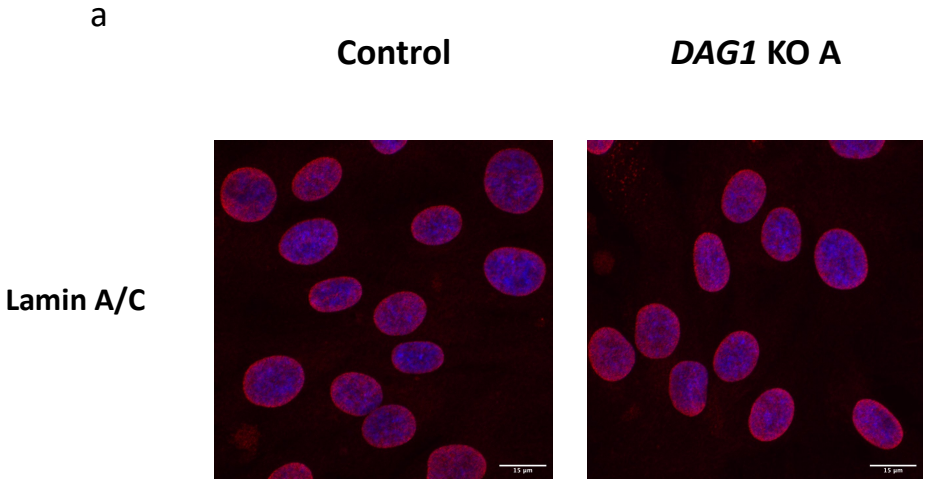

b

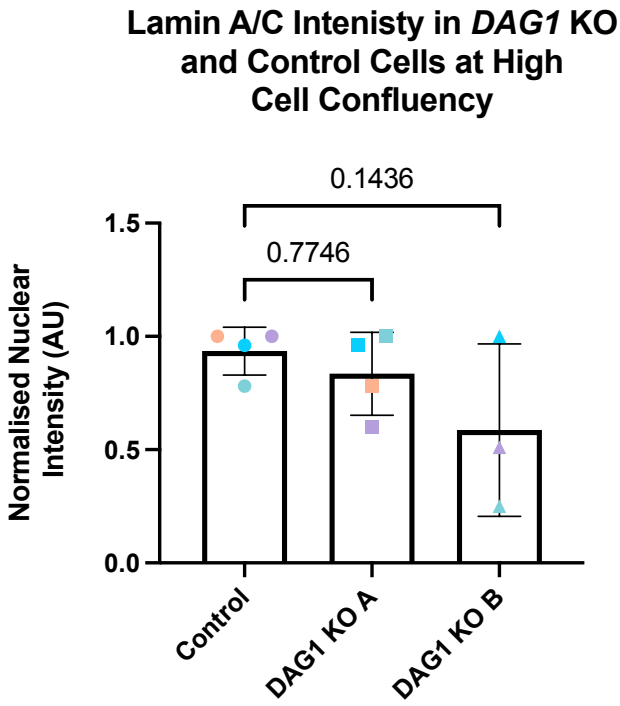

Figure 3.20 **Relative Lamin A/C intensity for control and DAG1 KO clones A-B at a high cell density determined by immunofluorescence.** Cells were grown for 24 hours before fixing and staining with DAPI and an antibody against lamin A/C to identify the levels of nuclear lamin A/C. Cells were imaged using the Nikon A1 confocal and the nuclear lamin A/C signal intensity was determined for analysis. Scale bar = 15μm. (a) Representative maximum projection images of lamin A/C stained control and DAG1 KO clone A and B cells grown at a high cell density. (b) Normalised lamin A/C intensity in control and DAG1 KO clones A-B. The different coloured points indicate the 4 independent experiments. Control n = 132, KO A n = 137 and KO B n = 129. Graph shows mean and standard deviation. There is no significant difference between the samples as determined by one-way ANOVA, p = 0.1950. p values for multiple comparisons using Dunnett's multiple comparisons test are on the graph.

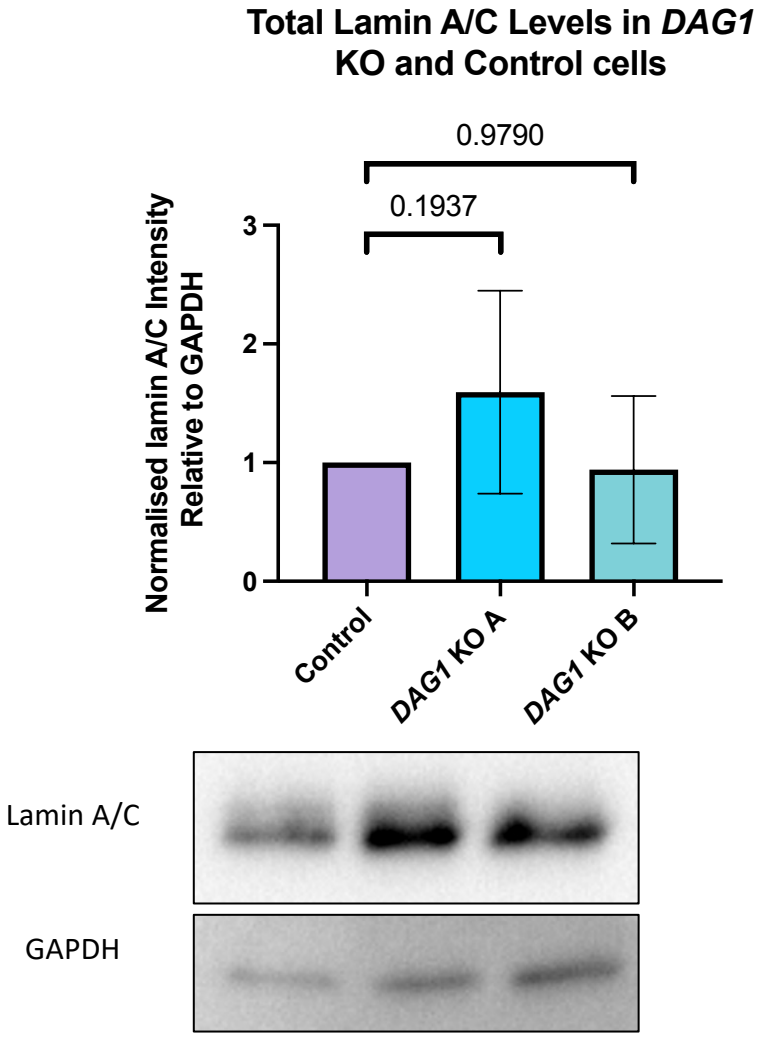

Figure 3.21 **Relative Lamin A/C levels of control and DAG1 KO clones A-B at a high cell density determined by western blot.** Western blot analysis of lamin A/C levels using densitometry analysis from BioRad ImageLab software and normalised to GAPDH. Representative blot from 6 independent experiments. Graph shows mean and standard deviation. There is no significant difference between the samples as determined by one-way ANOVA, p = 0.1572. p values for multiple comparisons using Dunnett's multiple comparisons test are on the graph.

3.2.6.2 Levels of lamin B1 in control and *DAG1* KO human myoblasts

As with lamin A/C levels, the levels of lamin B1 were assessed using immunofluorescence microscopy and western blotting. Lamin B1 stained cells were imaged and assessed manually for localisation outside of the nucleus but this was not observed in control or *DAG1* KO images (Figure *3.22*a). These images were then run through a FIJI script to measure the intensity of lamin B1 within the nucleus. Each mean grey value for each independent experiment was normalised to the largest value which gave an average normalised lamin B1 value of 0.87 for control cells and

0.89 and 0.99 for *DAG1* KO clone A and B respectively (Figure *3.22*b). The difference between the control value and the two KO values does not differ significantly suggesting the levels of lamin B1 are not affected by an absence of DG.

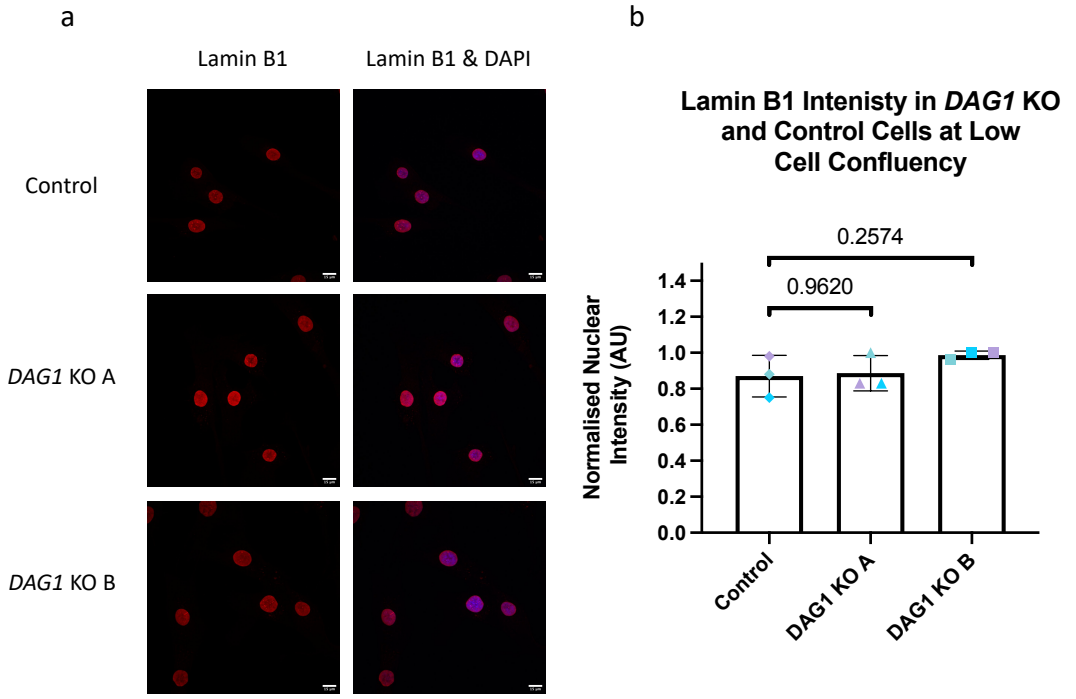

Figure 3.22 **Relative Lamin B1 intensity for control and DAG1 KO clones A-B at a low cell density determined by immunofluorescence.** Cells were grown for 24 hours before fixing and staining with DAPI and lamin B1 to identify the levels of nuclear lamin B1. Cells were imaged using the Nikon A1 confocal and the nuclear lamin B1 signal intensity was determined for analysis. Scale bar = 15μm. (a) Representative maximum projection images of lamin B1 stained control and DAG1 KO clone A and B cells grown at a low cell density. (b) Normalised lamin B1 intensity in control and DAG1 KO clones A-B. The different coloured points indicate the 3 independent experiments. Control n = 102, KO A n = 97 and KO B n = 110. Graph shows mean and standard deviation. There is no significant difference between the samples as determined by one-way ANOVA, p = 0.2910. p values for multiple comparisons using Dunnett's multiple comparisons test are on the graph.

In addition to the levels of lamin B1 at a low cell density, the levels were also assessed at a high cell density to determine whether DG affects the levels of lamin B1 when cells are 90-100% confluent. Again, on manual inspection there was no evidence of any localisation to the cytoplasm in either control or *DAG1* KO clones (Figure *3.23*a). Following analysis of the relative intensity of lamin B1 in control and *DAG1* KO cell lines there appears to be a significantly lower level of lamin B1 in *DAG1* KO clone A compared with the control but no difference for clone B (Figure *3.23*b). The average normalised value for control cells was 0.97 and 1.00 for *DAG1* KO clone B, the value for *DAG1* KO clone A was 0.72. The variation for these experiments was much lower

than observed for the low cell density experiment. This is a clear difference however, given the same trend is not observed in both KO clones this is unlikely to be due to the lack of DG and may be due to some other factor.

In order to confirm or contradict the finding that levels of lamin B1 are significantly reduced in *DAG1* KO clone A when cells are grown at a high cell confluency western blot analysis was used (Figure *3.24*). The total levels of lamin B1 were assessed using a lamin B1 antibody and GAPDH as a loading control and total levels were normalised to GAPDH. Contradictory to the immunofluorescence data the western blot data suggests there is no difference in the total levels of lamin B1 in either *DAG1* KO clone A or B when compared with the control. The average levels are slightly higher in KO samples but again there was large variation meaning these small differences were not statistically significant. Taken together this data would indicate that the levels of lamin B1 do not differ in control or *DAG1* KO human myoblasts.

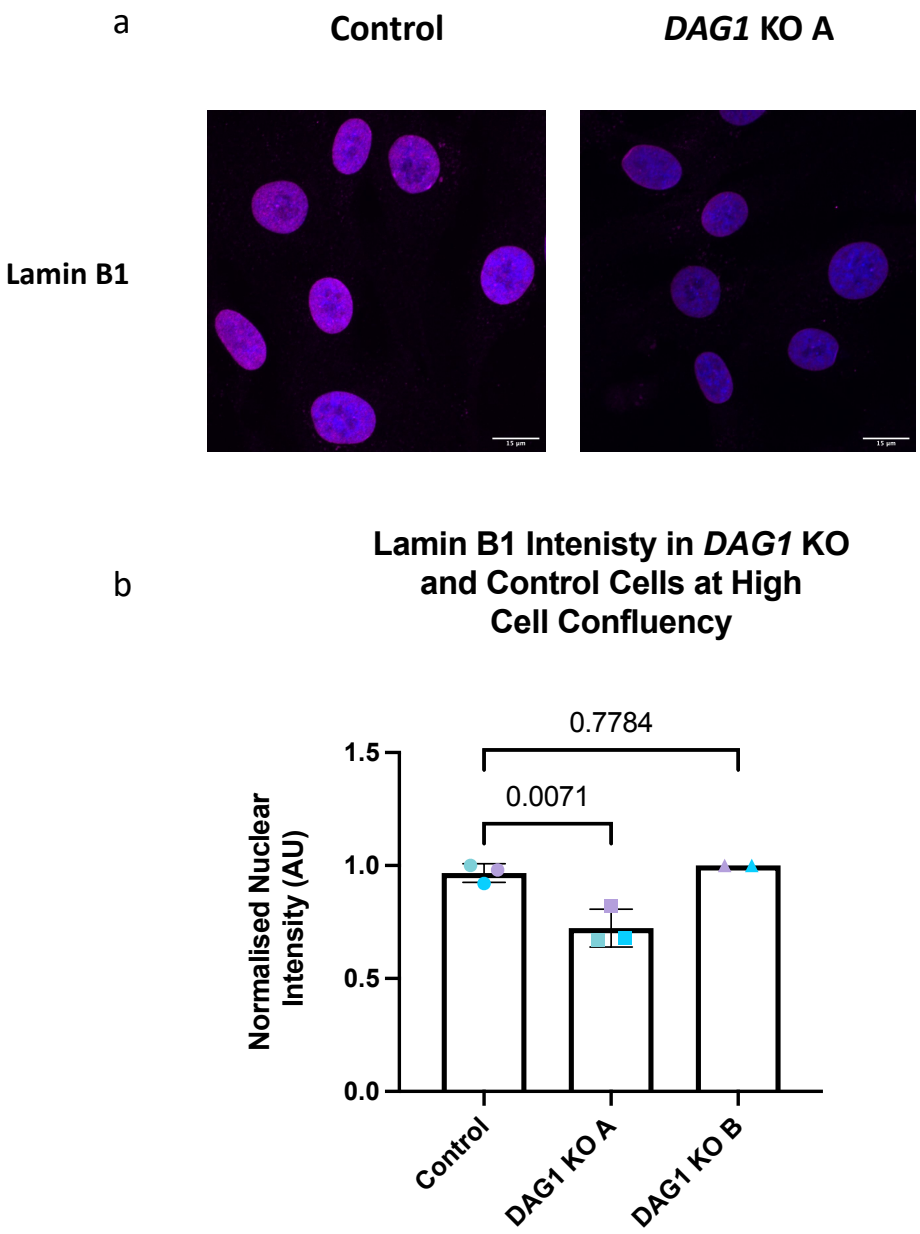

Figure 3.23 **Relative Lamin B1 intensity for control and DAG1 KO clones A-B at a high cell density determined by immunofluorescence.** Cells were grown for 24 hours before fixing and staining with DAPI and lamin B1 to identify the levels of nuclear lamin B1. Cells were imaged using the Nikon A1 confocal and the nuclear lamin B1 signal intensity was determined for analysis. Scale bar = 15μm. (a) Representative maximum projection images of lamin B1 stained control and DAG1 KO clone A and B cells grown at a high cell density. (b) Normalised lamin B1 intensity in control and DAG1 KO clones A-B. The different coloured points indicate the 3 independent experiments. Control n = 93, KO A n = 100 and KO B n = 98. Graph shows mean and standard deviation. There is a significant difference between the samples as determined by one-way ANOVA, p = 0.0053. p values for multiple comparisons using Dunnett's multiple comparisons test are on the graph.

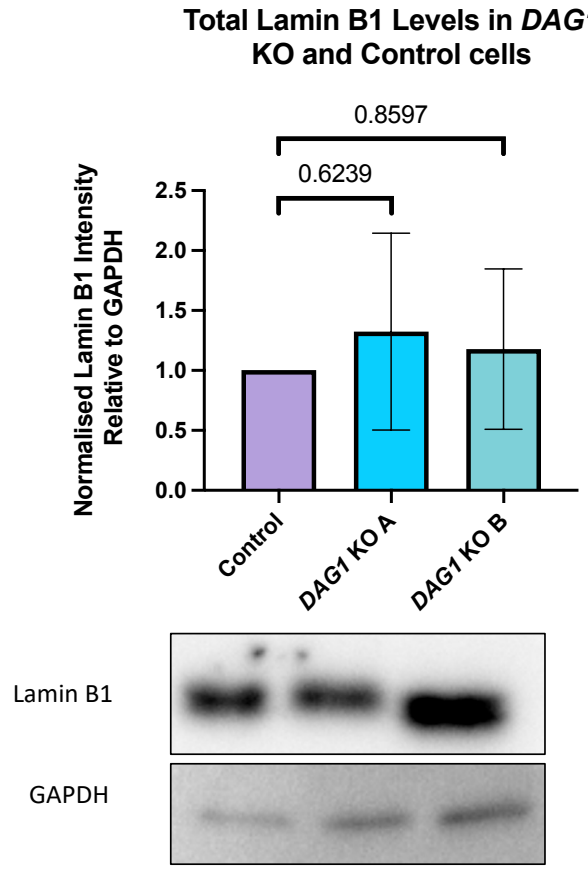

Figure 3.24 **Relative Lamin B1 levels of control and DAG1 KO clones A-B at a high cell density determined by western blot.** Western blot analysis of lamin B1 levels using densitometry analysis from BioRad ImageLab software and normalised to GAPDH. Representative blot from 5 independent experiments. Graph shows mean and standard deviation. There is no significant difference between the samples as determined by one-way ANOVA, p = 0.7102. p values for multiple comparisons using Dunnett's multiple comparisons test are on the graph.

3.2.6.3 Levels of emerin in control and *DAG1* KO human myoblasts

Levels of emerin were assessed in the same manner as lamin A/C and B1. Relative emerin intensity was determined using immunofluorescence microscopy (Figure *3.25*a). As with both lamin A/C and B1 there is no difference in the relative levels of emerin in *DAG1* KO clones A and B when compared with control cells (Figure *3.25*b). Control nuclei had a relative intensity value of 0.82 while *DAG1* KO clone A and B had relative intensity values of 0.94 and 0.85 respectively. These differences were not statistically significantly different with p values >0.7 as determined by a one-way ANOVA test.

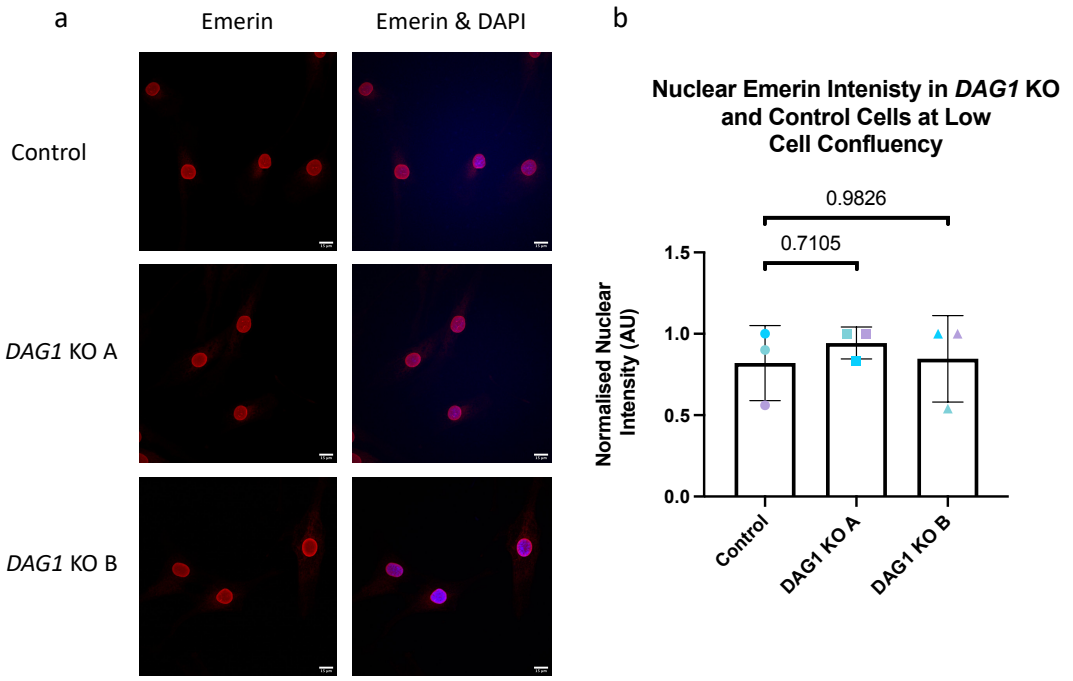

Figure 3.25 **Relative nuclear Emerin intensity for control and DAG1 KO clones A-B at a low cell density determined by immunofluorescence.** Cells were grown for 24 hours before fixing and staining with DAPI and emerin to identify the levels of nuclear emerin. Cells were imaged using the Nikon A1 confocal and the nuclear emerin signal intensity was determined for analysis. Scale bar = 15µm. (a) Representative maximum projection images of emerin stained control and DAG1 KO clone A and B cells grown at a low cell density. (b) Normalised emerin intensity in control and DAG1 KO clones A-B. The different coloured points indicate the 3 independent experiments. Control n = 92, KO A n = 104 and KO B n = 99. Graph shows mean and standard deviation. There is no significant difference between the samples as determined by one-way ANOVA, p = 0.7622. p values for multiple comparisons using Dunnett's multiple comparisons test are on the graph.

Unlike lamin A/C and B1 which localise almost exclusively to the nuclear periphery and nucleoplasm, emerin has some cytoplasmic localisation in addition to the nuclear localisation. From a manual assessment of all the images from control and *DAG1* KO samples it appeared that there was no difference in the localisation of emerin between these samples, so it was not tested quantitatively. A previous study suggested that perturbation of DG resulted in emerin aggregates accumulating in the cytoplasm (Martínez-Vieyra et al., 2013; Vélez-Aguilera et al., 2018) which was not observed in any cells of any sample in these experiments. However, given not all the emerin present within the cells is localised to the nucleus a follow up experiment was carried out where the levels of emerin within the whole cell were determined rather than just the nucleus (Figure *3.26*). As with just nuclear emerin there was no difference in the total levels of emerin when comparing *DAG1* KO clone A and B with controls. The control average relative value was 0.89 while *DAG1* KO clone A and B were 0.83 and 0.87 respectively.

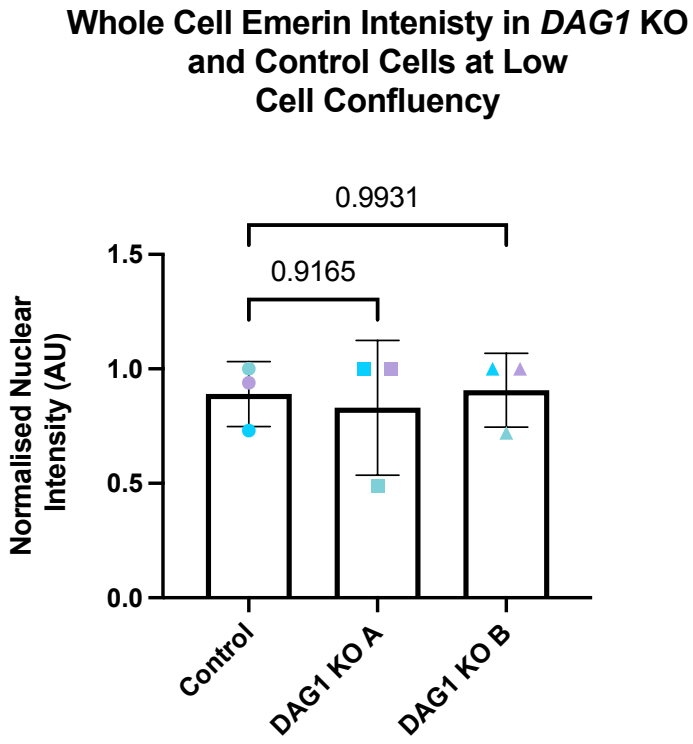

Figure 3.26 **Relative whole cell Emerin intensity for control and DAG1 KO clones A-B at a low cell density determined by immunofluorescence**. Normalised whole cell emerin intensity in control and DAG1 KO clones A-B. The different coloured points indicate the 3 independent experiments. Control n = 92, KO A n = 104 and KO B n = 99. Graph shows mean and standard deviation. There is no significant difference between the samples as determined by one-way ANOVA, p = 0.9377. p values for multiple comparisons using Dunnett's multiple comparisons test are on the graph.

The relative intensity of emerin in cells seeded and grown to a high density was again similar to that observed for low cell density (Figure *3.27*a). Each independent experiment had a large amount of variation with a different cell line having the largest value in each of the three independent experiments. This resulted in an average relative value of 0.60, 0.64 and 0.72 for control, *DAG1* KO A and B respectively (Figure *3.27*b). Based on this evidence there is no apparent difference in nuclear levels of emerin between *DAG1* KO cell lines and control cells at high cell confluency.

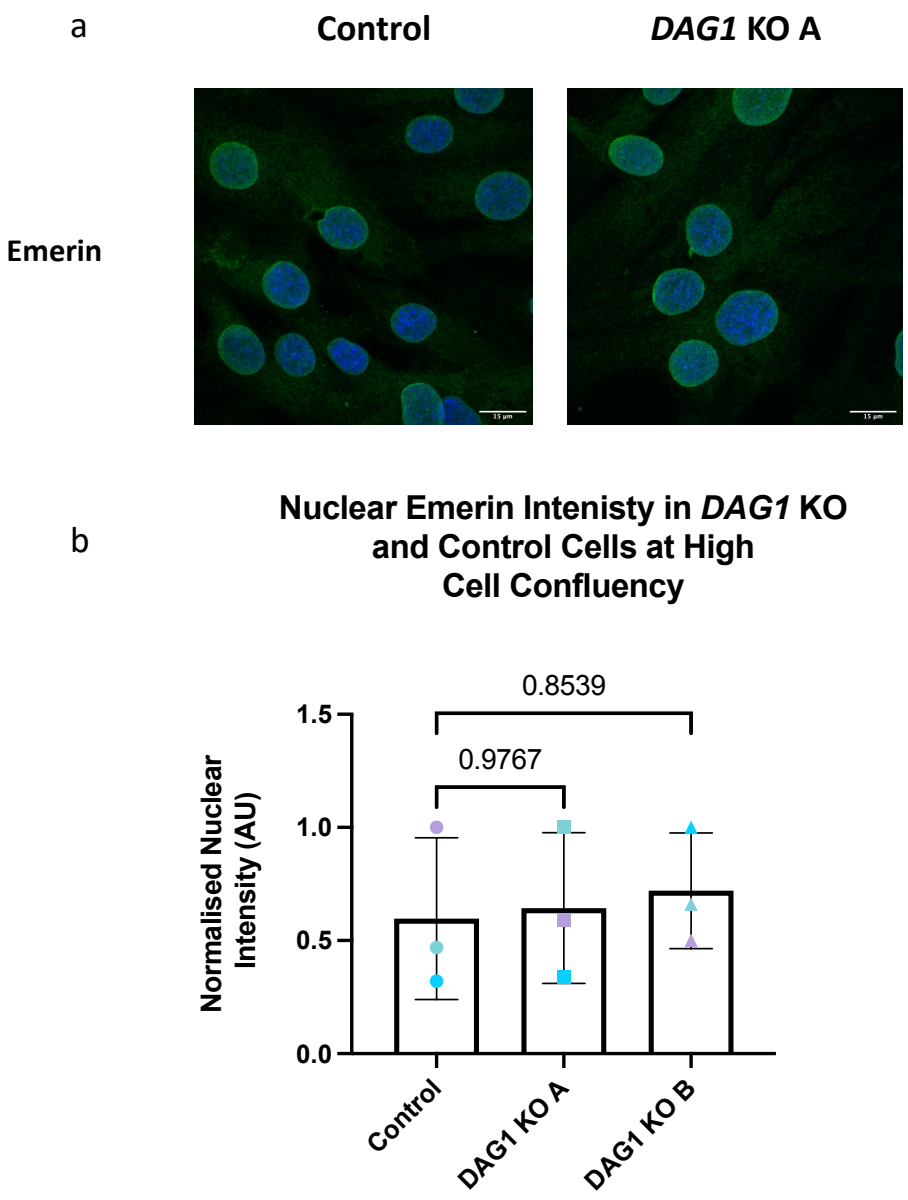

Figure 3.27 **Relative emerin intensity for control and DAG1 KO clones A-B at a high cell density determined by immunofluorescence.** Cells were grown for 24 hours before fixing and staining with DAPI and emerin to identify the levels of nuclear emerin. Cells were imaged using the Nikon A1 confocal and the nuclear emerin signal intensity was determined for analysis. Scale bar = 15μm (a) Representative maximum projection images of emerin stained control and DAG1 KO clone A and B cells grown at a high cell density. (b) Normalised emerin intensity in control and DAG1 KO clones A-B. The different coloured points indicate the 3 independent experiments. Control n = 107, KO A n = 94 and KO B n = 97. Graph shows mean and standard deviation. There is no significant difference between the samples as determined by one-way ANOVA, p = 0.8934. p values for multiple comparisons using Dunnett's multiple comparisons test are on the graph.

The total levels of emerin at high cell density were also assessed using western blot analysis. Emerin was probed for using an emerin specific antibody and GAPDH was used as a loading control and the emerin intensity values were normalised to the GAPDH values (Figure *3.28*). As with the immunofluorescence data, each

independent experiment resulted in a large amount of variation but gave the same result. There is no difference between the total levels of emerin when comparing *DAG1* KO clones A and B with control cells. Taken together, these data indicated that the total levels of emerin are not affected by the presence or absence of DG in human myoblasts at either high or low cell density. It is also clear from the microscopy images that emerin is not mislocalised in *DAG1* KO cell lines.

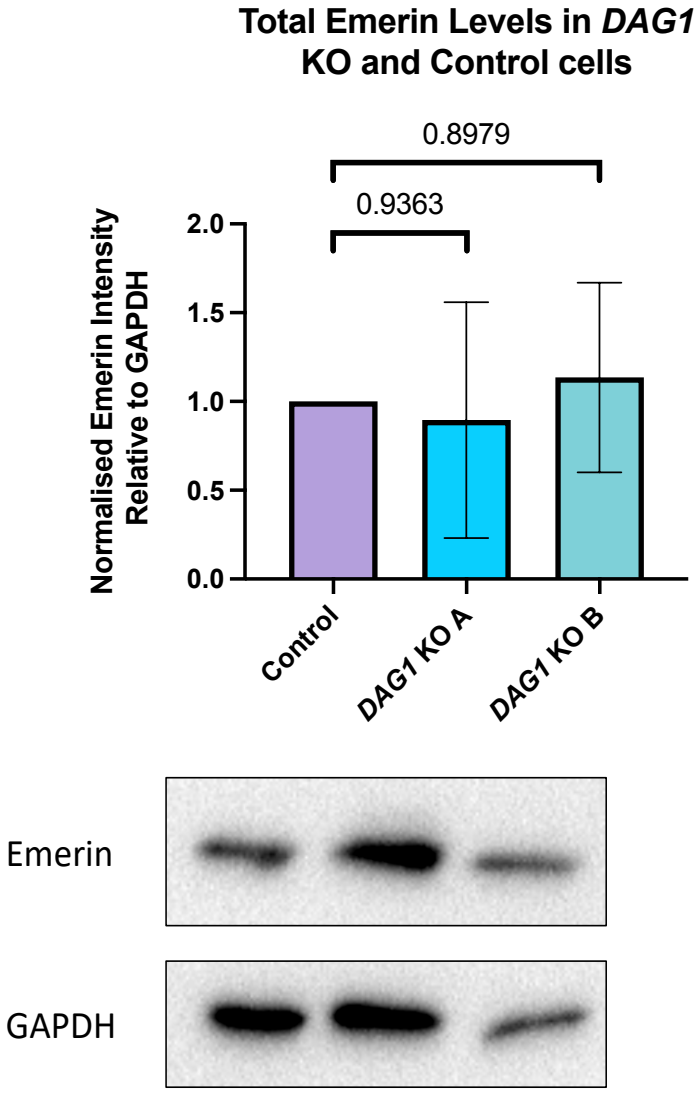

Figure 3.28 **Relative Emerin levels of control and DAG1 KO clones A-B at a high cell density determined by western blot.** Western blot analysis of emerin levels using densitometry analysis from BioRad ImageLab software and normalised to GAPDH. Representative blot from 4 independent experiments. Graph shows mean and standard deviation. There is no significant difference between the samples as determined by one-way ANOVA, p = 0.7925. p values for multiple comparisons using Dunnett's multiple comparisons test are on the graph.

3.3 Discussion

The results described in this chapter aimed to answer the question of whether perturbing DG in human myoblast cells resulted in abnormally shaped nuclei. An additional aim was to determine whether previously reported data, suggesting β-DG was required for correct localisation and regulation of lamin B1 and emerin in mouse C2C12 muscle cells (Martínez-Vieyra et al., 2013; Vélez-Aguilera et al., 2018), was also true in human myoblasts.

3.3.1 Limitations of β-DG antibodies

The primary antibodies against β-DG used in this study have long been used in the detection of β-DG for both western blot and immunofluorescence analysis. However, it has become apparent there are a number of limitations in their use. For all antibodies used here; MANDAG2, LG5, JAF1, C-20 and 1709 the binding site is located within the C-terminal region of the cytoplasmic region. This region has been identified as the binding site for the majority of the interacting partners that binds β-DG (see section 1.1.3.3). This being the case, the antibody binding site is likely to be in competition for binding with many other proteins which may reduce the efficacy of the antibody. The other issue with all of these antibodies is they have a high degree of background signal as can be seen in Figure 3.3. This is because all these antibodies, except MANDAG2 are polyclonal which results in a large amount of background signal due to the presence of non-specific antibodies in the serum. The other issue with these antibodies is the lack of batch-to-batch consistency which can cause difficulties when trying to reproduce data, this can be seen in part in Figure 3.4.

Despite these issues, MANDAG2, LG5, JAF1 and 1709 appear to have reduced signal in the *DAG1* KO cell lines as expected. However, C-20 appears to have almost identical staining in control and *DAG1* KO cells, additionally, there appears to be very prominent nucleoli staining in cells both containing and lacking DG. This is a concern as many of the reports in the literature relating to the role of β-DG in the nucleus use

this antibody. In early studies C-20 was used in immunofluorescence colocalisation studies to suggest co-localisation with nucleoli proteins Nopp140 and SC35. Additionally, it was used in co-immunoprecipitation assays to suggest a direct interaction between β-DG and Nopp140 (Martínez-Vieyra et al., 2013). C-20 has also been used more recently in a paper discussing the potential role of β-DG in the nucleoli (Azuara-Medina et al., 2019). In addition to the issue of C-20 binding non-specifically to the nucleoli, there is also data suggesting that a large amount of cross-reactivity occurs between C-20 and other primary antibodies – particularly those raised in mouse or rabbit (Figure *3.29*) (Matt Cook, personal communication). The evidence of cross-reactivity makes this antibody particularly unreliable for colocalisation analysis as presented in the Martínez-Vieyra et al. (2013) study described above.

The β-DG antibodies used in this chapter have some limitations as discussed, one of the main issues with this is obtaining an accurate understanding of specific localisation of β-DG because of the background noise. However, despite this issue it appears that β-DG staining is present within the nucleus in KM155 and CRISPR/Cas9 control cells and this nuclear staining is generally lost in the KO cells lacking β-DG. It is important when using these antibodies to be aware of these limitations and take this into consideration before making any conclusions.

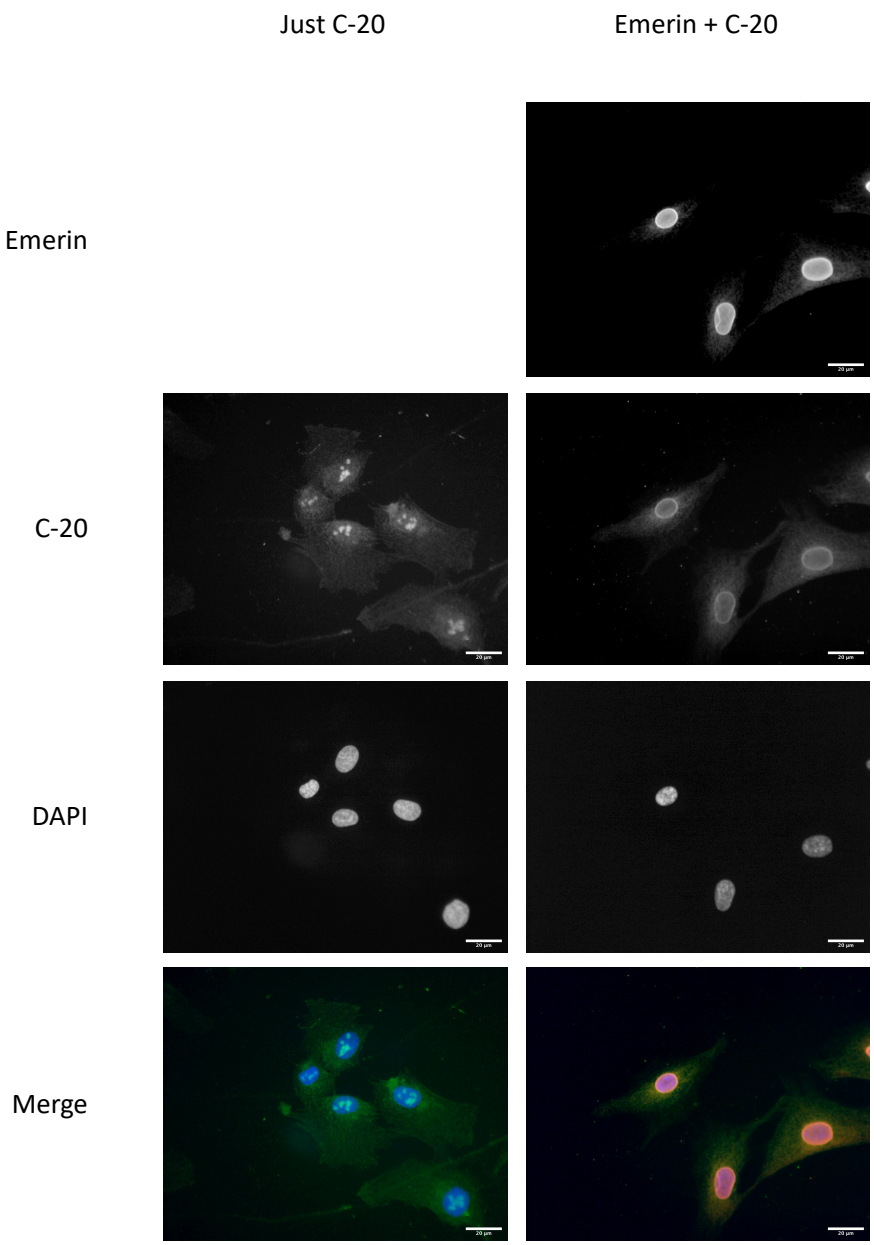

Figure 3.29 **Cross-reactivity between β-DG antibody C-20 and emerin antibody in KM155 human myoblast cells.** Representative images of KM155 myoblasts stained with either C-20 alone or stained with C-20 and emerin together. There is clear nuclear envelope stanning for C-20 in the C-20 + emerin sample which is not present when C-20 is used alone. Scale bar = 20μm.

3.3.2 Differences in observed nuclear shape phenotype

Changes in nuclear shape are often indicative of nuclear damage either mechanically or due to aberrant expression of nuclear lamina proteins including lamin A/C, B1 and emerin (Chen et al., 2018; Lammerding et al., 2006). Mutations in the *DAG1* gene, although rare, have been identified as a possible cause for abnormal nuclear shape

(Jacobs, 2017). In addition to this there have been multiple studies from the Cisneros lab group investigating the effects that perturbing β-DG has on the nucleus. In the original paper investigating this, they suggest that shRNA knockdown of β-DG resulted in an increase in abnormally shaped nuclei compared with the control (Martínez-Vieyra et al., 2013). However, the few images presented in this paper do not appear to be abnormally shaped. Additionally, nuclear abnormality has been assessed in an unblinded experiment which leaves it susceptible to bias. There is also no additional quantification such as nuclear circularity which would give a numerical value and allow a more confident conclusion to be drawn. In a follow up paper where the same group investigate the effects of knocking down α-dystrobrevin, another component of the DAPC, they conclude that the knock down results in more abnormally shaped nuclei (Aguilar et al., 2015) but this is assessed as above with no numerical values for shape.

In the most recent publication from the Cisneros lab, where a possible senescence phenotype is investigated, CRISPR/Cas9 knockout C2C12 cells are generated, and nuclear shape is assessed. They find that the nuclear circularity index for two *DAG1* KO clones is lower than the WT (Jimenez-Gutierrez et al., 2020). One criticism of this experiment is they did not compare the circularity of the KO nuclei with a suitable CRISPR/Cas9 treated control. Therefore, it is not possible to be sure that the tiny reduction in circularity is not due to the CRISPR/Cas9 treatment rather than a lack of DG. This should also be further confirmed by a rescue experiment to confirm it is indeed DG responsible for the phenotype. The same study also looked for the presence of micronuclei in the WT and *DAG1* KO cells and found that significantly more of the KO cells had micronuclei compared with the WT (Jimenez-Gutierrez et al., 2020).

It is clear from these studies that despite the issues with the methodology, the general conclusion from the data presented is that knocking out/down DG results in a small change in nuclear shape in less than 50% of the cells. This data is in stark contrast to the data presented in this chapter and the data presented by other members of the Winder lab (Cook, 2021). The obvious difference between this study

and the previous ones is the cell type that is used. This study focuses on human myoblasts whereas the previous investigations by the Cisneros lab have focused on mouse C2C12 myoblasts. However, I believe the most likely explanation is that the C2C12 *DAG1* KO cells used in the most recent study were senescent. In this chapter *DAG1* KO cell lines D and E were the only cell lines to have a reduced circularity phenotype and these cells then went on to become senescent as will be discussed below. Given that three of the five *DAG1* KO cell lines did not demonstrate this senescence phenotype it is more likely that this is a side effect of CRISPR/Cas9 or a result of clonal expansion. The fact only two KO cell lines were used means it is possible that their observed reduction in circularity is not a result of knocking out DG. A lack of a mock CRISPR/Cas9 control or a rescue experiment prevents any clear conclusions being made.

3.3.3 Differences in observed nuclear size phenotype

Unlike nuclear shape, the nuclear size of cells lacking DG has not been investigated until recently. The only report of nuclear size differences in cells with perturbed DG investigates the relationship between DG and cellular senescence as discussed in section 1.2.3.4 (Jimenez-Gutierrez et al., 2020). This study finds that the nuclei of C2C12 mouse myoblasts where *DAG1* has been knocked out have a significantly greater area than WT nuclei. In addition, it is also found that the KO cells have a greater area when compared to WT (Jimenez-Gutierrez et al., 2020). This is in agreement with the data presented in this study where all *DAG1* KO human myoblasts have larger nuclear and cellular areas compared with the control cells. Additionally, in this study we go on to show that the *DAG1* KO nuclei are not just larger in 2-dimensions but indeed 3-dimensions as demonstrated by the greater nuclear volume in *DAG1* KO clone B.

The data presented by Jimenez-Gutierrez et al. (2020) would suggest that this increase in nuclear size is due to an increase in cellular senescence in the *DAG1* KO cells. However, the data presented here do not fit with that general hypothesis. Either increased or decreased levels of lamin B1 are indicative of a senescent state

(Dreesen et al., 2013; Freund et al., 2012; Shah et al., 2013). A decrease in the levels of H3K9me3 which is indicative of reduced levels of heterochromatin is a common hallmark of cellular senescence (Deng et al., 2019; Sadaie et al., 2013), as is an increase in levels of DNA damage as indicated by γH2AX (Salunkhe et al., 2021; Zhang et al., 2016).

Focusing on *DAG1* KO clones A-C which exhibit a greater average nuclear and cellular size, however the experiments used to indicate senescence did not agree with the conclusion of a senescent phenotype. There is no reduction in the proliferation rate of KO cells compared with control, there is no difference in the relative levels of heterochromatin marker H3K9me3, the relative levels of γH2AX which is a marker of DNA damage or the relative levels of lamin B1. An additional argument against a senescent phenotype in *DAG1* KO clones A-C is the evidence of a reversable phenotype. Rescue experiments of *DAG1* KO clone B and C using tagged DG resulted in the rescue of the nuclear size phenotype. Given that cellular senescence is defined as irreversible cell-cycle arrest, if a lack of DG resulted in true cellular senescence this should not be rescued by the addition of exogenous DG.

In the case of *DAG1* KO clones D and E, they clearly have a significantly larger nuclear area than the control cells and are also the largest nuclei of all cell types measured with control nuclei being ~150μm^2, *DAG1* KO A-C ~170cm^2 and *DAG1* KO D-E ~220cm^2. In addition to this they had a significantly decreased proliferation rates compared with control cells – further they stopped growing altogether so they were unable to be used for the whole study. Additionally, clones D and E had increased levels of DNA damage as measured by levels of γH2AX. The only parameter these clones did not demonstrate an expected phenotype was levels of H3K9me3 where there was no difference in total levels between *DAG1* KO clones D-E and the control. This is possibly due to antibody sensitivity as there was a large range of values across experiments for all cell lines used. Ideally, the *DAG1* KO clones D-E would have been tested for cellular senescence using β-galactosidase senescence assay however, the cells stopped growing completely before this was carried out.

Based on the data presented here, there is very clear evidence that *DAG1* KO clones D-E were senescent while clones A-C did not have the hallmarks of cellular senescence. This diversity of responses within a range of *DAG1* KO cell lines calls into question the findings presented by Jimenez-Gutierrez et al. (2020). The data presented in that study is only based on two *DAG1* KO clones, if by chance in this study only *DAG1* clones D-E were used then we may have drawn the same conclusions. However, the lack of senescence phenotype observed in clones A-C suggests this is not the case. This calls into question the methodology of the Jimenez-Gutierrez et al. (2020) study, the heterogenicity of clonal expansion is well established therefore it is prudent to use as many separate clones as possible before making any definitive conclusions. Additionally, rescue experiments should be attempted to further validate the role of DG and exclude the possibility of observations being due to clonal expansion. Finally, it is important to compare the *DAG1* KO clones with passage matched clonally expanded controls in order to minimise differences, however, in the Jimenez-Gutierrez et al. (2020) study the *DAG1* KO clones were only compared with the WT C2C12 population.

Ultimately, it is possible to conclude from these data presented here that perturbation of DG does lead to an average increase in nuclear and cellular size however, this increase is not due to cellular senescence. The exact reason for this increase in size is yet to be determined.

3.3.4 Differences in observed nuclear envelope protein levels and localisation

It has been suggested previously that nuclear β-DG is involved in interactions with lamin A/C, lamin B1 and emerin (Gómez-Monsiváis et al., 2020; Martínez-Vieyra et al., 2013). It has also been suggested that the perturbation of β-DG or the *DAG1* gene results in reduced levels and mislocalisation of both lamin B1 and emerin but not lamin A/C. This then results in phenotypes associated with reduced levels of lamin B1 and emerin such as nuclear shape abnormalities and centrosome duplication

(Gómez-Monsiváis et al., 2020; Martínez-Vieyra et al., 2013; Vélez-Aguilera et al., 2018).

The results presented in these studies, conducted in the Cisneros lab, have shown consistently that in mouse C2C12 myoblasts either reduction or overexpression of β-DG results in reduced levels of lamin B1 and emerin. However, this is in stark contrast to data presented in this study where there is no detectable difference in the levels of lamin A/C, lamin B1 or emerin in control and *DAG1* KO cells. In addition to this there is no evidence to suggest any mislocalisation of lamin B1 and emerin in any cell lines investigated in this study. There are a few possibilities for the differences observed between the present study and previous studies. One possibility is the difference in cell lines used, in this study human myoblasts were used while previous studies have focused on mouse myoblasts. Despite mouse models being used extensively the disparity in results between this study and previous ones could be explained by this difference. However, when DG was knocked down in H2K mouse myoblasts, nuclear abnormalities were not reported suggesting there was no obvious nuclear morphology phenotype (Thompson et al., 2008). Alternatively, these differences could be a consequence of the different protocols used for the immortalisation of these cell lines.

An alternative explanation of the difference could be due to methodological differences. In the mouse cell studies quantification of protein localisation involved unblinded manual determination of protein localisation which is susceptible to bias (Martínez-Vieyra et al., 2013; Vélez-Aguilera et al., 2018). This should have been quantified as a cytoplasmic intensity as this is simple to automate and reduces bias. However, in human myoblasts there was no evidence of protein mislocalisation in any of the cell lines tested so this automated analysis was not required. The total levels of lamin B1 and emerin were assessed using western blotting analysis in mouse myoblasts while in this study both immunofluorescence and western blotting analysis was used for human myoblasts. Finally, the type of control samples used were different when *DAG1* was knocked out of mouse or human myoblasts. There

are the same issues relating to clonal expansion and a lack of any rescue experiments as discussed in section 3.3.3.

The phenotypes that have been described in this study and those from previous studies differ and this is likely to be a combination of differences in cell types and differences in methodological approach. Ultimately, the results presented here are robust enough to confidently conclude that in human myoblasts the knockout of the *DAG1* gene does not result in either mislocalisation or a reduction in levels of lamin A/C, lamin B1 or emerin.

4 Investigating the effect of perturbing *DAG1* on the inherent mechanical properties of myoblast nuclei using atomic force microscopy (AFM)

4.1 Introduction

4.1.1 Mechanical properties of cells and nuclei are determined by the cytoskeleton, nucleoskeleton and chromatin

Measuring the mechanical properties of cells, particularly using atomic force microscopy, allows the determination of the stiffness of the different cellular compartments i.e. the cytoplasm and the nucleus. However, these two compartments are mechanically linked making it difficult to separate the specific contribution of each. It is well established that cells mechanically sense their environment and adjust the mechanical properties of the cells to match that of the underlying substrate, predominantly through the reorganisation of the actin cytoskeleton (Doss et al., 2020). In a recent study, multiple mammalian cell types were measured on PDMS substrates with varying stiffness from 0.5-3MPa and in all cell types the cell stiffness increased with increased substrate stiffness (Wala and Das, 2020). Similar results were observed when cells were grown on glass, polystyrene or poly-L-lysine coated glass. Polystyrene and Poly-L-lysine-coated glass have a lower Young's modulus than glass and cells accordingly had reduced stiffness compared with those grown on uncoated glass (Caluori et al., 2018). However, it has been suggested that a decrease in cell stiffness at low substrate stiffness (<2kPa) is due to indenting the substrate as well as the sample but this can be accounted for depending on the model used to fit the data (Rheinlaender et al., 2020).

Stiff cells grown on stiff substrates have increased levels of actin which is organised in more rigid actin cables (Doss et al., 2020; Wala and Das, 2020). Therefore, perturbation of the actin cytoskeleton results in a decrease in cellular stiffness. When

human bladder cancer cells T24 and RT4 (Wang et al., 2018) and mouse embryonic fibroblast NIH3T3 cells (Zhang et al., 2020) were treated with Cytochalasin D, treatment resulted in a significant decrease in cell stiffness compared with untreated controls. However, when cells in these studies were treated with nocodazole to perturb the microtubules there were differing effects. Wang et al. (2018) reported that nocodazole treatment resulted in a decrease in cellular stiffness but this decrease was not as severe as CytoD treatment (or a combination of CytoD and nocodazole). Conversely, Zhang et al. (2020) reported an increase in cellular stiffness following nocodazole treatment and they suggest this is because the depolymerised microtubules result in an increase in actin polymerisation ultimately resulting in stiffer cells. The discrepancy between these results is possibly due to difference in cell type or difference in measuring technique, Wang et al. (2018) used AFM while Zhang et al. (2020) used Brillouin microscopy. Despite the differences it is clear from these experiments that the microtubule network has a lower impact on the mechanical properties of cells compared with the actin cytoskeleton. Cytoplasmic intermediate filaments also make up part of the cytoskeleton and it has been found that vimentin, a type III intermediate filament, that forms a protective cage around the nucleus contributes to the cell stiffness (Patteson et al., 2019a). Measuring the stiffness of *vim*$^{-/-}$ mouse embryonic fibroblasts over the nucleus gave an average apparent Young's modulus that was significantly lower than the *vim*$^{+/+}$ control, suggesting intermediate filaments also contribute to the overall stiffness of a cell (Patteson et al., 2019b).

Nuclear stiffness is determined by a combination of the nuclear lamina and chromatin (Hobson et al., 2020; Zhang et al., 2020). The contribution of lamin A to the mechanical properties of the nucleus was initially investigated in the nuclei of *Xenopus* oocytes due to their large nuclei (so reducing the impact of chromatin) and lack of endogenous lamins. Using this system it was found that the nuclear stiffness increased in a dose-dependent manner following lamin A expression (Schäpe et al., 2009). Mutant lamins have also been investigated using this method, the mutation E145K found in Hutchinson-Gilford progeria syndrome resulted in increased nuclear stiffness compared with WT lamin (Kaufmann et al., 2011). This has also been

observed in human patient samples (Apte et al., 2017). The fact a single mutation in lamin A can result in a significant increase in nuclear stiffness emphasises the important role lamins play. Further evidence that lamins play an essential role in regulating nuclear stiffness is observed in autosomal dominant leukodystrophy patient samples. These samples have reduced levels of lamin B1 in addition to a decrease in nuclear stiffness. Further, depletion of lamin B1 in HEK293 and neuronal N2a cells resulted in a decrease in nuclear stiffness while overexpression of lamin B1 resulted in an increase (Ferrera et al., 2014).

In addition to lamins, chromatin significantly contributes to the stiffness of nuclei. The stiffness of the nucleus is regulated by the relative ratios of heterochromatin and euchromatin. The addition of trichostatin A, a small molecule inhibitor of histone deacetylase, results in an increase in the proportion of heterochromatin compared with euchromatin and a decondensing of the chromatin. Treatment of multiple cell lines with TSA prior to mechanical measurement results in a significant decrease in nuclear and cellular stiffness (Krause et al., 2013; Mazumder et al., 2008; Zhang et al., 2020). This decrease in stiffness occurred in a dose-dependent manner (Krause et al., 2013; Zhang et al., 2020). When cells were compressed with an extremely stiff AFM cantilever the nuclei were compressed to 20% of the original height while treatment with TSA resulted in an additional 5% decrease in height, suggesting the importance the chromatin plays in maintaining nuclear rigidity (Krause et al., 2013).

Manipulating the levels of lamins and the state of chromatin influences the nuclear stiffness, however, these two components do not act independently of each other. When chromatin is no longer tethered to the INM by lamins and other INM proteins there is a reduction in nuclear stiffness (Schreiner et al., 2015). Additionally, chromatin in cells lacking lamin A/C have perturbed chromatin viscoelasticity with a decrease in local harmonic force (how much force is generated by the movement of chromatin) (Vivante et al., 2020). Two recent studies have looked at how the nuclear lamina and the chromatin respond to mechanical force of different types. They find that short extensions (following nuclear stretching) result in chromatin responding while longer extensions (>3μm) result in a response from the nuclear lamina

(Stephens et al., 2017). This observation was also confirmed using combined AFM and light sheet imaging to observe the chromatin and nuclear lamina. This study also found that chromatin responded to short extensions (indentations) while the nuclear lamina responded to longer extensions (Hobson et al., 2020). Ultimately, all these studies show that the mechanical properties of cells are regulated by an intricate balance between the cytoskeleton, nuclear lamina and chromatin.

4.1.2 Hypothesis and Aims

Previously published data discussed in section 1.2.3 suggests that disruption of DG results in a reduction of nuclear lamin proteins lamin A/C and B1 as well as mislocalisation of lamin B1 in mouse C2C12 cells. Both lamin A/C and lamin B1 have been reported to influence the mechanical properties of cells and nuclei. Therefore, the hypothesis is that perturbation of DG and subsequently the nuclear lamina would result in a decrease in nuclear stiffness. Despite the fact we do not see any observable effect on the nuclear lamina following *DAG1* KO in human myoblast cells it is important to investigate any difference in mechanical properties of control and KO cell lines.

The aims of the experiments presented in this chapter were to measure the Young's modulus of control and *DAG1* KO cell lines and directly compare these. Additionally, cells were treated with CytoD and TSA to determine the contribution of chromatin and the cytoskeleton. Further, isolated nuclei were measured to determine the mechanical properties of the nuclei in the absence of any cytoskeletal influence.

4.2 Results

4.2.1 Optimising the functionalisation of tipless cantilevers with 5μm polystyrene beads

The advantages of using a spherical tipped cantilever over sharp tips for mechanical measurements of cells has been well established (Zemła et al., 2020). One advantage is the more uniform distribution of applied force across the cell or organelle. This is not the case when a sharp tip is used as it results in localised force application and therefore a measurement of a smaller area of the cell. This localised application also increases the chance of damaging the sample.

The rectangular MLCT-O10 probe was used for cell and nuclear measurements discussed in this chapter as it had a low spring constant (nominally 0.02N/m) comparable to the stiffness expected for cells and nuclei (Zemła et al., 2020). The MLCT-O10 cantilevers are tipless (Figure *4.1*a) and required functionalising with a polystyrene bead that had a 5μm diameter. 5μm beads were chosen as that is the approximate size of the nuclei in KM155 human myoblasts. Multiple attempts were required to generate a procedure that could reliably produce functionalised cantilevers that were suitable for use. The first attempts involved using microscope slides cleaned with isopropanol and air dried, the adhesive and the beads stored in water were added to the slide. When the beads had dried the cantilever was dipped in the adhesive and then approached the surface over a single bead to pick it up. This method did not result in picking up the bead as it remained on the surface of the slide. The second method involved cleaning the slide with Piranha solution to reduce adhesion between the bead and the slide which would allow the bead to be picked up by the adhesive coated cantilever, but this was also unsuccessful. The third method was the same as the second, except the beads were washed extensively in ethanol before adding them to the slide. This was also unsuccessful. The following method was the same except the ethanol cleaned beads were allowed to air dry before adding to the slide. This was successful in terms of the cantilever coated in adhesive was able to pick up the bead from the slide. Despite the bead being stuck to the cantilever there was an excess of adhesive that resulted in adhesive covering most of the bead which is unsuitable for measurements as the spherical geometry is lost (Figure *4.1*b). The final and successful method involved cleaning the slides with Piranha solution and washing the beads in ethanol and allowing the ethanol to evaporate before adding them to the slide. The cantilever then approached and

contacted the adhesive and contacted the surface of the slide twice following contact with the adhesive to remove any excess and leaving just a thin layer on the cantilever. This left just enough adhesive to pick up and maintain the bead in place but not enough to run over the sides of the bead (Figure *4.1*c).

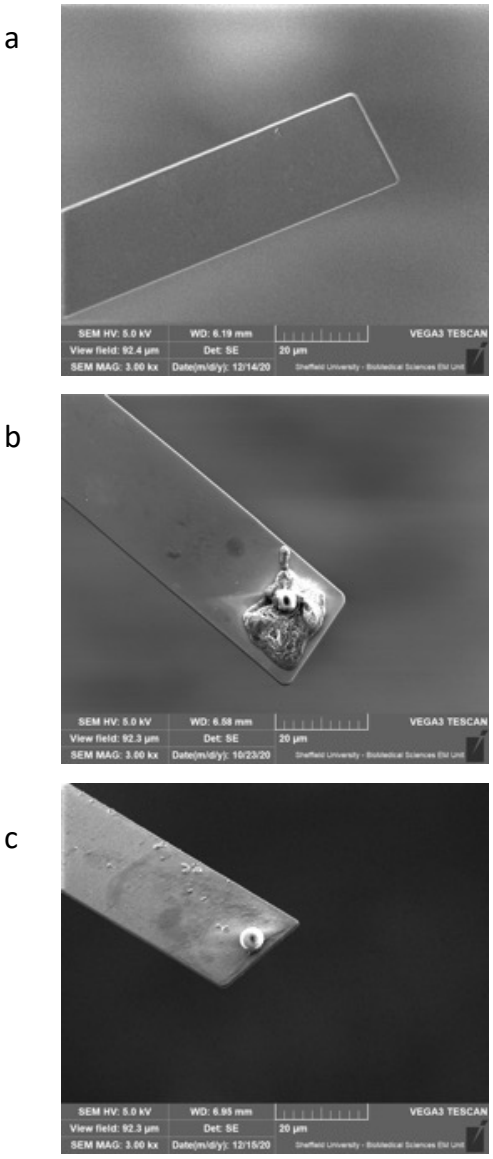

Figure 4.1 **SEM of MLCT-O10 cantilevers**. (a) MLCT-O10 cantilever prior to functionalisation with 5µm bead. (b) MLCT-O10 cantilever functionalised with 5µm bead with excess glue. (c) MLCT-O10 cantilever successfully functionalised with 5µm bead.

4.2.2 Force mapping of a single control cell in order to determine height and stiffness of different cellular regions

Force mapping of an entire cell allows determination of multiple parameters across the whole cell; it provides information on height/topography and a corresponding map of Young's moduli (*E*). Generating a force map of a control cell indicates the highest point of the cell is ~4.2μm and this corresponds to the nucleus (Figure *4.2*). Based on this height analysis the lowest cytoplasmic hight is ~2μm with it increasing moving towards the nucleus. This is important information as it means indentation must always be <2μm over the cytoplasmic region which it always was in subsequent experiments.

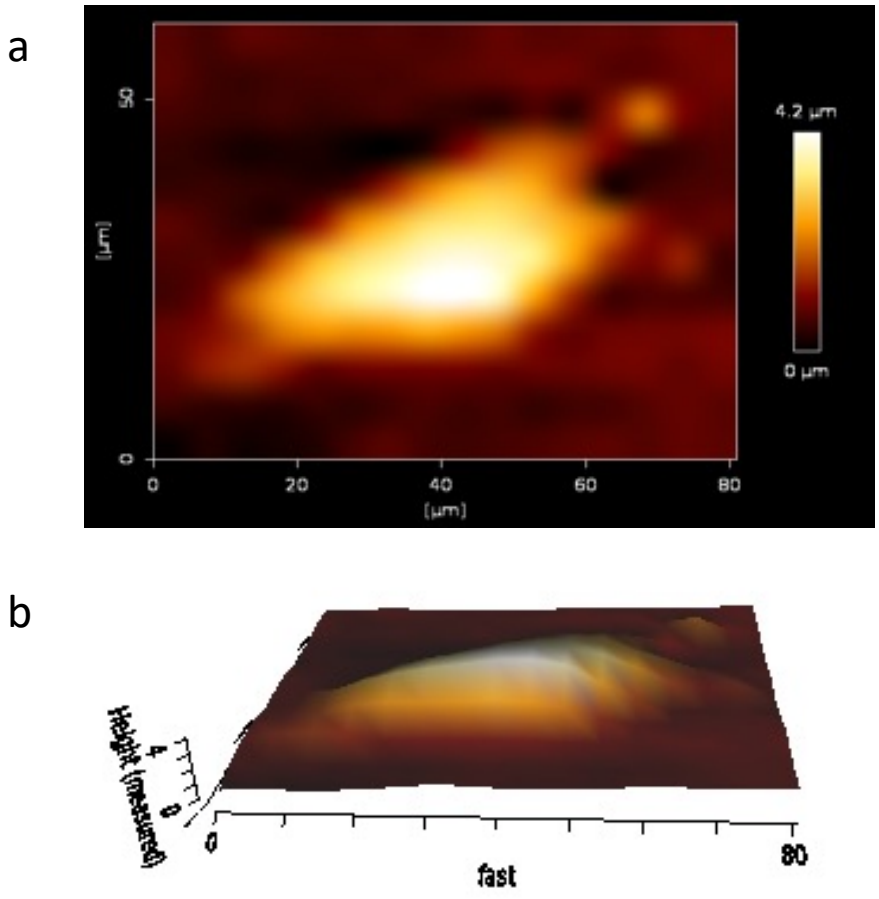

Figure 4.2 **Topographical height map of gRNA control cell**. (a) Map of cell height measured using a cantilever with 5μm bead. Measured with a setpoint of 3nN and a loading rate of 7μm/s. (b) 3D projection of the height map indicating the central nuclear region has the greatest height. Representative of 3 cells imaged.

From these measurements a map of Young's modulus across the whole cell was also generated (Figure *4.3*). The stiffest areas are at the cellular periphery as this is likely to include, in part, the stiffness of the underlying substrate (Figure *4.3*a). When the Young's moduli is thresholded to <12kPa and <6kPa the main body of the cell is within this range, with the nucleus being the softest region and the stiffness increasing moving further towards the cell periphery (Figure *4.3*b,c).

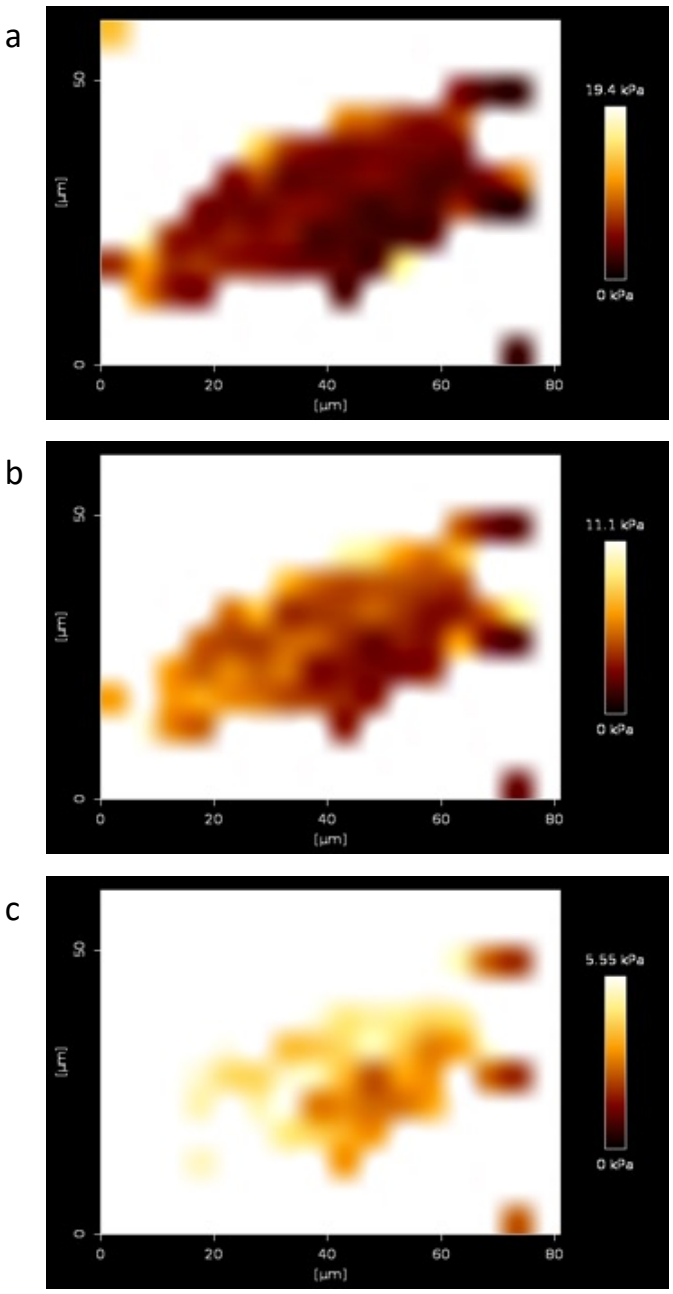

Figure 4.3 **Modulus maps of a gRNA control cell**. Modulus map of an entire cell measured using a cantilever with a 5µm bead. Measured with a setpoint of 3nN and a loading rate of 7µm/s. Force map thresholded at (a) 19.4kPa, (b) 11.1kPa and (c) 5.55kPa. Representative of 3 cells imaged.

4.2.3 Investigating the mechanical properties of asynchronous populations of control and *DAG1* KO cells

Following cell seeding the cells were incubated at 37°C for at least 24 hours to ensure secure attachment to the plastic petri dish. Measurements were taken in cell growth media at 37°C to keep the cells as close to physiological conditions as possible. Each cell was identified using the optical microscope associated with the AFM and 10 measurements were taken either directly above the centre of the nucleus or away from the nucleus to measure the cytoplasmic stiffness (Figure *4.4*a). The measurements produce a force-indentation curve (Figure *4.4*b) from which the Young's modulus can be calculated following the fitting of the Hertz model. To determine whether taking the average of 10 measurements resulted in a change in stiffness between the first and final measurements the *E* was determined following one approach and retraction cycle of the cantilever and then again using the 50th approach and retraction cycle (Figure *4.4*c). The first measurement was normalised to 1 and the 50th measurement was normalised accordingly with no significant difference between the value determined after 1 cycle and the value determined after the 50th cycle which confirms the stability of the *E* after 10 measurements. Additionally, the extent to which the nuclear stiffness was affected by cell contacts was also determined. In order to test this, control cells that were either isolated from all other cells or in contact with at least one other cell, were measured (Figure *4.4*d). The average *E* for cells with no contacts and those with contacts did not differ significantly. This data indicates it is not essential to only measure cells that are isolated from contact.

In the case of the nuclear measurements, the average Young's modulus of asynchronous control cells was slightly lower than that of all the KO clones (Figure *4.5*). However, none of these differences were statistically significant as determined by a one-way ANOVA test. The fact that the Young's modulus of all three *DAG1* clones were not significantly different from the control indicates β-DG, and DG more broadly, does not influence the nuclear stiffness of an asynchronous population of human myoblast cells.

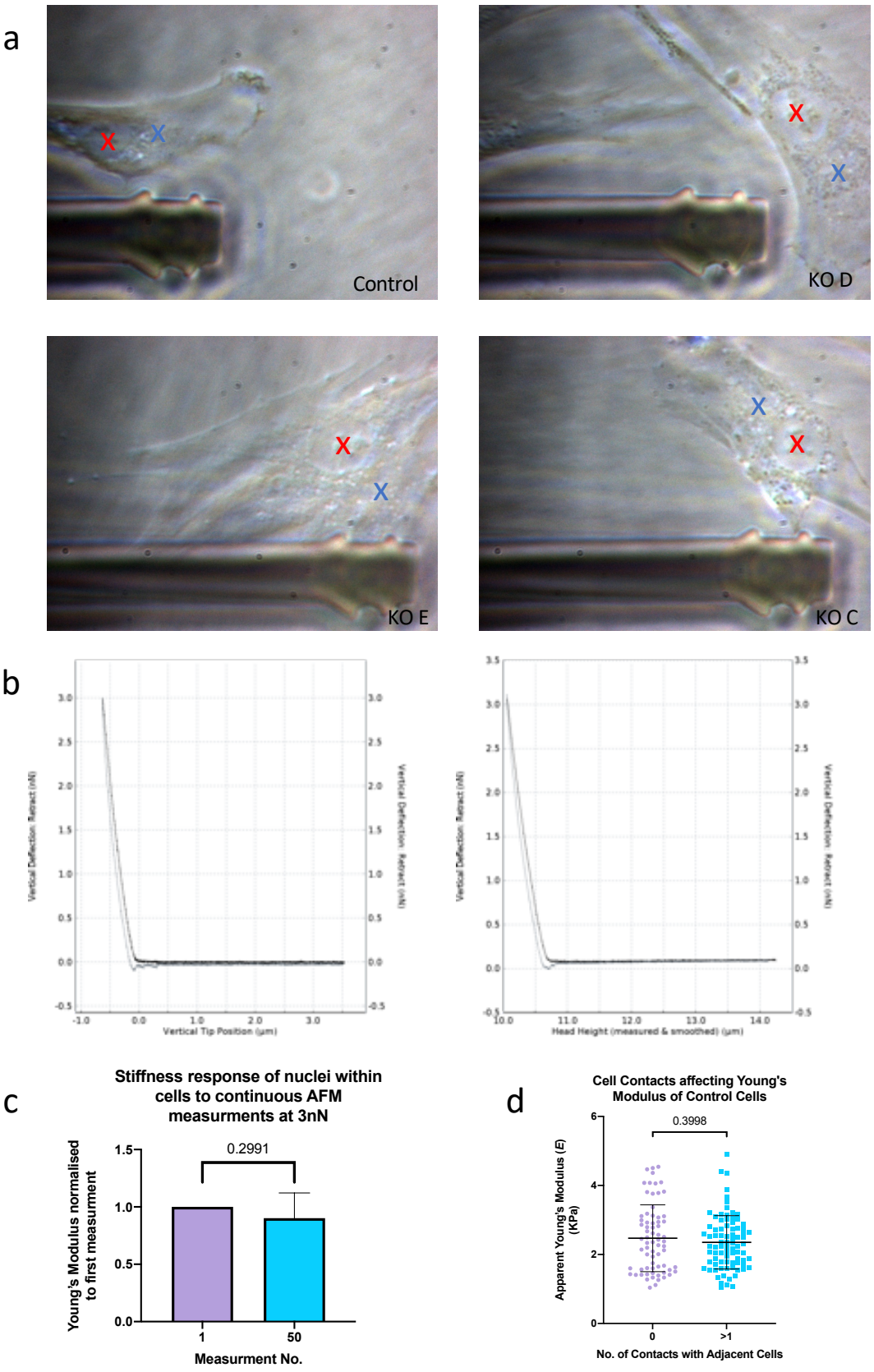

Figure 4.4 **Measurements of whole cells using AFM**. (a) Example brightfield images demonstrating the optical view using the AFM. In each image the cantilever is at the bottom. The nuclear regions measured are indicated with red crosses and cytoplasmic regions are indicated with blue crosses. (b) Example indentation curves of

control cells, the black curve indicates the approach while the grey curve indicates the retract. (c) Nuclear stiffness of gRNA control cells measured using the first measurement and the 50th measurement with each value for the 50th measurement being normalized to the first measurement. n = 6, no significant difference using students t-test, p = 0.2991. (d) Nuclear stiffness of gRNA control cells either in contact or isolated from other cells. 0 contacts n = 70, >1 contact n = 83, no significant difference using students t-test, p = 0.3998.

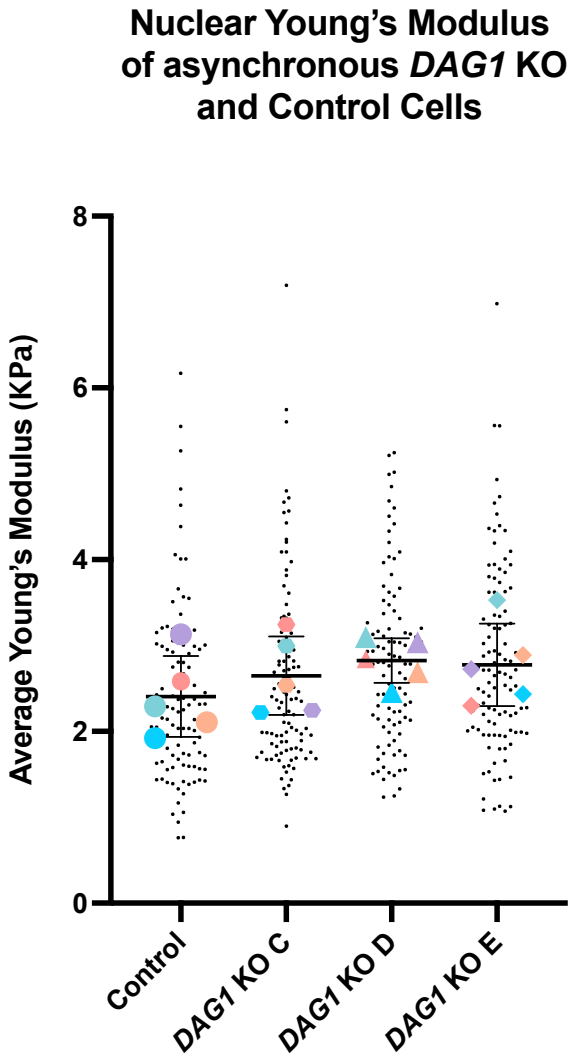

Cell Line	Average	SD	P value compared with control	Significance
Control	2.4068	0.4726	N/A	N/A
DAG1 KO C	2.6484	0.4565	0.7672	ns
DAG1 KO D	2.8256	0.2605	0.3661	ns
DAG1 KO E	2.7752	0.4812	0.4724	ns

Figure 4.5 **No difference in average nuclear Young's modulus between control and DAG1 KO cell lines in asynchronous populations**. Nuclei were measured using a functionalised cantilever. Small black points indicate values from individual cells while larger coloured points indicate the average for each independent experiment. 5 independent experiments were carried out with 125 nuclei measured per sample. Graph shows mean and standard deviation. A significant difference was not found between any of the samples as determined by one-way ANOVA test p = 0.4372. p values for multiple comparisons using Dunnett's multiple comparisons test are in the table.

Results from the measurements of the cytoplasmic regions of control and *DAG1* KO cells are similar to the nuclear region measurements. Control cells have an average cytoplasmic Young's modulus slightly lower than the *DAG1* KO cells (Figure *4.6*) but as observed with nuclear stiffness, the difference was not statistically significant. These data show that the perturbation of DG has no effect on the cytoplasmic stiffness in asynchronous myoblasts.

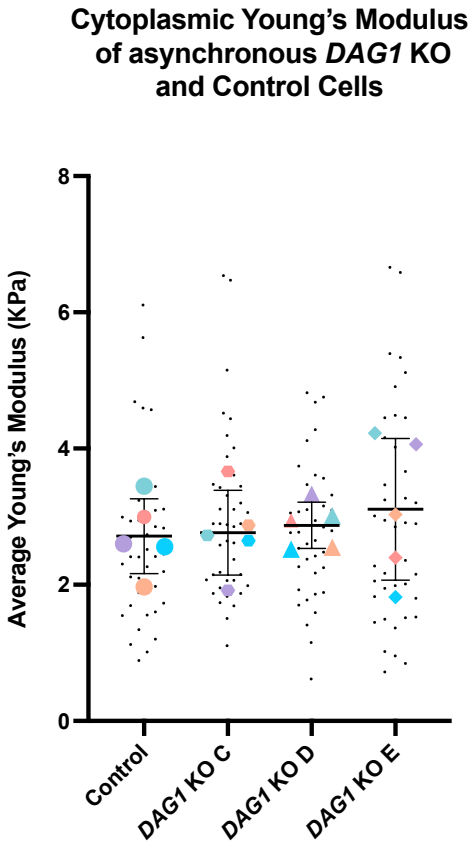

Cell Line	Average	SD	P value compared with control	Significance
Control	2.7134	0.5498	N/A	N/A
DAG1 KO C	2.7656	0.6224	0.9992	ns
DAG1 KO D	2.8728	0.3399	0.9777	ns
DAG1 KO E	3.1078	0.4812	0.759	ns

Figure 4.6 **No difference in average cytoplasmic Young's modulus between control and DAG1 KO cell lines in asynchronous populations**. Cells were measured using a functionalised cantilever. Small black points indicate values from individual cells while larger coloured points indicate the average for each independent experiment. 5 independent experiments were carried out with 125 cells measured per sample. Graph shows mean and standard deviation. A significant difference was not found between any of the samples as determined by one-way ANOVA test p = 0.8078. p values for multiple comparisons using Dunnett's multiple comparisons test are in the table.

The nuclear and cytoplasmic data was then combined to determine whether there is a difference between the nuclear stiffness and the cytoplasmic stiffness within each cell line (Figure *4.7*). Generally, the average cytoplasmic stiffness is greater than that of the nucleus but there is no statistically significant difference between these values. This is in agreement with previously reported data in human fibroblasts (Apte et al., 2017). Overall, these data indicate no difference between cytoplasmic or nuclear stiffness in asynchronous control or *DAG1* KO cells.

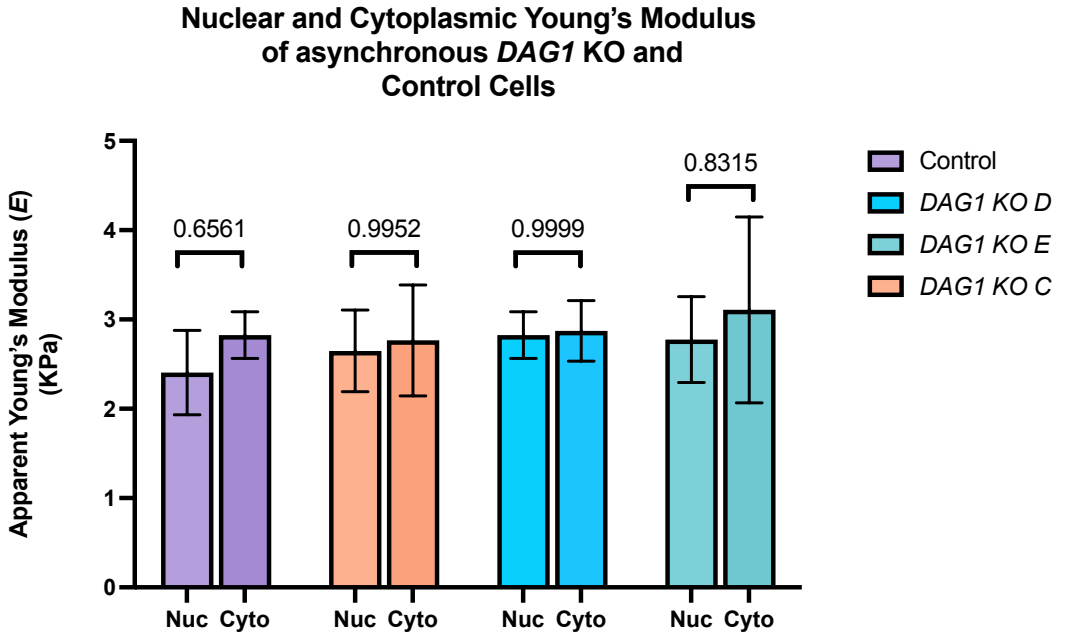

Figure 4.7 **Comparison between nuclear and cytoplasmic Young's modulus of asynchronous control and DAG1 KO cell lines.** This data is a combination of the data from figures 5 and 6. A significant difference was not found between any of the samples as determined by one-way ANOVA test p = 0.7009. p values for multiple comparisons using Šídák's multiple comparisons test are in the graph.

4.2.4 Investigating the mechanical properties of synchronised control and *DAG1* KO cells

As there appeared to be a slightly higher, although non-significant, average stiffness for both nucleus and cytoplasm in the *DAG1* KO cells compared with the control in an asynchronous population, the effect of synchronising the cells prior to AFM measurements was determined. Cell synchronisation was initially attempted using double thymidine block, however, this did not result in the synchronisation of control

cells (Figure *4.8*a). Cells were then synchronised using serum starvation which prevents progression from G1 phase of the cell cycle ensuring the population is almost entirely in G1 phase (Figure *4.8*b). Prior to serum starvation 63% of cells were in G1 phase, 15% in G2, and 22% in S phase while release from serum starvation resulted in >95% of cells being in G1 phase even 6 hours post-release (Figure *4.8*b).

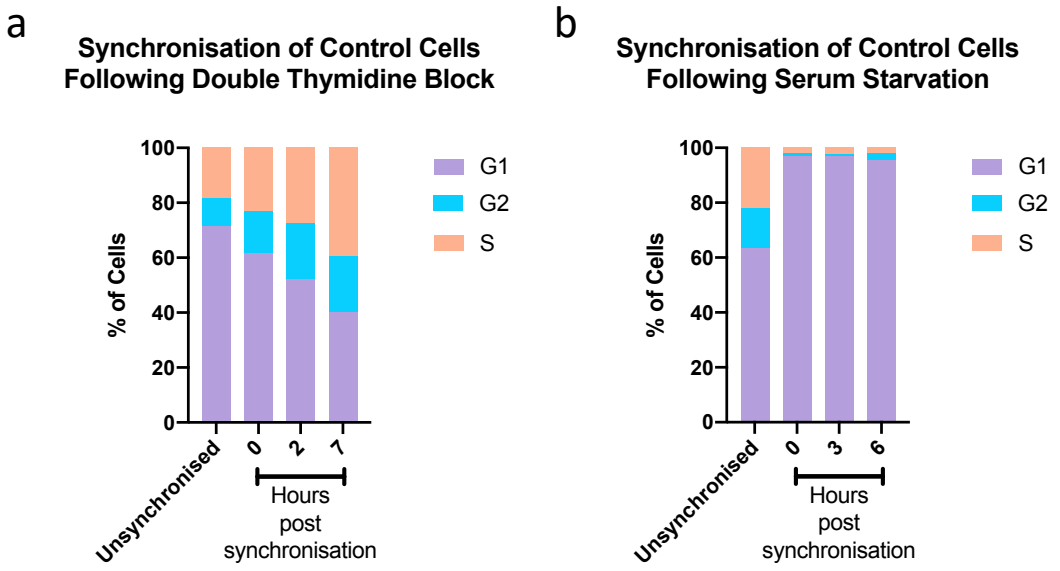

Figure 4.8 **Cell cycle synchronisation of control cells using double thymidine block and serum starvation.** (a) Synchronisation using double thymidine block did not result in cells synchronised in G1 phase as expected. (b) Synchronisation using serum starvation successfully synchronised cells in the G1 phase and >95% remained in G1 phase for the full 6 hours following release from serum starvation.

Following serum starvation cells were again measured either directly over the nucleus or adjacent to the nucleus to generate a measure of nuclear and cytoplasmic stiffness. Using the functionalised cantilever discussed in section 4.2.1, control cells and the *DAG1* KO clones A and B were measured. The results are similar to those observed in asynchronous cells whereby the KO clones had slightly stiffer nuclei compared with the controls (Figure *4.9*), however, only clone A is significantly stiffer with a p value of 0.0324.

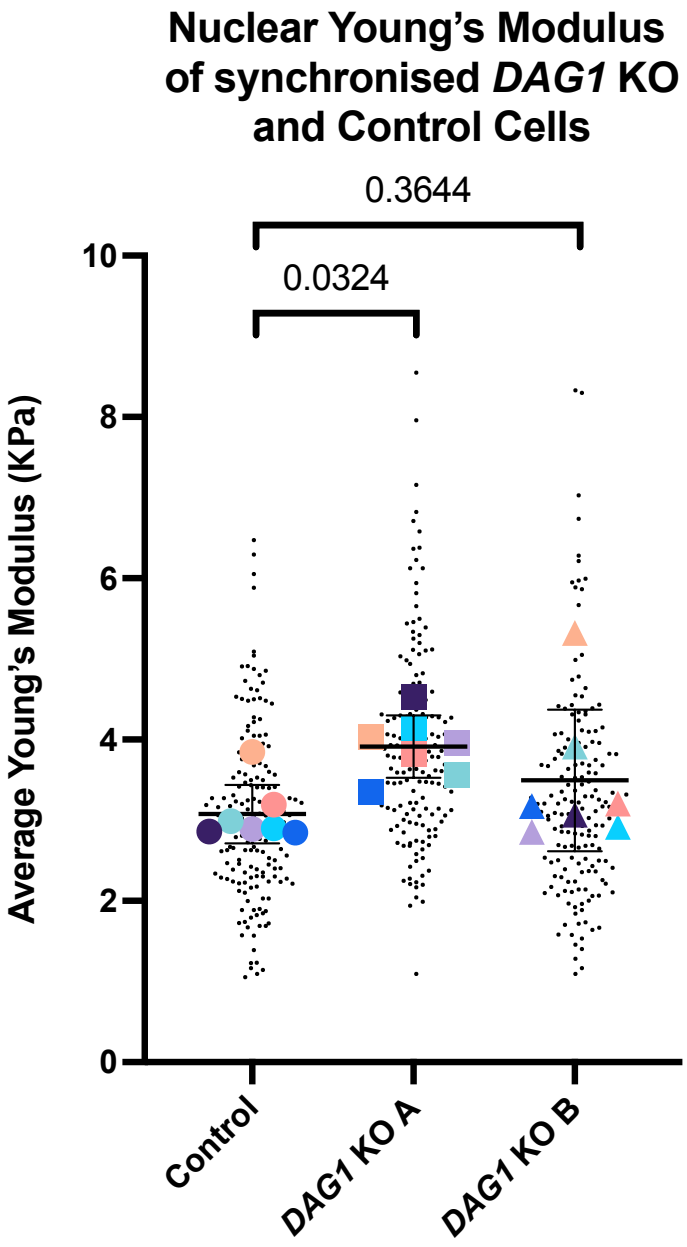

Figure 4.9 **Average nuclear Young's modulus of control and DAG1 KO cell lines in G1 synchronised populations using functionalised cantilevers**. Nuclei were measured using a functionalised cantilever. Small black points indicate values from individual cells while larger coloured points indicate the average for each independent experiment. 7 independent experiments were carried out with 181 nuclei measured per sample (except KO A where n = 173). Graph shows mean and standard deviation. A significant difference was not found between any of the samples as determined by one-way ANOVA test p = 0.0517. p values for multiple comparisons using Dunnett's multiple comparisons test are in the graph, this suggests the difference between control and DAG1 KO clone A is significantly different but not the difference between control and clone B.

Given that only one of the two *DAG1* KO clones was significantly stiffer than the control further validation was required in order to understand if it is a genuine phenotype of knocking out *DAG1*. To this end a commercial cantilever with a rounded tip (Figure *4.10*;inset) was used to repeat the measurements on all *DAG1* KO clones.

The measurements obtained with this cantilever are more reliable than the functionalised ones as it is possible to be certain prior to measurements that the probe is located at the centre of the cantilever allowing precise orientation of the probe directly above the nucleus. The resultant stiffness of the nuclear regions of all KO clones does not maintain the slightly stiffer phenotype observed using the functionalised cantilever. The resultant nuclear stiffness of control cells is lower than that determined using the functionalised cantilevers. The *DAG1* KO clones also had lower average Young's moduli compared with the functionalised cantilever (Figure *4.10*). None of the average moduli for *DAG1* KO clones are significantly different from the average of the control cells which confirms the conclusion that perturbing DG does not affect the nuclear mechanical properties of G1 synchronised myoblasts.

In addition to the nuclear mechanical properties of G1 synchronised myoblasts the cytoplasmic mechanical properties were also investigated. When using the functionalised cantilever the average modulus of clone A is slightly higher than the control while clone B is slightly lower than the control however, neither of these are significantly different from the control (Figure *4.11*). This was also confirmed using all available *DAG1* KO clones and using the commercial cantilever (Figure *4.12*). Only the difference between the control and *DAG1* KO clone B was significant but given the evidence from the functionalised cantilever experiment this is very likely to be an artefactual outlier. These data strongly suggests that disruption of the *DAG1* gene does not significantly influence the mechanical properties of the cytoplasm in myoblasts.

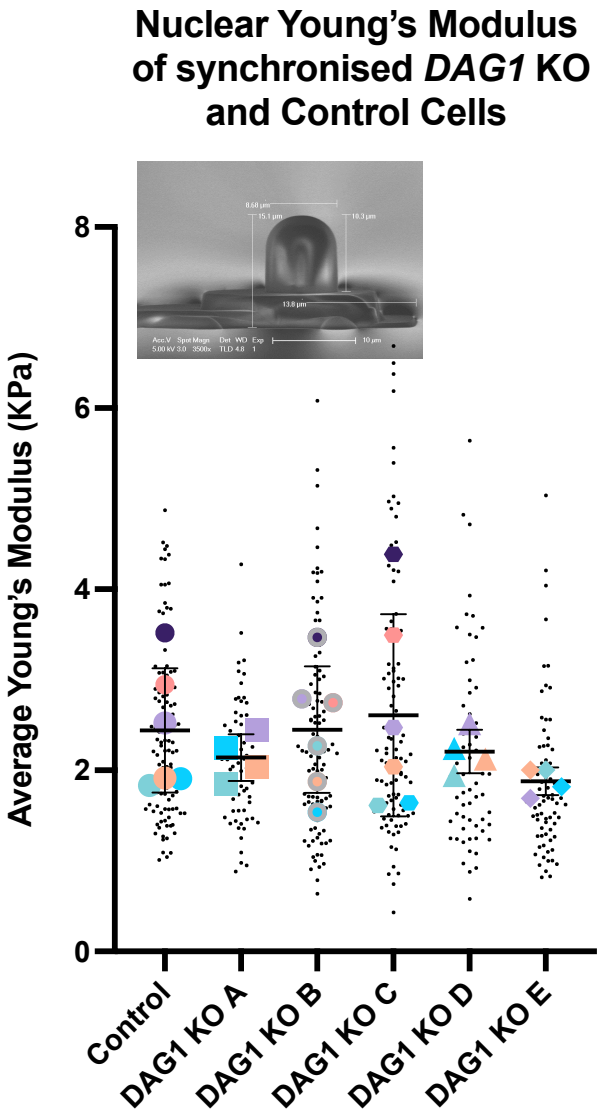

Cell Line	Average	SD	P value compared with control	Significance
Control	2.440	0.686	N/A	N/A
DAG1 KO A	2.141	0.257	0.9715	ns
DAG1 KO B	2.449	0.699	>0.9999	ns
DAG1 KO C	2.608	1.115	0.9965	ns
DAG1 KO D	2.207	0.240	0.9905	ns
DAG1 KO E	1.879	0.153	0.7127	ns

Figure 4.10 **Average nuclear Young's modulus of control and DAG1 KO cell lines in G1 synchronised populations using commercial cantilevers**. Nuclei were measured using a commercial cantilever (inset). Small black points indicate values from individual cells while larger coloured points indicate the average for each independent experiment. 6 independent experiments were carried out with 90 individual nuclei measured per sample. Graph shows mean and standard deviation. A significant difference was not found between any of the samples as determined by one-way ANOVA test p = 0.6389. p values for multiple comparisons using Dunnett's multiple comparisons test are in the table.

The nuclear and cytoplasmic data were combined, as previously, to determine the relationship between the nuclear and cytoplasmic stiffness within each cell line. As seen with unsynchronised cells the average cytoplasmic stiffness of synchronised cells is greater than that of the nucleus but not significantly so in most cases. In the case of the control, KO A and KO B cell lines measured with the functionalised cantilever the difference between the nuclear and cytoplasmic stiffness is significantly different in the control and *DAG1* KO A cells (Figure *4.13*). However, when we use the commercial cantilever there is no difference between the cytoplasmic and nuclear stiffness in control cells (Figure *4.14*). The only difference that is significant in this data set is between the nuclear and cytoplasmic stiffness of the *DAG1* KO B cell line. Taken together this data suggest that there is no real difference between the nuclear and cytoplasmic stiffness of control or KO cell lines following G1 phase cell synchronisation.

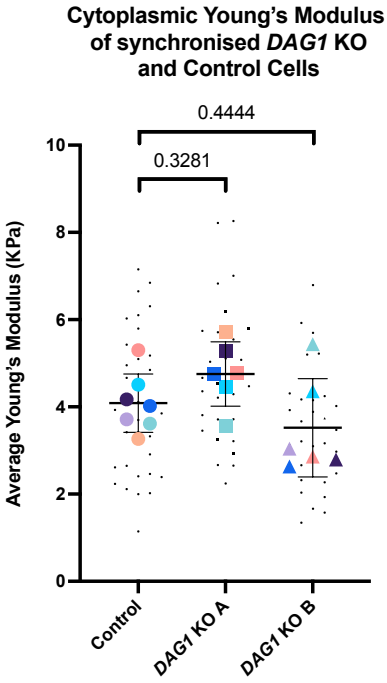

Figure 4.11 **Average cytoplasmic Young's modulus of control and DAG1 KO cell lines in G1 synchronised populations using functionalised cantilevers**. Cells were measured using a functionalised cantilever. Small black points indicate values from individual cells while larger coloured points indicate the average for each independent experiment. 7 independent experiments were carried out with 35 cells measured per sample. Graph shows mean and standard deviation. A significant difference was not found between any of the samples as determined by one-way ANOVA test p = 0.0725. p values for multiple comparisons using Dunnett's multiple comparisons test are in the graph.

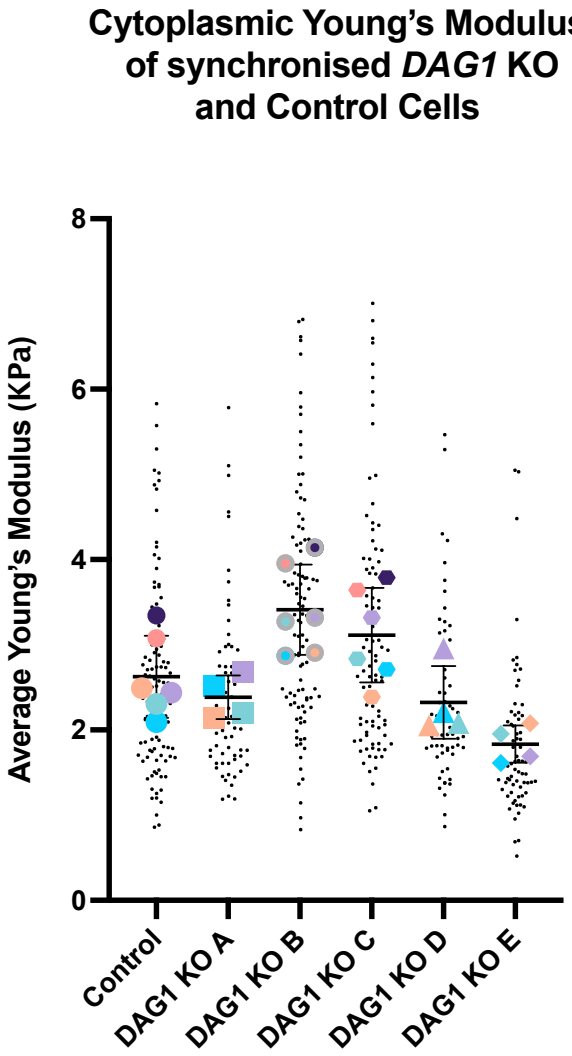

Cell Line	Average	SD	P value compared with control	Significance
Control	2.626	0.482	N/A	N/A
DAG1 KO A	2.384	0.256	0.934	ns
DAG1 KO B	3.411	0.529	0.0318	*
DAG1 KO C	3.114	0.555	0.3256	ns
DAG1 KO D	2.325	0.426	0.8509	ns
DAG1 KO E	1.834	0.219	0.0624	ns

Figure 4.12 **Average cytoplasmic Young's modulus of control and DAG1 KO cell lines in G1 synchronised populations using commercial cantilevers**. Cells were measured using commercial cantilevers. Small black points indicate values from individual cells while larger coloured points indicate the average for each independent experiment. 6 independent experiments were carried out with 90 individual cells measured per sample. Graph shows mean and standard deviation. A significant difference was found between the samples as determined by one-way ANOVA test p = 0.0002. p values for multiple comparisons using Dunnett's multiple comparisons test are in the table.

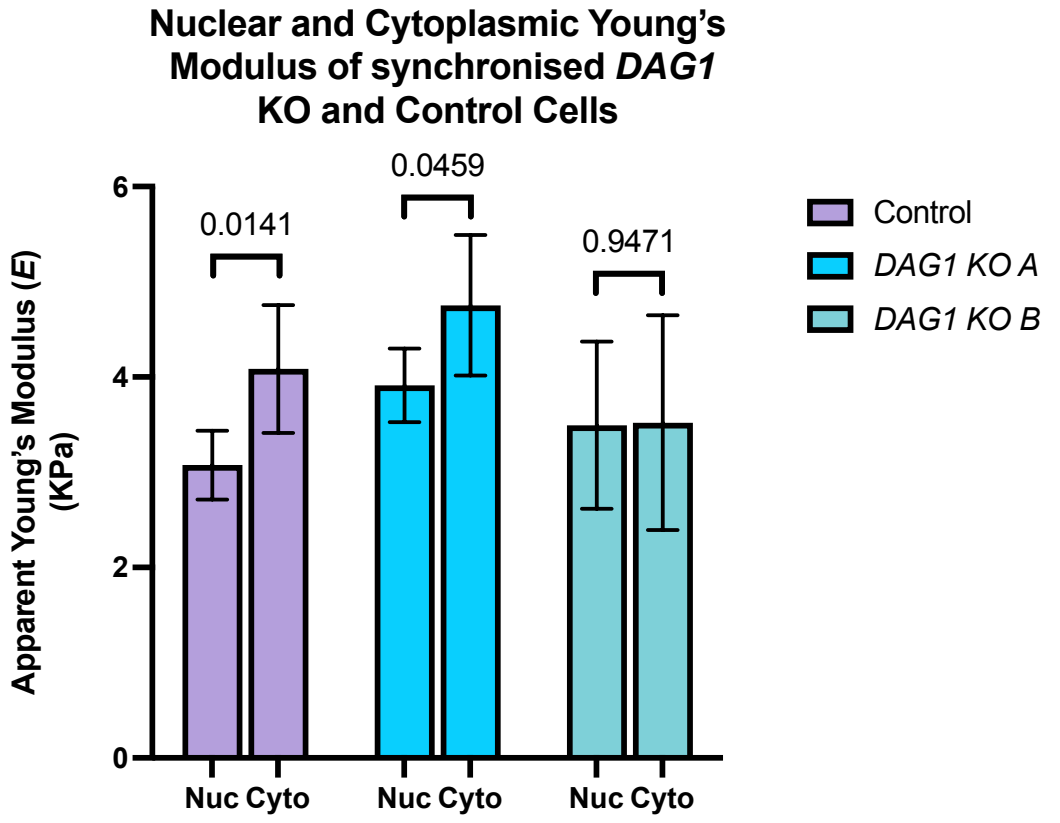

Figure 4.13 **Comparison between nuclear and cytoplasmic Young's modulus of G1 synchronised control and DAG1 KO cell lines measured with functionalised cantilevers.** This data is a combination of the data from figures 9 and 11. A significant difference was found between the samples as determined by one-way ANOVA test p = 0.0051. p values for multiple comparisons using Šídák's multiple comparisons test are in the graph.

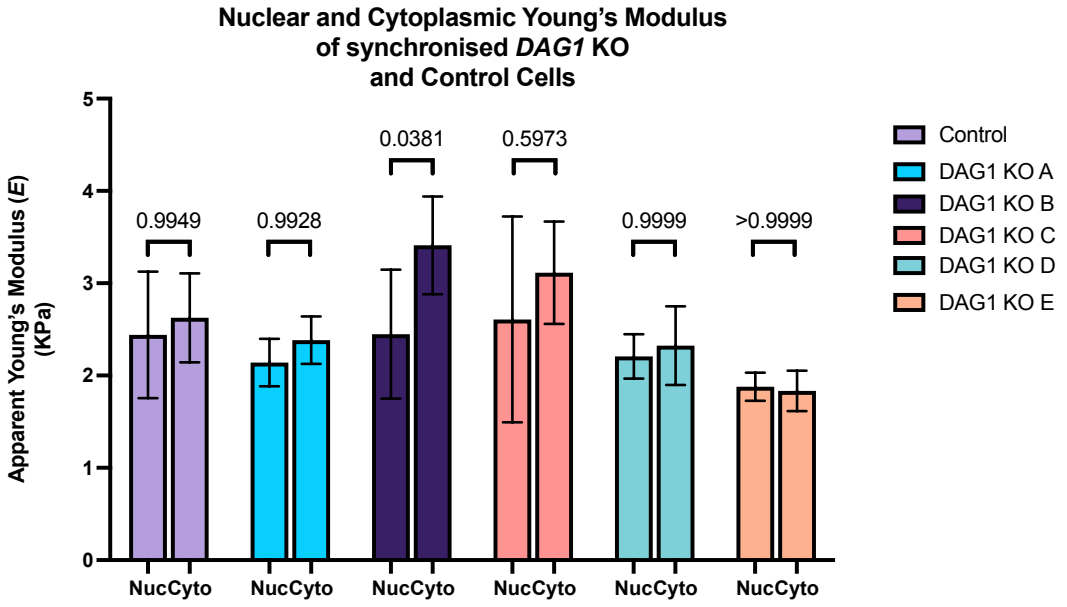

Figure 4.14 **Comparison between nuclear and cytoplasmic Young's modulus of G1 synchronised control and DAG1 KO cell lines measured with commercial cantilevers.** This data is a combination of the data from figures 10 and 12. A significant difference was found between the samples as determined by one-way ANOVA test p = 0.0030. p values for multiple comparisons using Šídák's multiple comparisons test are in the graph.

4.2.5 Investigating the mechanical properties of synchronised control and *DAG1* KO cells following trichostatin A treatment

TSA inhibits histone deacetylases, this results in an increase in DNA acetylation and ultimately a decondensing of the chromatin. The decondensed chromatin results in an increased nuclear size and a reduction in nuclear stiffness. Treating with TSA prior to AFM experiments provides information on the effects of condensed heterochromatin on the inherent mechanical properties of the nucleus. In order to determine the concentration to use for AFM experiments, TSA was added to control cells at concentrations ranging from 5nM to 300nM and incubated for 24 hours. The nuclei were then stained with DAPI and the nuclear size was determined (Figure *4.15*). The average nuclear area increases for all treatments with those at 100nM, 200nM and 300nM being significantly greater than the DMSO treated controls. Based on this, 300nM TSA was used for subsequent AFM experiments.

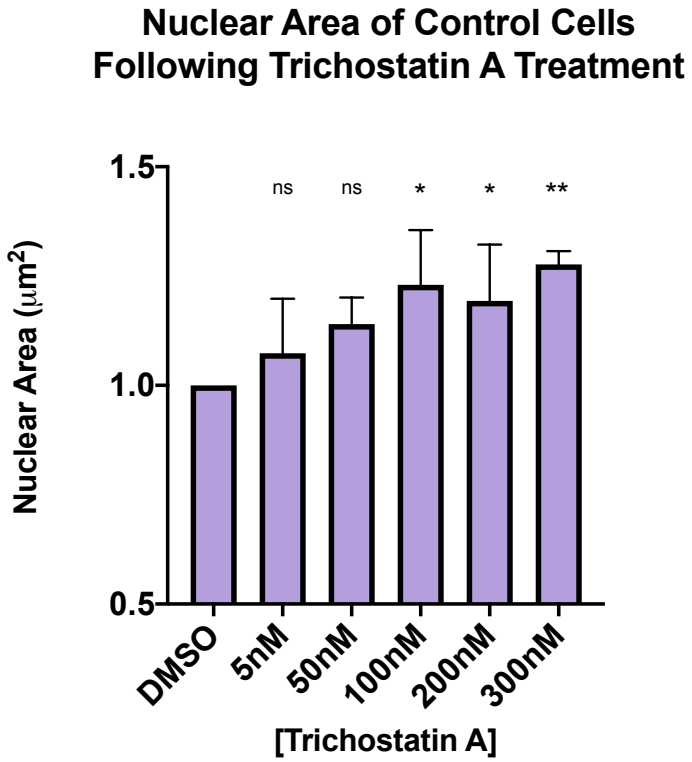

Figure 4.15 **Treatment with Trichostatin A results in an increase in nuclear area**. Nuclear area for each treatment was normalised to the DMSO treated control. n = 3 independent experiments measuring 77 DMSO, 75 5nM, 83 50nM, 74 100nM, 79 200nM and 83 300nM treated cells. A significant difference was found between the samples as determined by one-way ANOVA test p = 0.0315. p values for multiple comparisons using Dunnett's multiple comparisons test * = <0.0332, ** = <0.0021.

DAG1 KO clones A and B were used as representatives for the KO cell lines and compared with control cells. The measurements were carried out using the functionalised cantilevers. As with untreated cells there is no difference in the nuclear stiffness of control and KO cell lines (Figure *4.16*). This suggests TSA treatment does not affect the mechanical properties of control and *DAG1* KO cells differently. However, when we look at the nuclear stiffness of untreated and TSA treated cells there is a clear and significant decrease in the TSA treated cells as expected (Figure *4.17*). Again, when the nuclear and cytoplasmic stiffness of the three cell lines were compared the cytoplasmic average stiffness is slightly greater than the nuclear average stiffness, this difference is not significant for control or *DAG1* KO A cells but the difference between nuclear and cytoplasmic stiffness in *DAG1* KO B cells is statistically significant (Figure *4.18*).

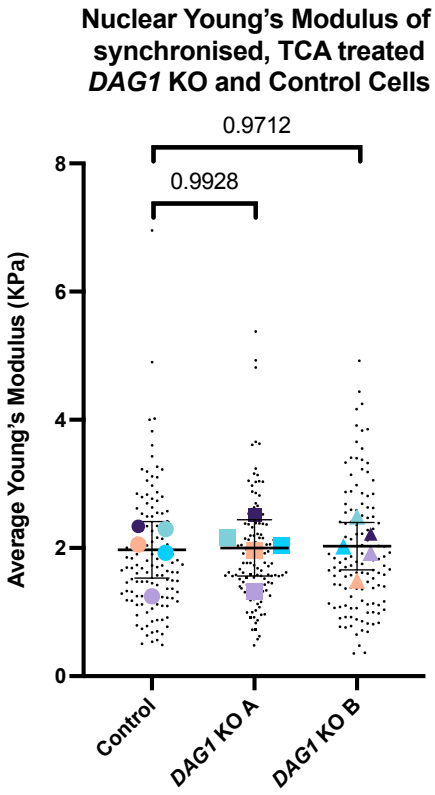

Figure 4.16 **Average nuclear Young's modulus of control and DAG1 KO cell lines following 300nM Trichostatin A treatment using functionalised cantilevers**. Nuclei were measured using a functionalised cantilever. Small black points indicate values from individual cells while larger coloured points indicate the average for each independent experiment. 5 independent experiments were carried out with 100 individual nuclei measured per sample. Graph shows mean and standard deviation. A significant difference was not found between any of the

samples as determined by one-way ANOVA test p = 0.9764. p values for multiple comparisons using Dunnett's multiple comparisons test are in the graph.

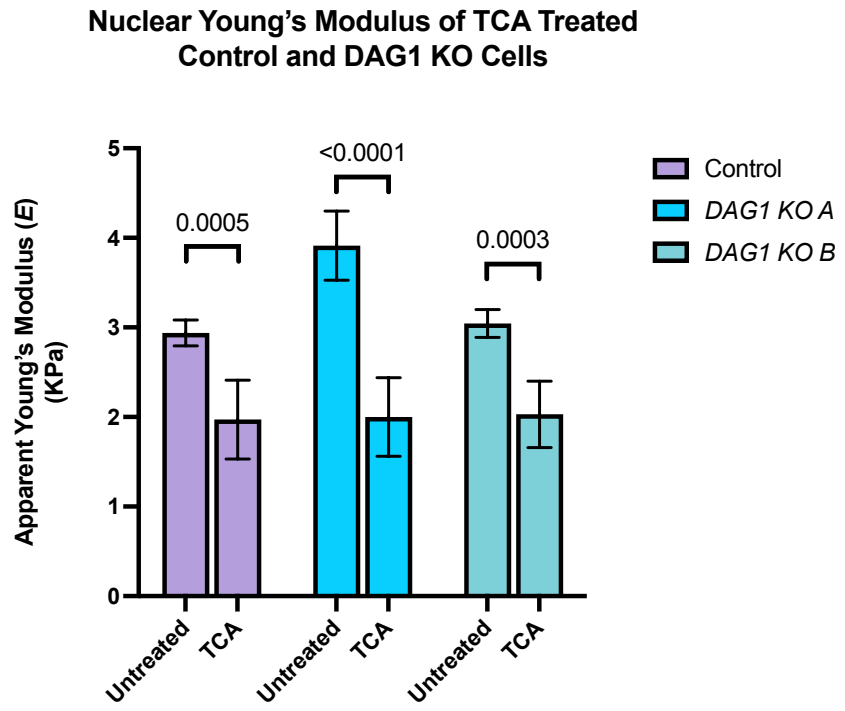

Figure 4.17 **Treatment of 300nM Trichostatin A for 24 hours results in a decrease in nuclear Young's modulus in control and DAG1 KO cell lines**. This data is a combination of the data from figures 9 and 16. A significant difference was found between the samples as determined by one-way ANOVA test p = <0.0001. p values for multiple comparisons using Šídák's multiple comparisons test are in the graph.

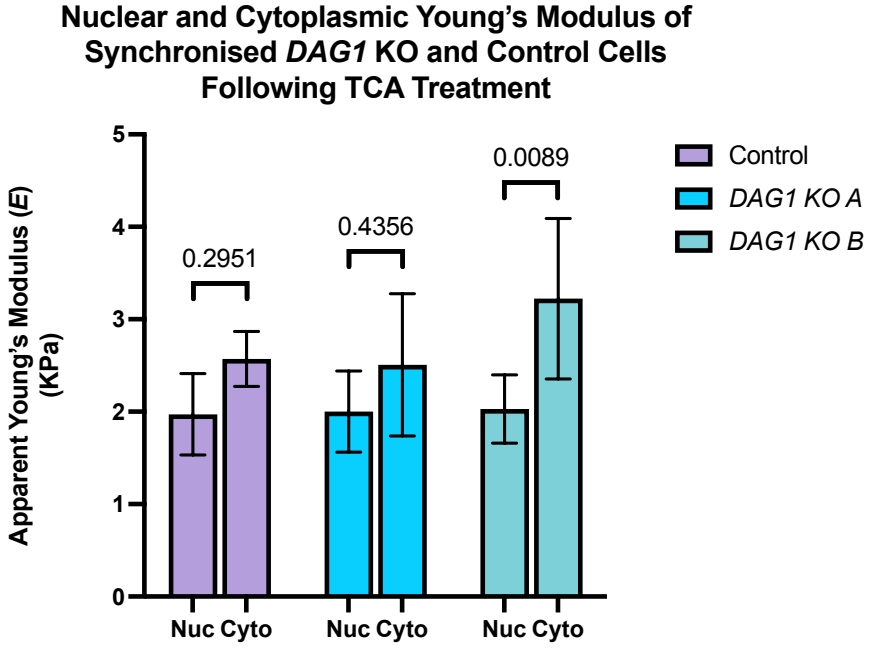

Figure 4.18 **Comparison between nuclear and cytoplasmic Young's modulus of control and DAG1 KO cell lines following 300nM Trichostatin A treatment using functionalised cantilevers**. A significant difference was found between the samples as determined by one-way ANOVA test p = 0.0132. p values for multiple comparisons using Šídák's multiple comparisons test are in the graph, only DAG1 KO B was significantly different.

4.2.6 Investigating the mechanical properties of synchronised control and *DAG1* KO cells following Cytochalasin D treatment

CytoD is used to perturb the actin cytoskeleton, it prevents association and dissociation of actin monomers from the actin filament. Disrupting the actin cytoskeleton prior to AFM measurements enables the determination of the nuclear stiffness without the contribution of the actin cytoskeleton. A range of concentrations of CytoD were tested from 50nM to 1000nM and cells were incubated for 24 hours. Cells were then stained with phalloidin to determine the extent of actin perturbation (Figure *4.19*). The actin cable staining was lost following all CytoD treatments and the phalloidin staining became more diffuse as the concentration of CytoD increased. At 1000nM the phalloidin staining is very diffuse but this concentration was not used as almost all cells had multiple nuclei, at 500nM only a few cells had multiple nuclei and there was no evidence of actin cables, this concentration was used for subsequent AFM experiments.

As with TSA treatment, the CytoD experiments used *DAG1* KO clones A and B as representative and were compared with the control cells. Measurements were carried out using the functionalised cantilever. Following CytoD treatment there is no statistically significant difference in the Young's modulus of *DAG1* KO nuclei compared with the controls (Figure *4.20*). Similarly, when the cytoplasmic region of CytoD treated cells were measured, there was no statistically significant difference between the Young's modulus of control and *DAG1* KO cells (Figure *4.21*). As expected, both the nuclear and cytoplasmic stiffness decreased significantly following CytoD treatment for both control and *DAG1* KO clones (Figure *4.22*). Additionally, the actin cytoskeleton perturbation does not affect the relationship between nuclear and cytoplasmic stiffness (Figure *4.23*). In control and *DAG1* KO cell lines the cytoplasmic stiffness is slightly greater than the nuclear stiffness but not significantly so, as seen for all other treatment conditions. Overall, this data suggests that cells lacking *DAG1* do not have a significant change in nuclear or cytoplasmic stiffness following actin cytoskeleton perturbation compared with control cells.

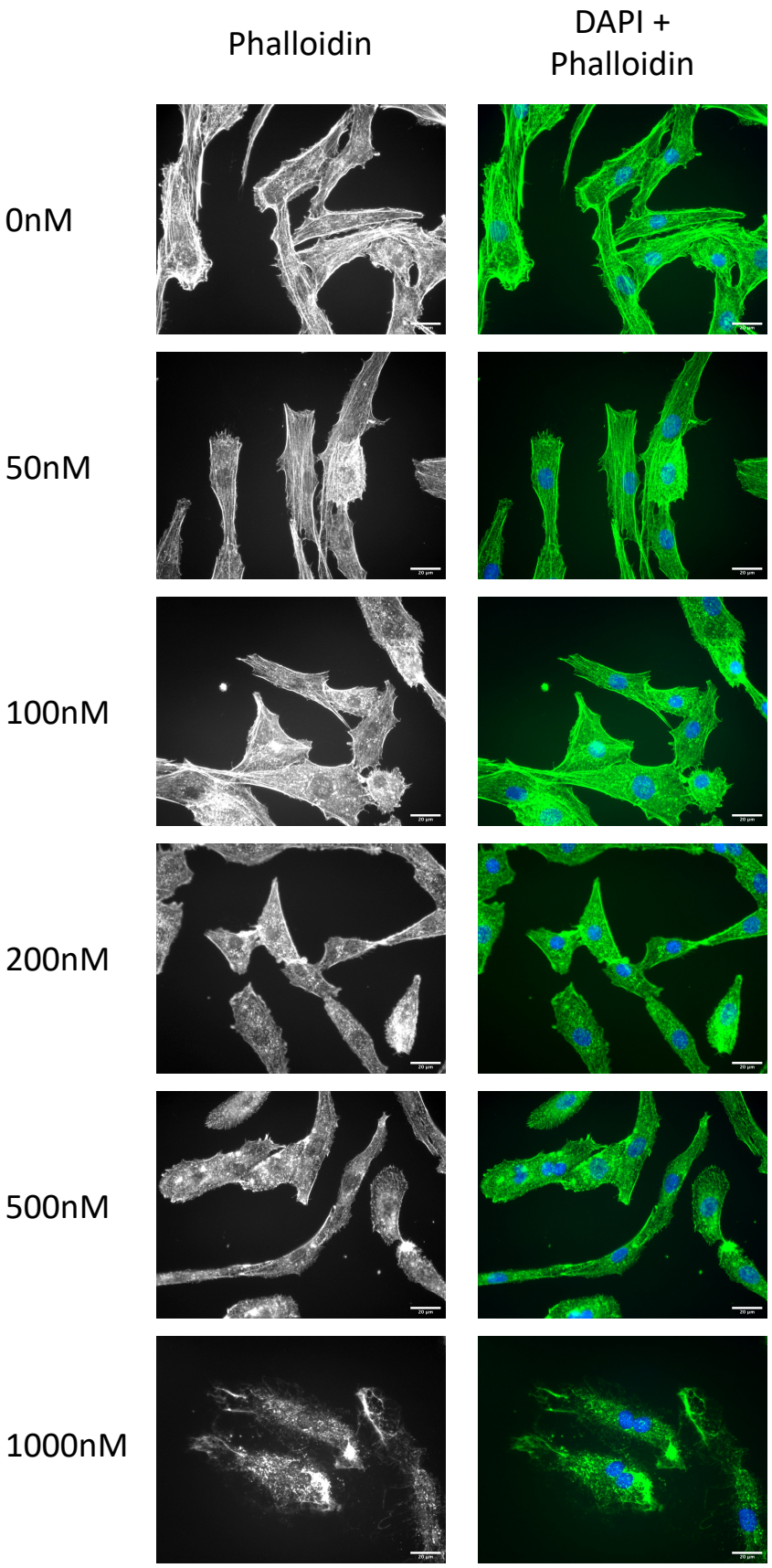

Figure 4.19 **Treatment with varying concentrations of cytochalasin D result in perturbation of actin filaments**. Control cells stained with DAPI to identify the nucleus, and phalloidin was used to determine the amount of

filamentous actin. Representative images of each CytoD concentration taken from 3 independent experiments. Scale bar = 20μm.

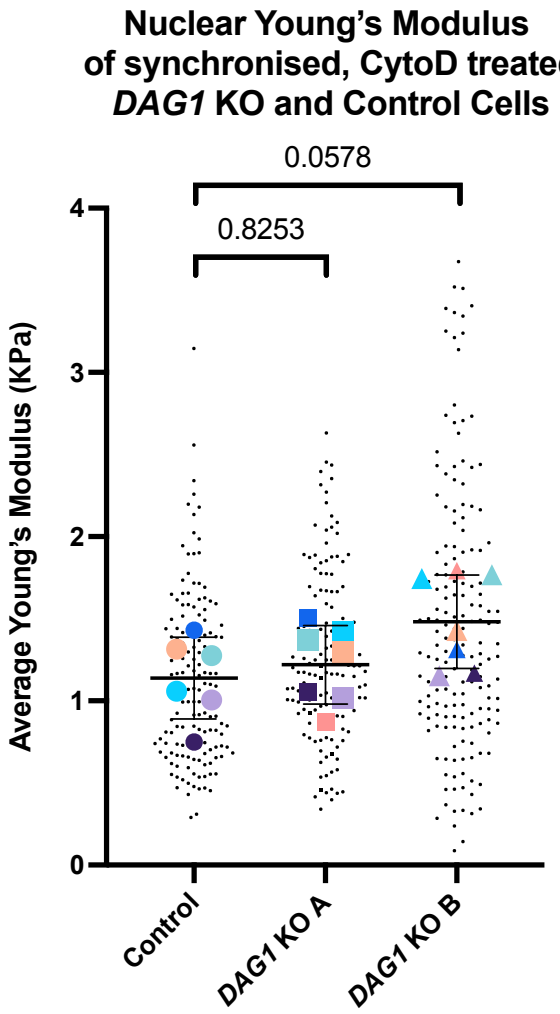

Figure 4.20 **Average nuclear Young's modulus of control and DAG1 KO cell lines following 500nM cytochalasin D treatment using functionalised cantilevers**. Nuclei were measured using a functionalised cantilever. Small black points indicate values from individual cells while larger coloured points indicate the average for each independent experiment. 7 independent experiments were carried out with 140 individual cells measured per sample (except KO A where n = 138). Graph shows mean and standard deviation. A significant difference was not found between any of the samples as determined by one-way ANOVA test p = 0.0663. p values for multiple comparisons using Dunnett's multiple comparisons test are in the graph.

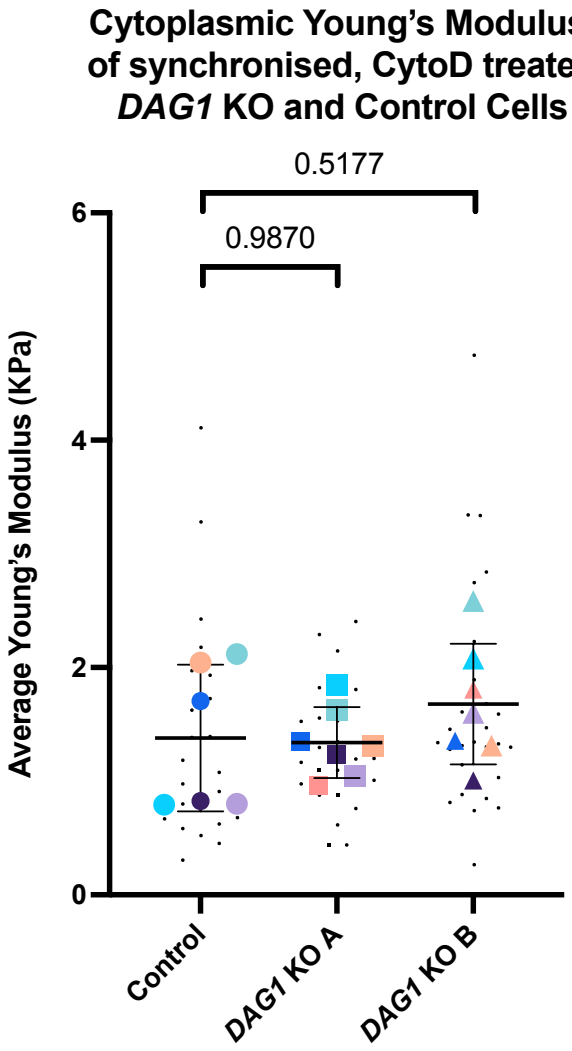

Figure 4.21 **Average cytoplasmic Young's modulus of control and DAG1 KO cell lines following 500nM cytochalasin D treatment using functionalised cantilevers**. Cells were measured using a functionalised cantilever. Small black points indicate values from individual cells while larger coloured points indicate the average for each independent experiment. 7 independent experiments were carried out with 35 individual cells measured per sample. Graph shows mean and standard deviation. A significant difference was not found between any of the samples as determined by one-way ANOVA test p = 0.4184. p values for multiple comparisons using Dunnett's multiple comparisons test are in the graph.

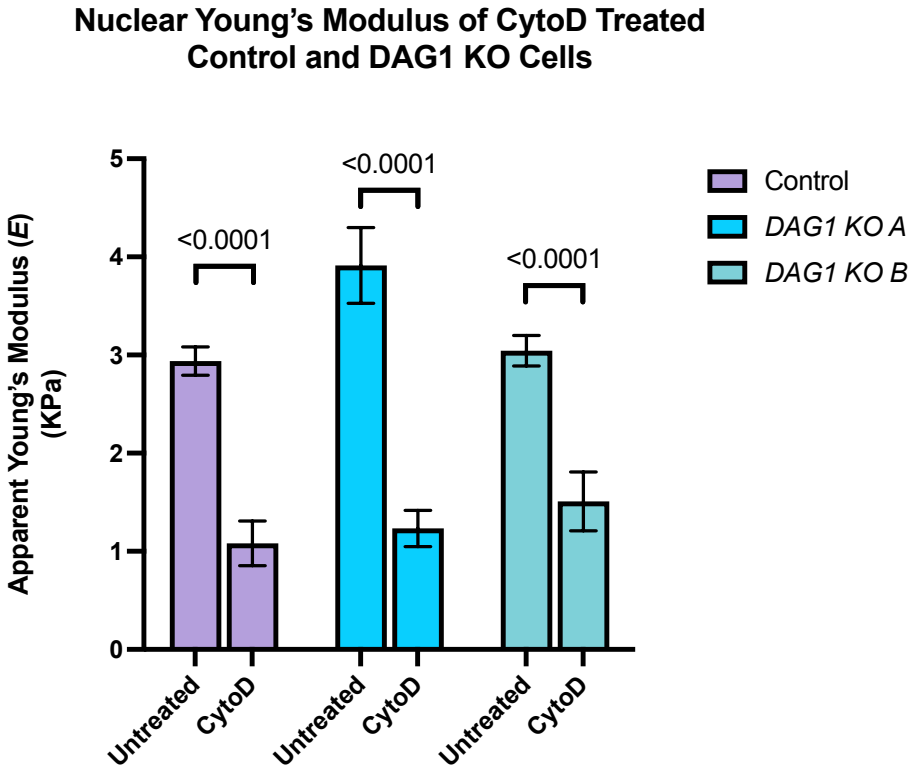

b

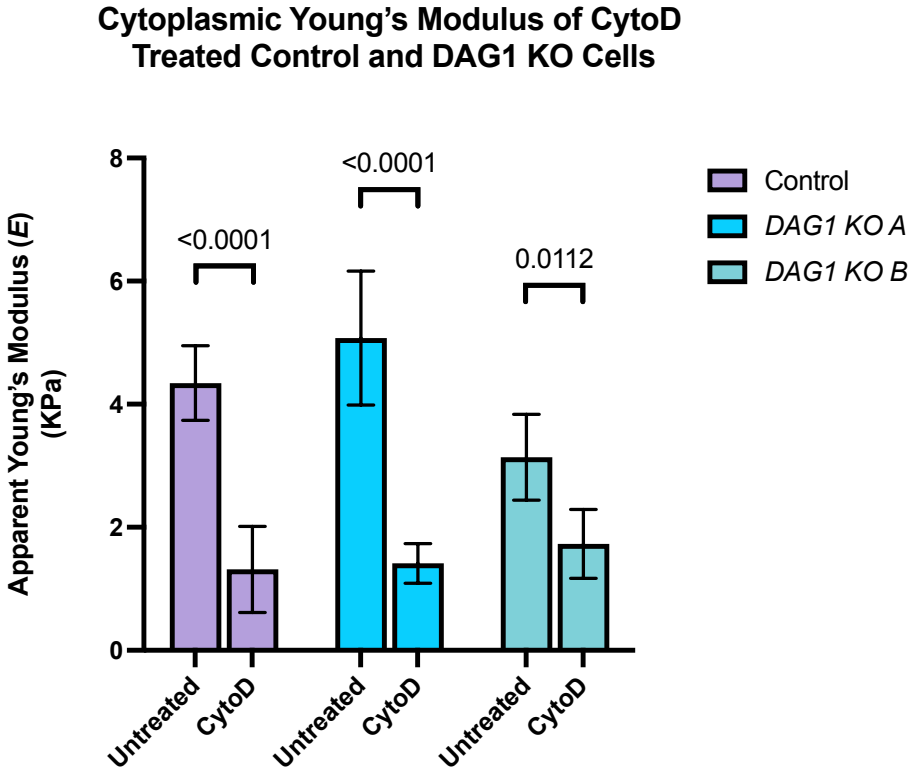

Figure 4.22 **Treatment with 500nM Cytochalasin D for 24 hours results in a decrease in nuclear and cytoplasmic Young's modulus in control and DAG1 KO cell lines**. (a) This data is a combination of the data from figures 9 and 20. A significant difference was found between the samples as determined by one-way ANOVA test p = <0.0001. p values for multiple comparisons using Šídák's multiple comparisons test are in the graph. (b) This data is a combination of the data from figures 11 and 21. A significant difference was found between the samples as

determined by one-way ANOVA test p = <0.0001. p values for multiple comparisons using Šídák's multiple comparisons test are in the graph.

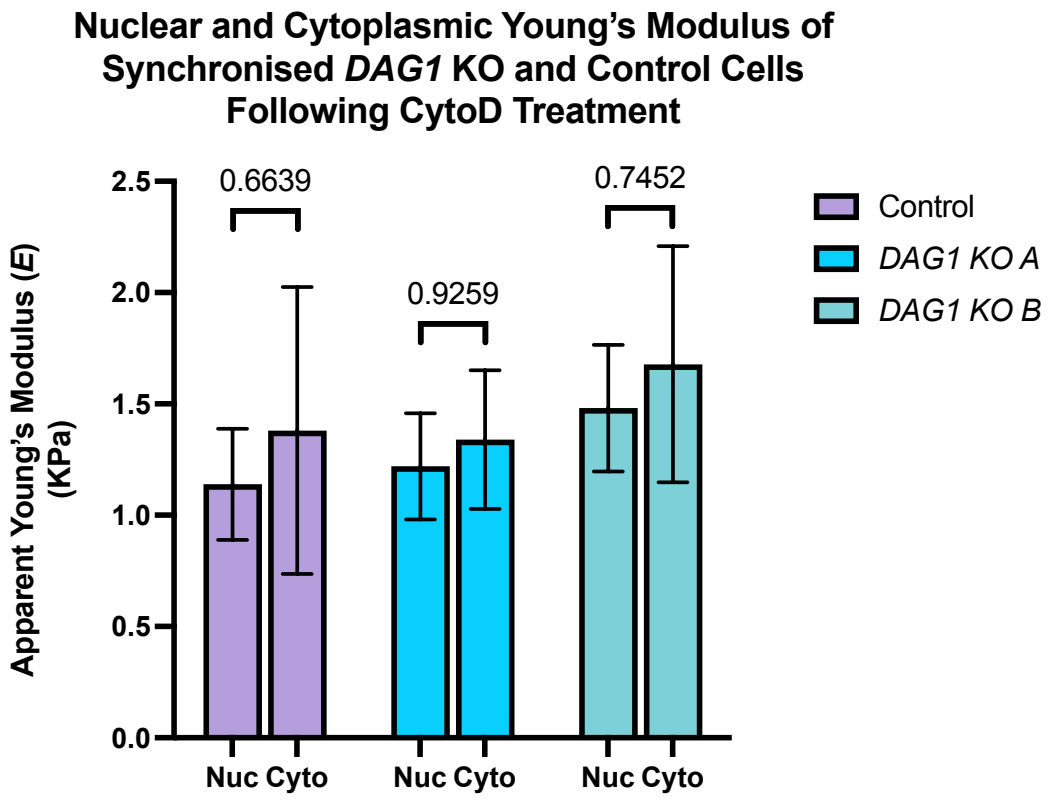

Figure 4.23 **Comparison between nuclear and cytoplasmic Young's modulus control and DAG1 KO cell lines following 500nM CytoD treatment using functionalised cantilevers**. A significant difference was not found between the samples as determined by one-way ANOVA test p = 0.2071. p values for multiple comparisons using Šídák's multiple comparisons test are in the graph.

4.2.7 Investigating the relationship between nuclear area and nuclear stiffness in control and *DAG1* KO cells

Given that almost all of the *DAG1* KO cell lines have larger nuclei than the control cells (see section 3.2.4) it was useful to determine whether there was any correlation between nuclear area and the Young's modulus of nuclei. The limitations associated with the optical microscope connected with the AFM means that the measurements of nuclear area are not as precise as those in chapter 3. However, all nuclei were measured in the same way so absolute values may not be accurate, but the values are all relative to each other making them valid for the investigation.

When nuclear area is plotted against nuclear Young's modulus of control cells there is no correlation between the two variables (Figure *4.24*). The correlation coefficient, r, is negative, with a value of -0.092 and an r^2 value of 0.00848. An r and r^2 value this small would be indicative of a very weak correlation if there is any correlation at all. However, the p value is 0.2577 meaning this weak correlation is not statistically significant and it can only be concluded that there is no correlation between nuclear area and nuclear Young's modulus in control cells.

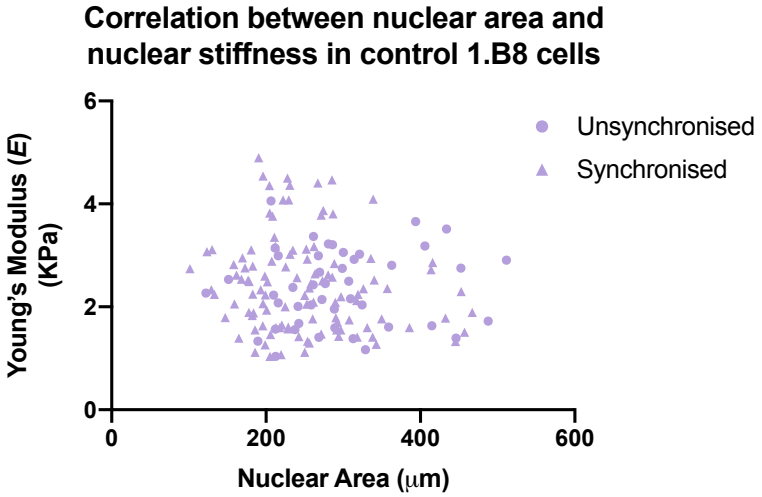

Figure 4.24 **There is no correlation between nuclear size and nuclear Young's modulus in control cells**. Data from control cells using a commercial cantilever was pooled to determine any correlation between nuclear area and nuclear stiffness. n = 153, Pearson correlation r = -0.09206, r^2 = 0.008475, p value = 0.2577.

The range of the nuclear area in control cells is smaller than the range observed in the *DAG1* KO cells – there are some *DAG1* KO nuclei much larger than any seen in control cells. Based on this a correlation between nuclear area and nuclear Young's modulus was carried out for all cell types combined (Figure *4.25*). These data suggest a slight positive correlation with an r value of 0.086 and an r^2 value of 0.00742. The p value for this correlation is 0.0236 indicating the slight positive correlation is statistically significant. However, given that the correlation coefficient is so small it is unlikely that this has any biological significance. Taken together these data would suggest there is no compelling evidence for a biologically relevent correlation between the nuclear area and nuclear Young's modulus in human myoblast cell lines.

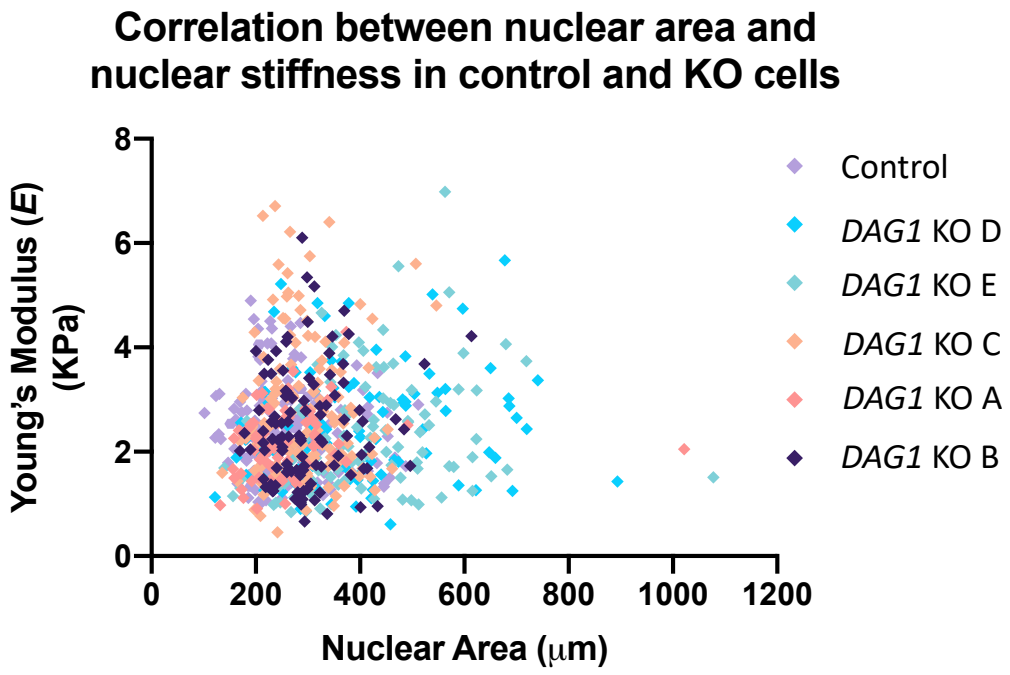

Figure 4.25 **There is no correlation between nuclear size and nuclear Young's modulus in control and DAG1 KO cells**. Data from all cells (control and DAG1 KO) using a commercial cantilever was pooled to determine any correlation between nuclear area and nuclear stiffness. n = 691, Pearson correlation r = -0.08612, r^2 = 0.007416, p value = 0.0236.

4.2.8 Optimisation of nuclear isolation in order to measure mechanical properties of isolated nuclei

In order to interrogate the mechanical properties of just the nuclei they need to be separated from all cytoplasmic and cytoskeletal contributions. A range of protocols were initially tested to determine a reliable and consistent method of producing isolated nuclei. Each of the protocols tested used slightly different methods. The first method relied on the use of a high salt buffer to osmotically lyse the cell membrane but leave the nuclear membrane intact (Ferrera et al., 2014). Following this method some lysis occurred but there was still membrane and cytoplasm associated with the nuclei (Figure *4.26*a). The second method involved the mechanical rupture of the plasma membrane using a Dounce homogeniser, again the expected result of this is plasma membrane rupture but not nuclear membrane rupture (Guilluy et al., 2014). In order to optimise this, the number of strokes with the Dounce homogeniser was varied. However, in all the conditions (between 10 and 30 Dounce strokes) there

appeared to be some PM rupture but still cytoplasm, as determined by emerin staining, associated with all the nuclei (Figure *4.26*b). The next method used a similar method involving the Dounce homogeniser to mechanically separate the cytoplasm and nucleus but this had the additional step of centrifuging the cells through a low concentration of sucrose in order to strip remaining cytoplasm from the nucleus (Dahl et al., 2005). This produced the most success with little intensity following phalloidin staining (Figure *4.26*c) but there was clearly some cytoplasmic remains still associated with the nucleus when viewed with brightfield (Figure *4.26*d).

The final method used was an adaptation of the relatively successful method involving mechanical lysis and sucrose gradient. This method used the same system but with a higher sucrose concentration which results in a greater viscosity that helps to strip excess cytoplasm and cytoskeleton from the nuclei (Martínez-Vieyra et al., 2013). Following nuclear isolation, the validity of the preparation was assessed by a combination of microscopy and western blotting analysis. Initially the quality was assessed by staining with DAPI and phalloidin to identify the nuclear and cytoplasmic components (Figure *4.27*a). Based on this it is clear that the majority of the nuclei were lacking any surrounding phalloidin staining (white arrows) while there were still a few remaining nuclei that had at least some filamentous actin associated with the nuclei (grey arrows). Those cells that appeared to be F-actin free were also looked at using a brightfield microscope to determine if there was any associated cytoplasm that did not contain F-actin (Figure *4.27*b). In addition to immunofluorescence and brightfield microscopy analysis, the purity was assessed using western blotting (Figure *4.28*). In this assay GAPDH was used as a cytoplasmic marker, lamin A/C was used as a nuclear marker and calnexin was used as a marker of the ER. From this it is clear that the nuclear fraction only contains the nuclear proteins lamin A/C and neither the cytoplasmic nor ER markers were present in this fraction. Conversely, the cytoplasm contains the cytoplasmic marker protein GAPDH and the ER protein calnexin with no signal for the nuclear marker lamin A/C. This confirms the purity of the whole preparation suggesting that even the ER has been removed from the NE. Based on all these data combined, the protocol produces sufficiently clean nuclei to be used to measure isolated nuclei with AFM.

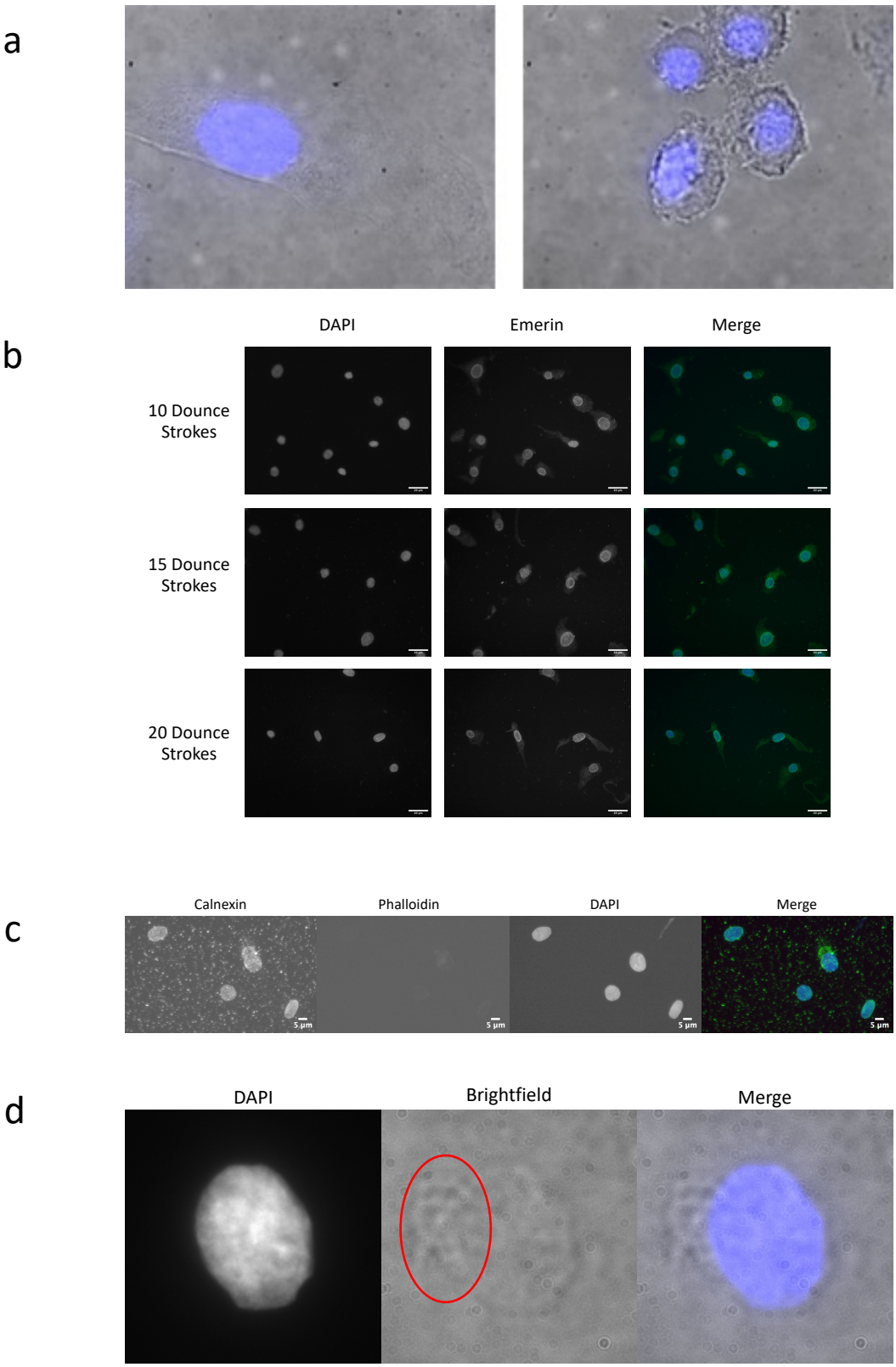

Figure 4.26 **Nuclear isolation methods**. (a) Representative brightfield microscopy of nuclear isolation following osmotic lysis, left image is untreated cell, right image is lysed cells where a large amount of cytoplasm is still present. Scale bar = 20µm. (b) Representative immunofluorescence images stained with DAPI and emerin following mechanical lysis using a Dounce homogenizer for varying numbers of strokes. (c) Representative immunofluorescence images stained with DAPI and calnexin following mechanical lysis followed by low-molarity sucrose gradient. Scale bar = 5µm. (d) Representative brightfield microscopy images of nuclei following mechanical lysis followed by low-molar sucrose gradient.

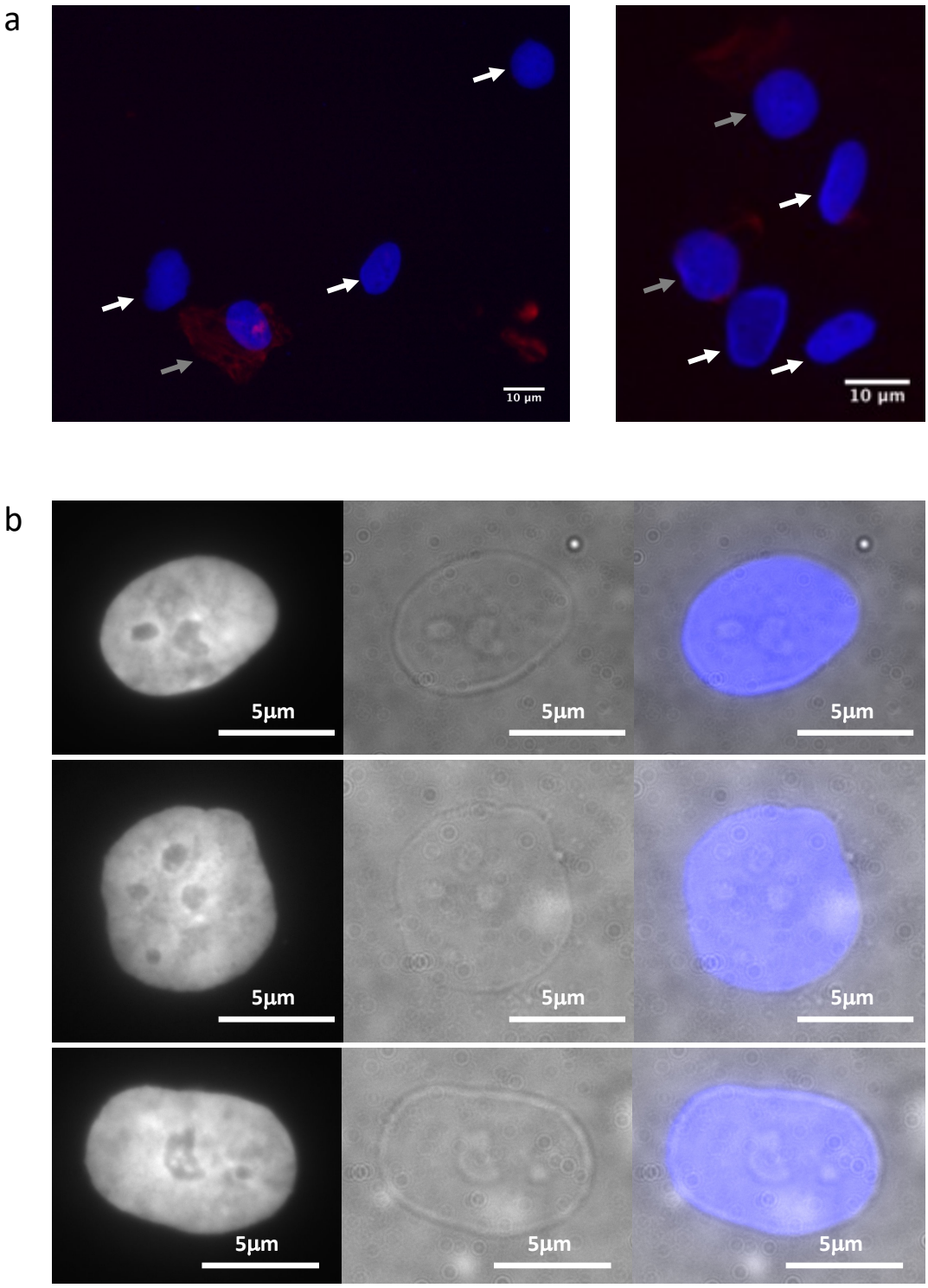

Figure 4.27 **Refined method of nuclear isolation involved mechanical lysis followed by high-molar sucrose gradient evaluated by microscopy**. (a) Representative nuclear isolation preparation stained with DAPI and phalloidin to identify the nucleus and any surrounding actin filaments indicative of cytoplasmic contamination. Cells lacking any phalloidin staining are indicated with white arrows while cells with some phalloidin staining remaining are indicated with grey arrows. Scale bar = 10µm. (b) Representative brightfield microscopy images of isolated nuclei with no surrounding cytoplasmic contaminants. Scale bar = 5µm.

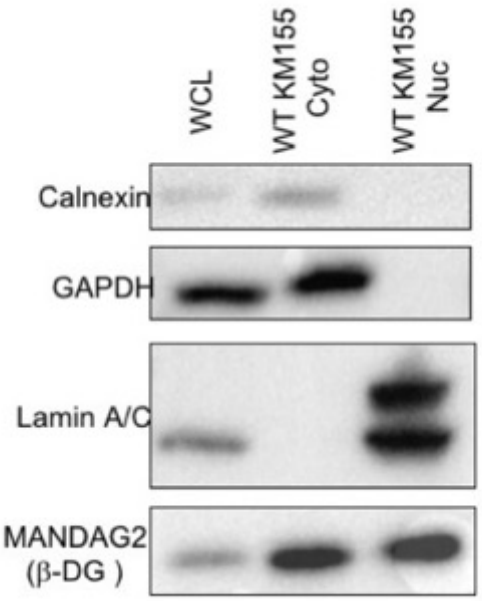

Figure 4.28 **Refined method of nuclear isolation involved mechanical lysis followed by high-molar sucrose gradient evaluated by western blotting**. Western blot analysis of nuclear and cytoplasmic fractions following mechanical lysis. GAPDH was used as the resident cytoplasmic protein marker, lamin A/C was used as the resident nuclear protein marker and calnexin was used as the resident ER marker protein. This representative blot indicates that the nuclear fraction did not contain the cytoplasmic or ER marker proteins.

4.2.9 Investigating the mechanical properties of nuclei isolated from control and *DAG1* KO myoblast cells

In order to measure the mechanical properties of the isolated nuclei, the nuclei need to be harvested just before AFM measurements with as little time between isolation and measurement as possible to prevent nuclear deterioration over time. To this end, following isolation, nuclei were allowed to settle and attached to the poly-L-lysine coated dish for 30 minutes. The dish was then washed twice to removed unattached nuclei or cell debris. Each nuclear sample was then measured for no longer than one hour before a new sample was prepared.

Preliminary AFM data was generated using the commercial MLCT pyramidal tip rather than the functionalised or commercial cantilevers discussed above. This preliminary data was generated to give an idea of nuclear mechanical properties prior to cantilever functionalisation. The data from 5 control cells and 5 *DAG1* KO B cells suggested the KO cells were significantly softer than the control (Figure *4.29*a). The average stiffness of control nuclei was 372±95 Pa while the average KO nuclei

was 116±68 Pa. These data suggest there may be a difference between the two samples with additional experiments and repeats required to validate the preliminary finding.

Mechanical measurements of control nuclei in addition to *DAG1* KO A and B nuclei were carried out using functionalised cantilevers. As with the preliminary data the KO nuclei were significantly softer than the control nuclei (Figure *4.29*b). The average nuclear stiffness for the control sample was 318±60 Pa while *DAG1* KO A and B nuclei were 151±24 Pa and 152±37 Pa respectively. The two data sets are in good agreement despite the preliminary data only including a total of 5 nuclei per sample. Taken together these data strongly suggest that isolated nuclei from *DAG1* KO cells are significantly softer than the control nuclei.

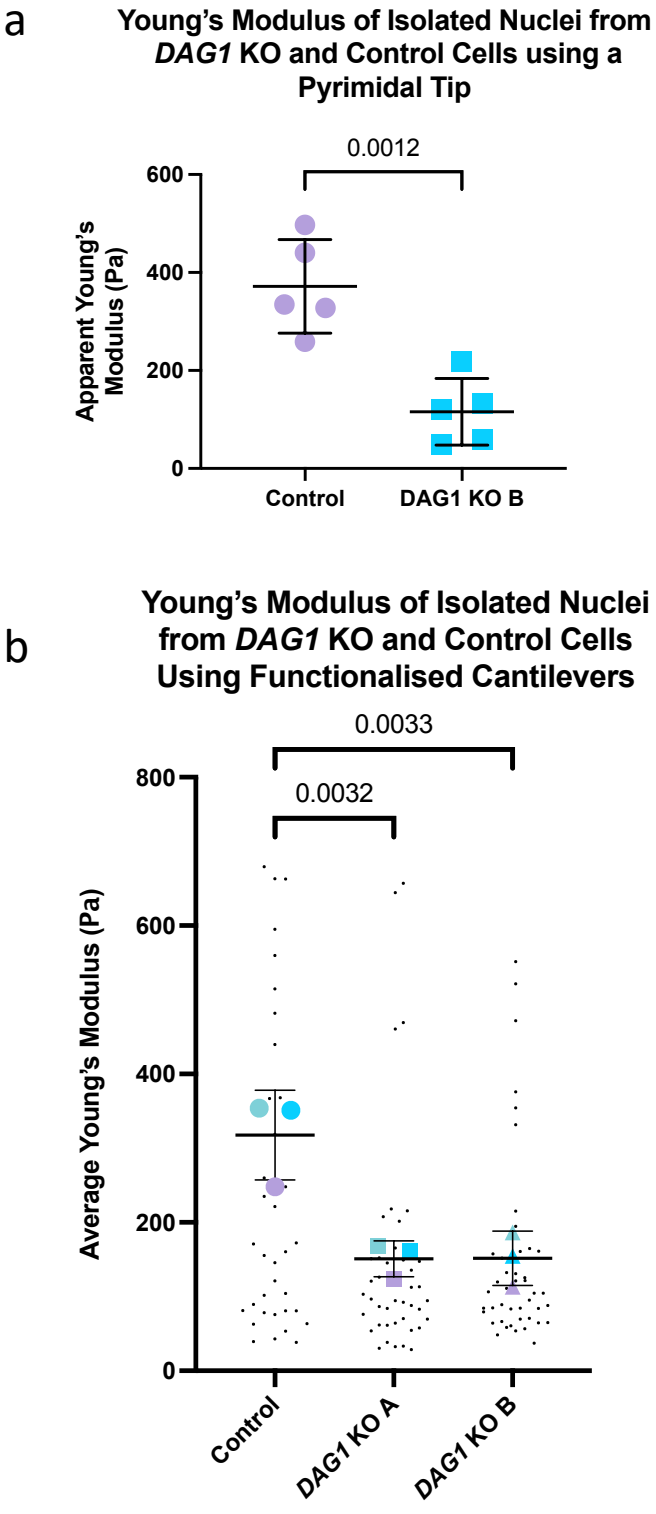

Figure 4.29 **Isolated nuclei from DAG1 KO cells are less stiff than isolated nuclei from control cells**. (a) Mechanical properties of isolated nuclei from control and DAG1 KO B as measured by a pyramidal MLCT cantilever. n = 5 nuclei, p = 0.0012, students t-test. (b) Mechanical properties of isolated nuclei from control and DAG1 KO A and B as measured by a functionalised MLCT cantilever. Small black points indicate individual nuclei while larger coloured points indicate the average of each experiment. Two individual outlier points from the control column were excluded to enable better visualisation, these values were 1121 Pa and 2553 Pa. n = 3 independent experiments with 35 individual cells measured per sample (except control where n = 36). Statistical analysis using one-way ANOVA test p = 0.0047. p values for multiple comparisons using Dunnett's multiple comparisons test are in the graph.

4.3 Discussion

The results described in this section were aimed at answering the question of whether a lack of DG results in a difference in mechanical properties of myoblasts when compared with appropriate controls. There has been some data presented in the literature which suggests the knock down of β-DG or the complete KO of the *DAG1* gene in mouse C2C12 myoblasts results in reduction or aberrant localisation of the key structural nuclear proteins lamin B1 and emerin (Jimenez-Gutierrez et al., 2020; Martínez-Vieyra et al., 2013). Given that these proteins contribute to the mechanical properties of the nucleus it would be expected that disruption of DG would result in a reduced nuclear Young's modulus.

This previously published data was the reason for carrying out these AFM measurements on *DAG1* KO human myoblasts. However, these cells do not exhibit the same lamin B1 or emerin phenotype which is discussed in detail in chapter 3. The results described in this chapter, demonstrate no clear difference in the Young's modulus of control and *DAG1* KO cells. These data fit with the data described in chapter 3 suggesting perturbation of DG does not affect the levels or structural organisation of the lamins in human myoblasts.

4.3.1 Comparison of Young's moduli

AFM has many advantages for measuring mechanical properties of cells however, it is very difficult to compare moduli between different studies as there are many factors that influence the final value (such as type of cantilever used, loading rate used, sample preparation, type of atomic force microscope and model used to determine the Young's modulus) (Caluori et al., 2018; Schillers et al., 2017; Weber et al., 2020). Despite the difficulties in comparing results across different studies, AFM is extremely useful for producing an apparent Young's modulus which can be compared across samples that have been handled and measured consistently (Zemła et al., 2020). Therefore, the values that other studies have determined for similar or

the same cell types may vary drastically depending on the parameters used. However, comparing these can give an indication of whether the measured data in this study is within the right range.

There have been no studies measuring the mechanical properties of the human myoblast cells used in this study, however, there are some data for mouse myoblasts. Mouse C2C12 myoblasts and myotubes were measured using a triangular tip, this study presented a Young's modulus of 3.15±0.24 kPa for myoblasts and 6.06±0.57 kPa for myotubes while myoblasts treated with blebistatin had a modulus of 2.37±0.30kPa (Streppa et al., 2018). This data is in good agreement with that presented here despite the difference in tip used. However, another earlier study using a cone shaped tip suggests the Young's modulus is between 11-45 kPa (Collinsworth et al., 2002). These two studies demonstrate the range in values that can be determined from different studies.

4.3.2 Reasons for variations in measurements

Throughout these data sets there are occasional occurrences of differences being statistically significant in one of the KO cell lines. There are three examples of this: (1) The nuclear measurements from the synchronised sample measured with the functionalised cantilever, *DAG1* KO A is significantly different from the control; (2) the cytoplasmic measurements from the synchronised sample measured with the commercial cantilever, *DAG1* KO B is significantly different from the control and (3) the nuclear measurements from the CytoD treated sample measured with the functionalised cantilever, *DAG1* KO B is significantly different from the control.

The most likely explanation for the differences between the two nuclear samples (1 and 3) is due to the use of the functionalised cantilever. The main problem with the functionalised cantilevers is a lack of consistency between cantilevers as the bead is unlikely to be stuck in the same position for each cantilever. Additionally, the functionalised cantilevers appeared to accumulate cell debris from the sample more readily than the commercial cantilever. This meant that each cantilever could only

be used once on one sample (or sometimes less). Conversely, the commercial cantilever was generally used for all samples within each repeat which allowed a more accurate comparison. Additionally, if only one of the KO samples demonstrated this difference this was generally regarded as a clonal artefact, but additional experiments with the commercial cantilever were carried out where possible to confirm this. It was only when both KO samples differed significantly from the control, as with the isolated nuclei experiments, that this was considered as a genuine difference.

The other variable result observed was using the commercial cantilever to measure the cytoplasmic stiffness of synchronised cells and *DAG1* KO B appeared to be significantly different than the control. This was not observed in any of the other cell lines, nor was it observed in the same cell line when measured with the functionalised cantilever. This combined evidence suggests this result was due to experimental variation rather than a clonal artifact. The most likely explanation for this is measuring an area of the cytoplasm that was too close the cell periphery resulting in the measurement including the contribution of the underlying substrate. It is also possible that simply by chance a stiffer subset of the KO cells was measured.

4.3.3 Differences in Young's modulus of isolated nuclei

Measuring the Young's modulus of isolated nuclei from control and *DAG1* KO clones A-B resulted in a significantly lower moduli for both *DAG1* KO clones when compared with the control nuclei. Here, it is clear from both the preliminary data and the follow up data using two *DAG1* KO cell lines that the KO isolated nuclei are softer than the control nuclei. It is possible that the two larger outlier values in the control sample resulted in skewed averages. However, when these outlier values are removed the difference between the control and *DAG1* KO samples was still significantly different. Ideally a rescue experiment where full-length β-DG or a mutant β-DG lacking the nuclear localisation signal would be used to confirm that the finding is due to β-DG and not either α-DG or an off-target effect of the CRISPR knockout. Unfortunately,

due to time and technical limitations this has not been possible. Additionally, confirmation with the commercial cantilevers was not possible due to the probe size being greater than that of the isolated nuclei. Based on the data presented in chapter 3 demonstrating that the structural nuclear proteins are not affected by knocking out *DAG1* the observed difference in nuclear Young's modulus is not easily explained. Additionally, the relative levels of heterochromatin and euchromatin are unaffected in *DAG1* KO cells compared with controls which means this is not the reason for the differences observed in the isolated nuclei experiments.

It would be possible to attempt to measure the relative contributions of the nuclear lamina or chromatin by varying the osmolarity of the buffer as has been done previously (Dahl et al., 2005). By subjecting the nuclei to a hypotonic solution, the nuclei swell and the contribution of the chromatin is reduced however, the contribution of the increased water pressure would need to be considered. Alternatively, it would be possible to treat the nuclei with DNase in order to remove the DNA and reduce the chromatin contribution. It is harder to remove the lamina while leaving the chromatin intact but nucleoli have been isolated for AFM measurements (Louvet et al., 2014). However, this additional information is unlikely to provide any clear answers given that no difference in the levels or localisation of any nuclear lamina proteins has been detected.

One explanation could be down to the sensitivity of the different experiments used. It may be that the levels of lamin B1 are slightly reduced in *DAG1* KO cell lines but this difference is too small to be detected by fluorescence microscopy or western blotting (chapter 3). Whereas the sensitivity of the AFM may be detecting these minute differences. These differences are lost in the whole cell measurements because cells have a Young's modulus in kPa range while the isolated nuclei are measured in Pa. Thus, the difference of 200 Pa between control and KO isolated nuclei is lost in the background of whole cells which are much stiffer.

Although there might not be an obvious explanation for the differences observed at the isolated nuclei level it is important to consider what the physiological

implications may be. As myoblasts differentiate into myotubes to form muscle fibres they are put under large amounts of mechanical pressure. Maintaining nuclear shape is required for correct cellular function (Mandigo et al., 2019) so maintaining a stiffer nucleus may be required for retaining correct nuclear shape. In the following chapter the response to a range of mechanical stressors will be investigated in order to determine whether a lower nuclear stiffness plays any role in resisting or responding to mechanical stress.

5 Investigating the role of DG in maintaining nuclear morphology and DNA integrity following mechanical stress

5.1 Introduction

Mammalian cells are capable of adapting to varying types of mechanical stimulus and there are many mechanisms involved in converting mechanical stimulus into a biochemical signal that cells can respond to. The external mechanical environment can be sensed through membrane proteins which result in downstream signalling through pathways such as the Hippo pathway which results in the regulation of cell proliferation and cell survival (Zou et al., 2020). Additionally, direct mechanical force can be transmitted through focal adhesions, through the cytoskeleton and directly to the chromatin within the nucleus via the LINC complex and nuclear lamina (Crisp et al., 2006). The nucleus plays a central role in the response to mechanical cues and the response to excessive mechanical stress. The nuclear response produced differs depending on the type of mechanical stress and the relative intensity or persistence of that stress (Gilbert et al., 2019; Nava et al., 2020; Raab et al., 2016). In order to test the effect of mechanical stress, there are three major types of mechanical stress that mammalian cells can easily be subjected to *in vivo*; (1) cell/nuclear compression/deformation, (2) cell stretching and (3) being subjected to sheer forces. Compression occurs during development but also commonly in migrating cells that have to negotiate through narrow gaps in ECM, this is particularly relevant for metastatic cancer cells (Denais et al., 2016). Stretching occurs in many tissues but is extreme and consistent in muscle and skin tissue. This means cells require mechanisms in order to cope with the constant strain. Sheer stress is common in endothelial cells lining the blood vessels. It is important that cells are able to detect and respond to these mechanical stressors to maintain tissue homeostasis.

5.1.1 Extreme cell/ nuclear compression results in an accumulation of DNA damage

Investigating the effects of compression on cells can be carried out in either an active or a passive manner. Active compression involves cells moving through gaps/pores/channels that are significantly smaller than the nucleus. The nucleus is the stiffest and largest organelle and represents the rate limiting component in migration through confined spaces (Mukherjee et al., 2020). The alternative, passive compression, simply involves cells growing *in situ* while a compressional force is applied on top of the cells. This allows a better understanding of the effects of the mechanical stress in isolation without additional variables such as migration.

Cell migration through a confining environment has generally made use of the Transwell migration assay. This involves seeding cells onto a membrane with pores of a defined size. The cells then migrate through these pores, and it is possible to fix and stain either the top (unmigrated cells) or the bottom (migrated cells) of the membrane and image these as with normal immunofluorescence techniques. These types of experiments have been done extensively in many cell types with the majority responding in the same way. When mammalian cells migrate through 3μm pores the nuclei are constricted and result in aberrant nuclear morphology including decreases in nuclear area (Patteson et al., 2019a), changes in nuclear aspect ratio (Irianto et al., 2017; Patteson et al., 2019a) and an increase in nuclear blebs (Irianto et al., 2017; Mukherjee et al., 2020; Patteson et al., 2019a; Pfeifer et al., 2018; Xia et al., 2019). The nuclear blebs are lamin A/C positive but lamin B1 negative as seen in nuclear blebs that have not resulted from mechanical stress (Pfeifer et al., 2018). In addition to nuclear morphology changes following migration through 3μm pores, there are also direct effects on the DNA and chromatin. There is an increase in DNA damage as determined by γH2AX intensity in migrated cells compared with non-migrated cells, while there is also mislocalisation of key repair protein Ku80. The DNA damage is not due to replication stress and is replication independent (Irianto et al., 2017; Mukherjee et al., 2020; Patteson et al., 2019a; Pfeifer et al., 2018; Xia et al., 2019). Additionally, there are gross chromosome changes including changes in chromosome copy number and changes in transcription profiles (Irianto et al., 2017; Xia et al., 2019). The increased DNA damage and transcriptional changes are not permanent and generally recover back to baseline levels within 24 hours post migration.

However, when key DNA double strand break repair proteins are knocked down there are increased levels of DNA damage following migration and this damage is persistent (Irianto et al., 2017; Pfeifer et al., 2018). Finally, there are changes in the cell-cycle following migration through 3μm pores. The cell-cycle is arrested following migration however, this is reversable as the cell-cycle is reinitiated following DNA damage repair (Pfeifer et al., 2018; Xia et al., 2019). The cell-cycle arrest is also partially alleviated by addition of an antioxidant suggesting accumulation of ROS contributes to the DNA damage response (Xia et al., 2019). In all of these experiments an appropriate control was used, cells migrated through 8μm pores which does not result in nuclear compression. In these control experiments none of the nuclear abnormalities, increases in DNA damage or arrested cell-cycles were observed indicating these responses are specific to confined migration (Irianto et al., 2017; Patteson et al., 2019a; Pfeifer et al., 2018; Xia et al., 2019).

One limitation of using the transwell migration assays discussed above is that it is not possible to visualise the cells as they migrate through the constricting pores. An alternative method for investigating migration through narrow pores is the use of microfluidic devices that allow real-time video microscopy to monitor progression through the pores (Keys et al., 2018). Using this method it was also found that nuclear morphology was affected and the levels of DNA damage increased following migration through constricting pores (Raab et al., 2016; Shah et al., 2020). Additionally, it is possible to obtain a greater depth of information on how these responses occur compared with the transwell assays. Shah and colleagues tested multiple cell lines and found two different mechanisms of DNA damage accumulation and each of these was found exclusively with none of the tested cell lines demonstrating both mechanisms. The first mechanism involved replication stress and replication fork failure which resulted in an accumulation of the DNA damage marker γH2AX following migration. The second mechanism involved nuclear rupture resulting in exchange of nuclear and cytoplasmic proteins, resulting in a loss of DNA repair factors in the nucleus and an increase in damaging cytoplasmic components such as nucleases (Shah et al., 2020). Pfeifer et al. (2018) found no evidence of replication stress, but they were using a breast cancer cell line that demonstrated

the nuclear rupture mechanism described by Shah et al. (2020). Additional studies using the microfluidic migration devices identified ESCRT III complex as a key component of nuclear envelope repair following a nuclear rupture event (Raab et al., 2016).

All of these migrational compression studies confirm that extreme compression of the relatively large nucleus results in an accumulation of DNA damage and this can occur either by exchange of nuclear/cytoplasmic components or by replication stress. However, the cells are able to deal with these DNA breaks by inhibiting the cell-cycle while DNA repair proteins repair the damage, and the cells are then released back into the cell-cycle. This mechanism allows cells to continue migrating through narrow gaps and also helps to explain some of the increase in genetic variation in metastatic cancer cells (Denais et al., 2016; Irianto et al., 2017).

These studies described above have all investigated the effects of cell/nuclear compression during active migration. When compression of cells grown *in situ* was investigated the results are similar. Using a custom-built device which compresses cells between two pieces of PDMS, the distance between the two PDMS plates was determined by the addition of glass beads with a well-defined height. It was found that compressed cells accumulated DNA damage within 30 minutes and the amount of damage increased as the compression height was decreased. There was some evidence of nuclear envelope rupture, but the majority of cells had increased levels of DNA damage without evidence of nuclear rupture. This was also observed using AFM combined with light-sheet microscopy, nuclei were compressed to a height of ~2μm and DNA damage accumulated without the need for nuclear rupture (Shah et al., 2020). This approach was also used in another study where AFM was used to compress the nucleus and they found increased levels of cGAS which binds to cytoplasmic DNA suggesting nuclear rupture resulting in DNA leakage (Cho et al., 2019). Additional studies find increased levels of cell death as levels of compression are increased. The levels of DNA damage were not investigated but it is likely that cell death increased as levels of DNA damage passed a threshold level (Patteson et

al., 2019a). Together these studies suggest that compression of cells/nuclei whether it is active or passive results in an increase in DNA damage.

5.1.2 Cyclic cell stretching results in cyto- and nucleoskeleton reorganisation in order to minimise DNA damage

Cyclic cell stretching results in a cellular response that aims to decouple the nucleus from the recurrent stress, but the types of response differ depending on the frequency of stretching. Following cyclic stretch at both high and low frequencies nuclear morphology of human epidermal stem cells is affected whereby the nucleus becomes more wrinkled and has a decrease in nuclear envelope tension (Nava et al., 2020). However, unlike with cell compression there is little evidence of nuclear envelope rupture in healthy cells. However, when lamin A/C is knocked down there is increased nuclear rupture during cyclic stretching (Cho et al., 2019). Nuclear size is also affected; at low-frequency cyclic stretching the cell size increases but the nuclear size does not, whereas at high-frequency stretching, the cell size remains the same but the nuclear size decreases (Gilbert et al., 2019). It has been shown that this change in nuclear size but not cell size is the result of nuclear decoupling, there is a decrease in levels of SUN2, a component of the LINC complex which links the nucleus to the cytoskeleton, thus preventing the force from being transmitted to the nucleus, especially at high-frequency stretching (Gilbert et al., 2019). This nuclear decoupling results in changes in transcription profiles resulting in increased levels of cytoskeletal proteins and decoupling also prevents the accumulation of DNA damage. Cyclic stretching results in a slight decrease in levels of DNA damage, however, overexpression of SUN2 which results in the nucleus being recoupled to the cell and subjected to the stretching forces results in an increase in DNA damage above basal levels (Gilbert et al., 2019; Heo et al., 2015). Based on this evidence it would suggest that the nuclear decoupling prevents stretching forces being transmitted to the nucleus and maintains DNA integrity.

In addition to nuclear decoupling the cells are also able to realign the cytoskeleton in the direction of low-frequency stretching which reduces the strain transmitted to the

nucleus (Nava et al., 2020), similar to what is seen in response to sheer stress. Importantly, the chromatin state also responds to the cyclic stretching by becoming less condensed. At low-frequency stretching the chromatin becomes less condensed and remains this way until the stretching has stopped. However, at high-frequency stretching the levels of heterochromatin decrease initially and then return to baseline levels during prolonged stretching (Nava et al., 2020). These heterochromatin changes allow the nucleus to disperse the force thus preventing excessive DNA damage. The chromatin decondensing is controlled by Ca^{2+} signalling (Heo et al., 2015) that enters through the Peizo1 ion channel. Preventing Ca^{2+} signalling or knockdown of Peizo1 prevents the chromatin from decondensing and results in an increase in DNA damage during cyclic stretching (Nava et al., 2020). The data from these studies would suggest that cells have the ability to respond to cyclic stretching and prevent DNA damage occurring.

5.1.3 Sheer stress results in changes in nuclear architecture

Biological sheer stress is most commonly associated with fluid flow, such as blood, lymph, urine and synovial fluid for example. Endothelia are the cells most commonly exposed to constant mechanical forces in the form of sheer stress due to blood flow. The sheer stress experienced can be classed as laminar or disturbed. Laminar flow results in consistent flow rate in a single direction. Disturbed or oscillatory flow is any flow that is not laminar, it is often changing direction and rate of flow, this occurs around branches or obstructions in the blood vessels (Ji, 2018; Zhu et al., 2020). The type of sheer stress has been shown to result in changes in transcription and this is regulated by the JAK/STAT pathway (Mahmoud et al., 2017; Zhu et al., 2020).

As with other forms of mechanical stress, sheer stress results in changes in nuclear morphology which is controlled by sheer stress-induced changes to the nuclear lamina. In MDCK epithelial cells subjected to sheer stress there was a decrease in both nuclear area and volume, this was controlled by the mechanosensitive channel Piezo1 (Jetta et al., 2019). In addition to changes in nuclear area and volume, nuclear shape was also affected by sheer stress. Nuclei had a decrease in nuclear circularity

following shear stress. The longer the cells were subjected to sheer stress the lower the value for nuclear circularity, the opposite was reported for elongation factor suggesting the nuclei become more elongated following sheer stress (Jiang and Ji, 2018; Philip and Dahl, 2008). These observed changes in nuclear shape were accompanied by changes in levels and localisation of lamin A/C. Following sheer stress, lamin A/C staining became more intense at the NE compared with unstressed controls (Philip and Dahl, 2008). Additionally, the total levels of lamin A/C increased following 6 hours of sheer stress (Jiang and Ji, 2018). These studies suggest that sheer stress results in changes in nuclear morphology and changes in localisation and levels of lamin A/C.

There have been a limited number of investigations into the effects of sheer stress on levels of DNA damage and how cells might adapt to minimise levels of DNA damage. However, it has been found that following sheer stress there is an increase in the percentage of apoptotic cells. The percentage of apoptotic cells also increases with the amount of time cells are subjected to sheer stress (Pan et al., 2017). Additionally, the levels of DNA fragmentation were investigated following sheer stress. The percentage of DNA fragmentation increased both with sheer level and with time (Triyoso and Good, 1999). Taken together these studies suggest that sheer stress results in nucleoskeletal reorganisation, changes in nuclear morphology and increased levels of apoptosis and DNA damage.

5.1.4 Hypothesis and aims

Data described in previous chapters suggests there is no difference in levels of nucleoskeletal proteins in *DAG1* KO cells compared with controls and this is also confirmed in the data that suggests the stiffness of *DAG1* KO nuclei within whole cells does not differ from that of the controls. However, it was found that when the nuclei are separated from all cytoskeletal influence the *DAG1* KO nuclei were significantly softer than the control nuclei. This then leads to the question of whether the difference in nuclear stiffness has any physiological relevance.

The aim of this chapter is to investigate the response of *DAG1* KO cells to mechanical compression and to determine whether the response differs from that of control cells. Cells have been subjected to active compression as they migrate through 3μm transwell pores in addition to passive compression with the addition of weighted inserts. Following these experiments the nuclear morphology was assessed in addition to the levels of DNA damage as determined by γH2AX staining.

5.2 Results

5.2.1 Determining baseline levels of DNA damage and nuclear morphology prior to mechanical and chemical stress

Before conducting experiments to determine the effects mechanical or chemical stress has on *DAG1* KO and control cells it is important to understand the baseline levels of DNA damage. The levels of γH2AX were therefore determined using immunofluorescence microscopy (Figure *5.1*a,b) as were the values for nuclear area (Figure *5.1*c), nuclear circularity (Figure *5.1*d) and nuclear aspect ratio (Figure *5.1*e). Although these experiments were carried out in chapter 3 it was important to ensure the results were consistent before starting this set of experiments.

In the case of levels of DNA damage as indicated by γH2AX staining the nuclear intensity appeared to be slightly lower in *DAG1* KO clones A and B compared with control cells. The difference between control and *DAG1* KO A was insignificant however, the difference between the control and *DAG1* KO B was just below the significance cut off of p = 0.05. The difference between the control and KO B was 0.0495 as determined by one-way ANOVA test (Figure *5.1*b).

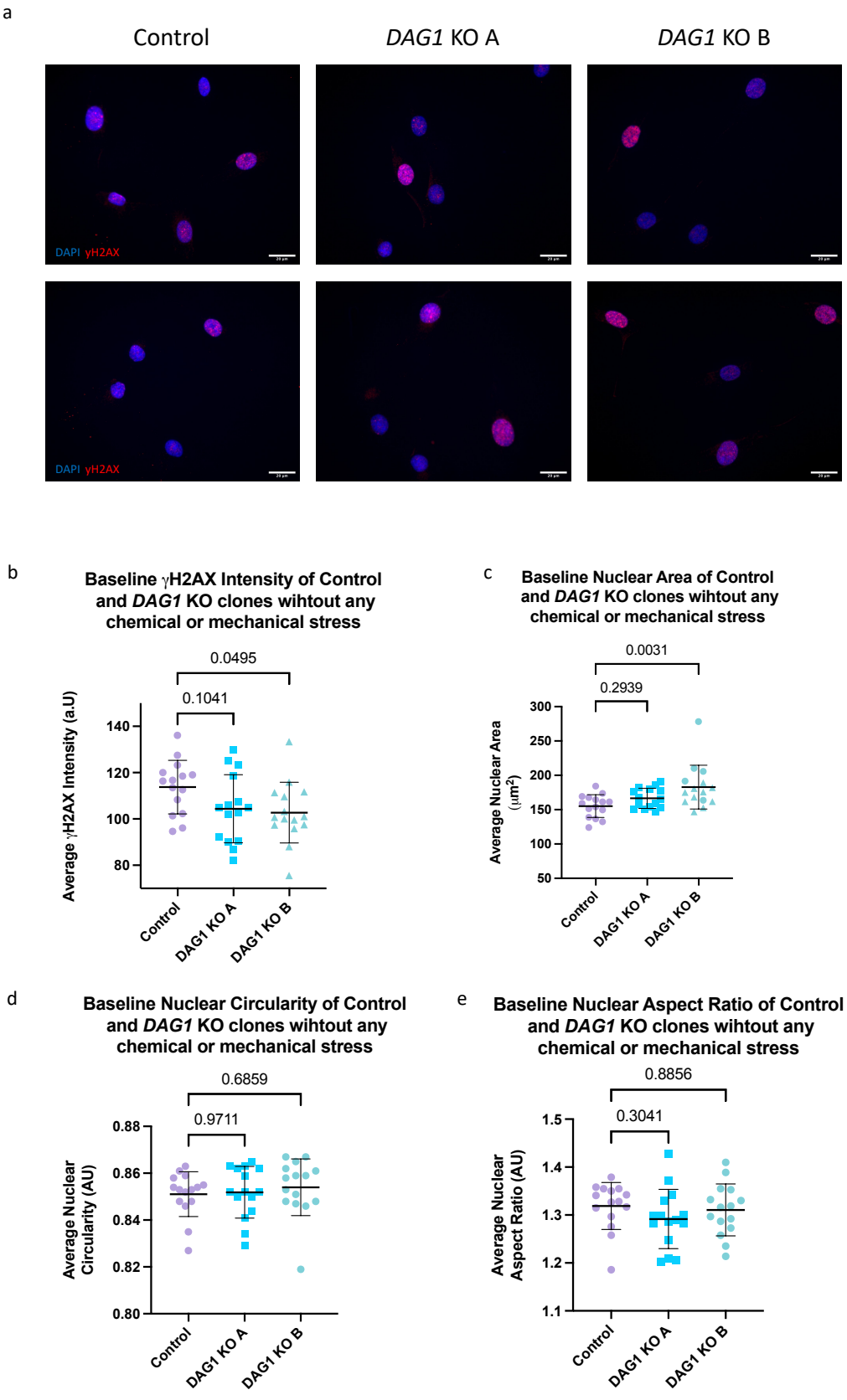

Figure 5.1 **Baseline averages for nuclear morphology and levels of γH2AX in control and DAG1 KO clones A and B without additional cell stress.** (a) Representative images of cells grown for 24 hours before fixing and staining with DAPI (blue) and γH2AX (red) to identify nuclear morphology and levels of DNA damage. Cells were imaged using the Leica fluorescence microscope. Scale bar = 20μm. (b) Nuclear levels of γH2AX without additional cell stress. Each coloured point indicates the average value for each independent experiment. 15 independent

experiments were carried out with 392 control, 401 KO A and 377 KO B cells measured. Graph shows mean and standard deviation. The one-way ANOVA test returned a p value of 0.0575 which is not below the significance threshold of 0.05. Using a Dunnett's multiple comparison test the difference between control and DAG1 KO clone B was significant with a p value of 0.0495. (c) Nuclear area without additional cell stress. As before. The one-way ANOVA test returned a p value of 0.0061 which is below the significance threshold of 0.05. Using a Dunnett's multiple comparison test the difference between control and DAG1 KO B was significant with a p value of 0.0031 while the difference between control and DAG1 KO A was not significant (p = 0.2939). (d) Nuclear circularity without additional cell stress. As before. The one-way ANOVA test returned a p value of 0.7156 which is below the significance threshold of 0.05. Dunnett's multiple comparison test was also carried out, p values are on the graph. (e) Nuclear aspect ratio without additional cell stress. As before. The one-way ANOVA test returned a p value of 0.3871 which is below the significance threshold of 0.05. Dunnett's multiple comparison test was also carried out, p values are on the graph.

When nuclear morphology was compared between control and *DAG1* KO clones A and B the results were as observed in chapter 3. In the case of nuclear area, both *DAG1* KO clones had a larger average nuclear area than the control but this difference was only significantly different between control and *DAG1* KO B (Figure *5.1*c). The nuclear shape parameters circularity and aspect ratio were investigated and as with chapter 3 there was no significant difference in the circularity or aspect ratio of control cells compared with *DAG1* KO clones A and B (Figure *5.1*d,e). Despite the differences not being significant the average nuclear circularity is slightly higher for *DAG1* KO clones than for control and the average nuclear aspect ratio is slightly lower for *DAG1* KO clones compared with controls.

Given that there are differences (even if not statistically significant) between control and *DAG1* KO cells, the values for all mechanical and chemical stress experiments have been normalised to the untreated value for each cell line. This will allow the identification of relative changes between the cell lines rather than absolute changes.

5.2.2 Investigating the response of control and *DAG1* KO cells to oxidative stress following treatment with H_2O_2

In order to determine if *DAG1* KO cells respond to mechanical stress differently to control cells, it is important to understand if the two cell types respond differently to non-mechanical stress. Oxidative stress as induced by treatment with H_2O_2 was used to investigate any differences in response between control and *DAG1* KO clones. In

order to determine the most appropriate concentration of H_2O_2 to use, control and *DAG1* KO A cells were subjected to a range of concentrations and cell viability was crudely assessed by calculating the percentage of trypan blue negative cells following treatment (Figure *5.2*). Untreated cells had almost 100% viability as did those cells treated with 0.1mM H_2O_2, following treatments with 1mM and 2mM cell viability dropped to just above 50% and the percentage of viable cells continued to drop for 3mM, 4mM and 5mM. Based on this, 2mM was chosen as it is clearly sufficient to induce a response and there was still >50% cell viability.

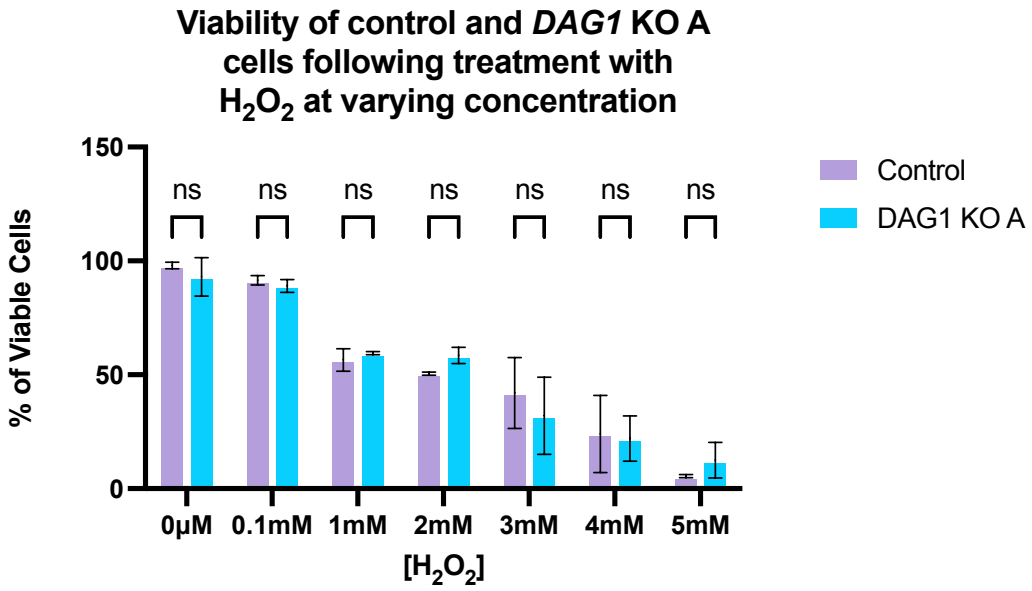

Figure 5.2 **Optimisation of H_2O_2 concentration.** Control and DAG1 KO A cells were treated with varying concentrations of H_2O_2 and percentage of cell viability was assessed. 2 independent experiments were carried out with at least 100 cells counted per sample per experiment. Graph shows mean and actual range. The differences between control and DAG1 KO A were tested using multiple t tests with none of the p values being <0.05.

Control cells and *DAG1* KO clones A and B were either untreated (0mM) or H_2O_2 treated (2mM) for 1 hour. Cells were then fixed and stained for γH2AX as a read out of DNA damage and nuclear morphology was assessed (Figure *5.3*a). As expected, the intensity of γH2AX staining increased significantly following H_2O_2 treatment in all cell types (Figure *5.3*b). When comparing the relative levels of γH2AX following H_2O_2 treatment in control and *DAG1* KO A cells there is no significant difference. However, the difference between control and *DAG1* KO B was significant as tested by one-way

ANOVA (p = 0.0381). This difference is possibly due to clonal variation however, if the difference in response is not present in both *DAG1* KO clones then it is not considered a genuine consequence of knocking out the *DAG1* gene.

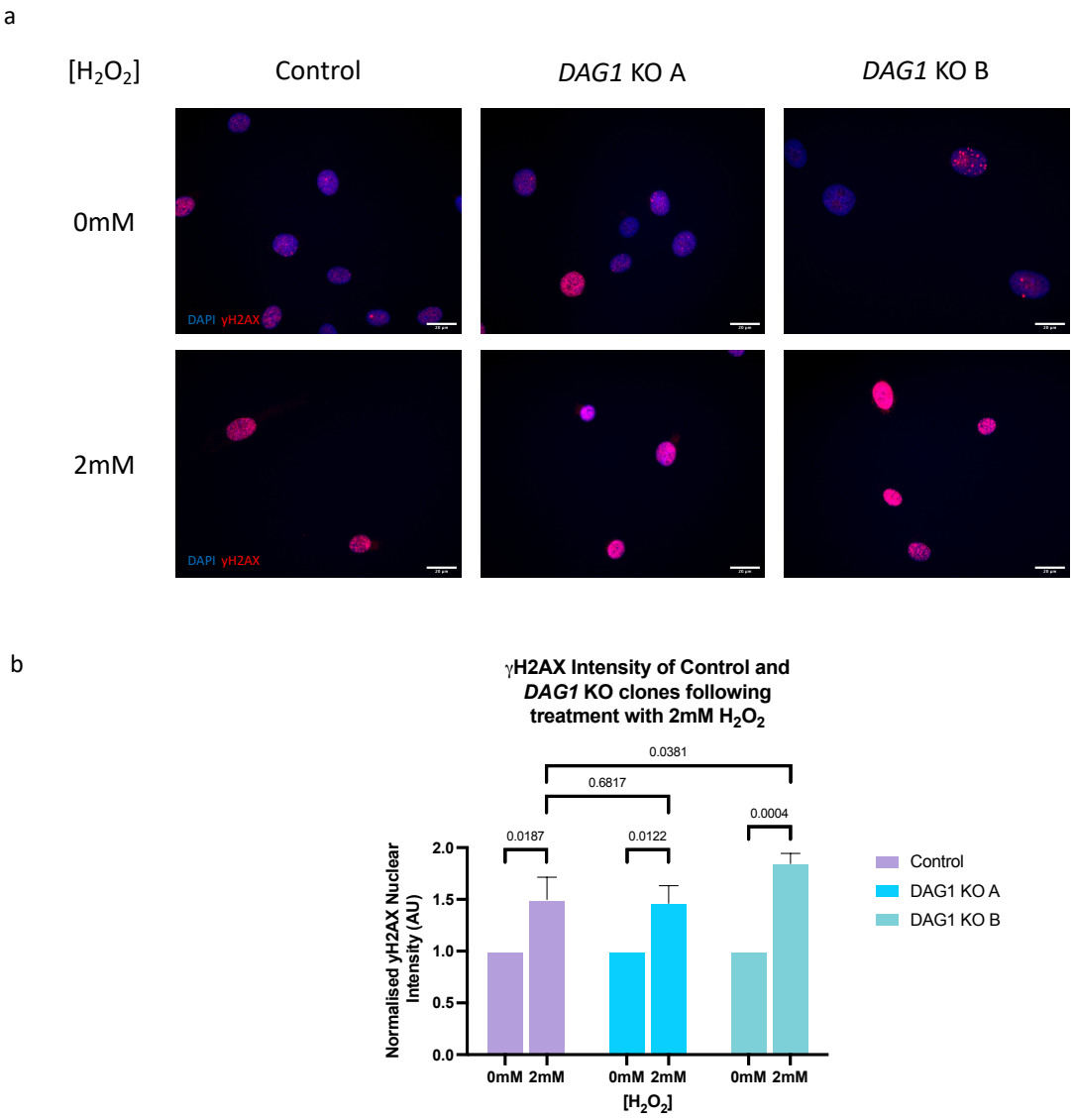

Figure 5.3 **Average nuclear levels of γH2AX in control and DAG1 KO clones A and B with and without H_2O_2 treatment.** (a) Representative images of cells grown for 24 hours before treating with 0mM or 2mM H_2O_2 and then fixing and staining with DAPI and γH2AX to identify nuclear morphology and levels of DNA damage with and without H_2O_2 treatment. Cells were imaged using the Leica fluorescence microscope. Scale bar = 20μm (b) Normalised nuclear levels of γH2AX following treatment with 0mM or 2mM H_2O_2. 4 independent experiments were carried out. Control 0mM n = 102, 2mM n = 107. KO A 0mM n = 110, 2mM n = 123. KO B 0mM n = 117, 2mM n = 104. Graph shows mean and standard deviation. The one-way ANOVA test returned a p value of 0.0004 which is below the significance threshold of 0.05. for multiple comparisons, a Šídák's multiple comparisons test was used and the p values can be seen on the graph.

In addition to γH2AX levels, the nuclear area, circularity and aspect ratio were assessed in treated and untreated cells (Figure *5.4*). Nuclear area was consistently

lower in treated cells compared with untreated for control and *DAG1* KO cells alike. This difference was significant in both control and *DAG1* KO A but not in *DAG1* KO B (Figure *5.4*a), this could be due to clonal variation or the fact that *DAG1* KO B nuclei are significantly larger to start with. Relative nuclear area of treated cells was also compared between control and *DAG1* KO cells. The difference between control and *DAG1* KO A was significant while the difference between control and *DAG1* KO B was not. Again, only significant differences observed between control and both KO clones were considered to be different due to a lack of DG.

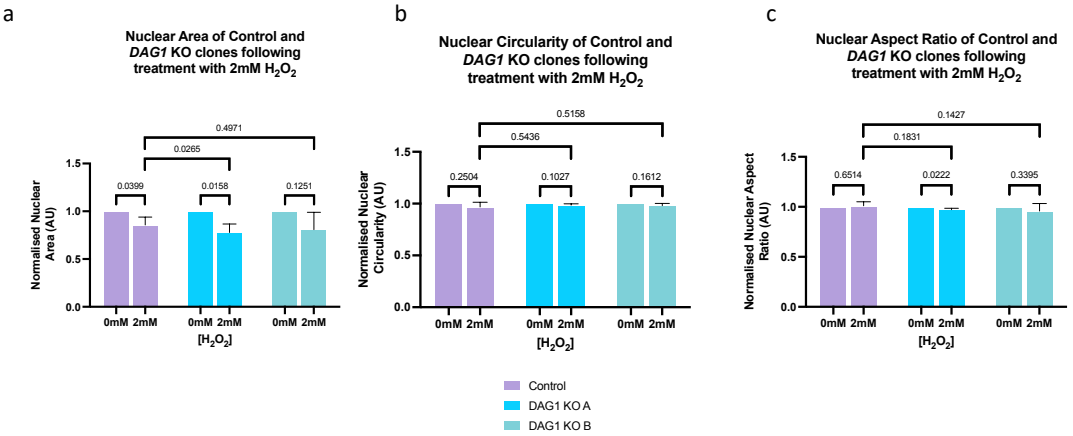

Figure 5.4 **Nuclear morphology of control and DAG1 KO clones A and B with and without H_2O_2 treatment.** (a) Normalised nuclear area with and without treatment with 2mM H_2O_2. 4 independent experiments were carried out. Control 0mM n = 102, 2mM n = 107. KO A 0mM n = 110, 2mM n = 123. KO B 0mM n = 117, 2mM n = 104. Graph shows mean and standard deviation. The one-way ANOVA test returned a p value of 0.0468 which is below the significance threshold of 0.05. For multiple comparisons, a Šídák's multiple comparisons test was used and the p values can be seen on the graph. (b) Normalised nuclear circularity with and without treatment with 2mM H_2O_2. As before. The one-way ANOVA test returned a p value of 0.2766 which is not below the significance threshold of 0.05. For multiple comparisons, a Šídák's multiple comparisons test was used and the p values can be seen on the graph. (c) Normalised nuclear aspect ratio with and without treatment with 2mM H_2O_2. As before. The one-way ANOVA test returned a p value of 0.3131 which is not below the significance threshold of 0.05. For multiple comparisons, a Šídák's multiple comparisons test was used and the p values can be seen on the graph.

When testing the effect of H_2O_2 treatment on nuclear shape it was found that neither nuclear circularity nor nuclear aspect ratio was different in treated or untreated cells in any of the cell lines (Figure *5.4*b,c). Additionally, when comparing H_2O_2 treated control with *DAG1* KO clones there was no significant difference in either nuclear circularity or nuclear aspect ratio.

Taken together these data suggest that following H_2O_2 treatment there is no clear difference in how *DAG1* KO clones respond compared with control cells when assessing levels of γH2AX staining and nuclear morphology.

5.2.3 Investigating the response of control and *DAG1* KO cells to osmotic stress following treatment with NaCl and PEG

In addition to treating cells with H_2O_2 in order to subject them to oxidative stress, cells were also subjected to two forms of osmotic stress. The addition of NaCl results in the hyperosmotic stress of the cells and therefore nuclei too as they lose water, resulting in a reduction in volume and a crinkled nuclear morphology. Additionally, if cells are treated with polyethylene glycol (PEG) with a molecular mass of 4000 Da then cells are also hyperosmotically stressed but they also experience compressional forces. It is suggested that this osmotic pressure is similar to the forces exerted by cytoskeletal contractility (Damodaran et al., 2018; Khavari and Ehrlicher, 2019). It is also suggested that osmotically stressing cells and nuclei with PEG allows cell compression to be investigated without the need for complex technical set ups and direct contact with the cells (Zhou et al., 2009). Furthermore, this system can be used to determine the relationship between compression and volume in order to observe and track force changes in 3D cell systems (Khavari and Ehrlicher, 2019).

In order to determine an appropriate concentration of NaCl to use, control cells were treated with a range of concentrations between 0mM and 500mM and the nuclear area was measured (Figure *5.5*). There were slight decreases in the average nuclear area when between 20mM and 100mM was used. The clearest reduction in nuclear area was following addition of 500mM NaCl as expected, however, there was a decrease in the number of viable cells in this condition. Therefore, it was decided that cells would be treated with both 200mM and 500mM as both conditions resulted in a significant decrease in nuclear area.

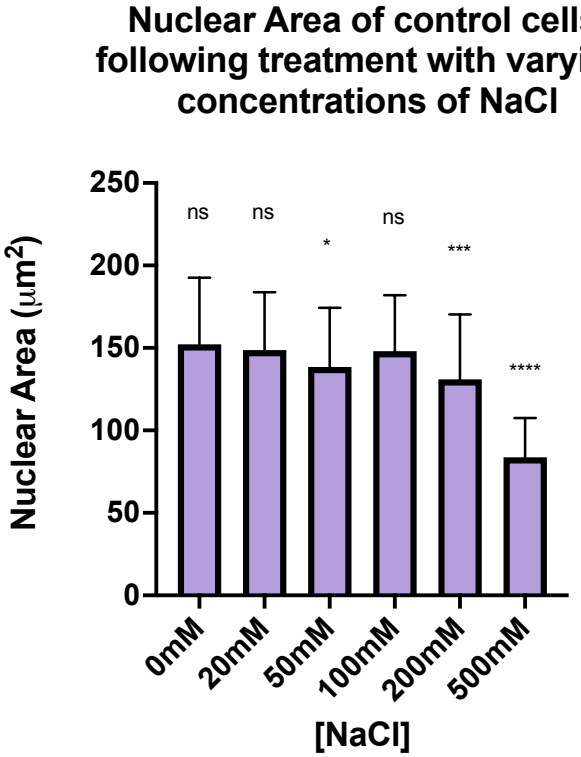

Figure 5.5 **Optimisation of NaCl concentration based on nuclear area of control cells.** Control cells were treated with varying concentrations of NaCl and nuclear area was assessed. 2 independent experiments were carried out with 110 0mM, 118 20mM, 100 50mM, 123 100mM, 104 200mM and 102 500mM treated cells. Graph shows mean and standard deviation. The one-way ANOVA test returned a p value of <0.0001 which is below the significance threshold of 0.05. For multiple comparisons, a Dunnett's multiple comparisons test was used, p values; * = <0.0332, ** = <0.0021, *** = <0.0002 and **** = <0.0001.

In order to determine if control cells respond to osmotic stress any differently to DAG1 KO cells, control and both *DAG1* KO clones A and B were subjected to 0mM, 200mM or 500mM NaCl and the levels of γH2AX were determined (Figure *5.6*). When the total nuclear levels of γH2AX were assessed, it was clear that the lower NaCl concentration did not affect the relative levels, however the higher concentration did. This was consistent across control and *DAG1* KO cell lines (Figure *5.6*b). When relative levels of γH2AX in control and *DAG1* KO cells subjected to osmotic stress were compared there was no significant difference between the control and either *DAG1* KO clone.

a

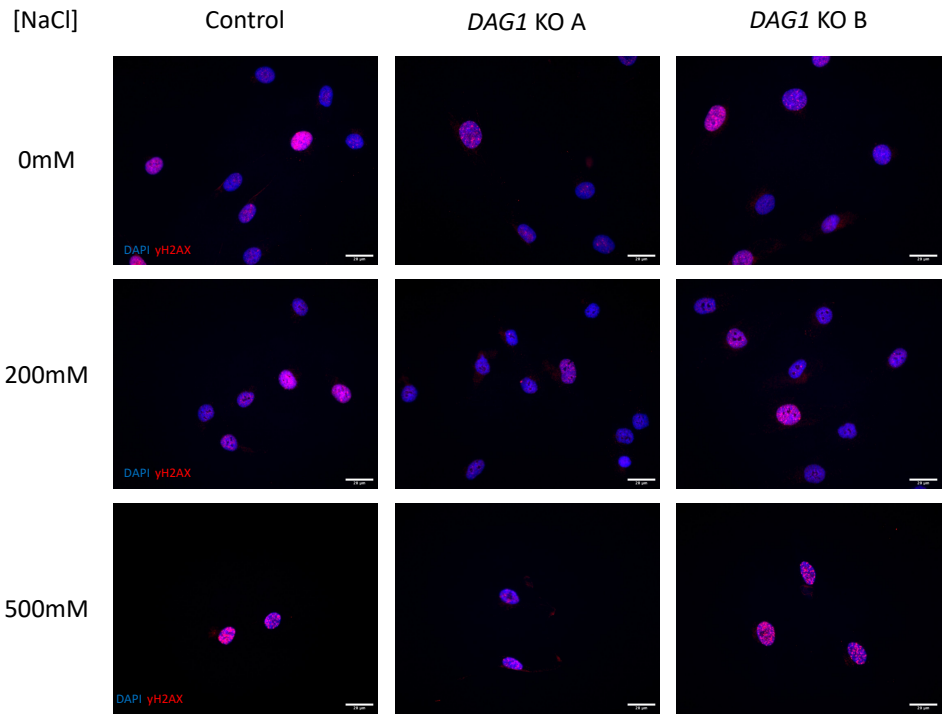

b

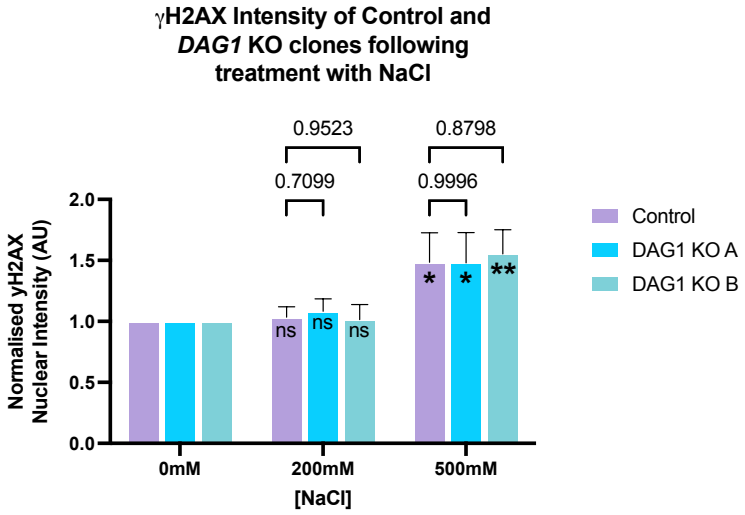

Figure 5.6 **Average nuclear levels of γH2AX in control and DAG1 KO clones A and B following 0mM, 200mM or 500mM NaCl treatment.** (a) Representative images of cells grown for 24 hours before treating with NaCl for 1 hour followed by fixing and staining with DAPI and γH2AX to identify levels of DNA damage at varying NaCl treatments. Cells were imaged using the Leica fluorescence microscope. Scale bar = 20μm. (b) Normalised nuclear levels of γH2AX following 0mM, 200mM or 500mM NaCl treatment. 4 independent experiments were carried out. Control 0mM n = 111, 200mM n = 115 and 500mM n = 103. KO A 0mM n = 126, 200mM n = 119 and 500mM n = 121. KO B 0mM n = 105, 200mM n = 131 and 500mM n = 109. Graph shows mean and standard deviation. Following a two-way ANOVA test a Dunnett's multiple comparison test was used to determine the difference between 0mM, 200mM and 500mM treatment in each cell line (p value; * = <0.0332, ** = <0.0021). A Turkey's multiple comparison test was used to determine the difference between cell lines in each treatment condition – p values are on the graph.

In addition to levels of γH2AX, changes in nuclear morphology were also investigated in all three cells lines subjected to 0mM, 200mM or 500mM NaCl. As previously, nuclear morphology was assessed using the parameters nuclear area, nuclear circularity and nuclear aspect ratio. The nuclear area significantly decreased in all cell lines when either 200mM or 500mM NaCl was added to the culture medium, except in the control cells treated with 500mM (Figure *5.7*a). In the control sample treated with 500mM NaCl there was a decrease in nuclear area however, this decrease was not statistically significant. Importantly, there was no difference in the relative nuclear area between control and *DAG1* KO clones when treated with either 200mM or 500mM NaCl. A similar trend is observed in the nuclear circularity experiment. The nuclear circularity is significantly lower in all cell lines following treatment with 200mM or 500mM NaCl while there is no significant difference between the control and either *DAG1* KO clone following 200mM or 500mM NaCl treatment (Figure *5.7*b). When nuclear aspect ratio was compared following NaCl treatment there was no difference between the untreated and the 200mM treated conditions for either control or *DAG1* KO B however, there was a significant difference between untreated and 200mM treated *DAG1* KO A cells (Figure *5.7*c). When cells were treated with 500mM NaCl there was a significant increase in nuclear aspect ratio compared with untreated cells and this was the case for control and *DAG1* KO cells alike. When the 200mM condition was compared, there was a significant difference between control and *DAG1* KO A but not *DAG1* KO B suggesting this was not a DG specific difference and likely due to clonal variation. For the 500mM condition there is no significant difference between the control and either *DAG1* KO. Overall, these data suggest that *DAG1* KO cells respond to osmotic stress caused by an increase in NaCl concentration in the same way as control cells.

As with NaCl the appropriate concentration of PEG4000 was assessed by treating control cells with a range of concentrations and measuring the nuclear area (Figure *5.8*). Interestingly, treating with 5% had no effect on cell area whereas treating with 10% and 20% resulted in a significant decrease in cell area in a dose dependent manner. However, treatment with 30% resulted in no significant decrease in nuclear area while 40% resulted in a slight but significant decrease in nuclear area. Based on

this, 20% and 40% PEG4000 was used as both resulted in a decrease in nuclear area but interestingly, not in a concentration dependent manner.

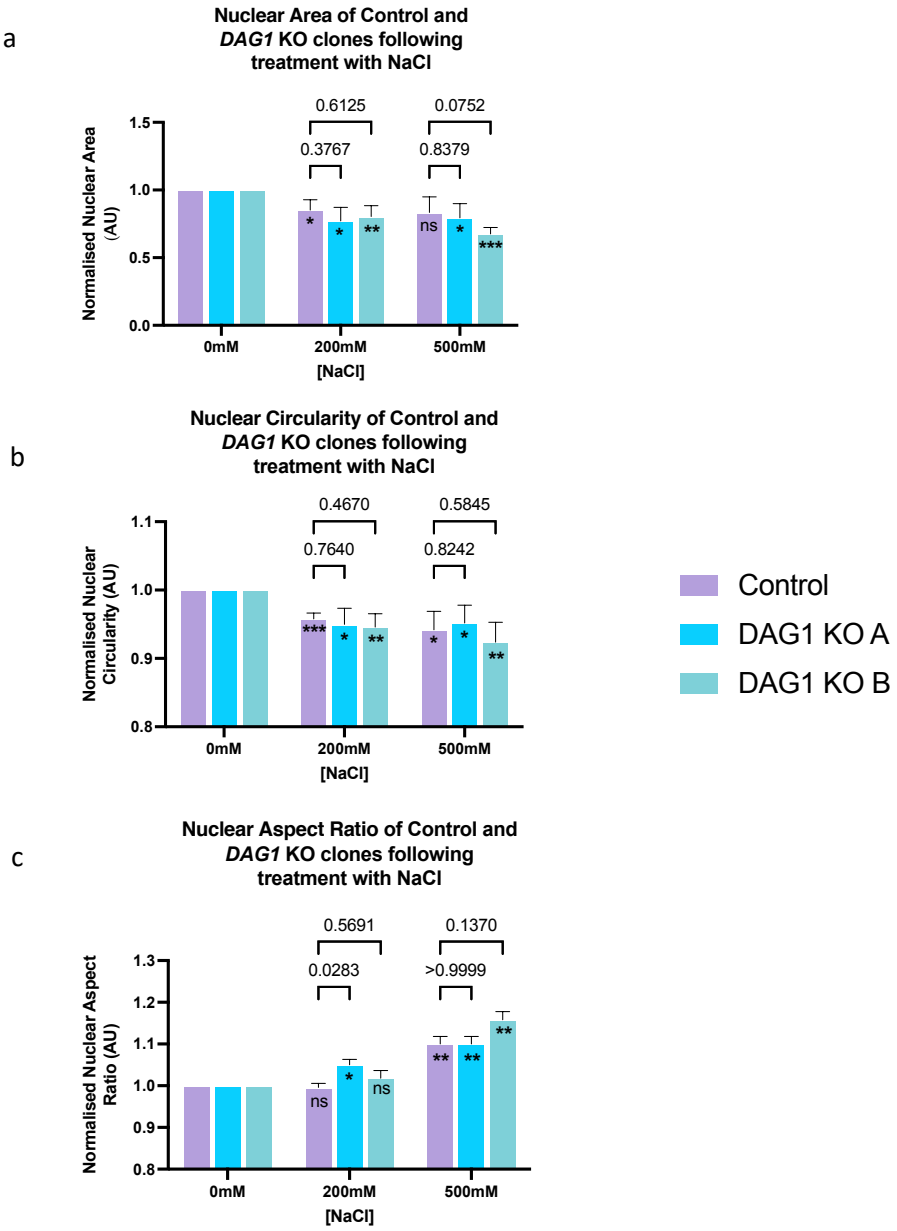

Figure 5.7 **Nuclear morphology of control and DAG1 KO clones A and B following 0mM, 200mM or 500mM NaCl treatment.** (a) Normalised nuclear area (b) normalised nuclear circularity and (c) normalised nuclear aspect ratio following 0mM, 200mM or 500mM NaCl treatment. 4 independent experiments were carried out. Control 0mM n = 111, 200mM n = 115 and 500mM n = 103. KO A 0mM n = 126, 200mM n = 119 and 500mM n = 121. KO B 0mM n = 105, 200mM n = 131 and 500mM n = 109. Graph shows mean and standard deviation. Following a two-way ANOVA test a Dunnett's multiple comparison test was used to determine the difference between 0mM, 200mM and 500mM treatment in each cell line (p value; * = <0.0332, ** = <0.0021, *** = <0.0002). A Turkey's multiple comparison test was used to determine the difference between cell lines in each treatment condition – p values are on the graph.

In order to determine if there is a difference in response between control and *DAG1* KO cells following osmotic and slight compressional stress by PEG4000 treatment, cells were subjected to either 0%, 20% or 40% PEG4000 for 30 minutes. Cells were then fixed and stained for γH2AX in order to determine levels of DNA damage and assess changes in nuclear morphology (Figure *5.9*a). Treating all cell lines with 20% PEG4000 had no effect on the levels of γH2AX as these did not differ significantly from the untreated cells (Figure *5.9*b). Additionally, there was no difference in the levels between control and *DAG1* KO clones following treatment with 20% PEG4000. Somewhat surprisingly, following treatment with 40% PEG4000 there was a decrease in the average γH2AX intensity in all conditions, this decrease was significant for control and *DAG1* KO clone B but not statistically significant for *DAG1* KO clone A. When the difference between control and *DAG1* KO clones was investigated, there was no significant difference in the relative γH2AX levels between control and KO clones (Figure *5.9*b).

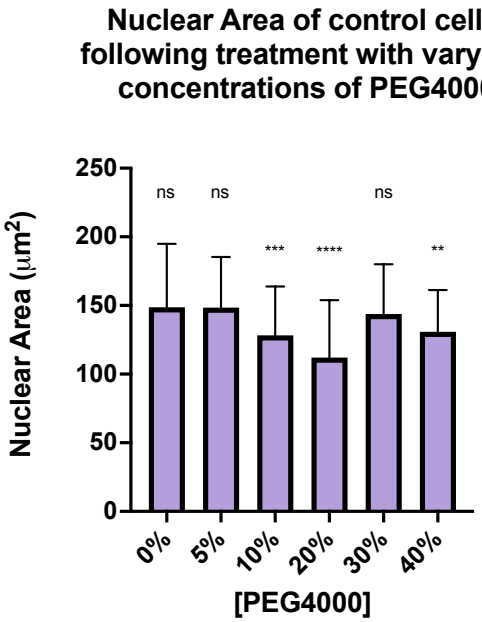

Figure 5.8 **Optimisation of PEG4000 concentration based on nuclear area of control cells.** Control cells were treated with varying concentrations of PEG4000 and nuclear area was assessed. 2 independent experiments were carried out with 109 0%, 114 5%, 106 10%, 111 20%, 136 30% and 113 40% treated cells. Graph shows mean and actual range. The one-way ANOVA test returned a p value of <0.0001 which is below the significance threshold of 0.05. For multiple comparisons, a Dunnett's multiple comparisons test was used, p values; * = <0.0332, ** = <0.0021, *** = <0.0002 and **** = <0.0001.

In addition to measuring DNA damage levels in cells treated with PEG4000, the nuclear morphology was also assessed. In the case of nuclear area there was a decrease in nuclear area for all cell lines following treatment with 20% PEG4000. However, this decrease was not statistically significant for control cells but was for both *DAG1* KO cell lines (Figure *5.10*a). Importantly, there was no statistical difference in the nuclear area of control and *DAG1* KO clones following treatment with 20% PEG4000. Surprisingly, following treatment with 40% PEG4000 there was no decrease in nuclear area for any cell line and there was no difference in the area of control or *DAG1* KO cells (Figure *5.10*a). In regard to nuclear circularity and nuclear aspect ratio there was no change in shape in any cell lines following treatment with either 20% or 40% PEG4000. There were also no differences in the nuclear circularity or aspect ratio of *DAG1* KO clones when compared with controls (Figure *5.10*b,c).

a

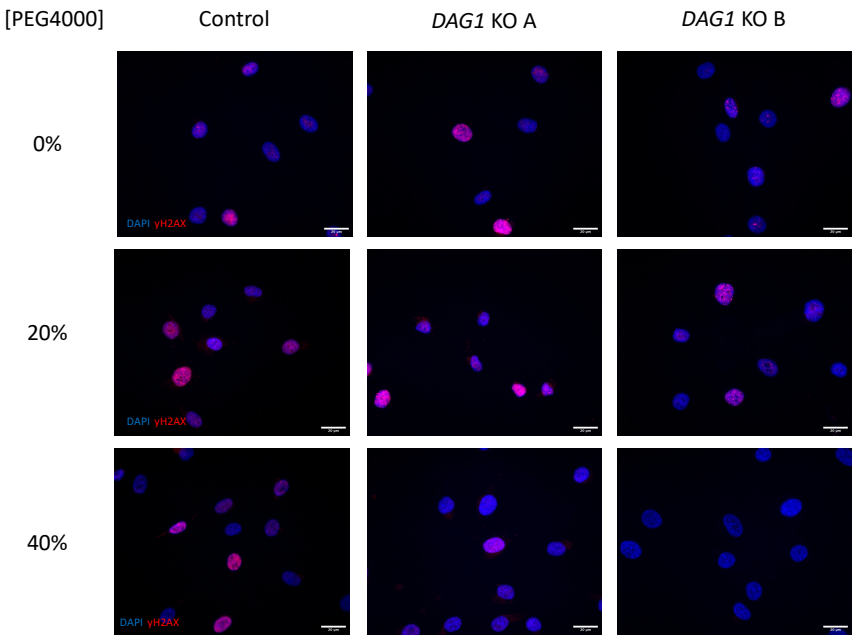

b

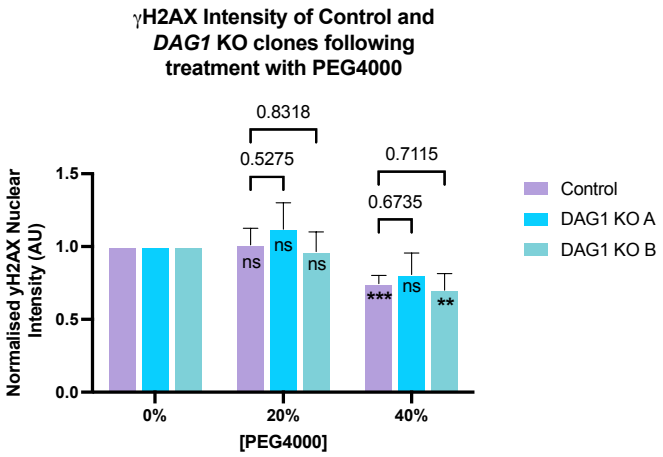

Figure 5.9 **Average nuclear levels of γH2AX in control and DAG1 KO clones A and B following 0%, 20% or 40% PEG4000 treatment.** (a) Representative images of cells grown for 24 hours before treating with PEG4000 for 30 minutes followed by fixing and staining with DAPI and γH2AX to identify levels of DNA damage at varying PEG4000 treatments. Cells were imaged using the Leica fluorescence microscope. Scale bar = 20μm. (b) Normalised nuclear levels of γH2AX following 0%, 20% or 40% PEG4000 treatment. 4 independent experiments were carried out. Control 0% n = 115, 20% n = 117 and 40% n = 124. KO A 0% n = 100, 20% n = 107 and 40% n = 102. KO B 0% n = 137, 20% n = 127 and 40% n = 113. Graph shows mean and standard deviation. Following a two-way ANOVA test a Dunnett's multiple comparison test was used to determine the difference between 0%, 20% and 40% treatment in each cell line (p value; * = <0.0332, ** = <0.0021, *** = <0.0002). A Turkey's multiple comparison test was used to determine the difference between cell lines in each treatment condition – p values are on the graph.

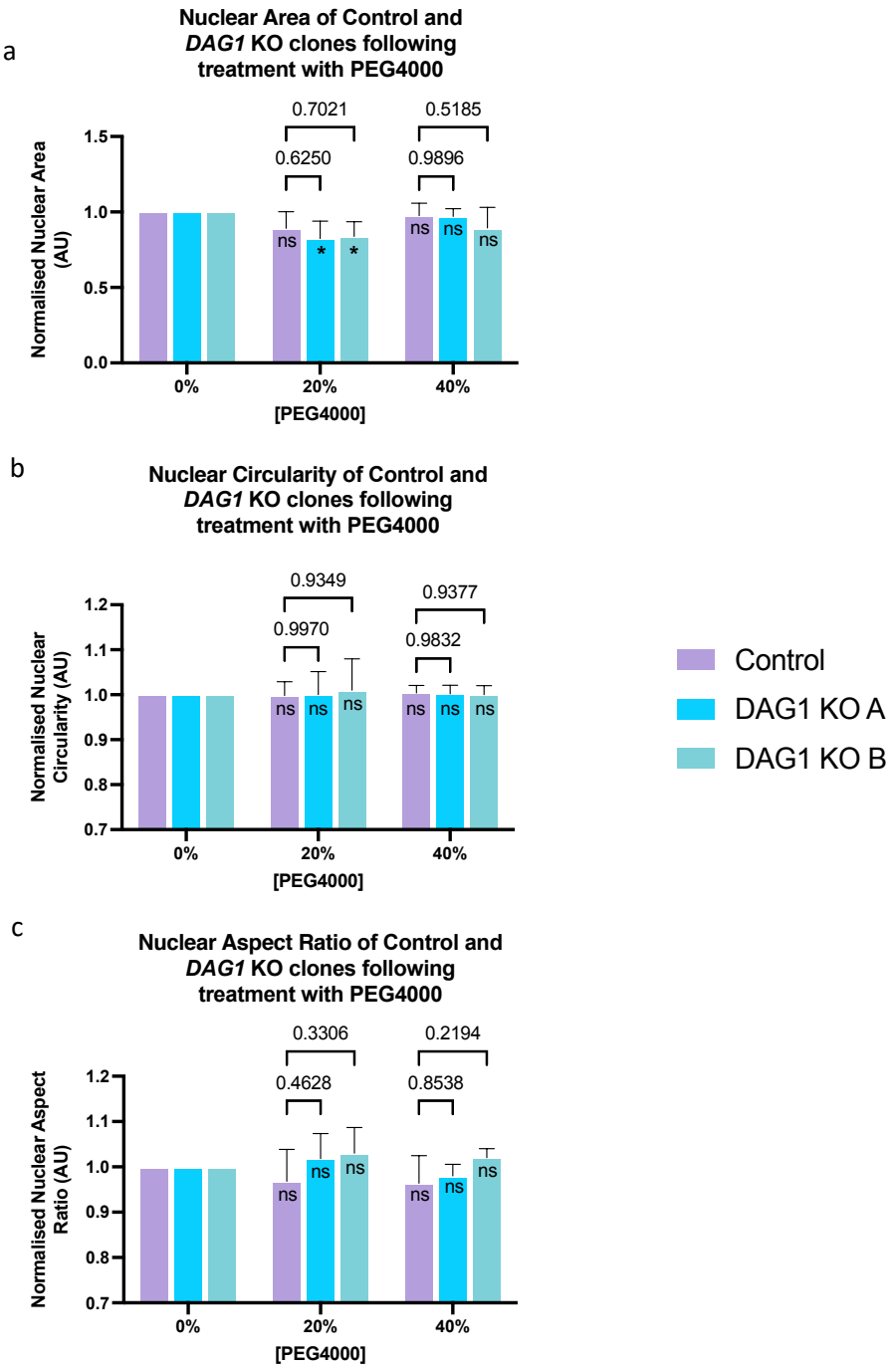

Figure 5.10 **Nuclear morphology of control and DAG1 KO clones A and B following 0%, 20% and 40% PEG4000 treatment.** (a) Normalised nuclear area (b) normalised nuclear circularity and (c) normalised nuclear aspect ratio following 0%, 20% or 40% PEG4000 treatment. 4 independent experiments were carried out. Control 0% n = 115, 20% n = 117 and 40% n = 124. KO A 0% n = 100, 20% n = 107 and 40% n = 102. KO B 0% n = 137, 20% n = 127 and 40% n = 113. Graph shows mean and standard deviation. Following a two-way ANOVA test a Dunnett's multiple comparison test was used to determine the difference between 0%, 20% and 40% treatment in each cell line (p value; * = <0.0332, ** = <0.0021, *** = <0.0002). A Turkey's multiple comparison test was used to determine the difference between cell lines in each treatment condition – p values are on the graph.

5.2.4 Investigating the response of control and *DAG1* KO cells to nuclear compression following migration through narrow pores

In order to investigate how control and *DAG1* KO cells respond to migration through restricting spaces, it is important to first understand the migration capabilities of these cell types. It has been demonstrated previously that reduced levels of β-DG in myoblasts result in reduced migration velocity while overexpressing β-DG increases migration velocity (Thompson et al., 2010b). The effect of disrupting the *DAG1* gene on cell migration has been investigated in this study. Control and *DAG1* KO cells were plated in the same glass bottom dish following treatment with CellTracker in order to identify the two cell lines. The cells were then imaged every 10 minutes for 15 hours in order to track the cell movement in normal cell culture conditions. Following analysis of this data it was found that *DAG1* KO did indeed have impaired cellular migration (Figure *5.11*). Migration velocity was significantly reduced in both *DAG1* KO clones A and B when compared with control cells (Figure *5.11*a). As would be expected from cells that migrate more slowly, *DAG1* KO cells also migrated a shorter total distance than the controls (Figure *5.11*b). Anecdotally, the control cells still migrated the greatest distance despite 58% migrating out of the frame of view within the 15 hours, while only 16% and 23% of *DAG1* KO clones A and B respectively migrated out of the frame of view within 15 hours.

Given that *DAG1* KO cells migrate more slowly, it is not possible to determine how well KO cells migrate through narrow pores compared with control cells using a transwell migration assay. However, it is possible to determine how the cells respond to constricted migration by assessing levels of DNA damage and quantifying the nuclear morphology. Cell migration through pores was initially carried out using transwell membranes containing 8μm pores (Figure *5.12*a). 8μm pores are large enough that even the larger *DAG1* KO B nuclei are not compressed during migration. This experiment was used as a control to ensure that any differences observed when cells migrated through narrow 3μm pores is due to the constriction and not due to the process of migration. Following migration through 8μm pores, control and *DAG1* KO clones were fixed and stained for γH2AX (Figure *5.12*). When comparing the relative levels of γH2AX between cells at the bottom (migrated) or the top (unmigrated) of the membrane there was no significant difference in any of the cell

lines (Figure *5.12*b). Additionally, there was no difference in the relative levels of γH2AX when either *DAG1* KO clone was compared with the control (Figure *5.12*b).

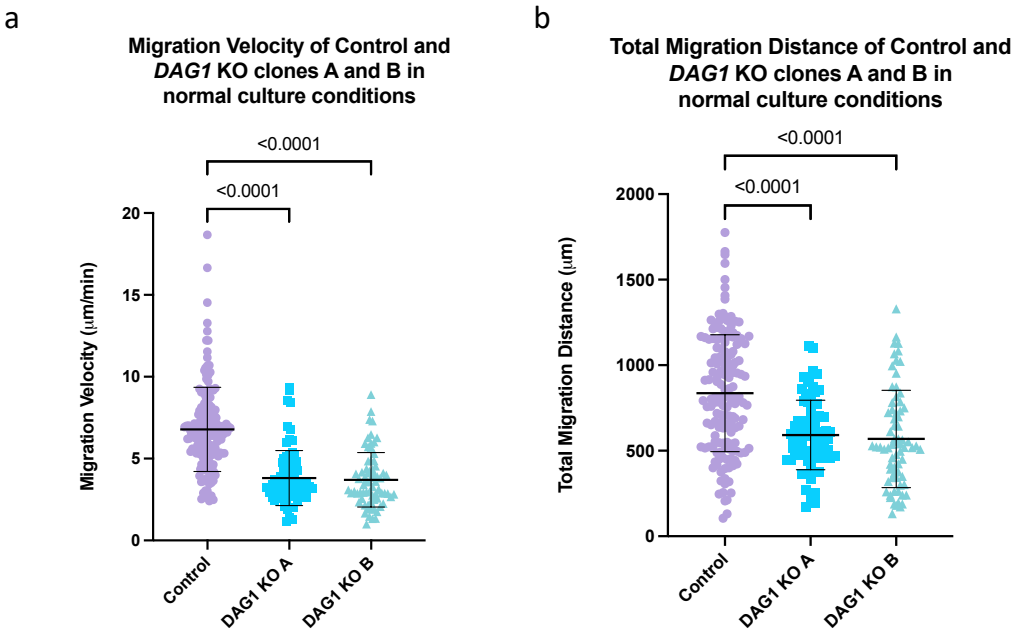

Figure 5.11 **Migration velocity and distance in control and DAG1 KO clones A and B.** (a) Cell velocity. (b) Total migration distance in 16 hours. Each coloured point indicates an individual cell. 2 independent experiments were carried out with 160 control, 150 KO A and 143 KO B cells. Graph shows mean and standard deviation. The one-way ANOVA test returned a p value of <0.0001 which is below the significance threshold of 0.05. Dunnett's multiple comparison test was also carried out, p values are on the graph.

The nuclear morphology of cells at the top or the bottom of the membrane were also quantified. The nuclear area of all cell lines was lower in the migrated cells compared with the unmigrated cells. However, this difference was only statistically significant for control and *DAG1* KO clone A (Figure *5.13*a). There was also no difference in the nuclear area when control and *DAG1* KO clone A were compared but there was a significant difference between control and *DAG1* KO clone B (Figure *5.13*a). When nuclear circularity was compared there was no statistically significant difference between migrated and unmigrated cells and there was also no difference between control and *DAG1* KO clones following migration (Figure *5.13*b). There is no difference in the nuclear aspect ratio when comparing cells at the top and bottom of the membrane for control and *DAG1* KO clone B however, there is a small but significant decrease in *DAG1* KO clone A cells following migration (Figure *5.13*c). Focusing just on migrated cells, there is no difference in the aspect ratios between

control and *DAG1* KO B but there is a small but significant difference between control and *DAG1* KO clone A (Figure *5.13*a).

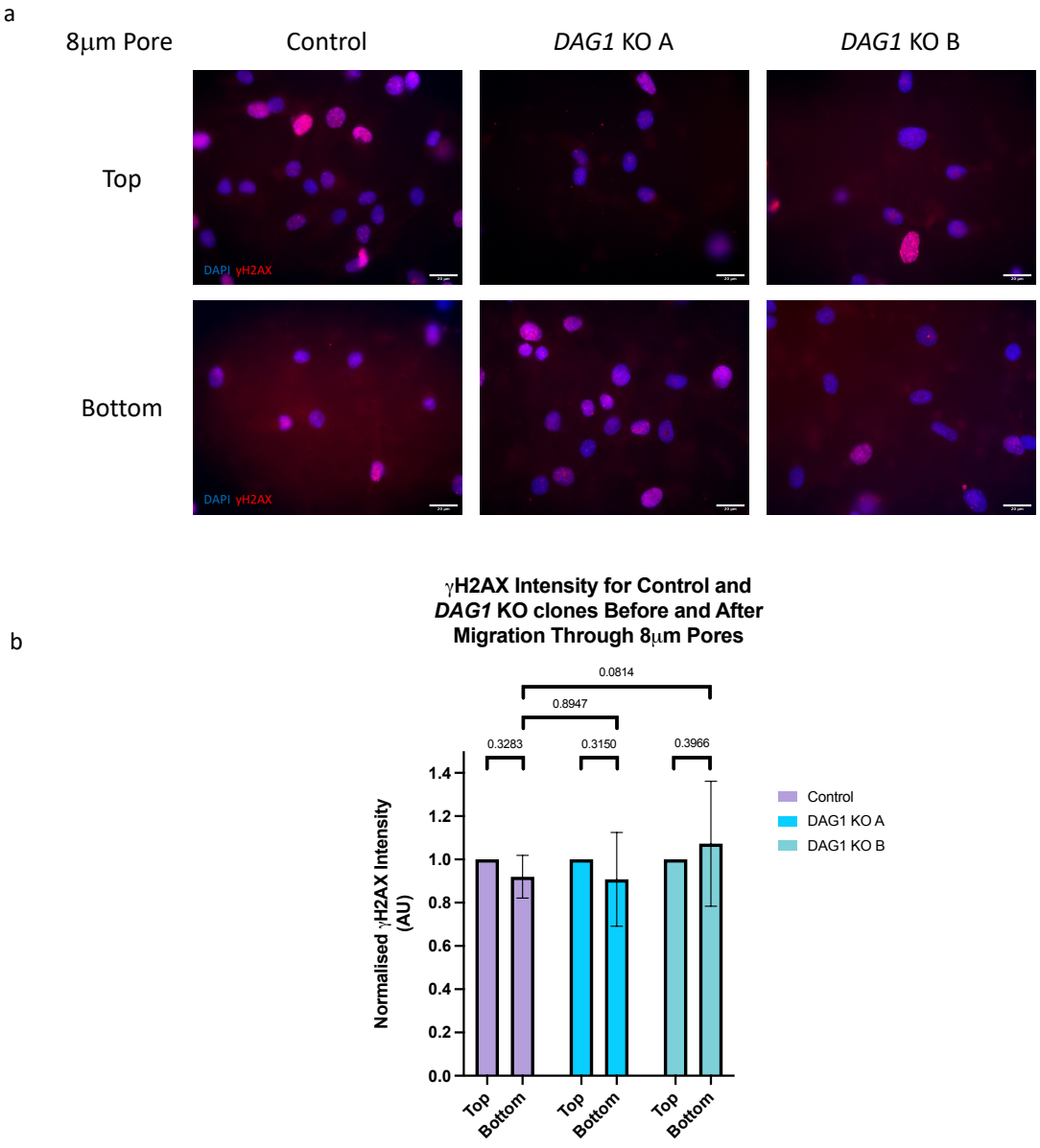

Figure 5.12 **Average nuclear levels of γH2AX in control and DAG1 KO clones A and B before and after migration through 8μm pores.** (a) Representative images of cells on either the top (unmigrated cells) or bottom (migrated cells) of the Transwell membrane. Cells were stained with DAPI and γH2AX to determine nuclear morphology and levels of DNA damage. Cells were imaged using a Leica DMIRE2 fluorescence microscope. Scale bar = 20μm. (b) Normalised nuclear levels of γH2AX in migrated or non-migrated cells. 6 independent experiments were carried out. Control top n = 159, bottom n = 162. KO A top n = 172, bottom n = 154. KO B top n = 166, bottom n = 182. Graph shows mean and standard deviation. The one-way ANOVA test returned a p value of 0.4686 which is not below the significance threshold of 0.05. For multiple comparisons, a Šídák's multiple comparisons test was used and the p values can be seen on the graph.

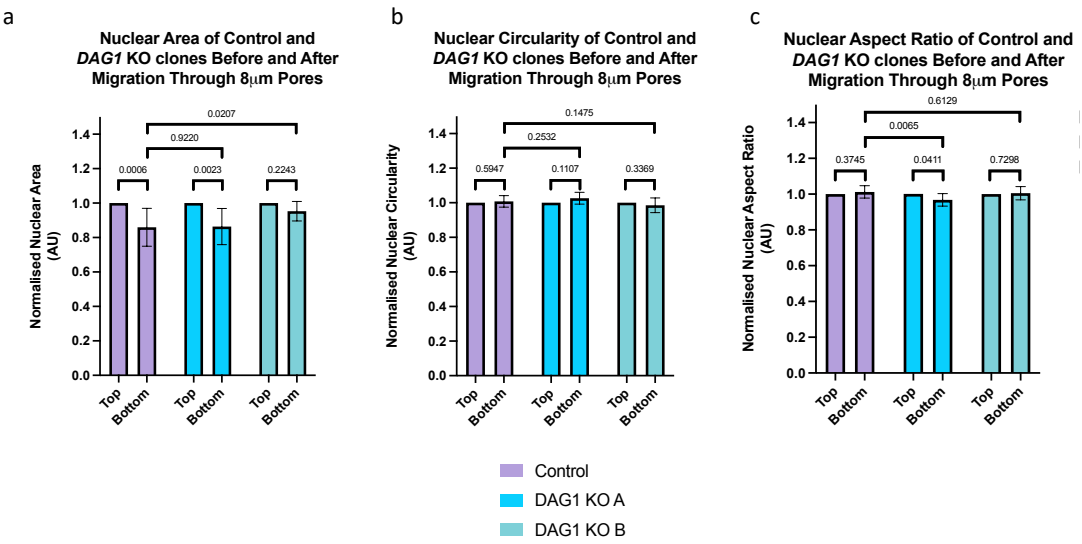

Figure 5.13 **Nuclear morphology of control and DAG1 KO clones A and B before and after migration through 8μm pores.** (a) Normalised nuclear area in migrated or non-migrated cells. 6 independent experiments were carried out. Control top n = 159, bottom n = 162. KO A top n = 172, bottom n = 154. KO B top n = 166, bottom n = 182. Graph shows mean and standard deviation. The one-way ANOVA test returned a p value of 0.0005 which is below the significance threshold of 0.05. For multiple comparisons, a Šídák's multiple comparisons test was used and the p values can be seen on the graph. (b) Normalised nuclear circularity in migrated or non-migrated cells. As above. The one-way ANOVA test returned a p value of 0.2884 which is not below the significance threshold of 0.05. For multiple comparisons, a Šídák's multiple comparisons test was used and the p values can be seen on the graph. (c) Normalised nuclear aspect ratio in migrated or non-migrated cells. As above. The one-way ANOVA test returned a p value of 0.1287 which is not below the significance threshold of 0.05. For multiple comparisons, a Šídák's multiple comparisons test was used and the p values can be seen on the graph.

Given that there are no consistent differences in how control and *DAG1* KO cells respond to migration through 8μm non-constrictive pores, these cells were then subjected to migration through 3μm constrictive pores (Figure *5.14*a). Contrary to what was expected, cells on the bottom of the membrane (therefore had migrated through the pores) did not appear to have increased levels of DNA damage (Figure *5.14*b). There was no significant difference in γH2AX intensity between the top and bottom cells in any of the cell lines but there was a large amount of variation between each independent experiment, this will be considered further in the discussion.

a

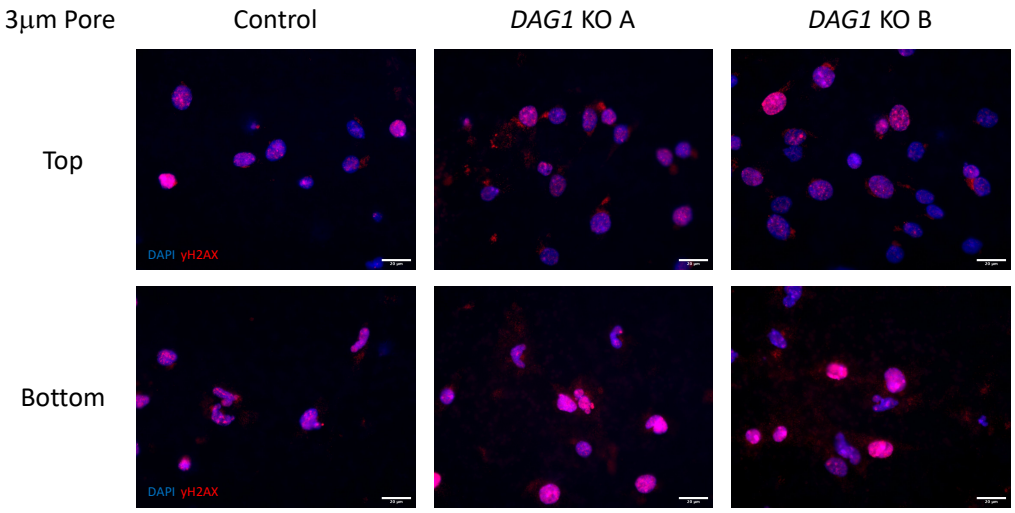

b

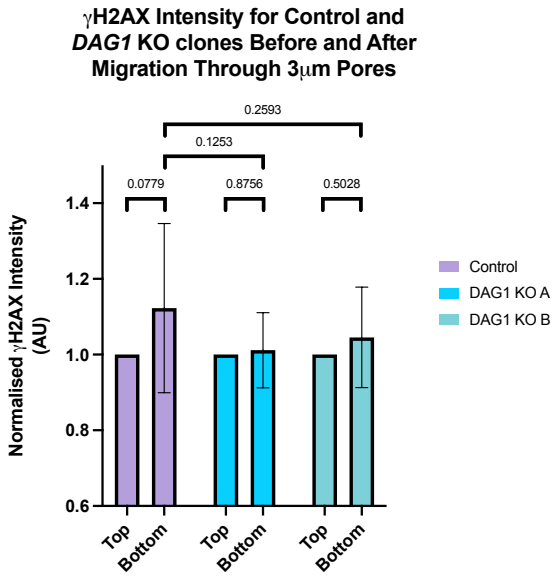

Figure 5.14 **Average nuclear levels of γH2AX in control and DAG1 KO clones A and B before and after migration through 3μm pores.** (a) Representative images of cells on either the top (unmigrated cells) or bottom (migrated cells) of the Transwell membrane. Cells were stained with DAPI and γH2AX to determine nuclear morphology and levels of DNA damage. Cells were imaged using a Leica DMIRE2 fluorescence microscope. Scale bar = 20μm (b) Normalised nuclear levels of γH2AX in migrated or non-migrated cells. 6 independent experiments were carried out. Control top n = 174, bottom n = 182. KO A top n = 173, bottom n = 168. KO B top n = 154, bottom n = 147. Graph shows mean and standard deviation. The one-way ANOVA test returned a p value of 0.4153 which is not below the significance threshold of 0.05. For multiple comparisons, a Šídák's multiple comparisons test was used and the p values can be seen on the graph.

As with migration through 8μm pores, nuclear area and nuclear shape were quantified following migration. Interestingly, there was no reduction in nuclear area for control or *DAG1* KO clone A following migration as observed in the 8μm pore experiment. However, *DAG1* KO clone B cells that had migrated had a significantly

reduced nuclear area compared with unmigrated cells (Figure *5.15*a). When comparing nuclear area of migrated cells there was no difference in the relative area between control and *DAG1* KO A but there was a significant difference between control and *DAG1* KO B (Figure *5.15*a). When nuclear circularity was quantified, there was a clear significant difference between cells on the top and the bottom of the membrane for all cell types (Figure *5.15*b). The significant reduction in nuclear circularity indicates that migration results in a loss of nuclear shape. However, the extent of nuclear circularity change between control and *DAG1* KO clones following migration is not significantly different. A similar trend was observed when nuclear aspect ratio was measured (Figure *5.15*c). A consistent increase in nuclear aspect ratio was measured in migrated cells compared with non-migrated cells for both control and *DAG1* KO cells. There is also no statistically significant difference between the relative aspect ratios of control or *DAG1* KO A migrated cells. However, there is a significant difference between the control and *DAG1* KO B migrated cells, but this difference is very small (Figure *5.15*c).

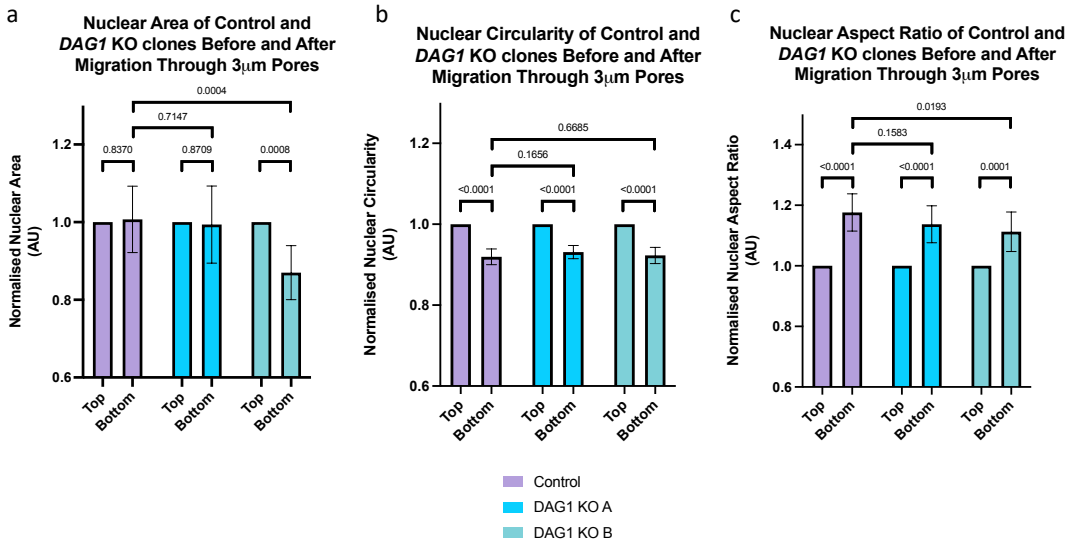

Figure 5.15 **Nuclear morphology of control and DAG1 KO clones A and B before and after migration through 3μm pores.** (a) Normalised nuclear area in migrated or non-migrated cells. 6 independent experiments were carried out. Control top n = 174, bottom n = 182. KO A top n = 173, bottom n = 168. KO B top n = 154, bottom n = 147. Graph shows mean and standard deviation. The one-way ANOVA test returned a p value of 0.0029 which is below the significance threshold of 0.05. For multiple comparisons, a Šídák's multiple comparisons test was used and the p values can be seen on the graph. (b) Normalised nuclear circularity and (c) normalised nuclear aspect ratio in migrated or non-migrated cells. As before. The one-way ANOVA test returned a p value of <0.0001 which is below the significance threshold of 0.05. For multiple comparisons, a Šídák's multiple comparisons test was used and the p values can be seen on the graph.

Taken together, the data from migration through 8μm pores suggest that migrating through a non-constricting environment results in a small reduction in nuclear area but has no effect on levels of γH2AX or nuclear shape. While migration through the constricting 3μm environment does not result in a reduction in nuclear area and does not affect the levels of γH2AX but does result in large and significant changes in nuclear shape. Importantly, this data demonstrates that *DAG1* KO cells do not respond differently than control cells to confined migration when DNA damage and nuclear morphology are measured.

5.2.5 Investigating the response of control and *DAG1* KO cells to nuclear compression *in situ*

In addition to investigating the response to active compression as cells migrate through narrow pores, passive compression was also tested by placing a weighted insert on top of growing cells *in situ*. The weighted inserts had a mass of ~14g which equates to ~800 Pa of compressive force. Due to the technical limitations, it is not possible to fix and stain cells following cell compression, so cells were imaged live after 1 hour of compression (Figure *5.16*a). Therefore, it was only possible to assess nuclear morphology in this assay while levels of DNA damage were not determined. Following 1 hour of compression the relative nuclear area was reduced significantly in compressed cells compared with non-compressed cells, this was true for control and both *DAG1* KO clones (Figure *5.16*b). Additionally, there was a significant difference between compressed control cells and compressed *DAG1* KO A cells however, there was no difference between control and *DAG1* KO B cells. In regard to nuclear circularity there was a significant decrease in compressed compared with non-compressed cells for both control and *DAG1* KO A samples however, no difference between the two *DAG1* KO B conditions (Figure *5.16*c). The difference in circularity between compressed control and *DAG1* KO A samples was not significant whereas the control and *DAG1* KO B samples differed significantly. Overall, this data suggests that there are nuclear morphology changes following passive compression,

as with active compression, but there is no consistent difference in the response between control cells and *DAG1* KO cells.

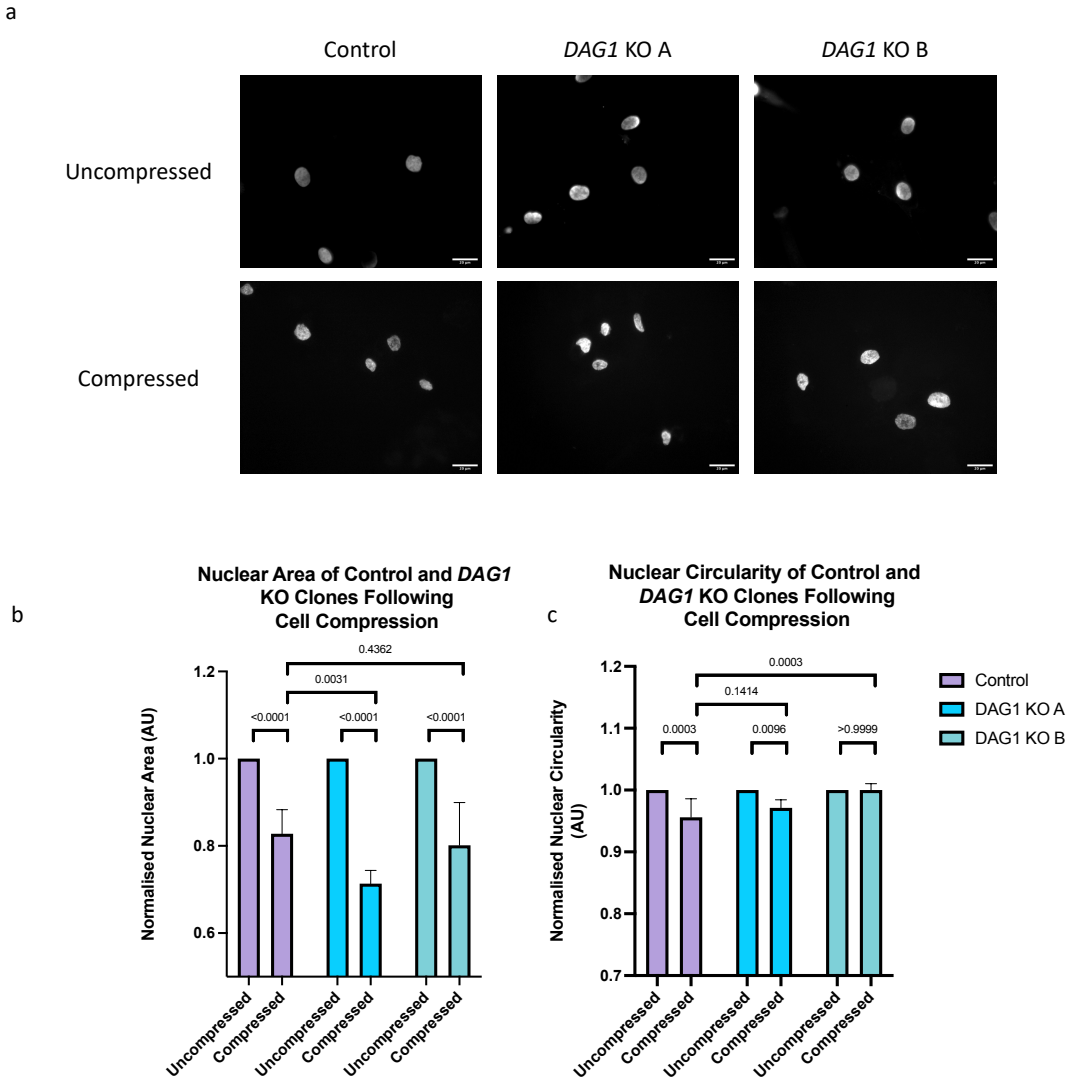

Figure 5.16 **Nuclear morphology of control and DAG1 KO clones A and B subjected to passive compressional stress.** (a) Representative images of either compressed or uncompressed cells. Cells were stained with Hoechst 33342 to determine nuclear morphology of live cells. Cells were imaged using a Leica DMIRE2 fluorescence microscope. Scale bar = 20μm. (b) Normalised nuclear area of compressed or uncompressed cells. 4 independent experiments were carried out. Control uncompressed n = 119, compressed n = 123. KO A uncompressed n = 133, compressed n = 107. KO B uncompressed n = 127, compressed n = 102. Graph shows mean and standard deviation. The one-way ANOVA test returned a p value of <0.0001 which is below the significance threshold of 0.05. For multiple comparisons, a Šídák's multiple comparisons test was used and the p values can be seen on the graph. (c) Normalised nuclear circularity of compressed or uncompressed cells. As before. The one-way ANOVA test returned a p value of 0.0005 which is below the significance threshold of 0.05. For multiple comparisons, a Šídák's multiple comparisons test was used and the p values can be seen on the graph.

It is possible to use AFM to subject cells/nuclei to compressive forces. This is generally used in concert with high-resolution imaging to study biochemical responses to

compression (Cho et al., 2019). Additionally, it has been suggested that mechanical stress in the form of cell stretching may result in changes to nuclear stiffness (Ahrens et al., 2019). Therefore, in this study AFM was used to compress the cells over the nuclear region with a force of ~1 kPa and then the change in nuclear stiffness was measured over a period of 30 minutes. A preliminary assessment using a single control cell suggested that there was an initial increase in nuclear stiffness following compression followed by a decrease to a lower stiffness than the starting value (Figure *5.17*a). The next question following this is whether this was a consistent trend for all control cells and then further, is it consistent in *DAG1* KO clones as well. This was tested with at least 12 cells for each sample. This initial trend noticed in a lone control cell was not consistently the case when multiple cells were measured resulting in an almost consistent normalised value of 1 throughout the full 30 minutes (Figure *5.17*b). The same results were observed for *DAG1* KO clones A and B, the normalised value remained at ~1 during the 30-minute time period (Figure *5.17*b). No statistical test was carried out as there was so much overlap between values. These data suggest that there is no clear trend in mechanical response to low-level nuclear compression produced by an AFM cantilever in control or *DAG1* KO cells.

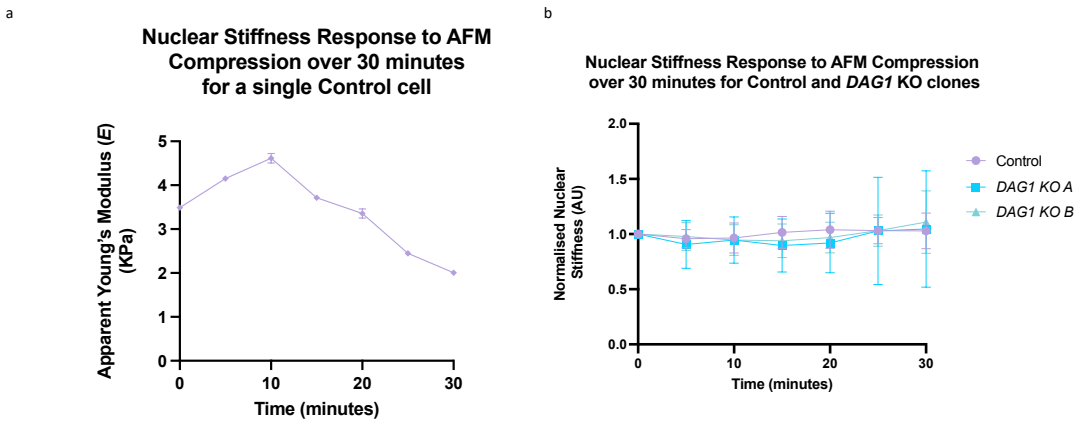

Figure 5.17 **Mechanical response to cell compression.** (a) Preliminary test of a single control cell. The cell was compressed over the nuclear region and the nuclear stiffness was measured every 5 minutes for 30 minutes. (b) Mechanical response to nuclear compression of control and DAG1 KO clones A and B were measured using AFM. The nuclear stiffness was measured every 5 minutes for a total of 30 minutes.

5.3 Discussion

The work presented in this chapter has aimed to determine if the response to mechanical stress differs in *DAG1* KO cells when compared with control. On the whole, the data presented here would suggest that this is not the case, the *DAG1* KO cells appear to respond to chemical, osmotic and compressional stress in a broadly similar way as controls. There are multiple examples throughout this chapter where one of the *DAG1* KO clones responds differently to the control, however it is only those differences that are consistent across both KO clones that would be considered a genuine difference. This was not the case for any experiments described in this chapter and any differences observed could be due to clonal variation or other artefactual variation.

5.3.1 Discrepancies from PEG4000 treatment

PEG has been used previously to osmotically stress mammalian cells and in these studies an increase in PEG concentration results in an increase in osmotic pressure and ultimately a decrease in nuclear volume (Khavari and Ehrlicher, 2019; Zhou et al., 2009). There is no evidence of a bimodal response where nuclear size decrease with concentration up to a point where it then increases again as observed in this study (shown in Figure *5.8*). The observation of a bimodal response was further confirmed following treatment with 20% and 40% PEG4000 where not all cell types had a significantly reduced nuclear area following 20% treatment and none of the cell types had a significantly reduced area following the 40% treatment. One explanation for the disparity between these results and those previously published is that lower molecular weight PEG was used for the two studies mentioned previously. Zhou et al. (2009) used 400 Da PEG while Khavari and Ehrlicher (2019) used 1500 Da PEG. However, this is unlikely to be the reason as in both these cases the range of concentrations used result in pressures between 0.5 MPa and 5 MPa (Cohen et al., 2009) and these all resulted in a decrease in nuclear volume. The

concentrations of 20% and 40% of PEG4000 result in pressures of 0.72 MPa and 4.3 MPa respectively (Cohen et al., 2009). These values sit between the values tested in the previous studies. Therefore, it is unlikely that the molecular weight of the PEG used would explain this discrepancy. An alternative explanation is that the cells did not have long enough to equilibrate in the PEG containing media, however, this again is unlikely to be the reason as Khavari and Ehrlicher (2019) observe their results within 20 minutes of incubation while cells in this study were incubated for 30 minutes prior to staining and imaging. The only other difference between the experiments carried out here and those described previously is that at least one of the studies used detached cells that were imaged on a thin layer of agar (Khavari and Ehrlicher, 2019) while in this study cells were attached to stiff glass coverslips. This could explain the discrepancy in these results as it has been shown that both cell and nuclear size decreases on softer matrix (Swift et al., 2013a), so this could potentially exacerbate the nuclear size differences. Ultimately, it is unclear why the nuclear area in this study doesn't follow a dose dependent regime as PEG concentration increases.

Unlike nuclear area, following treatment with PEG, there is no previous evidence to indicate how DNA damage is affected by PEG. Therefore, it is unknown whether the result suggesting the levels of DNA damage decreased in cells treated with 40% PEG are consistent across other cell types. However, one would expect that following osmotic stress and possible low levels of compressive stress there would be an increase in levels of γH2AX as observed in NaCl osmotic stress experiments (shown in Figure *5.6*). Conversely, in cells treated with 40% PEG there is a decrease in levels of γH2AX in both control and *DAG1* KO clone B cells (shown in Figure *5.9*). As mentioned before, this has not been investigated in mammalian cells, however it has been studied in plants. PEG is used in plants to better understand growing conditions and it has been found that levels of antioxidant proteins increase following treatment with PEG, however, this is at much lower concentrations than those used in this study and plants likely have very different mechanisms for dealing with osmotic stress (Jamshidi Goharrizi et al., 2020; Sahoo et al., 2020). One explanation is that the increase in osmotic pressure results in loss of nuclear water and therefore results in macromolecular crowding (Finan et al., 2009) and this may reduce the mobility of

DNA damage response factors resulting in a reduction in γH2AX. However, this is unlikely for two reasons; (1) an increase in γH2AX is observed in cells treated with 500mM NaCl which results in extreme osmotic stress and (2) there is no decrease in nuclear area when cells are treated with 40% PEG suggesting the nuclei are not osmotically stressed to the point of extreme macromolecular crowding. As with the unexpected nuclear area results there is no clear explanation for the observed decrease in γH2AX following treatment with 40% PEG.

5.3.2 Observations from Transwell migration experiments

It is clear from the data presented in this chapter that *DAG1* KO cells do not respond to migrating through narrow pores any differently than control cells when DNA damage and nuclear morphology is assessed. However, there are two results from these experiments that were not as expected. The first is that nuclear area decreased in control and *DAG1* KO A cells but not *DAG1* KO B cells following migration through 8μm pores but following migration through 3μm pores conversely only *DAG1* KO B cells had a decreased area (as shown in Figure *5.13*a and Figure *5.15*a). The second unexpected result is that following migration through 3μm pores there was no increase in levels of γH2AX which has been observed across many previous studies (Irianto et al., 2017; Mukherjee et al., 2020; Patteson et al., 2019a; Pfeifer et al., 2018; Xia et al., 2019), but there was evidence of abnormal nuclear morphology.

One possible explanation for why there is a decrease in nuclear area following migration through 8μm pores but not 3μm pores is due to cell density. Cell density is one of the key regulators of cell and nuclear size as it is regulated by YAP (Mugahid et al., 2020). High cell density results in a decrease in nuclear size. Cells were seeded at an extremely high cell density at the start of the experiment and then allowed to grow and migrate freely for 48 hours. In the 8μm experiment cells are able to migrate through the pores with relative ease which results in a large number migrating through the pores. This could result in a high cell density at the bottom and a lower cell density at the top. The high cell density at the bottom would result in a reduction

in nuclear size at the bottom and less so at the top which would explain the results in Figure *5.13*a. On the other hand, it is difficult and requires a lot more time for cells to migrate through the 3μm pores which could mean there is a higher cell density at the top and a lower cell density at the bottom or at least a more equal density distribution. This would either result in the cells at the top being slightly smaller due to high cell density or neither top nor bottom having sufficiently high cell density to affect nuclear size, resulting in the more equal values observed in Figure *5.15*a. This does not explain the difference seen in *DAG1* KO clone B but any differences here could be due to the fact the nuclei and cells were larger to start with or could simply be down to clonal variation.

An alternative explanation for the nuclear area differences above and below the filter, could be due to selectivity. In the relatively large population of cells there will be some smaller and some larger cells, some of these larger cells may be larger than the pore size and therefore do not migrate through while smaller cells migrate through quickly, resulting in an accumulation of the smaller cells on the bottom of the 8μm pore membrane. In the case of the 3μm pores, all cells are too large for the pores, so this selection pressure is reduced. The fact that *DAG1* KO clone B doesn't fit the trend for either 3μm or 8μm pores provides support for this suggestion. This clone is, on average, significantly larger than the other two cells. It is possible that there are far fewer smaller cells, making the selection pressure less of a factor. Ultimately, it is not possible to determine the reason behind this observation using Transwell migration assays, it would require live visualisation of the cells migrating through channels in order to answer this question.

The question of why the levels of γH2AX did not increase following migration through 3μm pores is more perplexing. It is clear from previous reports that DNA damage increases following constricting migration and that this damage can accumulate through multiple rounds of migration (Pfeifer et al., 2018) or it can be repaired and returned to baseline levels (Irianto et al., 2017). Given that there is an obvious difference in the nuclear shape between the top and the bottom as described in

other studies (Irianto et al., 2017; Patteson et al., 2019a; Pfeifer et al., 2018; Xia et al., 2019), it is clear that the correct side of the membrane is being imaged and that the cells on the bottom of the membrane have indeed migrated through the pores. Two possible explanations for this difference are (1) the increased level of background intensity has resulted in a large amount of variation between independent experiments and (2) cells may have repaired the DNA damage prior to cell fixing and staining.

Six independent experiments were carried out for the 3μm Transwell migration assay and for all three cell lines at least 4 of the 6 values indicated an increase in levels of γH2AX compared with the unmigrated cells. However, some of these experiments resulted in a value <1 indicating there was less γH2AX in the migrated nuclei compared with the unmigrated. This suggests that there is a general trend for an increase in levels of γH2AX but this was not consistently the case. It is possible that this discrepancy is due to increased background intensity on both the top and the bottom of the membrane as the membrane appeared to retain more antibodies and therefore more fluorophore than would normally be seen on glass coverslips.

The other possible explanation for the lack of difference in DNA damage between migrated and unmigrated cells is the amount of time that cells were allowed to migrate. Cells were seeded and then incubated for 48 hours before fixing and staining. This time frame was chosen as after 24 hours there were almost no cells on the bottom of the membrane in any condition, this would not give a sufficient number of cells for any meaningful statistical analysis. Previous reports using this assay have only allowed cells to migrated for 24 hours (Irianto et al., 2017; Pfeifer et al., 2018; Xia et al., 2019), however, they have used cancer cell lines which are both far softer than myoblasts and more migratory (Efremov et al., 2014; Krause et al., 2013; Lekka and Pabijan, 2019). Importantly, it has been shown that DNA repair following migration through narrow pores/channels occurs within 24 hours and can occur even more rapidly than that (Raab et al., 2016; Shah et al., 2020). This means that the methodology used in this study is not capable of identifying differences in

levels of DNA damage due to the longer time scale it takes for cells to migrate but the relatively quick time scale in which cells can repair DNA damage following constricted migration.

The transwell migration assay provides a good starting point for investigating cell migration through narrow channels however, the main limitation is the inability to track the migration in real time. In an ideal situation it would be possible to observe the migration of control and *DAG1* KO cells live using a microfluidic device with defined pore sizes as described in section 5.1.1. However, due to the technical and financial requirements to establish these devices it was not possible within the bounds and timescale of this project. If this had been achievable it would have been used to observe cell migration directly and it would be possible to track levels of DNA damage as they occur.

5.3.3 Limitations of passive cell compression assay

As with active cell compression the ideal set up for carrying out passive cell compression assays is to use a specifically designed device like that described by Shah et al. (2020). This allows the specific adjustment for compression to a pre-determined height, it allows removal and reapplication of compressional stress and it allows cells to be fixed and stained which allows additional information to be obtained (Shah et al., 2020). Similar to the migration microfluidic device, the technical, financial and time requirements to establish this process was not possible for this project. Despite this the methodology used was sufficient to provide information on nuclear morphology and this was in general agreement with the constricted migration data. In both cases compression resulted in a reduction in nuclear circularity for both control and *DAG1* KO A cells. There was also a significant reduction in nuclear area when cells were passively compressed which may indicate this might be the case as cells migrate through constricted environments, however, nuclear area recovers more rapidly than nuclear circularity when the cells have finished migrating.

The other limitation with the passive compression assays is the AFM method used. Ideally, the AFM would have the capabilities to carry out high-resolution fluorescence imaging with either an associated light sheet or confocal microscope. This would allow the tracking of key cytoskeletal/nucleoskeletal proteins and levels of DNA damage as the cells respond to nuclear compression. The other limitation, particularly with the experiment outlined here, is the flexibility of the cantilever. The most accurate way to carry out this experiment would be to use a very stiff cantilever to compress the cells to ensure all compressional forces was imparted on the cell and not dissipated through the cantilever. However, the cantilever needs to be soft in order to accurately measure the mechanical properties of the soft cell and it is not possible to easily switch between cantilevers in a relevant time frame to carry out this experiment. Therefore, these limitations may have had tangible impacts on the results observed.

5.3.4 Other forms of mechanical stress that were investigated

In addition to cell compression there are other forms of mechanical stress that can be applied to cells. Cell stretching is a popular form of generating cell stress and this can be applied either as a single stretching event or applied as cyclic stretching. Additionally, cells can be stretched uniaxially or biaxially. An attempt to establish a cell stretching set up for this study was made, however, this was unfortunately unsuccessful due to time constraints. If these attempts had been successful, this would have been the preferred method of mechanical stress applied to myoblasts as this is closest to the type of stresses they would be subjected to *in vivo*. Myoblasts are subjected to passive stretching as they migrate along muscle filaments which are contracting and relaxing. Additionally, they have the potential to differentiate into myotubes which are subjected to constant stretching and relaxation cycles during muscle contraction (Chen et al., 2020; Soltow et al., 2013).

An alternative form of mechanical stress is shear stress – this can be most easily applied by simply pumping media over cultured cells and this can replicate shear stress forces exerted on endothelial cells during blood flow (Deguchi et al., 2005;

Jetta et al., 2019). In this study a set up for applying shear stress was established, however, actual experiments were not carried out. There are two main reasons for this; (1) there is very little physiological relevance as myoblasts are unlikely to be subjected to forms of shear stress and (2) this was only going to be investigated if *DAG1* KO cells responded differently to control cells following compressional forces in order to determine if the response was specific to compression or was universal for multiple forms of mechanical stress.

Compressional stress was used as the form of mechanical stress applied in this study because it was an affordable, commercially available way of investigating mechanical properties that has been reported extensively in the literature. Therefore, there was no requirement to design a new technically demanding protocol. Additionally, cell compression, particularly through confined migration, may be physiologically relevant. Myoblasts are involved in migration through basement membrane during embryogenesis and there is eclectic research implicating DG in cancer and cancer progression as discussed in section 1.1.5.2. In the context of cancer, confined migration is extremely important in transformation from non-malignant to malignant forms.

In summary, the results presented in this chapter suggest that cells lacking DG do not respond differently to cells expressing DG when subjected to chemical, osmotic or mechanical stress. These data, along with data presented in chapter 4, suggest that DG has minimal effects on nuclear mechanics and nuclear response to mechanical stress in human myoblasts.

6 Discussion

There has been fairly extensive research into the nuclear role of β-DG, however, the majority of this research has been conducted by a single group. The published articles investigating nuclear β-DG vary in quality with some being rigorous and very convincing while others lack appropriate controls to draw any genuine conclusions. This range of quality makes it difficult to comprehensively understand the role β-DG has in the nucleus. In addition to the varying quality of published literature, this present study and Matt Cook's study (Cook, 2021) directly contradict many of the findings in the literature. This further complicates the overall understanding of a role for β-DG in the nucleus.

Based on all the available evidence it is probable that β-DG is found in the nucleus, however, whether it resides at the NE or if it is present transiently is not immediately clear. Additionally, the role of β-DG at the nucleus is not conclusive and it is possible that we, as investigators, have not yet asked the right questions to allow us to fully dissect the nuclear function.

6.1 Role of DG in the nucleus

6.1.1 Nuclear localisation of β-DG

β-DG has been frequently reported to localise to the nucleus in a range of cell lines from multiple organisms including human and mouse (Fuentes-Mera et al., 2006; Gonzalez-Ramirez et al., 2008; Mathew et al., 2013; Rodríguez-Munoz et al., 2015; Villarreal-Silva et al., 2010). Further, in this study β-DG has been shown to be present in the nucleus of KM155 human myoblast cells as shown by immunofluorescence staining and western blotting of nuclear and cytoplasmic cell fractions (chapter 3, Figure *3.1* and Figure 3.2). However, when a range of full-length tagged DG constructs were used to better identify subcellular localisation without the use of β-DG antibodies, there appeared to be little nuclear localisation (Cook, 2021; Leocadio-

Victoria, 2015). This lack of nuclear localisation could be due to incorrect processing due to the addition of tags, but processing was investigated and fragment sizes were as expected, however, it is possible the tags altered or affected other forms of post-translational modifications. These results call into question the validity of β-DG antibodies when trying to determine nuclear localisation. GFP tagged β-DG has also been used previously, this comes with its own processing caveats but there is compelling evidence that mutating the nuclear exit signal in a β-DG-GFP construct results in consistent nuclear accumulation. These results also indicated that the mutant β-DG-GFP construct accumulated in the nucleoplasm and was not restricted to any particular nuclear compartment (NE or nucleoli) (Vélez-Aguilera et al., 2018).

Mass spectrometry has been used abundantly to identify interacting proteins or proteins that reside in specific cellular compartments. Looking at available mass spectrometry data it is possible to probe for the presence of β-DG at the nucleus. In multiple studies when either the nucleus or just NE fractions from a range of cell types including muscle were subjected to mass spectrometry analysis there was no evidence of DG (Buchwalter et al., 2019; Korfali et al., 2012; Schirmer et al., 2003; Swift et al., 2013b; Wilkie et al., 2011). Additionally, when the interactomes of nuclear envelope proteins LEM2, MAN1 and emerin were assessed DG was not associated with any of these proteins (Moser et al., 2020). Further, a BioID experiment using ONM protein Nesprin-1α was carried out, DG was not identified (Gimpel et al., 2017). However, this would be expected if β-DG localises to the INM. VAPB, which is a membrane protein that localises to both the ER and the INM, was used to identify proteins at the INM and DG was not identified, but interestingly dystrophin was (James et al., 2019). This is in agreement with earlier studies investigating the nuclear localisation of the short dystrophin isoform Dp71 (Fuentes-Mera et al., 2006; González et al., 2000; Marquez et al., 2003; Oppizzi et al., 2008). Despite the lack of evidence of nuclear DG in mammalian cell lines investigated using mass spectrometry data there is some evidence of nuclear DG from *Drosophila* when studied with mass spectrometry. In this study the DG interactome was investigated and identified multiple nuclear proteins. A number of histones were associated with

DG as were two NE proteins; baf and msp300 - equivalent to mammalian nesprins (Yatsenko et al., 2020). However, one issue with this particular study is they did not look at the nuclear fraction specifically, these interactions were determined from whole cell lysates which means the interactions could occur in other organelles such as the ER during processing, or they could occur following nuclear/cell rupture. Thus, these interactions are not necessarily indicative of nuclear localisation of DG.

In addition to localisation studies by either visualisation or mass spectrometry analysis the functional nuclear data must also be considered. There have been reports of increased nuclear-centrosome distance in β-DG knockdown cells (Martínez-Vieyra et al., 2013), *DAG1* KO mouse cells (Gómez-Monsiváis et al., 2020) and cells subjected to nuclear accumulation of β-DG (Vélez-Aguilera et al., 2018). Additionally, increased nuclear-centrosome distance has also been observed in the *DAG1* KO human myoblasts used in this study (Cook, 2021). Emerin is thought to play a key role in regulating nuclear-centrosome distance (Salpingidou et al., 2007), however, it has been shown both in this study and by Matt Cook (Cook, 2021) that the level and localisation of emerin is not changed in *DAG1* disrupted cells. This change in nuclear-centrosome distance had been previously attributed to a mislocalisation of emerin (Gómez-Monsiváis et al., 2020; Martínez-Vieyra et al., 2013; Vélez-Aguilera et al., 2018), however, the same observation in KM155 human myoblasts where localisation of emerin is not affected suggests this is not the case. This leads to the question that if β-DG is not localised to the nucleus and is not involved in regulating emerin localisation how does a lack of, or accumulation of, β-DG result in this increased distance. This question requires further study as DG may be involved in regulating the levels or localisation of an as yet unidentified protein involved in regulating nuclear-centrosome distance.

In addition to nuclear-centrosome distance, nuclear stiffness is also different in *DAG1* KO cells compared with control. This is not the case when the nuclei are measured within the whole cell environment, but isolation of the nuclei allowed small differences to be measured (chapter 4, Figure *4.29*). As these nuclei are separated

from all cytoplasmic and cytoskeletal influence the observed differences must come from a difference in the nucleus itself. There are a limited number of studies that investigate isolated nuclei stiffness and even fewer that look at the influence of different nuclear proteins. However, one study does suggest that reduced levels of lamin B1 result in a decrease in isolated nuclear stiffness and an increase in lamin B1 results in increased stiffness (Ferrera et al., 2014). However, the levels of lamin B1 in *DAG1* KO cells used in this study do not differ significantly from the control so this is unlikely to be the explanation. It is possible that this small difference in nuclear stiffness is related to the difference in nuclear size, however, it is not possible to conclude that from this study. Further experiments are required to gain a better understanding of the impact DG has on isolated nuclear stiffness.

Based on the data presented in this study and that of studies published previously it is difficult to convincingly conclude either way whether under normal wild type conditions β-DG is localised to the nucleus or not. There is certainly strong evidence for nuclear localisation however, it is difficult to understand why β-DG is not detected in any mass spec experiments. Despite this there are sparse but clear phenotypic differences (nuclear stiffness, nucleus-centrosome distance) between the nuclei of cells lacking β-DG and cells expressing it. This therefore suggests that β-DG does localise to the nucleus, however, its exact function is still yet to be identified.

6.1.2 Regulation of the levels and localisation of lamin B1 and emerin

As mentioned above it has been frequently reported that both lamin B1 and emerin are mislocalised and total levels reduced in cells with perturbed levels of DG (Gómez-Monsiváis et al., 2020; Jimenez-Gutierrez et al., 2020; Martínez-Vieyra et al., 2013; Vélez-Aguilera et al., 2018). The perturbations involved in these studies include β-DG knockdown, *DAG1* KO or nuclear accumulation of β-DG and each of these result in a reduction and mislocalisation of lamin B1 and emerin. However, all of these experiments have been carried out in mouse C2C12 myoblasts and has not been tested in other cell lines. In this present study the levels and localisation of emerin

and lamin B1 appear unaffected by *DAG1* KO in human myoblasts (chapter 3, figure 3.22-3.28). This would suggest that these observations in C2C12 cells are not necessarily consistent across cell types or different organisms. Both levels and post-translational modifications of DG vary between cell types so it is possible that differences in levels and post-translational modifications may result in different phenotypes. In order to further elucidate the role of β-DG in the regulation of lamin B1 and emerin it would be sensible to knock down β-DG in a range of cell types from a range of different organisms in order to understand the prevalence of this phenotype in multiple cell types. It would also be useful to carry out mutagenesis studies in order to determine which parts of DG are required for this regulation, phosphorylation states can also be investigated with the use of phosphomimetic mutants. An investigation into which cell types β-DG is required for correct localisation of emerin and lamin B1 is an important question to answer for the field.

6.1.3 Contribution to mechanical properties of myoblast nuclei

This study is the first to investigate the potential role DG has on the mechanical properties of the nucleus. This study was prompted by the available evidence suggesting that a lack or reduction of DG resulted in abnormally shaped nuclei (Jacobs, 2017), reduced levels of lamin B1 and emerin and potential interactions between β-DG and lamin A/C, B1 and emerin (Gómez-Monsiváis et al., 2020; Jimenez-Gutierrez et al., 2020; Martínez-Vieyra et al., 2013; Vélez-Aguilera et al., 2018). Lamin A/C, B1 and emerin play key structural roles in the NE and are largely responsible for the mechanical properties of nuclei (Ferrera et al., 2014; Lammerding et al., 2006; Rowat et al., 2006), based on this previous evidence it was hypothesised that cells/nuclei lacking DG would have altered nuclear mechanical properties.

There are multiple techniques that can be used for assessing mechanical properties of cells such as optical stretching (Guck et al., 2001), magnetic twisting cytometry (Tajik et al., 2016), micropipette aspiration (Dahl et al., 2005; Davidson et al., 2019) and more recently the contact-free imaging method Brillouin microscopy (Zhang et

al., 2020). However, AFM was used due to the medium throughput (greater than micropipette aspiration but lower than magnetic twisting cytometry, optical stretching and Brillouin microscopy), the ability to measure cells in their usual culture conditions (which isn't possible using optical stretching) and the availability of specialist equipment (Brillouin microscopy is still in its infancy and being developed). The other advantage of using AFM is the well-defined and well-established mathematical models which are used to calculate mechanical properties, such as Young's modulus, from force indentation curves (Bouchonville and Nicolas, 2019).

Using AFM, the mechanical properties of myoblast nuclei, either with or without functional DG, were investigated extensively (chapter 4). The results suggest that the mechanical properties of nuclei without DG did not differ significantly from the control nuclei when tested with two types of cantilevers and following treatments including cell synchronisation, chromatin decondensation and actin cytoskeleton perturbation. There are no published data to compare these results to, as nuclei of KM155 human myoblasts have not been measured previously and there has been no comparison of nuclei with or without DG in any cell lines. The results from this study allow the conclusion that DG does not influence the mechanical properties of nuclei when in a whole cell environment. These data fit with data presented in chapter 3 suggesting that levels of key structural proteins lamin A/C, B1 and emerin are also unaffected by disruption of DG. However, when nuclei were isolated from the surrounding cytoplasm and cytoskeleton there was a small but significant decrease in Young's modulus for both *DAG1* KO cells measured. This suggest that DG may indeed play a role in the mechanical properties of myoblast nuclei, but the contribution is so small that it becomes insignificant in the background of a whole cell.

As the impact of DG on the mechanical properties of the nucleus appeared so small it was important to investigate whether it plays any part in responding to mechanical stimuli. Following compression, cells lacking DG did not respond any differently to cells expressing DG. This suggests that the small difference in nuclear mechanical properties does not make a functional difference when cell compression was

assessed. Ideally, cells would have been subjected to mechanical stretching, but it was not possible to establish this technique despite extensive efforts.

6.2 Conclusions and future work

In summary, the work presented in this thesis aimed to understand the functional relevance of β-DG in the nucleus and determine whether it played a role in determining the mechanical properties of human myoblast nuclei. Based on the detailed analysis it is possible to conclude that disruption of DG in these cells results in an increase in nuclear and cell area that can be rescued by the addition of exogenous DG. It is also possible to conclude that DG may contribute to the mechanical properties of nuclei, however, the magnitude of this contribution is small and is not relevant at a whole cell level using the testing regimes employed here. It is also possible to conclude from this study that, at least in human myoblasts, DG is not involved in maintaining nuclear shape, regulating levels or localisation of lamin A/C, B1 or emerin or responding to mechanical compression.

The evidence presented in this work provides no compelling reason to continue investigating a mechanical role for DG in the nucleus. However, there are other avenues that can be investigated in terms of the role of DG. The most interesting of these is the consistent observation that cells where DG is disrupted are larger, as is the nucleus. Jimenez-Gutierrez et al., (2020) suggest this difference in size is due to cellular senescence however, there are some methodological issues with this investigation. Additionally, the results presented in this present study suggest that cellular senescence is not consistently observed in cells lacking DG and that this phenotype can be rescued by the addition of exogenous DG. Further investigations could involve rescue experiments with a range of DG constructs such as one lacking the NLS to determine whether nuclear localisation of DG is involved. Additionally, it is important to get a handle on the extent of nuclear localisation of β-DG across a range of cell types and organisms, this will be required in the attempt to better understand the role β-DG plays in the nucleus.

7 References

Adams, J.C., and Brancaccio, A. (2015). The evolution of the dystroglycan complex, a major mediator of muscle integrity. Biol. Open *4*, 1163–1179.

Adams, M.E., Butler, M.H., Dwyer, T.M., Peters, M.F., Murnane, A.A., and Froehner, S.C. (1993). Two forms of mouse syntrophin, a 58 kd dystrophin-associated protein, differ in primary structure and tissue distribution. Neuron *11*, 531–540.

Agrawal, S., Anderson, P., Durbeej, M., Van Rooijen, N., Ivars, F., Opdenakker, G., and Sorokin, L.M. (2006). Dystroglycan is selectively cleaved at the parenchymal basement membrane at sites of leukocyte extravasation in experimental autoimmune encephalomyelitis. J. Exp. Med. *203*, 1007–1016.

Aguilar, A., Wagsta, K.M., Suárez-Sánchez, R., Zinker, S., Jans, D.A., and Cisneros, B. (2015). Nuclear localization of the dystrophin-associated protein α-dystrobrevin through importin α2/β1 is critical for interaction with the nuclear lamina/maintenance of nuclear integrity. FASEB J. *29*, 1842–1858.

Ahmed, S.B.M., and Prigent, S.A. (2017). Insights into the Shc family of adaptor proteins. J. Mol. Signal. *12*, 1–17.

Ahn, A.H., and Kunkel, L.M. (1995). Syntrophin binds to an alternatively spliced exon of dystrophin. J. Cell Biol. *128*, 363–371.

Ahn, A.H., Freener, C.A., Gussoni, E., Yoshida, M., Ozawa, E., and Kunkel, L.M. (1996). The three human syntrophin genes are expressed in diverse tissues, have distinct chromosomal locations, and each bind to dystrophin and its relatives. J. Biol. Chem. *271*, 2724–2730.

Ahrens, Rubner, Springer, Hampe, Gehlen, Magin, Hoffmann, and Merkel (2019). A Combined AFM and Lateral Stretch Device Enables Microindentation Analyses of Living Cells at High Strains. Methods Protoc. *2*, 43.

Akhavan, A., Crivelli, S.N., Singh, M., Lingappa, V.R., and Muschler, J.L. (2008). SEA domain proteolysis determines the functional composition of dystroglycan. FASEB J. *22*, 612–621.

Aleman, V., Osorio, B., Chavez, O., Rendon, A., Mornet, D., and Martinez, D. (2001). Subcellular localization of Dp71 dystrophin isoforms in cultured hippocampal neurons and forebrain astrocytes. Histochem. Cell Biol. *115*, 243–254.

Amann, K.J., Renley, B.A., and Ervasti, J.M. (1998). A cluster of basic repeats in the dystrophin rod domain binds F-actin through an electrostatic interaction. J. Biol. Chem. *273*, 28419–28423.

Amann, K.J., Guo, A.W.X., and Ervasti, J.M. (1999). Utrophin lacks the rod domain

actin binding activity of dystrophin. J. Biol. Chem. *274*, 35375–35380.

Ambrose, H.J., Blake, D.J., Nawrotzki, R.A., and Davies, K.E. (1997). Genomic organization of the mouse dystrobrevin gene: Comparative analysis with the dystrophin gene. Genomics *39*, 359–369.

Amiry-Moghaddam, M., Otsuka, T., Hurn, P.D., Traystman, R.J., Haug, F.M., Froehner, S.C., Adams, M.E., Neely, J.D., Agre, P., Ottersen, O.P., et al. (2003). An α-syntrophin-dependent pool of AQP4 in astroglial end-feet confers bidirectional water flow between blood and brain. Proc. Natl. Acad. Sci. U. S. A. *100*, 2106–2111.

Apte, K., Stick, R., and Radmacher, M. (2017). Mechanics in human fibroblasts and progeria: Lamin A mutation E145K results in stiffening of nuclei. J. Mol. Recognit. *30*, 1–11.

Aragón, J., Martínez-Herrera, A., Romo-Yáñez, J., Ceja, V., Azotla-Vilchis, C., Siqueiros-Márquez, L., Soid-Raggi, G., Herrera-Salazar, A., and Montañez, C. (2016). Identification of Dp71 Isoforms Expressed in PC12 Cells: Subcellular Localization and Colocalization with β-Dystroglycan and α1-Syntrophin. J. Mol. Neurosci. *58*, 201–209.

Azuara-Medina, P.M., Sandoval-Duarte, A.M., Morales-Lázaro, S.L., Modragón-González, R., Vélez-Aguilera, G., Gómez-López, J. de D., Jiménez-Gutiérrez, G.E., Tiburcio-Félix, R., Martínez-Vieyra, I., Suárez-Sánchez, R., et al. (2019). The intracellular domain of β-dystroglycan mediates the nucleolar stress response by suppressing UBF transcriptional activity. Cell Death Dis.

Barascu, A., Le Chalony, C., Pennarun, G., Genet, D., Imam, N., Lopez, B., and Bertrand, P. (2012). Oxidative stress induces an ATM-independent senescence pathway through p38 MAPK-mediated lamin B1 accumulation. EMBO J. *31*, 1080–1094.

Barresi, R., and Campbell, K.P. (2006). Dystroglycan: From biosynthesis to pathogenesis of human disease. J. Cell Sci. *119*, 199–207.

Beck, K., Hunter, I., and Engel, J. (1990). Structure and function of laminin: anatomy of a multidomain glycoprotein. FASEB J. *4*, 148–160.

Belanto, J.J., Mader, T.L., Eckhoff, M.D., Strandjord, D.M., Banks, G.B., Gardner, M.K., Lowe, D.A., and Ervasti, J.M. (2014). Microtubule binding distinguishes dystrophin from utrophin. Proc. Natl. Acad. Sci. U. S. A. *111*, 5723–5728.

Bellin, R.M., Sernett, S.W., Beckert, B., Ip, W., Huiatt, T.W., and Robson, R.M. (1999). Molecular characteristics and interactions of the intermediate filament protein synemin. Interactions with α-actinin may anchor synemin-containing heterofilaments. J. Biol. Chem. *274*, 29493–29499.

Bellin, R.M., Huiatt, T.W., Critchley, D.R., and Robson, R.M. (2001). Synemin May Function to Directly Link Muscle Cell Intermediate Filaments to Both Myofibrillar Z-lines and Costameres. J. Biol. Chem. *276*, 32330–32337.

Beltran-Valero de Bernabé, D., Voit, T., Longman, C., Steinbrecher, A., Straub, V., Yuva, Y., Herrmann, R., Sperner, J., Korenke, C., Diesen, C., et al. (2004). Mutations in the FKRP gene can cause muscle-eye-brain disease and Walker-Warburg syndrome. J. Med. Genet. *41*, 1–5.

Beltrán-Valero de Bernabé, D., Currier, S., Steinbrecher, A., Celli, J., Van Beusekom, E., Van der Zwaag, B., Kayserili, H., Merlini, L., Chitayat, D., Dobyns, W.B., et al. (2002). Mutations in the O-mannosyltransferase gene POMT1 give rise to the severe neuronal migration disorder Walker-Warburg syndrome. Am. J. Hum. Genet. *71*, 1033–1043.

Beltrán-Valero de Bernabé, D., Van bokhoven, H., Van beusekom, E., Van der AKKer, W., Kant, S., Dobyns, W.B., Cormand, B., Currier, S., Hamel, B., Talim, B., et al. (2003). A homozygous nonsense mutation in the Fukutin gene causes a Walker-Warburg syndrome phenotype. J. Med. Genet. *40*, 845–848.

Bhosle, R.C., Michele, D.E., Campbell, K.P., Li, Z., and Robson, R.M. (2006). Interactions of intermediate filament protein synemin with dystrophin and utrophin. Biochem. Biophys. Res. Commun. *346*, 768–777.

Bian, Y., Song, C., Cheng, K., Dong, M., Wang, F., Huang, J., Sun, D., Wang, L., Ye, M., and Zou, H. (2014). An enzyme assisted RP-RPLC approach for in-depth analysis of human liver phosphoproteome. J. Proteomics *96*, 253–262.

Blake, D.J., Love, D.R., Tinsley, J., Morris, G.E., Turley, H., Gatter, K., Dickson, G., Edwards, Y.H., and Davies, K.E. (1992). Characterization of a 4.8kb transcript from the duchenne muscular dystrophy locus expressed in schwannoma cells. Hum. Mol. Genet. *1*, 103–109.

Blake, D.J., Tinsley, J., Davies, K.E., Knight, A., Winder, S.J., and Kendrick-Jones, J. (1995a). Coiled-coil regions in the carboxy-terminal domains of dystrophin and related proteins: potentials for protein-protein interactions. Trends Biochem. Sci. *April*, 133–135.

Blake, D.J., Schofield, J.N., Zuellig, R.A., Górecki, D.C., Phelps, S.R., Barnard, E.A., Edwards, Y.H., and Davies, K.E. (1995b). G-utrophin, the autosomal homologue of dystrophin Dp116, is expressed in sensory ganglia and brain. Proc. Natl. Acad. Sci. U. S. A. *92*, 3697–3701.

Blake, D.J., Nawrotzki, R., Peters, M.F., Froehner, S.C., and Davies, K.E. (1996). Isoform diversity of dystrobrevin, the murine 87-kDa postsynaptic protein. J. Biol. Chem. *271*, 7802–7810.

Blake, D.J., Weir, A., Newey, S.E., and Davies, K.E. (2002). Function and genetics of dystrophin and dystrophin-related proteins in muscle. Physiol. Rev. *82*, 291–329.

Boffi, A., Bozzi, M., Sciandra, F., Woellner, C., Bigotti, M.G., Ilari, A., and Brancaccio, A. (2001). Plasticity of secondary structure in the N-terminal region of β-dystroglycan. Biochim. Biophys. Acta - Protein Struct. Mol. Enzymol. *1546*, 114–121.

Bork, P., and Sudol, M. (1994). The WW domain: a signalling site in dystrophin? Trends Biochem. Sci. *19*, 531–533.

Bouchonville, N., and Nicolas, A. (2019). Quantification of the elastic properties of soft and sticky materials using AFM. *1886*, 281–290.

Bowe, M.A., Deyst, K.A., Leszyk, J.D., and Fallon, J.R. (1994). Identification and purification of an agrin receptor from torpedo postsynaptic membranes: A heteromeric complex related to the dystroglycans. Neuron *12*, 1173–1180.

Bowe, M.A., Mendis, D.B., and Fallon, J.R. (2000). The small leucine-rich repeat proteoglycan biglycan binds to α-dystroglycan and is upregulated in dystrophic muscle. J. Cell Biol. *148*, 801–810.

Boyce, F.M., Beggs, A.H., Feener, C., and Kunkel, L.M. (1991). Dystrophin is transcribed in brain from a distant upstream promoter. Proc. Natl. Acad. Sci. U. S. A. *88*, 1276–1280.

Bozic, D., Sciandra, F., Lamba, D., and Brancaccio, A. (2004). The structure of the N-terminal region of murine skeletal muscle α-dystroglycan discloses a modular architecture. J. Biol. Chem. *279*, 44812–44816.

Bozzi, M., Inzitari, R., Sbardell, D., Monaco, S., Pavoni, E., Gioia, M., Marini, S., Morlacchi, S., Sciandra, F., Castagnola, M., et al. (2009). Enzymatic processing of β-dystroglycan recombinant ectodomain by MMP-9: Identification of the main cleavage site. IUBMB Life *61*, 1143–1152.

Bozzi, M., Cassetta, A., Covaceuszach, S., Bigotti, M.G., Bannister, S., Hübner, W., Sciandra, F., Lamba, D., and Brancaccio, A. (2015). The structure of the T190M mutant of murine α-dystroglycan at high resolution: Insight into the molecular basis of a primary dystroglycanopathy. PLoS One *10*, 1–21.

Brancaccio, A., and Adams, J.C. (2017). An evaluation of the evolution of the gene structure of dystroglycan. BMC Res. Notes *10*, 1–12.

Brancaccio, A., Schulthess, T., Gesemann, M., and Engel, J. (1995). Electron microscopic evidence for a mucin-like region in chick muscle α-dystroglycan. FEBS Lett. *368*, 139–142.

Brancaccio, A., Schulthess, T., Gesemann, M., and Engel, J. (1997). The N-terminal

region of α-dystroglycan is an autonomous globular domain. Eur. J. Biochem. *246*, 166–172.

Briggs, D.C., Yoshida-Moriguchi, T., Zheng, T., Venzke, D., Anderson, M.E., Strazzulli, A., Moracci, M., Yu, L., Hohenester, E., and Campbell, K.P. (2016). Structural basis of laminin binding to the LARGE glycans on dystroglycan. Nat. Chem. Biol. *12*, 810–814.

Brockington, M., Yuva, Y., Prandini, P., Brown, S.C., Torelli, S., Benson, M.A., Herrmann, R., Anderson, L., Bashir, R., Burgunder, J., et al. (2001). Mutations in the fukutin-related protein gene (FKRP) identify limb girdle muscular dystrophy 2I as a milder allelic variant of congenital muscular dystrophy MDC1C. Hum. Mol. Genet. *10*, 2851–2859.

Brown, S.C., Torelli, S., Brockington, M., Yuva, Y., Jimenez, C., Feng, L., Anderson, L., Ugo, I., Kroger, S., Bushby, K., et al. (2004). Abnormalities in α-Dystroglycan Expression in MDC1C and LGMD2I Muscular Dystrophies. Am. J. Pathol. *164*, 727–737.

Buchwalter, A., Schulte, R., Tsai, H., Capitanio, J., and Hetzer, M. (2019). Selective clearance of the inner nuclear membrane protein emerin by vesicular transport during ER stress. BioRxiv 1–29.

Buisson, N., Sirour, C., Moreau, N., Denker, E., Le Bouffant, R., Goullancourt, A., Darribere, T., and Bello, V. (2014). An adhesome comprising laminin, dystroglycan and myosin IIA is required during notochord development in Xenopus laevis. Development *141*, 4569–4579.

Bulfield, G., Siller, W.G., Wight, P.A.L., and Mooret, K.J. (1984). X chromosome-linked muscular dystrophy (mdx) in the mouse (animal model).

Burton, E.A., Tinsley, J.M., Holzfeind, P.J., Rodrigues, N.R., and Davies, K.E. (1999). A second promoter provides an alternative target for therapeutic up-regulation of utrophin in Duchenne muscular dystrophy. Proc. Natl. Acad. Sci. U. S. A. *96*, 14025–14030.

Butler, M.H., Douville, K., Murnane, A.A., Kramarcy, N.R., Cohen, J.B., Sealock, R., and Froehner, S.C. (1992). Association of the M(r) 58,000 postsynaptic protein of electric tissue with Torpedo dystrophin and the M(r) 87,000 postsynaptic protein. J. Biol. Chem. *267*, 6213–6218.

Byers, T.J., Lidov, H.G.W., and Kunkel, L.M. (1993). An alternative dystrophin transcript specific to peripheral nerve. Nat. Genet. *4*, 77–81.

Caluori, G., Pribyl, J., Pesl, M., Oliver-De La Cruz, J., Nardone, G., Skladal, P., and Forte, G. (2018). Advanced and rationalized atomic force microscopy analysis unveils specific properties of controlled cell mechanics. Front. Physiol. *9*.

Campanelll, J.T., Roberds, S.L., Campbell, K.P., and Scheller, R.H. (1994). A role for dystrophin-associated glycoproteins and utrophin in agrin-induced AChR clustering. Cell *77*, 663–674.

Cantwell, H., and Nurse, P. (2019a). A homeostatic mechanism rapidly corrects aberrant nucleocytoplasmic ratios maintaining nuclear size in fission yeast. J. Cell Sci. *132*.

Cantwell, H., and Nurse, P. (2019b). A systematic genetic screen identifies essential factors involved in nuclear size control. PLoS Genet. *15*, 1–19.

Cartaud, A., Coutant, S., Petrucci, T.C., and Cartaud, J. (1998). Evidence for in situ and in vitro association between β-dystroglycan and the subsynaptic 43k rapsyn protein: Consequence for acetylcholine receptor clustering at the synapse. J. Biol. Chem. *273*, 11321–11326.

Cavaldesi, M., Macchia, G., Barca, S., Defilippi, P., Tarone, G., and Petrucci, T.C. (1999). Association of the dystroglycan complex isolated from bovine brain synaptosomes with proteins involved in signal transduction. J. Neurochem. *72*, 1648–1655.

Cerecedo, D., Cisneros, B., Suárez-Sánchez, R., Hernández-González, E., and Galván, I. (2008). β-Dystroglycan modulates the interplay between actin and microtubules in human-adhered platelets. Br. J. Haematol. *141*, 517–528.

Chaki, S.P., and Rivera, G.M. (2013). Integration of signaling and cytoskeletal remodeling by Nck in directional cell migration. Bioarchitecture *3*, 57–63.

Chan, Y.M., Bönnemann, C.G., Lidov, H.G.W., and Kunkel, L.M. (1998). Molecular organization of sarcoglycan complex in mouse myotubes in culture. J. Cell Biol. *143*, 2033–2044.

Chelly, J., Hamard, G., Koulakoff, A., Kaplan, J.C., Kahn, A., and Berwald-Netter, Y. (1990). Dystrophin gene transcribed from different promoters in neuronal and glial cells. Nature *344*, 64–65.

Chen, N.Y., Kim, P., Weston, T.A., Edillo, L., Tu, Y., Fong, L.G., and Young, S.G. (2018). Fibroblasts lacking nuclear lamins do not have nuclear blebs or protrusions but nevertheless have frequent nuclear membrane ruptures. Proc. Natl. Acad. Sci. *115*, 201812622.

Chen, X., Du, W., Cai, Z., Ji, S., Dwivedi, M., Chen, J., Zhao, G., and Chu, J. (2020). Uniaxial Stretching of Cell-Laden Microfibers for Promoting C2C12 Myoblasts Alignment and Myofibers Formation. ACS Appl. Mater. Interfaces *12*, 2162–2170.

Chen, Y.-J., Spence, H.J., Cameron, J.M., Jess, T., Ilsley, J.L., and Winder, S.J. (2003).

Direct interaction of beta-dystroglycan with F-actin. Biochem. J. *375*, 329–337.

Chiba, A., Matsumura, K., Yamada, H., Inazu, T., Shimizu, T., Kusunoki, S., Kanazawa, I., Kobata, A., and Endo, T. (1997). Structures of Sialylated O -Linked Oligosaccharides of Bovine Peripheral Nerve α-Dystroglycan . J. Biol. Chem. *272*, 2156–2162.

Cho, E.B., Yoo, W., Yoon, S.K., and Yoon, J.B. (2018). β-dystroglycan is regulated by a balance between WWP1-mediated degradation and protection from WWP1 by dystrophin and utrophin. Biochim. Biophys. Acta - Mol. Basis Dis. *1864*, 2199–2213.

Cho, S., Vashisth, M., Abbas, A., Majkut, S., Vogel, K., Xia, Y., Ivanovska, I.L., Irianto, J., Tewari, M., Zhu, K., et al. (2019). Mechanosensing by the Lamina Protects against Nuclear Rupture, DNA Damage, and Cell-Cycle Arrest. Dev. Cell *49*, 920-935.e5.

Cohen, J.A., Podgornik, R., Hansen, P.L., and Parsegian, V.A. (2009). A phenomenological one-parameter equation of state for osmotic pressures of PEG and other neutral flexible polymers in good solvents. J. Phys. Chem. B *113*, 3709–3714.

Collinsworth, A.M., Zhang, S., Kraus, W.E., and Truskey, G.A. (2002). Apparent elastic modulus and hysteresis of skeletal muscle cells throughout differentiation. Am. J. Physiol. - Cell Physiol. *283*, 1219–1227.

Connors, N.C., Adams, M.E., Froehner, S.C., and Kofuji, P. (2004). The potassium channel Kir4.1 associates with the dystrophin-glycoprotein complex via α-syntrophin in glia. J. Biol. Chem. *279*, 28387–28392.

Consolino, C.M., and Brooks, S. V. (2004). Susceptibility to sarcomere injury induced by single stretches of maximally activated muscles of mdx mice. J. Appl. Physiol. *96*, 633–638.

Cook, M. (2021). The Requirement of β-Dystroglycan, and a Sun1 Protein Interactome in Myonuclei. University of Sheffield.

Corrado, K., Rafael, J.A., Mills, P.L., Cole, N.M., Faulkner, J.A., Wang, K., and Chamberlain, J.S. (1996). Transgenic mdx mice expressing dystrophin with a deletion in the actin- binding domain display a “mild Becker” phenotype. J. Cell Biol. *134*, 873–884.

Coulton, G.R., Morgan, J.E., Partridge, T.A., and Sloper, J.C. (1988). The mdx mouse skeletal muscle myopathy : I. Biochemical Investigation. Neuropathol. Appl. Neurobiol. *14*, 53–70.

Covaceuszach, S., Bozzi, M., Bigotti, M.G., Sciandra, F., Konarev, P.V., Brancaccio, A., and Cassetta, A. (2017a). Structural flexibility of human α-dystroglycan. FEBS Open Bio *7*, 1064–1077.

Covaceuszach, S., Bozzi, M., Bigotti, M.G., Sciandra, F., Konarev, P. V., Brancaccio, A., and Cassetta, A. (2017b). The effect of the pathological V72I, D109N and T190M missense mutations on the molecular structure of α-dystroglycan. PLoS One *12*, 1–23.

Crisp, M., Liu, Q., Roux, K., Rattner, J.B., Shanahan, C., Burke, B., Stahl, P.D., and Hodzic, D. (2006). Coupling of the nucleus and cytoplasm: Role of the LINC complex. J. Cell Biol. *172*, 41–53.

Crosbie, R.H., Heighway, J., Venzke, D.P., Lee, J.C., and Campbell, K.P. (1997). Sarcospan, the 25-kDa transmembrane component of the dystrophin- glycoprotein complex. J. Biol. Chem. *272*, 31221–31224.

Crosbie, R.H., Lebakken, C.S., Holt, K.H., Venzke, D.P., Straub, V., Lee, J.C., Grady, R.M., Chamberlain, J.S., Sanes, J.R., and Campbell, K.P. (1999). Membrane targeting and stabilization of sarcospan is mediated by the sarcoglycan subcomplex. J. Cell Biol. *145*, 153–165.

Cross, S.S., Lippitt, J., Mitchell, A., Hollingsbury, F., Balasubramanian, S.P., Reed, M.W.R., Eaton, C., Catto, J.W., Hamdy, F., and Winder, S.J. (2008). Expression of β-dystroglycan is reduced or absent in many human carcinomas. Histopathology *53*, 561–566.

D'souza, V.N., Man, N.T., Morris, G.E., Karges, W., Pillers, D.A.M., and Ray, P.N. (1995). A novel dystrophin isoform is required for normal retinal electrophysiology. Hum. Mol. Genet. *4*, 837–842.

Dahl, K.N., Engler, A.J., Pajerowski, J.D., and Discher, D.E. (2005). Power-Law Rheology of Isolated Nuclei with Deformation Mapping of Nuclear Substructures. Biophys. J. *89*, 2855–2864.

Dai, Y., Liang, S., Dong, X., Zhao, Y., Ren, H., Guan, Y., Yin, H., Li, C., Chen, L., Cui, L., et al. (2018). Whole exome sequencing identified a novel DAG1 mutation in a patient with rare, mild and late age of onset muscular dystrophy-dystroglycanopathy. J. Cell. Mol. Med. *23*, 811–818.

Damodaran, K., Venkatachalapathy, S., Alisafaei, F., Radhakrishnan, A. V., Jokhun, D.S., Shenoy, V.B., and Shivashankar, G. V. (2018). Compressive force induces reversible chromatin condensation and cell geometry–dependent transcriptional response. Mol. Biol. Cell *29*, 3039–3051.

Davidson, P.M., Fedorchak, G.R., Mondésert-Deveraux, S., Bell, E.S., Isermann, P., Aubry, D., Allena, R., and Lammerding, J. (2019). High-throughput microfluidic micropipette aspiration device to probe time-scale dependent nuclear mechanics in intact cells. Lab Chip 3652–3663.

Deguchi, S., Maeda, K., Ohashi, T., and Sato, M. (2005). Flow-induced hardening of endothelial nucleus as an intracellular stress-bearing organelle. J. Biomech. *38*, 1751–1759.
Dellorusso, C., Crawford, R.W., Chamberlain, J.S., and Brooks, S. V. (2001). Tibialis anterior muscles in mdx mice are highly susceptible to contraction-induced injury. J. Muscle Res. Cell Motil. *22*, 467–475.

Denais, C.M., Gilbert, R.M., Isermann, P., McGregor, A.L., Lindert, M., Weigelin, B., Davidson, P.M., Friedl, P., Wolf, K., Lammerding, J., et al. (2016). Nuclear envelope rupture and repair during cancer cell migration. Science (80-.). *352*, 353–358.

Deng, L., Ren, R., Liu, Z., Song, M., Li, J., Wu, Z., Ren, X., Fu, L., Li, W., Zhang, W., et al. (2019). Stabilizing heterochromatin by DGCR8 alleviates senescence and osteoarthritis. Nat. Commun. *10*.

Dennis, C.L., Tinsley, J.M., Deconinck, A.E., and Davies, K.E. (1996). Molecular and functional analysis of the utrophin promoter. Nucleic Acids Res. *24*, 1646–1652.

DeWolf, C., McCauley, P., Sikorski, A.F., Winlove, C.P., Bailey, A.I., Kahana, E., Pinder, J.C., and Gratzer, W.B. (1997). Interaction of dystrophin fragments with model membranes. Biophys. J. *72*, 2599–2604.

Deyst, K.A., Bowe, M.A., Leszyk, J.D., and Fallon, J.R. (1995). The α-Dystroglycan-β-Dystroglycan Complex. J. Biol. Chem. *270*, 25956–25959.

Al Dhaibani, M.A., El-Hattab, A.W., Ismayl, O., and Suleiman, J. (2018). B3GALNT2 - Related Dystroglycanopathy: Expansion of the Phenotype with Novel Mutation Associated with Muscle-Eye-Brain Disease, Walker-Warburg Syndrome, Epileptic Encephalopathy-West Syndrome, and Sensorineural Hearing Loss. Neuropediatrics *49*, 289–295.

Dong, M., Noguchi, S., Endo, Y., Hayashi, Y.K., Yoshida, S., Nonaka, I., and Nishino, I. (2015). DAG1 mutations associated with asymptomatic hyperCKemia and hypoglycosylation of α-dystroglycan. Neurology *84*, 273–279.

Doss, B.L., Pan, M., Gupta, M., Grenci, G., Mège, R.-M., Lim, C.T., Sheetz, M.P., Voituriez, R., and Ladoux, B. (2020). Cell response to substrate rigidity is regulated by active and passive cytoskeletal stress. Proc. Natl. Acad. Sci. *117*.

Dreesen, O., Chojnowski, A., Ong, P.F., Zhao, T.Y., Common, J.E., Lunny, D., Lane, E.B., Lee, S.J., Vardy, L.A., Stewart, C.L., et al. (2013). Lamin B1 fluctuations have differential effects on cellular proliferation and senescence. J. Cell Biol. *200*, 605–617.

Duclos, F., Straub, V., Moore, S.A., Venzke, D.P., Hrstka, R.F., Crosbie, R.H., Durbeej, M., Lebakken, C.S., Ettinger, A.J., Van Der Meulen, J., et al. (1998). Progressive muscular dystrophy in α-sarcoglycan-deficient mice. J. Cell Biol. *142*, 1461–1471.

Durbeej, M., Talts, J.E., Henry, M.D., Yurchenco, P.D., Campbell, K.P., and Ekblom, P. (2001). Dystroglycan binding to laminin α1LG4 module influences epithelial morphogenesis of salivary gland and lung in vitro. Differentiation *69*, 121–134.

Dwyer, T.M., and Froehner, S.C. (1995). Direct binding of Torpedo syntrophin to dystrophin and the 87 kDa dystrophin homologue. FEBS Lett. *375*, 91–94.

Edens, L.J., White, K.H., Jevtic, P., Li, X., and Levy, D.L. (2013). Nuclear size regulation: From single cells to development and disease. Trends Cell Biol. *23*, 151–159.

Efremov, Y.M., Lomakina, M.E., Bagrov, D. V., Makhnovskiy, P.I., Alexandrova, A.Y., Kirpichnikov, M.P., and Shaitan, K. V. (2014). Mechanical properties of fibroblasts depend on level of cancer transformation. Biochim. Biophys. Acta - Mol. Cell Res. *1843*, 1013–1019.

Eid Mutlak, Y., Aweida, D., Volodin, A., Ayalon, B., Dahan, N., Parnis, A., and Cohen, S. (2020). A signaling hub of insulin receptor, dystrophin glycoprotein complex and plakoglobin regulates muscle size. Nat. Commun. *11*, 1381.

En, A., Takauji, Y., Ayusawa, D., and Fujii, M. (2020). The role of lamin B receptor in the regulation of senescence-associated secretory phenotype (SASP). Exp. Cell Res. *390*, 111927.
Ervasti, J.M., and Campbell, K.P. (1991). Membrane organization of the dystrophin-glycoprotein complex. Cell *66*, 1121–1131.

Ervasti, J.M., and Campbell, K.P. (1993). A role for the dystrophin-glycoprotein complex as a transmembrane linker between laminin and actin. J. Cell Biol. *122*, 809–823.

Ervasti, J.M., Ohlendieck, K., Kahl, S.D., Gaver, M.G., and Campbell, K.P. (1990). Deficiency of a glycoprotein component of the dystrophin complex in dystrophic muscle. Nature *345*, 315–319.

Esapa, C.T., Bentham, G.R.B., Schröder, J.E., Kröger, S., and Blake, D.J. (2003). The effects of post-translational processing on dystroglycan synthesis and trafficking. FEBS Lett. *555*, 209–216.

Fenech, M., Kirsch-Volders, M., Natarajan, A.T., Surralles, J., Crott, J.W., Parry, J., Norppa, H., Eastmond, D.A., Tucker, J.D., and Thomas, P. (2011). Molecular mechanisms of micronucleus, nucleoplasmic bridge and nuclear bud formation in mammalian and human cells. Mutagenesis *26*, 125–132.

Ferrera, D., Canale, C., Marotta, R., Mazzaro, N., Gritti, M., Mazzanti, M., Capellari, S., Cortelli, P., and Gasparini, L. (2014). Lamin B1 overexpression increases nuclear rigidity in autosomal dominant leukodystrophy fibroblasts. FASEB J. *28*, 3906–3918.

Finan, J.D., Chalut, K.J., Wax, A., and Guilak, F. (2009). Nonlinear osmotic properties of the cell nucleus. Ann. Biomed. Eng. *37*, 477–491.

Freund, A., Laberge, R.M., Demaria, M., and Campisi, J. (2012). Lamin B1 loss is a senescence-associated biomarker. Mol. Biol. Cell *23*, 2066–2075.

Friedrich, M.V.K., Göhring, W., Mörgelin, M., Brancaccio, A., David, G., and Timpl, R. (1999). Structural basis of glycosaminoglycan modification and of heterotypic interactions of perlecan domain V. J. Mol. Biol. *294*, 259–270.

Fuentes-Mera, L., Rodríguez-Muñoz, R., González-Ramírez, R., García-Sierra, F., González, E., Mornet, D., and Cisneros, B. (2006). Characterization of a novel Dp71 dystrophin-associated protein complex (DAPC) present in the nucleus of HeLa cells: Members of the nuclear DAPC associate with the nuclear matrix. Exp. Cell Res. *312*, 3023–3035.

Gardner, K.L., Kearney, J.A., Edwards, J.D., and Rafael-Fortney, J.A. (2006). Restoration of all dystrophin protein interactions by functional domains in trans does not rescue dystrophy. Gene Ther. *13*, 744–751.

Gautam, M., Noakes, P.G., Mudd, J., Nichol, M., Chu, G.C., Sanes, J.R., and Merlie, J.P. (1995). Failure of postsynaptic specialization to develop at neuromuscular junctions of rapsyn-deficient mice. Nature *377*, 232–236.

Gavillet, B., Rougier, J.S., Domenighetti, A.A., Behar, R., Boixel, C., Ruchat, P., Lehr, H.A., Pedrazzini, T., and Abriel, H. (2006). Cardiac sodium channel Nav1.5 is regulated by a multiprotein complex composed of syntrophins and dystrophin. Circ. Res. *99*, 407–414.

Gee, S.H., Blacher, R.W., Douville, P.J., Provost, P.R., Yurchenco, P.D., and Carbonetto, S. (1993). Laminin-binding protein 120 from brain is closely related to the dystrophin-associated glycoprotein, dystroglycan, and binds with high affinity to the major heparin binding domain of laminin. J. Biol. Chem. *268*, 14972–14980.

Gee, S.H., Montanaro, F., Lindenbaum, M.H., and Carbonetto, S. (1994). Dystroglycan-α, a dystrophin-associated glycoprotein, is a functional agrin receptor. Cell *77*, 675–686.

Geis, T., Marquard, K., Rödl, T., Reihle, C., Schirmer, S., Von Kalle, T., Bornemann, A., Hehr, U., and Blankenburg, M. (2013). Homozygous dystroglycan mutation associated with a novel muscle-eye-brain disease-like phenotype with multicystic leucodystrophy. Neurogenetics *14*, 205–213.

Gesemann, M., Cavalli, V., Denzer, A.J., Brancaccio, A., Schumacher, B., and Ruegg, M.A. (1996). Alternative splicing of agrin alters its binding to heparin, dystroglycan, and the putative agrin receptor. Neuron *16*, 755–767.

Gilbert, H.T.J., Mallikarjun, V., Dobre, O., Jackson, M.R., Pedley, R., Gilmore, A.P., Richardson, S.M., and Swift, J. (2019). Nuclear decoupling is part of a rapid protein-level cellular response to high-intensity mechanical loading. Nat. Commun. *10*, 1–15.

Gimpel, P., Lee, Y.L., Sobota, M., Burke, B., Gomes, E.R., Gimpel, P., Lee, Y.L., Sobota, R.M., Calvi, A., Koullourou, V., et al. (2017). Nesprin-1 a -Dependent Microtubule Nucleation from the Nuclear Envelope via Akap450 Is Necessary for Nuclear Positioning in Muscle Cells. Curr. Biol. *27*, 2999–3009.

Gómez-Monsiváis, W.L., Monterrubio-ledezma, F., Huerta-cantillo, J., Mondragón-González, R., Alamillo-Iniesta, A., Garcia-Aguirre, I., Azuara-medina, P.M., Arguello-Garcia, R., Rivera-monroy, J.E., Holaska, J.M., et al. (2020). The Molecular Basis and Biologic Significance of the β -Dystroglycan-Emerin Interaction. Int. J. Mol. Sci. *21*.

Gonzalez-Ramirez, R., Morales-Lazaro, S.., Tapia-Ramirez, V., Mornet, D., and Cisneros, B. (2008). Nuclear and Nuclear Envelope Localization of Dystrophin Dp71 and Dystrophin-associated Proteins (DAPs) in the C2C12 Muscle Cells: DAPs Nuclear Localization Is Modulated During Myogenesis. J. Cell. Biochem. *105*, 735–745.

González, E., Montañez, C., Ray, P.N., Howard, P.L., García-Sierra, F., Mornet, D., and Cisneros, B. (2000). Alternative splicing regulates the nuclear or cytoplasmic localization of dystrophin Dp71. FEBS Lett. *482*, 209–214.

Górecki, D.C., Monaco, A.P., Derry, J.M.J., Walker, A.P., Barnard, E.A., and Barnard, P.J. (1992). Expression of four alternative dystrophin transcripts in brain regions regulated by different promoters. Hum. Mol. Genet. *1*, 505–510.

Gouw, M., Michael, S., Sámano-Sánchez, H., Kumar, M., Zeke, A., Lang, B., Bely, B., Chemes, L.B., Davey, N.E., Deng, Z., et al. (2018). The eukaryotic linear motif resource - 2018 update. Nucleic Acids Res. *46*, D428–D434.

Gracida-Jiménez, V., Mondragón-González, R., Vélez-Aguilera, G., Vásquez-Limeta, A., Laredo-Cisneros, M.S., Gómez-López, J. de D., Vaca, L., Gourlay, S.C., Jacobs, L.A., Winder, S.J., et al. (2017). Retrograde trafficking of β-dystroglycan from the plasma membrane to the nucleus. Sci. Rep. *7*, 9906.

Guck, J., Ananthakrishnan, R., Mahmood, H., Moon, T.J., Cunningham, C.C., and Käs, J. (2001). The optical stretcher: A novel laser tool to micromanipulate cells. Biophys. J. *81*, 767–784.

Guilluy, C., Osborne, L.D., Van Landeghem, L., Sharek, L., Superfine, R., Garcia-mata, R., and Burridge, K. (2014). Isolated nuclei adapt to force and reveal a mechanotransduction pathway within the nucleus. Nat. Cell Biol. *16*, 376–381.

Hara, Y., Balci-Hayta, B., Yoshida-Moriguchi, T., Kanagawa, M., Beltran-Valero de

Bernabe, D., Gundesli, H., Willer, T., Satz, J.S., Crawford, R.W., Burden, S.J., et al. (2011). A dystroglycan mutation associated with limb-girdle muscular dystrophy. N. Engl. J. Med. *364*, 939–946.

Harrison, R., Hitchen, P.G., Panico, M., Morris, H.R., Mekhaiel, D., Pleass, R.J., Dell, A., Hewitt, J.E., and Haslam, S.M. (2012). Glycoproteomic characterization of recombinant mouse -dystroglycan. Glycobiology *22*, 662–675.

Hayashi, Y.K., Ogawa, M., Tagawa, K., Noguchi, S., Ishihara, T., Nonaka, I., and Arahata, K. (2001). Selective deficiency of α-dystroglycan in Fukuyama-type congenital muscular dystrophy. Neurology *57*, 115–121.

Hemming, M.L., Elias, J.E., Gygi, S.P., and Selkoe, D.J. (2008). Proteomic profiling of γ-secretase substrates and mapping of substrate requirements. PLoS Biol. *6*, 2314–2328.
Henry, M.D., Cohen, M.B., and Campbell, K.P. (2001). Reduced expression of dystroglycan in breast and prostate cancer. Hum. Pathol. *32*, 791–795.

Heo, S.J., Thorpe, S.D., Driscoll, T.P., Duncan, R.L., Lee, D.A., and Mauck, R.L. (2015). Biophysical regulation of chromatin architecture instills a mechanical memory in mesenchymal stem cells. Sci. Rep. *5*, 1–14.

Hobson, C.M., Kern, M., O'Brien, E.T., Stephens, A.D., Falvo, M.R., and Superfine, R. (2020). Correlating nuclear morphology and external force with combined atomic force microscopy and light sheet imaging separates roles of chromatin and lamin A/C in nuclear mechanics. Mol. Biol. Cell *31*, 1788–1801.

Holder, E., Maeda, M., and Bies, R.D. (1996). Expression and regulation of the dystrophin Purkinje promoter in human skeletal muscle, heart, and brain. Hum. Genet. *97*, 232–239.
Holt, K.H., Crosbie, R.H., Venzke, D.P., and Campbell, K.P. (2000). Biosynthesis of dystroglycan: Processing of a precursor propeptide. FEBS Lett. *468*, 79–83.

Huang, X., Poy, F., Zhang, R., Joachimiak, A., Sudol, M., and Eck, M.J. (2000). Structure of a WW domain containing fragment of dystrophin in complex with β-dystroglycan. Nat. Struct. Biol. *7*, 634–638.

Ibraghimov-Beskrovnaya, O., Ervasti, J.M., Leveille, C.J., Slaughter, C.A., Sernett, S.W., and Campbell, K.P. (1992). Primary structure of dystrophin-associated glycoproteins linking dystrophin to the extracellular matrix. Nature *355*, 696–702.

Ibraghimov-Beskrovnaya, O., Milatovich, A., Ozcelik, T., Yang, B., Koepnick, K., Francke, U., and Campbell, K.P. (1993). Human dystroglycan: Skeletal muscle cDNA, genomic structure, origin of tissue specific isoforms and chromosomal localization. Hum. Mol. Genet. *2*, 1651–1657.

Ilsley, J.L., Sudol, M., and Winder, S.J. (2001). The interaction of dystrophin with β-

dystroglycan is regulated by tyrosine phosphorylation. Cell. Signal. *13*, 625–632.

Imamura, M., Mochizuki, Y., Engvall, E., and Takeda, S. (2005). E-Sarcoglycan compensates for lack of α-sarcoglycan in a mouse model of limb-girdle muscular dystrophy. Hum. Mol. Genet. *14*, 775–783.

Imperiali, M., Thoma, C., Pavoni, E., Brancaccio, A., Callewaert, N., and Oxenius, A. (2005). O Mannosylation of α-Dystroglycan Is Essential for Lymphocytic Choriomeningitis Virus Receptor Function. J. Virol. *79*, 14297–14308.

Irianto, J., Xia, Y., Pfeifer, C.R., Athirasala, A., Ji, J., Alvey, C., Tewari, M., Bennett, R.R., Harding, S.M., Liu, A.J., et al. (2017). DNA Damage Follows Repair Factor Depletion and Portends Genome Variation in Cancer Cells after Pore Migration. Curr. Biol. *27*, 210–223.

Iwata, Y., Sampaolesi, M., Shigekawa, M., and Wakabayashi, S. (2004). Syntrophin is an actin-binding protein the cellular localization of which is regulated through cytoskeletal reorganization in skeletal muscle cells. Eur. J. Cell Biol. *83*, 555–565.

Jacob, J.T., Nair, R.R., Poll, B.G., Pineda, C.M., Hobbs, R.P., Matunis, M.J., and Coulombe, P.A. (2020). Keratin 17 regulates nuclear morphology and chromatin organization. J. Cell Sci. *133*.

Jacobs, L. (2017). Dystroglycan in the nucleus and the cell cycle. University of Sheffield.

Jae, L.T., Raaben, M., Riemersma, M., Van Beusekom, E., Blomen, V.A., Velds, A., Kerkhoven, R.M., Carette, J.E., Topaloglu, H., Meinecke, P., et al. (2013). Deciphering the glycosylome of dystroglycanopathies using haploid screens for Lassa virus entry. Science (80-.). *340*, 479–483.

James, C., Müller, M., Goldberg, M.W., Lenz, C., Urlaub, H., and Kehlenbach, R.H. (2019). Proteomic mapping by rapamycin-dependent targeting of APEX2 identifies binding partners of VAPB at the inner nuclear membrane. J. Biol. Chem. *294*, jbc.RA118.007283.

James, M., Nuttall, A., Ilsley, J.L., Ottersbach, K., Tinsley, J.M., Sudol, M., and Winder, S.J. (2000). Adhesion-dependent tyrosine phosphorylation of (beta)-dystroglycan regulates its interaction with utrophin. J. Cell Sci. *113 (Pt 1*, 1717–1726.

Jamshidi Goharrizi, K., Moosavi, S.S., Amirmahani, F., Salehi, F., and Nazari, M. (2020). Assessment of changes in growth traits, oxidative stress parameters, and enzymatic and non-enzymatic antioxidant defense mechanisms in Lepidium draba plant under osmotic stress induced by polyethylene glycol. Protoplasma *257*, 459–473.

Jetta, D., Gottlieb, P.A., Verma, D., Sachs, F., and Hua, S.Z. (2019). Shear stress-

induced nuclear shrinkage through activation of Piezo1 channels in epithelial cells. J. Cell Sci. *132*.

Jevtić, P., Edens, L.J., Li, X., Nguyen, T., Chen, P., and Levy, D.L. (2015). Concentration-dependent effects of nuclear lamins on nuclear size in xenopus and mammalian cells. J. Biol. Chem. *290*, 27557–27571.

Jevtić, P., Schibler, A.C., Wesley, C.C., Pegoraro, G., Misteli, T., and Levy, D.L. (2019). The nucleoporin ELYS regulates nuclear size by controlling NPC number and nuclear import capacity. EMBO Rep. *20*, 1–16.

Ji, J.Y. (2018). Endothelial Nuclear Lamina in Mechanotransduction Under Shear Stress. In Molecular, Cellular and Tissue Engineering of the Vascular System, pp. 83–104.

Jiang, Y., and Ji, J.Y. (2018). Expression of Nuclear Lamin Proteins in Endothelial Cells is Sensitive to Cell Passage and Fluid Shear Stress. Cell. Mol. Bioeng. *11*, 53–64.

Jimenez-Gutierrez, G.E., Mondragon-Gonzalez, R., Soto-Ponce, L.A., Gómez-Monsiváis, W.L., García-Aguirre, I., Pacheco-Rivera, R.A., Suárez-Sánchez, R., Brancaccio, A., Magaña, J.J., Perlingeiro, R.C.R., et al. (2020). Loss of dystroglycan drives cellular senescence via defective mitosis-mediated genomic instability. Int. J. Mol. Sci. *21*, 1–18.

Jimenez-Mallebrera, C., Torelli, S., Feng, L., Kim, J., Godfrey, C., Clement, E., Mein, R., Abbs, S., Brown, S.C., Campbell, K.P., et al. (2009). A comparative study of α-dystroglycan glycosylation in dystroglycanopathies suggests that the hypoglycosylation of α-dystroglycan does not consistently correlate with clinical severity. Brain Pathol. *19*, 596–611.

Jing, J., Lien, C.F., Sharma, S., Rice, J., Brennan, P.A., and Górecki, D.C. (2004). Aberrant expression, processing and degradation of dystroglycan in squamous cell carcinomas. Eur. J. Cancer *40*, 2143–2151.

Jung, D., Yang, B., Meyer, J., Chamberlain, J.S., and Campbell, K.P. (1995). Identification and characterization of the dystrophin anchoring site on β-dystroglycan. J. Biol. Chem. *270*, 27305–27310.

Kanagawa, M., Omori, Y., Sato, S., Kobayashi, K., Miyagoe-Suzuki, Y., Takeda, S., Endo, T., Furukawa, T., and Toda, T. (2010). Post-translational maturation of dystroglycan is necessary for pikachurin binding and ribbon synaptic localization. J. Biol. Chem. *285*, 31208–31216.

Kano, H., Kobayashi, K., Tachikawa, M., Toda, T., Kano, H., Yoshikawa, H., Herrmann, R., Straub, V., Voit, T., Manya, H., et al. (2002). Deficiency of α-dystroglycan in muscle-eye-brain disease. Biochem. Biophys. Res. Commun. *291*, 1283–1286.

Kärkkäinen, S., Hiipakka, M., Wang, J.H., Kleino, I., Vähä-Jaakkola, M., Renkema, G.H., Liss, M., Wagner, R., and Saksela, K. (2006). Identification of preferred protein interactions by phage-display of the human Src homology-3 proteome. EMBO Rep. *7*, 186–191.

Kaufmann, A., Heinemann, F., Radmacher, M., and Stick, R. (2011). Amphibian oocyte nuclei expressing lamin A with the progeria mutation E145K exhibit an increased elastic modulus. Nucleus *2*, 310–319.

Keep, N.H., Winder, S.J., Moores, C.A., Walke, S., Norwood, F.L.M., and Kendrick-Jones, J. (1999a). Crystal structure of the actin-binding region of utrophin reveals a head-to-tail dimer. Structure *7*, 1539–1546.

Keep, N.H., Norwood, F.L.M., Moores, C.A., Winder, S.J., and Kendrick-Jones, J. (1999b). The 2.0 Å structure of the second calponin homology domain from the actin-binding region of the dystrophin homologue utrophin. J. Mol. Biol. *285*, 1257–1264.

Keys, J., Windsor, A., and Lammerding, J. (2018). Assembly and Use of a Microfluidic Device to Study Cell Migration in Confined Environments. Methods Mol. Biol. *1840*, 101–118.

Khavari, A., and Ehrlicher, A.J. (2019). Nuclei deformation reveals pressure distributions in 3D cell clusters. PLoS One *14*, 1–13.

Khurana, T.S., Hoffman, E.P., and Kunkel, L.M. (1990). Identification of a chromosome 6-encoded dystrophin-related protein. J. Biol. Chem. *265*, 16717–16720.

Kim, J.K., Louhghalam, A., Lee, G., Schafer, B.W., Wirtz, D., and Kim, D.H. (2017). Nuclear lamin A/C harnesses the perinuclear apical actin cables to protect nuclear morphology. Nat. Commun. *8*, 1–13.

Kobayashi, K., Nakahori, Y., Miyake, M., Matsumura, K., Kondo-Iida, E., Nomura, Y., Segawa, M., Yoshioka, M., Saito, K., Osawa, M., et al. (1998). Anancient retrotransposal insertioncauses Fukuyama-typecongenital musculardystrophy. Nature *394*, 388–392.

Koenig, M., and Kunkel, L.M. (1990). Detailed analysis of the repeat domain of dystrophin reveals four potential hinge segments that may confer flexibility. J. Biol. Chem. *265*, 4560–4566.

Korfali, N., Wilkie, G.S., Swanson, S.K., Srsen, V., de las Heras, J., Batrakou, D.G., Malik, P., Zuleger, N., Kerr, A.R.W., Florens, L., et al. (2012). The nuclear envelope proteome differs notably between tissues. Nucleus *3*.

Kramarcy, N.R., Vidal, A., Froehner, S.C., and Sealock, R. (1994). Association of utrophin and multiple dystrophin short forms with the mammalian M(r) 58,000 dystrophin-associated protein (syntrophin). J. Biol. Chem. *269*, 2870–2876.

Krause, M., Te Riet, J., and Wolf, K. (2013). Probing the compressibility of tumor cell nuclei by combined atomic force-confocal microscopy. Phys. Biol. *10*.

Kume, K., Cantwell, H., Burrell, A., and Nurse, P. (2019). Nuclear membrane protein Lem2 regulates nuclear size through membrane flow. Nat. Commun. *10*, 1–8.

Kunz, S., Sevilla, N., McGavern, D.B., Campbell, K.P., and Oldstone, M.B.A. (2001). Molecular analysis of the interaction of LCMV with its cellular receptor α-dystroglycan. J. Cell Biol. *155*, 301–310.

Kunz, S., Rojek, J.M., Perez, M., Spiropoulou, C.F., and Oldstone, M.B.A. (2005). Characterization of the Interaction of Lassa Fever Virus with Its Cellular Receptor α-Dystroglycan. J. Virol. *79*, 5979–5987.

Lammerding, J., Hsiao, J., Schulze, P.C., Kozlov, S., Stewart, C.L., and Lee, R.T. (2005). Abnormal nuclear shape and impaired mechanotransduction in emerin-deficient cells. J. Cell Biol. *170*, 781–791.

Lammerding, J., Fong, L.G., Ji, J.Y., Reue, K., Stewart, C.L., Young, S.G., and Lee, R.T. (2006). Lamins a and C but not lamin B1 regulate nuclear mechanics. J. Biol. Chem. *281*, 25768–25780.

Lara-Chacón, B., De León, M.B., Leocadio, D., Gómez, P., Fuentes-Mera, L., Martínez-Vieyra, I., Ortega, A., Jans, D.A., and Cisneros, B. (2010). Characterization of an importin in α/β-recognized nuclear localization signal in β-dystroglycan. J. Cell. Biochem. *110*, 706–717.

Legardinier, S., Hubert, J.F., Bihan, O. Le, Tascon, C., Rocher, C., Raguénès-Nicol, C., Bondon, A., Hardy, S., and Rumeur, E. Le (2008). Sub-domains of the dystrophin rod domain display contrasting lipid-binding and stability properties. Biochim. Biophys. Acta - Proteins Proteomics *1784*, 672–682.

Lekka, M., and Pabijan, J. (2019). Measuring elastic properties of single cancer cells by AFM. In Methods in Molecular Biology, pp. 315–324.

Leocadio-Victoria, D. (2015). Post-translational modification and nuclear targeting of beta-dystroglycan. University of Sheffield.

Leocadio, D., Mitchell, A., and Winder, S.J. (2016). γ-Secretase Dependent Nuclear Targeting of Dystroglycan. J. Cell. Biochem. *117*, 2149–2157.

Leschziner, A., Moukhles, H., Lindenbaum, M., Gee, S.H., Butterworth, J., Campbell, K.P., and Carbonetto, S. (2000). Neural regulation of α-dystroglycan biosynthesis

and glycosylation in skeletal muscle. J. Neurochem. *74*, 70–80.

Lidov, H.G.W., Selig, S., and Kunkel, L.M. (1995). Dp140: A novel 140 kDa CNS transcript from the dystrophin locus. Hum. Mol. Genet. *4*, 329–335.

Lin, Z., Yang, Z., Xie, R., Ji, Z., Guan, K., and Zhang, M. (2019). Decoding WW domain tandem-mediated target recognitions in tissue growth and cell polarity. Elife *8*, 1–24.

Lipscomb, L., Piggott, R.W., Emmerson, T., and Winder, S.J. (2016). Dasatinib as a treatment for Duchenne muscular dystrophy. Hum. Mol. Genet. *25*, 266–274.

Loh, N.Y., Ambrose, H.J., Guay-Woodford, L.M., DasGupta, S., Nawrotzki, R.A., Blake, D.J., and Davies, K.E. (1998). Genomic organization and refined mapping of the mouse β-dystrobrevin gene. Mamm. Genome *9*, 857–862.

Losasso, C., Di Tommaso, F., Sgambato, A., Ardito, R., Cittadini, A., Giardina, B., Petrucci, T.C., and Brancaccio, A. (2000). Anomalous dystroglycan in carcinoma cell lines. FEBS Lett. *484*, 194–198.

Louvet, E., Yoshida, A., Kumeta, M., and Takeyasu, K. (2014). Probing the stiffness of isolated nucleoli by atomic force microscopy. Histochem. Cell Biol. *141*, 365–381.

Love, D.R., Morris, G.E., Ellis, J.M., Fairbrother, U., Marsden, R.F., Bloomfield, J.F., Edwards, Y.H., Slater, C.P., Parry, D.J., and Davies, K.E. (1991). Tissue distribution of the dystrophin-related gene product and expression in the mdx and dy mouse. Proc. Natl. Acad. Sci. U. S. A. *88*, 3243–3247.

Lüke, Y., Zaim, H., Karakesisoglou, I., Jaeger, V.M., Sellin, L., Lu, W., Schneider, M., Neumann, S., Beijer, A., Munck, M., et al. (2008). Nesprin-2 Giant (NUANCE) maintains nuclear envelope architecture and composition in skin. J. Cell Sci. *121*, 1887–1898.

Lumeng, C.N., Phelps, S.F., Rafael, J.A., Cox, G.A., Hutchinson, T.L., Begy, C.R., Adkins, E., Wiltshire, R., and Chamberlain, J.S. (1999). Characterization of dystrophin and utrophin diversity in the mouse. Hum. Mol. Genet. *8*, 593–599.

Maass, K.K., Rosing, F., Ronchi, P., Willmund, K. V., Devens, F., Hergt, M., Herrmann, H., Lichter, P., and Ernst, A. (2018). Altered nuclear envelope structure and proteasome function of micronuclei. Exp. Cell Res. *371*, 353–363.

Macao, B., Johansson, D.G.A., Hansson, G.C., and Härd, T. (2006). Autoproteolysis coupled to protein folding in the SEA domain of the membrane-bound MUC1 mucin. Nat. Struct. Mol. Biol. *13*, 71–76.

Mahmoud, M.M., Serbanovic-Canic, J., Feng, S., Souilhol, C., Xing, R., Hsiao, S., Mammoto, A., Chen, J., Ariaans, M., Francis, S.E., et al. (2017). Shear stress induces

endothelial-To-mesenchymal transition via the transcription factor Snail. Sci. Rep. *7*, 1–12.

Mamchaoui, K., Trollet, C., Bigot, A., Negroni, E., Chaouch, S., Wolff, A., Kandalla, P.K., Marie, S., Di Santo, J., St Guily, J., et al. (2011). Immortalized pathological human myoblasts: towards a universal tool for the study of neuromuscular disorders. Skelet. Muscle *1*, 34.

Mandigo, T.R., Turcich, B.D., Anderson, A.J., Hussey, M.R., and Folker, E.S. (2019). Drosophila emerins control LINC complex localization and transcription to regulate myonuclear position . J. Cell Sci. jcs.235580.

Markiewicz, E., Tilgner, K., Barker, N., Van De Wetering, M., Clevers, H., Dorobek, M., Hausmanowa-Petrusewicz, I., Ramaekers, F.C.S.S., Broers, J.L.V. V, Blankesteijn, W.M., et al. (2006). The inner nuclear membrane protein Emerin regulates β-catenin activity by restricting its accumulation in the nucleus. EMBO J. *25*, 3275–3285.

Marquez, F.G., Cisneros, B., Garcia, F., Ceja, V., Velázquez, F., Depardón, F., Cervantes, L., Rendón, A., Mornet, D., Rosas-Vargas, H., et al. (2003). Differential expression and subcellular distribution of dystrophin Dp71 isoforms during differentiation process. Neuroscience *118*, 957–966.

Martin, P.T. (2003). Dystroglycan glycosylation and its role in matrix binding in skeletal muscle. Glycobiology *13*, 55–66.

Martin, C., Chen, S., Maya-Mendoza, A., Lovric, J., Sims, P.F.G., and Jackson, D.A. (2009). Lamin B1 maintains the functional plasticity of nucleoli. J. Cell Sci. *122*, 1551–1562.

Martínez-Vieyra, I.A., Vásquez-Limeta, A., González-Ramírez, R., Morales-Lázaro, S.L., Mondragón, M., Mondragón, R., Ortega, A., Winder, S.J., and Cisneros, B. (2013). A role for β-dystroglycan in the organization and structure of the nucleus in myoblasts. Biochim. Biophys. Acta - Mol. Cell Res. *1833*, 698–711.

Mathew, G., Mitchell, A., Down, J.M., Jacobs, L.A., Hamdy, F.C., Eaton, C., Rosario, D.J., Cross, S.S., and Winder, S.J. (2013). Nuclear targeting of dystroglycan promotes the expression of androgen regulated transcription factors in prostate cancer. Sci. Rep. *3*, 2792.

Matsuda, R., Nishikawa, A., and Tanaka, H. (1995). Visualization of dystrophic muscle fibers in mdx mouse by vital staining with evans blue: Evidence of apoptosis in dystrophin-deficient muscle. J. Biochem. *118*, 959–963.

Matsumura, K., Ervasti, J.M., Ohlendieck, K., Kahl, S.D., and Campbell, K.P. (1992). Association of dystrophin-related protein with dystrophin associated proteins in mdx mouse muscle. Nature *360*, 588–591.

Mazumder, A., Roopa, T., Basu, A., Mahadevan, L., and Shivashankar, G. V. (2008). Dynamics of chromatin decondensation reveals the structural integrity of a mechanically prestressed nucleus. Biophys. J. *95*, 3028–3035.

McDearmon, E.L., Combs, A.C., Sekiguchi, K., Fujiwara, H., and Ervasti, J.M. (2006). Brain α-dystroglycan displays unique glycoepitopes and preferential binding to laminin-10/11. FEBS Lett. *580*, 3381–3385.

Meng, C., Sasmal, A., Zhang, Y., Gao, T., Liu, C.C., Khan, N., Varki, A., Wang, F., and Cao, H. (2018). Chemoenzymatic Assembly of Mammalian O-Mannose Glycans. Angew. Chemie - Int. Ed. *57*, 9003–9007.

Mercuri, E., D'Amico, A., Tessa, A., Berardinelli, A., Pane, M., Messina, S., van Reeuwijk, J., Bertini, E., Muntoni, F., and Santorelli, F.M. (2006). POMT2 mutation in a patient with "MEB-like" phenotype. Neuromuscul. Disord. *16*, 446–448.

Mias-Lucquin, D., Dos Santos Morais, R., Chéron, A., Lagarrigue, M., Winder, S.J., Chenuel, T., Pérez, J., Appavou, M.S., Martel, A., Alviset, G., et al. (2020). How the central domain of dystrophin acts to bridge F-actin to sarcolemmal lipids. J. Struct. Biol. *209*, 107411.

Michele, D.E., Barresi, R., Kanagawa, M., Salto, F., Cohn, R.D., Satz, J.S., Dollar, J., Nishino, I., Kelley, R.I., Somer, H., et al. (2002). Post-translational disruption of dystroglycan-ligand interactions in congenital muscular dystrophies. Nature *418*, 417–422.

Mitchell, A., Mathew, G., Jiang, T., Hamdy, F.C., Cross, S.S., Eaton, C., and Winder, S.J. (2013). Dystroglycan function is a novel determinant of tumor growth and behavior in prostate cancer. Prostate *73*, 398–408.

Mizuno, Y., Thompson, T.G., Guyon, J.R., Lidov, H.G.W., Brosius, M., Imamura, M., Ozawa, E., Watkins, S.C., and Kunkel, L.M. (2001). Desmuslin, an intermediate filament protein that interacts with α-dystrobrevin and desmin. Proc. Natl. Acad. Sci. U. S. A. *98*, 6156–6161.

Moores, C.A., Keep, N.H., and Kendrick-Jones, J. (2000). Structure of the utrophin actin-binding domain bound to F-actin reveals binding by an induced fit mechanism. J. Mol. Biol. *297*, 465–480.

Morikawa, Y., Heallen, T., Leach, J., Xiao, Y., and Martin, J.F. (2017). Dystrophin-glycoprotein complex sequesters Yap to inhibit cardiomyocyte proliferation. Nature *547*, 227–231.

Moser, B., Basílio, J., Gotzmann, J., Brachner, A., and Foisner, R. (2020). Comparative Interactome Analysis of Emerin, MAN1 and LEM2 Reveals a Unique Role for LEM2 in Nucleotide Excision Repair. Cells *9*.

Mugahid, D., Kalocsay, M., Liu, X., Gruver, J.S., Peshkin, L., and Kirschner, M.W. (2020). YAP regulates cell size and growth dynamics via non-cell autonomous mediators. Elife *9*, 482836.

Mukherjee, A., Barai, A., Singh, R.K., Yan, W., and Sen, S. (2020). Nuclear plasticity increases susceptibility to damage during confined migration. PLoS Comput. Biol. *16*, 1–23.

Nava, M.M., Miroshnikova, Y.A., Biggs, L.C., Whitefield, D.B., Metge, F., Boucas, J., Vihinen, H., Jokitalo, E., Li, X., García Arcos, J.M., et al. (2020). Heterochromatin-Driven Nuclear Softening Protects the Genome against Mechanical Stress-Induced Damage. Cell 1–18.

Nawrotzki, R., Loh, N.Y., Ruegg, M.A., Davies, K.E., and Blake, D.J. (1998). Characterisation of α-dystrobrevin in muscle. J. Cell Sci. *111*, 2595–2605.

Neely, J.D., Amiry-Moghaddam, M., Ottersen, O.P., Froehner, S.C., Agre, P., and Adams, M.E. (2001). Syntrophin-dependent expression and localization of Aquaporin-4 water channel protein. Proc. Natl. Acad. Sci. U. S. A. *98*, 14108–14113.

Newey, S.E., Benson, M.A., Ponting, C.P., Davies, K.E., and Blake, D.J. (2000). Alternative splicing of dystrobrevin regulates the stoichiometry of syntrophin binding to the dystrophin protein complex. Curr. Biol. *10*, 1295–1298.

Newey, S.E., Howman, E. V., Ponting, C.P., Benson, M.A., Nawrotzki, R., Loh, N.Y., Davies, K.E., and Blake, D.J. (2001). Syncoilin, a Novel Member of the Intermediate Filament Superfamily That Interacts with α-Dystrobrevin in Skeletal Muscle. J. Biol. Chem. *276*, 6645–6655.

Nilsson, J., Nilsson, J., Larson, G., and Grahn, A. (2010). Characterization of site-specific O-glycan structures within the mucin-like domain of α-dystroglycan from human skeletal muscle. Glycobiology *20*, 1160–1169.

Nishida, A., Yasuno, S., Takeuchi, A., Awano, H., Lee, T., Niba, E.T.E., Fujimoto, T., Itoh, K., Takeshima, Y., Nishio, H., et al. (2016). HEK293 cells express dystrophin Dp71 with nucleus-specific localization of Dp71ab. Histochem. Cell Biol. *146*, 301–309.

Nmezi, B., Xu, J., Fu, R., Armiger, T.J., Rodriguez-Bey, G., Powell, J.S., Ma, H., Sullivan, M., Tu, Y., Chen, N.Y., et al. (2019). Concentric organization of A- and B-type lamins predicts their distinct roles in the spatial organization and stability of the nuclear lamina. Proc. Natl. Acad. Sci. *116*, 201810070.

Oppizzi, M.L., Akhavan, A., Singh, M., Fata, J.E., and L, J. (2008). Nuclear Translocation of B-Dystroglycan Reveals a Distinctive Trafficking Pattern of Autoproteolyzed Mucins. Traffic *9*, 2063–2072.

Ott, C.M., and Lingappa, V.R. (2002). Integral membrane protein biosynthesis: Why topology is hard to predict. J. Cell Sci. *115*, 2003–2009.

Pall, E.A., Bolton, K.M., and Ervasti, J.M. (1996). Differential heparin inhibition of skeletal muscle α-dystroglycan binding to laminins. J. Biol. Chem. *271*, 3817–3821.

Pan, L., Hong, Z., Yu, L., Gao, Y., Zhang, R., Feng, H., Su, L., and Wang, G. (2017). Shear stress induces human aortic endothelial cell apoptosis via interleukin-1 receptor-associated kinase 2-induced endoplasmic reticulum stress. Mol. Med. Rep. *16*, 7205–7212.

Parberry-Clark, C., Bury, J.P., Cross, S.S., and Winder, S.J. (2011). Loss of dystroglycan function in oesophageal cancer. Histopathology *59*, 180–187.

Patteson, A.E., Vahabikashi, A., Pogoda, K., Adam, S.A., Mandal, K., Kittisopikul, M., Sivagurunathan, S., Goldman, A., Goldman, R.D., and Janmey, P.A. (2019a). Vimentin protects cells against nuclear rupture and DNA damage during migration. J. Cell Biol. jcb.201902046.

Patteson, A.E., Pogoda, K., Byfield, F.J., Mandal, K., Ostrowska-Podhorodecka, Z., Charrier, E.E., Galie, P.A., Deptuła, P., Bucki, R., McCulloch, C.A., et al. (2019b). Loss of Vimentin Enhances Cell Motility through Small Confining Spaces. Small *15*, 1–10.

Peters, M.F., Adams, M.E., and Froehner, S.C. (1997a). Differential association of syntrophin pairs with the dystrophin complex. J. Cell Biol. *138*, 81–93.

Peters, M.F., O'Brien, K.F., Sadoulet-Puccio, H.M., Kunkel, L.M., Adams, M.E., and Froehner, S.C. (1997b). β-Dystrobrevin, a new member of the dystrophin family: Identification, cloning, and protein associations. J. Biol. Chem. *272*, 31561–31569.

Peters, M.F., Sadoulet-Puccio, H.M., Grady, R.M., Kramarcy, N.R., Kunkel, L.M., Sanes, J.R., Sealock, R., and Froehner, S.C. (1998). Differential membrane localization and intermolecular associations of α-dystrobrevin isoforms in skeletal muscle. J. Cell Biol. *142*, 1269–1278.

Petrof, B.J., Shrager, J.B., Stedman, H.H., Kelly, A.M., and Sweeney, H.L. (1993). Dystrophin protects the sarcolemma from stresses developed during muscle contraction. Proc. Natl. Acad. Sci. U. S. A. *90*, 3710–3714.

Pfeifer, C.R., Xia, Y., Zhu, K., Liu, D., Irianto, J., Morales García, V.M., Santiago Millán, L.M., Niese, B., Harding, S., Deviri, D., et al. (2018). Constricted migration increases DNA damage and independently represses cell cycle. Mol. Biol. Cell *29*, 1948–1962.

Philip, J.T., and Dahl, K.N. (2008). Nuclear mechanotransduction: Response of the lamina to extracellular stress with implications in aging. J. Biomech. *41*, 3164–3170.

Piggott, R. (2014). The Regulation of Beta- Dystroglycan Internalization. University of Sheffield.

Piluso, G., Mirabella, M., Ricci, E., Belsito, A., Abbondanza, C., Servidei, S., Puca, A.A., Tonali, P., Puca, G.A., and Nigro, V. (2000). Γ1- and Γ2-Syntrophins, Two Novel Dystrophin-Binding Proteins Localized in Neuronal Cells. J. Biol. Chem. *275*, 15851–15860.

Poon, E., Howman, E. V., Newey, S.E., and Davies, K.E. (2002). Association of syncoilin and desmin: Linking intermediate filament proteins to the dystrophin-associated protein complex. J. Biol. Chem. *277*, 3433–3439.

Porter, G.A., Dmytrenko, G.M., Winkelmann, J.C., and Bloch, R.J. (1992). Dystrophin colocalizes with β-spectrin in distinct subsarcolemmal domains in mammalian skeletal muscle. J. Cell Biol. *117*, 997–1005.

Prins, K.W., Humston, J.L., Mehta, A., Tate, V., Ralston, E., and Ervasti, J.M. (2009). Dystrophin is a microtubule-associated protein. J. Cell Biol. *186*, 363–369.

Raab, M., Gentili, M., De Belly, H., Thiam, H.R., Vargas, P., Jimenez, A.J., Lautenschlaeger, F., Voituriez, R., Lennon-Duménil, A.M., Manel, N., et al. (2016). ESCRT III repairs nuclear envelope ruptures during cell migration to limit DNA damage and cell death. Science (80-.). *352*, 359–362.

Rambukkana, A., Yamada, H., Zanazzi, G., Mathus, T., Salzer, J.L., Yurchenco, P.D., Campbell, K.P., and Fischetti, V.A. (1998). Role of α-dystroglycan as a Schwann cell receptor for Mycobacterium leprae. Science (80-.). *282*, 2076–2079.

Ranade, D., Pradhan, R., Jayakrishnan, M., Hegde, S., and Sengupta, K. (2019). Lamin A / C and Emerin depletion impacts chromatin organization and dynamics in the interphase nucleus. BMC Mol. Cell Biol. *5*, 1–20.

van Reeuwijk, J., Grewal, P.K., Salih, M.A.M., Beltrán-Valero de Bernabé, D., McLaughlan, J.M., Michielse, C.B., Herrmann, R., Hewitt, J.E., Steinbrecher, A., Seidahmed, M.Z., et al. (2007). Intragenic deletion in the LARGE gene causes Walker-Warburg syndrome. Hum. Genet. *121*, 685–690.

Van Reeuwijk, J., Janssen, M., Van Den Elzen, C., Beltran-Valero De Bernabé, D., Sabatelli, P., Merlini, L., Boon, M., Scheffer, H., Brockington, M., Muntoni, F., et al. (2005). POMT2 mutations cause α-dystroglycan hypoglycosylation and Walker-Warburg syndrome. J. Med. Genet. *42*, 907–912.

Reis-Sobreiro, M., Chen, J.-F., Novitskaya, T., You, S., Morley, S., Steadman, K., Kaur Gill, N., Eskaros, A., Rotinen, M., Chu, C.-Y., et al. (2018). Emerin deregulation links nuclear shape instability to metastatic potential. Cancer Res. *78*, canres.0608.2018.

Rezniczek, G.A., Konieczny, P., Nikolic, B., Reipert, S., Schneller, D., Abrahamsberg, C., Davies, K.E., Winder, S.J., and Wiche, G. (2007). Plectin 1f scaffolding at the sarcolemma of dystrophic (mdx) muscle fibers through multiple interactions with β-dystroglycan. J. Cell Biol. *176*, 965–977.

Rheinlaender, J., Dimitracopoulos, A., Wallmeyer, B., Kronenberg, N.M., Chalut, K.J., Gather, M.C., Betz, T., Charras, G.T., and Franze, K. (2020). Cortical cell stiffness is independent of substrate mechanics. Nat. Mater.

Riemersma, M., Mandel, H., van Beusekom, E., Gazzoli, I., Roscioli, T., Eran, A., Gershoni-Baruch, R., Gershoni, M., Pietrokovski, S., Vissers, L.E., et al. (2015). Absence of α- and β-dystroglycan is associated with Walker-Warburg syndrome. Neurology *84*, 2177 LP – 2182.

Rodríguez-Munoz, R., Cardenas-Aguayo, M.D.C., Aleman, V., Osorio, B., Chavez-Gonzalez, O., Rendon, A., Martínez-Rojas, D., and Meraz-Ríos, M.A. (2015). Novel nuclear protein complexes of dystrophin 71 isoforms in rat cultured hippocampal gabaergic and glutamatergic neurons. PLoS One *10*, 1–22.

Rodríguez-Muñoz, R., Villarreal-Silva, M., González-Ramírez, R., García-Sierra, F., Mondragón, M., Mondragón, R., Cerna, J., and Cisneros, B. (2008). Neuronal differentiation modulates the dystrophin Dp71d binding to the nuclear matrix. Biochem. Biophys. Res. Commun. *375*, 303–307.

Rowat, A.C., Lammerding, J., and Ipsen, J.H. (2006). Mechanical properties of the cell nucleus and the effect of emerin deficiency. Biophys. J. *91*, 4649–4664.

Le Rumeur, E., Fichou, Y., Pottier, S., Gaboriau, F., Rondeau-Mouro, C., Vincent, M., Gallay, J., and Bondon, A. (2003). Interaction of dystrophin rod domain with membrane phospholipids: Evidence of a close proximity between tryptophan residues and lipids. J. Biol. Chem. *278*, 5993–6001.

Le Rumeur, E., Pottier, S., Da Costa, G., Metzinger, L., Mouret, L., Rocher, C., Fourage, M., Rondeau-Mouro, C., and Bondon, A. (2007). Binding of the dystrophin second repeat to membrane di-oleyl phospholipids is dependent upon lipid packing. Biochim. Biophys. Acta - Biomembr. *1768*, 648–654.

Russo, K., Di Stasio, E., Macchia, G., Rosa, G., Brancaccio, A., and Corinna Petrucci, T. (2000). Characterization of the β-dystroglycan-growth factor receptor 2 (Grb2) interaction. Biochem. Biophys. Res. Commun. *274*, 93–98.

Rybakova, I.N., and Ervasti, J.M. (1997). Dystrophin-glycoprotein complex is monomeric and stabilizes actin filaments in vitro through a lateral association. J. Biol. Chem. *272*, 28771–28778.

Rybakova, I.N., Amann, K.J., and Ervasti, J.M. (1996). A new model for the interaction of dystrophin with F-actin. J. Cell Biol. *135*, 661–672.

Rybakova, I.N., Patel, J.R., and Ervasti, J.M. (2000). The dystrophin complex forms a mechanically strong link between the sarcolemma and costameric actin. J. Cell Biol. *150*, 1209–1214.

Rybakova, I.N., Patel, J.R., Davies, K.E., Yurchenco, P.D., and Ervasti, J.M. (2002). Utrophin Binds Laterally along Actin Filaments and Can Couple Costameric Actin with Sarcolemma When Overexpressed in Dystrophin-deficient Muscle. Mol. Biol. Cell *13*, 1512–1521.

Sabourin, J., Lamiche, C., Vandebrouck, A., Magaud, C., Rivet, J., Cognard, C., Bourmeyster, N., and Constantin, B. (2009). Regulation of TRPC1 and TRPC4 cation channels requires an α1-syntrophin-dependent complex in skeletal mouse myotubes. J. Biol. Chem. *284*, 36248–36261.

Sadaie, M., Salama, R., Carroll, T., Tomimatsu, K., Chandra, T., Young, A.R.J., Narita, M., Pérez-Mancera, P.A., Bennett, D.C., Chong, H., et al. (2013). Redistribution of the Lamin B1 genomic binding profile affects rearrangement of heterochromatic domains and SAHF formation during senescence. Genes Dev. *27*, 1800–1808.

Sadaie, M., Dillon, C., Narita, M., Young, A.R.J., Cairney, C.J., Godwin, L.S., Torrance, C.J., Bennett, D.C., and Keith, W.N. (2015). Cell-based screen for altered nuclear phenotypes reveals senescence progression in polyploid cells after Aurora kinase B inhibition. Mol. Biol. Cell *26*, 2971–2985.

Sadoulet-Puccio, H.M., Rajala, M., and Kunkel, L.M. (1997). Dystrobrevin and dystrophin: An interaction through coiled-coil motifs. Proc. Natl. Acad. Sci. U. S. A. *94*, 12413–12418.

Sahoo, M.R., Devi, T.R., Dasgupta, M., Nongdam, P., and Prakash, N. (2020). Reactive oxygen species scavenging mechanisms associated with polyethylene glycol mediated osmotic stress tolerance in Chinese potato. Sci. Rep. *10*, 1–9.

Salpingidou, G., Smertenko, A., Hausmanowa-Petrucewicz, I., Hussey, P.J., and Hutchison, C.J. (2007). A novel role for the nuclear membrane protein emerin in association of the centrosome to the outer nuclear membrane. J. Cell Biol. *178*, 897–904.

Salunkhe, S., Mishra, S. V., Nair, J., Shah, S., Gardi, N., Thorat, R., Sarkar, D., Rajendra, J., Kaur, E., and Dutt, S. (2021). Nuclear localization of p65 reverses therapy-induced senescence. J. Cell Sci. *134*.

Sandoval, I. V., Colaco, C.A.L.S., and Lazarides, E. (1983). Purification of the intermediate filament-associated protein, synemin, from chicken smooth muscle. Studies on its physicochemical properties, interaction with desmin, and phosphorylation. J. Biol. Chem. *258*, 2568–2576.

Sankaran, J.S., Sen, B., Dudakovic, A., Paradise, C.R., Perdue, T., Xie, Z., McGrath, C., Styner, M., Newberg, J., Uzer, G., et al. (2020). Knockdown of formin mDia2 alters lamin B1 levels and increases osteogenesis in stem cells. Stem Cells *38*, 102–117.

Santavuori, P., Somer, H., Sainio, K., Rapola, J., Kruus, S., Nikitin, T., Ketonen, L., and Leisti, J. (1989). Muscle-eye-brain disease (MEB). Brain Dev. *11*, 147–153.

Santos-Zas, I., Cid-Díaz, T., González-Sánchez, J., Gurriarán-Rodriguez, U., Seoane-Mosteiro, C., Porteiro, B., Nogueiras, R., Casabiell, X., Luis Relova, J., Gallego, R., et al. (2017). Obestatin controls skeletal muscle fiber-type determination. Sci. Rep. *7*, 1–14.

Dos Santos Morais, R., Delalande, O., Pérez, J., Mias-Lucquin, D., Lagarrigue, M., Martel, A., Molza, A.E., Chéron, A., Raguénès-Nicol, C., Chenuel, T., et al. (2018). Human Dystrophin Structural Changes upon Binding to Anionic Membrane Lipids. Biophys. J. *115*, 1231–1239.

Sasaki, T., Yamada, H., Matsumura, K., Shimizu, T., Kobata, A., and Endo, T. (1998). Detection of O-mannosyl glycans in rabbit skeletal muscle α-dystroglycan. Biochim. Biophys. Acta - Gen. Subj. *1425*, 599–606.

Schäpe, J., Praußе, S., Radmacher, M., and Stick, R. (2009). Influence of lamin A on the mechanical properties of amphibian oocyte nuclei measured by atomic force microscopy. Biophys. J. *96*, 4319–4325.

Schillers, H., Rianna, C., Schäpe, J., Luque, T., Doschke, H., Wälte, M., Uriarte, J.J., Campillo, N., Michanetzis, G.P.A., Dumitru, A., et al. (2017). Standardized Nanomechanical Atomic Force Microscopy Procedure (SNAP) for Measuring Soft and Biological Samples. Sci. Rep. *7*, 1–9.

Schirmer, E.C., Florens, L., Guan, T., Yates, J.R., and Gerace, L. (2003). Nuclear membrane proteins with potential disease links found by subtractive proteomics. Science (80-.). *301*, 1380–1382.

Schreiner, S.M., Koo, P.K., Zhao, Y., Mochrie, S.G.J., and King, M.C. (2015). The tethering of chromatin to the nuclear envelope supports nuclear mechanics. Nat. Commun. *6*.

Sciandra, F., Schneider, M., Giardina, B., Baumgartner, S., Petrucci, T.C., and Brancaccio, A. (2001). Identification of the β-dystroglycan binding epitope within the C-terminal region of α-dystroglycan. Eur. J. Biochem. *268*, 4590–4597.

Sgambato, A., Migaldi, M., Montanari, M., Camerini, A., Brancaccio, A., Rossi, G., Cangiano, R., Losasso, C., Capelli, G., Trentini, G.P., et al. (2003). Dystroglycan expression is frequently reduced in human breast and colon cancers and is associated with tumor progression. Am. J. Pathol. *162*, 849–860.

Sgambato, A., Tarquini, E., Resci, F., De Paola, B., Faraglia, B., Camerini, A., Rettino, A., Migaldi, M., Cittadini, A., and Zannoni, G.F. (2006). Aberrant expression of α-dystroglycan in cervical and vulvar cancer. Gynecol. Oncol. *103*, 397–404.

Shah, P., Hobson, C.M., Cheng, S., Colville, M.J., Paszek, M.J., Superfine, R., Lammerding, J., Hobson, C.M., Colville, M.J., and Paszek, M.J. (2020). Nuclear Deformation Causes DNA Damage by Increasing Replication Stress. Curr. Biol. 1–13.

Shah, P.P., Donahue, G., Otte, G.L., Capell, B.C., Nelson, D.M., Cao, K., Aggarwala, V., Cruickshanks, H.A., Rai, T.S., McBryan, T., et al. (2013). Lamin B1 depletion in senescent cells triggers large-scale changes in gene expression and the chromatin landscape. Genes Dev. *27*, 1787–1799.

Sheckler, L.R., Henry, L., Sugita, S., Südhof, T.C., and Rudenko, G. (2006). Crystal structure of the second LNS/LG domain from neurexin 1α: Ca2+ binding and the effects of alternative splicing. J. Biol. Chem. *281*, 22896–22905.

Shen, J.G., Xu, C.Y., Li, X., Dong, M.J., Jiang, Z.N., Wang, J., and Wang, L.B. (2012). Dystroglycan is associated with tumor progression and patient survival in gastric cancer. Pathol. Oncol. Res. *18*, 79–84.

Shimi, T., Kittisopikul, M., Tran, J., Goldman, A.E., Adam, S.A., Zheng, Y., Jaqaman, K., and Goldman, R.D. (2015). Structural organization of nuclear lamins A, C, B1, and B2 revealed by superresolution microscopy. Mol. Biol. Cell *26*, 4075–4086.

Shimojima, M., Yuasa, S., Motoda, C., Yozu, G., Nagai, T., Ito, S., Lachmann, M., Kashimura, S., Takei, M., Kusumoto, D., et al. (2017). Emerin plays a crucial role in nuclear invagination and in the nuclear calcium transient. Sci. Rep. *7*, 1–16.

Shimojo, H., Kobayashi, M., Kamigaito, T., Shimojo, Y., Fukuda, M., and Nakayama, J. (2011). Reduced glycosylation of α-dystroglycans on carcinoma cells contributes to formation of highly infiltrative histological patterns in prostate cancer. Prostate *71*, 1151–1157.

Signorino, G., Covaceuszach, S., Bozzi, M., Hübner, W., Mönkemöller, V., Konarev, P. V., Cassetta, A., Brancaccio, A., and Sciandra, F. (2017). A dystroglycan mutation (p.Cys667Phe) associated to muscle-eye-brain disease with multicystic leucodystrophy results in ER-retention of the mutant protein. Hum. Mutat. *39*, 266–280.

Smalheiser, N.R., and Schwartz, N.B. (1987). Cranin: a laminin-binding protein of cell membranes. Proc. Natl. Acad. Sci. U. S. A. *84*, 6457–6461.

Smirnov, S.P., McDearmon, E.L., Li, S., Ervasti, J.M., Tryggvason, K., and Yurchenco, P.D. (2002). Contributions of the LG modules and furin processing to laminin-2 functions. J. Biol. Chem. *277*, 18928–18937.

Snyers, L., Erhart, R., Laffer, S., Pusch, O., Weipoltshammer, K., and Schöfer, C. (2017). LEM4/ANKLE-2 deficiency impairs post-mitotic re-localization of BAF, LAP2α and LaminA to the nucleus, causes nuclear envelope instability in telophase and leads to hyperploidy in HeLa cells. Eur. J. Cell Biol.

Soltow, Q.A., Zeanah, E.H., Lira, V.A., and Criswell, D.S. (2013). Cessation of cyclic stretch induces atrophy of C2C12 myotubes. Biochem. Biophys. Res. Commun. *434*, 316–321.

Sotgia, F., Lee, J.K., Das, K., Bedford, M., Petrucci, T.C., Macioce, P., Sargiacomo, M., Bricarelli, F.D., Minetti, C., Sudol, M., et al. (2000). Caveolin-3 directly interacts with the C-terminal tail of β-dystroglycan. Identification of a central WW-like domain within caveolin family members. J. Biol. Chem. *275*, 38048–38058.

Sotgia, F., Lee, H., Bedford, M.T., Petrucci, T., Sudol, M., and Lisanti, M.P. (2001). Tyrosine phosphorylation of β-dystroglycan at its WW domain binding motif, PPxY, recruits SH2 domain containing proteins. Biochemistry *40*, 14585–14592.

Sotgia, F., Bonuccelli, G., Bedford, M., Brancaccio, A., Mayer, U., Wilson, M.T., Campos-Gonzalez, R., Brooks, J.W., Sudol, M., and Lisanti, M.P. (2003). Localization of phospho-beta-dystroglycan (pY892) to an intracellular vesicular compartment in cultured cells and skeletal muscle fibers in vivo. Biochemistry *42*, 7110–7123.

Soto, M., García-Santisteban, I., Krenning, L., Medema, R.H., and Raaijmakers, J.A. (2018). Chromosomes trapped in micronuclei are liable to segregation errors. J. Cell Sci. *131*.

Spence, H.J., Dhillon, A.S., James, M., and Winder, S.J. (2004a). Dystroglycan, a scaffold for the ERK-MAP kinase cascade. EMBO Rep. *5*, 484–489.

Spence, H.J., Chen, Y.-J., Batchelor, C.L., Higginson, J.R., Suila, H., Carpen, O., and Winder, S.J. (2004b). Ezrin-dependent regulation of the actin cytoskeleton by beta-dystroglycan. Hum. Mol. Genet. *13*, 1657–1668.

Stalnaker, S.H., Hashmi, S., Lim, J.M., Aoki, K., Porterfield, M., Gutierrez-Sanchez, G., Wheeler, J., Ervasti, J.M., Bergmann, C., Tiemeyer, M., et al. (2010). Site mapping and characterization of O-glycan structures on α-dystroglycan isolated from rabbit skeletal muscle. J. Biol. Chem. *285*, 24882–24891.

Di Stasio, E., Sciandra, F., Maras, B., Di Tommaso, F., Petrucci, T.C., Giardina, B., and Brancaccio, A. (1999). Structural and functional analysis of the N-terminal extracellular region of β-dystroglycan. Biochem. Biophys. Res. Commun. *266*, 274–278.

Stephens, A.D., Banigan, E.J., Adam, S.A., Goldman, R.D., and Marko, J.F. (2017). Chromatin and lamin a determine two different mechanical response regimes of the cell nucleus. Mol. Biol. Cell *28*, 1984–1996.

Stetefeld, J., Alexandrescu, A.T., Maciejewski, M.W., Jenny, M., Rathgeb-Szabo, K., Schulthess, T., Landwehr, R., Frank, S., Ruegg, M.A., and Kammerer, R.A. (2004). Modulation of agrin function by alternative splicing and Ca2+ binding. Structure *12*, 503–515.

Stone, M.R., O'Neill, A., Catino, D., and Bloch, R.J. (2005). Specific Interaction of the Actin-binding Domain of Dystrophin with Intermediate Filaments Containing Keratin 19. Mol. Biol. Cell *16*, 4280–4293.

Stone, M.R., O'Neill, A., Lovering, R.M., Strong, J., Resneck, W.G., Reed, P.W., Toivola, D.M., Ursitti, J.A., Omary, M.B., and Bloch, R.J. (2007). Absence of keratin 19 in mice causes skeletal myopathy with mitochondrial and sarcolemmal reorganization. J. Cell Sci. *120*, 3999–4008.

Strang-Karlsson, S., Johnson, K., Töpf, A., Xu, L., Lek, M., MacArthur, D.G., Casar-Borota, O., Williams, M., Straub, V., and Wallgren-Pettersson, C. (2018). A novel compound heterozygous mutation in the POMK gene causing limb-girdle muscular dystrophy-dystroglycanopathy in a sib pair. Neuromuscul. Disord. *28*, 614–618.

Straub, V., Bittner, R.E., Leger, J.J., and Voit, T. (1992). Direct visualization of the dystrophin network on skeletal muscle fiber membrane. J. Cell Biol. *119*, 1183–1192.

Streppa, L., Ratti, F., Goillot, E., Devin, A., Schaeffer, L., Arneodo, A., and Argoul, F. (2018). Prestressed cells are prone to cytoskeleton failures under localized shear strain: An experimental demonstration on muscle precursor cells. Sci. Rep. *8*, 1–16.

Suárez-Sánchez, R., Aguilar, A., Wagstaff, K.M., Velez, G., Azuara-Medina, P.M., Gomez, P., Vásquez-Limeta, A., Hernández-Hernández, O., Lieu, K.G., Jans, D.A., et al. (2014). Nucleocytoplasmic shuttling of the Duchenne muscular dystrophy gene product dystrophin Dp71d is dependent on the importin α/β and CRM1 nuclear transporters and microtubule motor dynein. Biochim. Biophys. Acta - Mol. Cell Res. *1843*, 985–1001.

Sugita, S., Saito, F., Tang, J., Satz, J., Campbell, K., and Südhof, T.C. (2001). A stoichiometric complex of neurexins and dystroglycan in brain. J. Cell Biol. *154*, 435–445.

Sumita, K., Sato, Y., Iida, J., Kawata, A., Hamano, M., Hirabayashi, S., Ohno, K., Peles, E., and Hata, Y. (2007). Synaptic scaffolding molecule (S-SCAM) membrane-associated guanylate kinase with inverted organization (MAGI)-2 is associated with cell adhesion molecules at inhibitory synapses in rat hippocampal neurons. J. Neurochem. *100*, 154–166.

Sun, Y., Liu, W.Z., Liu, T., Feng, X., Yang, N., and Zhou, H.F. (2015). Signaling pathway of MAPK/ERK in cell proliferation, differentiation, migration, senescence and

apoptosis. J. Recept. Signal Transduct. *35*, 600–604.

Suzuki, A., Yoshida, M., Yamamoto, H., and Ozawa, E. (1992). Glycoprotein-binding site of dystrophin is confined to the cysteine-rich domain and the first half of the carboxy-terminal domain. FEBS Lett. *308*, 154–160.

Suzuki, A., Yoshida, M., and Ozawa, E. (1995). Mammalian α1- and β1-syntrophin bind to the alternative splice-prone region of the dystrophin COOH terminus. J. Cell Biol. *128*, 373–381.

Suzuki, K., Bose, P., Leong-Quong, R.Y., Fujita, D.J., and Riabowol, K. (2010). REAP: A two minute cell fractionation method. BMC Res. Notes *3*, 294.

Swift, J., Ivanovska, I.L., Buxboim, A., Harada, T., Dingal, P.C.D.P., Pinter, J., Pajerowski, J.D., Spinler, K.R., Shin, J.W., Tewari, M., et al. (2013a). Nuclear lamin-A scales with tissue stiffness and enhances matrix-directed differentiation. Science (80-.). *341*, 1–36.

Swift, J., Ivanovska, I.L., Buxboim, A., Harada, T., Dingal, P.C.D.D.P., Pinter, J., Pajerowski, J.D., Spinler, K.R., Shin, J.-W.W., Tewari, M., et al. (2013b). Nuclear lamin-A scales with tissue stiffness and enhances matrix-directed differentiation. Science (80-.). *341*, 1–36.

Tajik, A., Zhang, Y., Wei, F., Sun, J., Jia, Q., Zhou, W., Singh, R., Khanna, N., Belmont, A.S., and Wang, N. (2016). Transcription upregulation via force-induced direct stretching of chromatin. Nat. Mater. *15*, 1287–1296.

Talts, J.F., Mann, K., Yamada, Y., and Timpl, R. (1998). Structural analysis and proteolytic processing of recombinant G domain of mouse laminin α2 chain. FEBS Lett. *426*, 71–76.

Talts, J.F., Andac, Z., Göhring, W., Brancaccio, A., and Timpl, R. (1999). Binding of the G domains of laminin α1 and α2 chains and perlecan to heparin, sulfatides, α-dystroglycan and several extracellular matrix proteins. EMBO J. *18*, 863–870.

Talts, J.F., Sasaki, T., Miosge, N., Göhring, W., Mann, K., Mayne, R., and Timpl, R. (2000). Structural and functional analysis of the recombinant G domain of the laminin α4 chain and its proteolytic processing in tissues. J. Biol. Chem. *275*, 35192–35199.

Tanoue, T., Adachi, M., Moriguchi, T., and Nishida, E. (2000). A conserved docking motif in MAP kinases common to substrates, activators and regulators. Nat. Cell Biol. *2*, 110–116.

Thompson, O., Kleino, I., Crimaldi, L., Gimona, M., Saksela, K., and Winder, S.J. (2008). Dystroglycan, Tks5 and Src mediated assembly of podosomes in myoblasts. PLoS One *3*, e3638.

Thompson, O., Moore, C.J., Hussain, S.-A., Kleino, I., Peckham, M., Hohenester, E., Ayscough, K.R., Saksela, K., and Winder, S.J. (2010a). Modulation of cell spreading and cell-substrate adhesion dynamics by dystroglycan. J. Cell Sci. *123*, 118–127.

Thompson, O., Moore, C.J., Hussain, S.A., Kleino, I., Peckham, M., Hohenester, E., Ayscough, K.R., Saksela, K., and Winder, S.J. (2010b). Modulation of cell spreading and cell-substrate adhesion dynamics by dystroglycan. J. Cell Sci. *123*, 118–127.

Timpl, R., Tisi, D., Talts, J.F., Andac, Z., Sasaki, T., and Hohenester, E. (2000). Structure and function of laminin LG modules. Matrix Biol. *19*, 309–317.

Tinsley, J.M., Blake, D.J., Roche, A., Fairbrother, U., Riss, J., Byth, B.C., Knight, A.E., Kendrick-Jones, J., Suthers, G.K., Love, D.R., et al. (1992). Primary structure of dystrophin-related protein. Nature *360*, 591–593.

Toda, T., Kobayashi, K., Kondo-Iida, E., Sasaki, J., and Nakamura, Y. (2000). The Fukuyama congenital muscular dystrophy story. Neuromuscul. Disord. *10*, 153–159.

Triyoso, D.H., and Good, T.A. (1999). Pulsatile shear stress leads to DNA fragmentation in human SH-SY5Y neuroblastoma cell line. J. Physiol. *515*, 355–365.

Vandebrouck, A., Ducret, T., Basset, O., Sebille, S., Raymond, G., Ruegg, U., Gailly, P., Cognard, C., and Constantin, B. (2006). Regulation of store-operated calcium entries and mitochondrial uptake by minidystrophin expression in cultured myotubes. FASEB J. *20*, 136–138.

Vásquez-Limeta, A., Wagstaff, K.M., Ortega, A., Crouch, D.H., Jans, D.A., and Cisneros, B. (2014). Nuclear import of β-dystroglycan is facilitated by ezrin-mediated cytoskeleton reorganization. PLoS One *9*.

Vélez-Aguilera, G., Gómez-López, J., Jiménez-Gutiérrez, G., Vásquez-Limeta, A., Laredo-Cisneros, M., Gómez, P., Winder, S., and Cisneros, B. (2018). Control of nuclear β-dystroglycan content is crucial for the maintenance of nuclear envelope integrity and function. BBA - Mol. Cell Res. *1865*, 406–420.

Villarreal-Silva, M., Suárez-Sánchez, R., Rodríguez-Muñoz, R., Mornet, D., and Cisneros, B. (2010). Dystrophin Dp71 is critical for stability of the DAPs in the nucleus of PC12 cells. Neurochem. Res. *35*, 366–373.

Villarreal-Silva, M., Centeno-Cruz, F., Suárez-Sánchez, R., Garrido, E., and Cisneros, B. (2011). Knockdown of dystrophin Dp71 impairs PC12 cells cycle: Localization in the spindle and cytokinesis structures implies a role for Dp71 in cell division. PLoS One *6*.

Vivante, A., Bronshtein, I., and Garini, Y. (2020). Chromatin Viscoelasticity Measured by Local Dynamic Analysis. Biophys. J. *118*, 2258–2267.

Wala, J., and Das, S. (2020). Mapping of biomechanical properties of cell lines on altered matrix stiffness using atomic force microscopy. Biomech. Model. Mechanobiol.

Wang, X., Liu, H., Zhu, M., Cao, C., Xu, Z., Tsatskis, Y., Lau, K., Kuok, C., Filleter, T., McNeill, H., et al. (2018). Mechanical stability of the cell nucleus: roles played by the cytoskeleton in nuclear deformation and strain recovery. J. Cell Sci.

Way, M., Pope, B., Cross, R.A., Kendrick-Jones, J., and Weeds, A.G. (1992). Expression of the N-terminal domain of dystrophin in E. coli and demonstration of binding to F-actin. FEBS Lett. *301*, 243–245.

Weber, A., Zbiral, B., Iturri, J., Benitez, R., and Toca-Herrera, J.L. (2020). Measuring (biological) materials mechanics with atomic force microscopy. 2. Influence of the loading rate and applied force (colloidal particles). Microsc. Res. Tech. 1–11.

Wheeler, M.T., Zarnegar, S., and McNally, E.M. (2002). zeta-Sarcoglycan, a novel component of the sarcoglycan complex, is reduced in muscular dystrophy. Hum. Mol. Genet. *11*, 2147–2154.

Wilkie, G.S., Korfali, N., Swanson, S.K., Malik, P., Srsen, V., Batrakou, D.G., De Las Heras, J., Zuleger, N., Kerr, A.R.W., Florens, L., et al. (2011). Several novel nuclear envelope transmembrane proteins identified in skeletal muscle have cytoskeletal associations. Mol. Cell. Proteomics *10*, M110.003129.

Wilson, J., Putt, W., Jimenez, C., and Edwards, Y.H. (1999). Up71 and Up140, two novel transcripts of utrophin that are homologues of short forms of dystrophin. Hum. Mol. Genet. *8*, 1271–1278.

Winder, S.J., Hemmings, L., Maciver, S.K., Bolton, S.J., Tinsley, J.M., Davies, K.E., Critchley, D.R., and Kendrick-Jones, J. (1995). Utrophin actin binding domain: Analysis of actin binding and cellular targeting. J. Cell Sci. *108*, 63–71.

Wizemann, H., Garbe, J.H.O., Friedrich, M.V.K., Timpl, R., Sasaki, T., and Hohenester, E. (2003). Distinct requirements for heparin and α-dystroglycan binding revealed by structure-based mutagenesis of the laminin α2 LG4-LG5 domain pair. J. Mol. Biol. *332*, 635–642.

Wright, K.M., Lyon, K.A., Leung, H., Leahy, D.J., Ma, L., and Ginty, D.D. (2012). Dystroglycan Organizes Axon Guidance Cue Localization and Axonal Pathfinding. Neuron *76*, 931–944.

Xia, Y., Pfeifer, C.R., Zhu, K., Irianto, J., Liu, D., Pannell, K., Chen, E.J., Dooling, L.J., Tobin, M.P., Wang, M., et al. (2019). Rescue of DNA damage after constricted migration reveals a mechano-regulated threshold for cell cycle. J. Cell Biol. *218*, 2542–2563.

Yamada, H., Saito, F., Fukuta-Ohi, H., Zhong, D., Hase, A., Arai, K., Okuyama, A., Maekawa, R., Shimizu, T., and Matsumura, K. (2001). Processing of beta-dystroglycan by matrix metalloproteinase disrupts the link between the extracellular matrix and cell membrane via the dystroglycan complex. Hum. Mol. Genet. *10*, 1563–1569.

Yang, B., Jung, D., Motto, D., Meyer, J., Koretzky, G., and Campbell, K.P. (1995). SH3 domain-mediated interaction of dystroglycan and Grb2. J. Biol. Chem. *270*, 11711–11714.

Yatsenko, A.S., Kucherenko, M.M., Xie, Y., Aweida, D., Urlaub, H., Scheibe, R.J., Cohen, S., and Shcherbata, H.R. (2020). Profiling of the muscle-specific dystroglycan interactome reveals the role of Hippo signaling in muscular dystrophy and age-dependent muscle atrophy. BMC Med. 1–26.

Yoshida-Moriguchi, T., Willer, T., Anderson, M.E., Venzke, D., Whyte, T., Muntoni, F., Lee, H., Nelson, S.F., Yu, L., and Campbell, K.P. (2013). SGK196 is a glycosylation-specific O-mannose kinase required for dystroglycan function. Science (80-.). *341*, 896–899.

Yoshida, A., Kobayashi, K., Manya, H., Taniguchi, K., Kano, H., Mizuno, M., Inazu, T., Mitsuhashi, H., Takahashi, S., Takeuchi, M., et al. (2001). Muscular Dystrophy and Neuronal Migration Disorder Caused by Mutations in a Glycosyltransferase, POMGnT1. Dev. Cell *1*, 717–724.

Yoshida, M., Hama, H., Ishikawa-Sakurai, M., Imamura, M., Araishi, K., Wakabayashi-Takai, E., Noguchi, S., Sasaoka, T., and Ozawa, E. (2000). Biochemical evidence for association of dystrobrevin with the sarcoglycan-sarcospan complex as a basis for understanding sarcoglycanopathy. Hum. Mol. Genet. *9*, 1033–1040.

Zemła, J., Bobrowska, J., Kubiak, A., Zieliński, T., Pabijan, J., Pogoda, K., Bobrowski, P., and Lekka, M. (2020). Indenting soft samples (hydrogels and cells) with cantilevers possessing various shapes of probing tip. Eur. Biophys. J. *49*, 485–495.

Zhang, H., Sun, L., Wang, K., Wu, D., Trappio, M., Witting, C., and Cao, K. (2016). Loss of H3K9me3 correlates with ATM activation and histone H2AX phosphorylation deficiencies in Hutchinson-Gilford progeria syndrome. PLoS One *11*, 1–25.

Zhang, J., Alisafaei, F., Nikolić, M., Nou, X.A., Kim, H., Shenoy, V.B., and Scarcelli, G. (2020). Nuclear Mechanics within Intact Cells Is Regulated by Cytoskeletal Network and Internal Nanostructures. Small *1907688*, 1–13.

Zhong, D., Saito, F., Saito, Y., Nakamura, A., Shimizu, T., and Matsumura, K. (2006). Characterization of the protease activity that cleaves the extracellular domain of β-dystroglycan. Biochem. Biophys. Res. Commun. *345*, 867–871.

Zhou, E.H., Trepat, X., Park, C.Y., Lenormand, G., Oliver, M.N., Mijailovich, S.M., Hardin, C., Weitz, D.A., Butler, J.P., and Fredberg, J.J. (2009). Universal behavior of the osmotically compressed cell and its analogy to the colloidal glass transition. Proc. Natl. Acad. Sci. U. S. A. *106*, 10632–10637.

Zhou, H., Di Palma, S., Preisinger, C., Peng, M., Polat, A.N., Heck, A.J.R., and Mohammed, S. (2013). Toward a comprehensive characterization of a human cancer cell phosphoproteome. J. Proteome Res. *12*, 260–271.

Zhu, L., Wang, F., Yang, H., Zhang, J., and Chen, S. (2020). Low shear stress damages endothelial function through STAT1 in endothelial cells (ECs). J. Physiol. Biochem. *76*, 147–157.

Zou, R., Xu, Y., Feng, Y., Shen, M., Yuan, F., and Yuan, Y. (2020). YAP nuclear-cytoplasmic translocation is regulated by mechanical signaling, protein modification, and metabolism. Cell Biol. Int. *00*, 1–10.

Zubrzycka-Gaarn, E.E., Bulman, D.E., Karpati, G., Burghes, A.H.M., Belfall, B., Klamut, H.J., Talbot, J., Hodges, R.S., Ray, P.N., and Worton, R.G. (1988). The Duchenne muscular dystrophy gene product is localized in sarcolemma of human skeletal muscle. Nature *333*, 466–469.